SYNTHESIS, FRACTIONATION, AND THIN FILM PROCESSING OF NANOPARTICLES USING THE

TUNABLE SOLVENT PROPERTIES OF CARBON DIOXIDE GAS EXPANDED LIQUIDS

Except where reference is made to the work of others, the work described in this dissertation is my own or was done in collaboration with my advisory committee. This dissertation does not include proprietary or classified information.

_____

Madhu Anand

Certificate of Approval:

_____ _____

Ram B. Gupta   Christopher B. Roberts, Chair
Alumni Professor   Uthlaut Professor
Chemical Engineering   Chemical Engineering

_____ _____

W. Robert Ashurst   Bart Prorok
Assistant Professor   Assistant Professor
Chemical Engineering   Materials Engineering

_____

George T. Flowers
Interim Dean
Graduate School

SYNTHESIS, FRACTIONATION, AND THIN FILM PROCESSING OF NANOPARTICLES USING THE

TUNABLE SOLVENT PROPERTIES OF CARBON DIOXIDE GAS EXPANDED LIQUIDS

Madhu Anand

A Dissertation

Submitted to

the Graduate Faculty of

Auburn University

in Partial Fulfillment of the

Requirements for the

Degree of

Doctor of Philosophy

Auburn, Alabama
May 10, 2007

SYNTHESIS, FRACTIONATION, AND THIN FILM PROCESSING OF NANOPARTICLES USING THE

TUNABLE SOLVENT PROPERTIES OF CARBON DIOXIDE GAS EXPANDED LIQUIDS

Madhu Anand

_____

Signature of Author

_____

Date of Graduation

Madhu Anand, daughter of Mohinder Pal Anand, was born on November 1st, 1978, in New Delhi, India. She graduated from Shri Guru Harkrishan Public School in Sri Ganganagar, Rajasthan in 1996 and entered Panjab University in Chandigarh, India in 1997. Following four years of school including summer internship at Indian Oil Corporation Limited, a Fortune 500 company, she graduated with a Bachelor of Engineering degree in Chemical Engineering (distinction) in May 2001. Following graduation, she worked in Research and Development department of Shriram Fertilizers and Chemicals, Kota, India. After working there for two years, she entered the Graduate School at Auburn University in August of 2003 where she began working on her Doctorate of Philosophy in the field of nanoparticles processing using compressed fluids.

DISSERTATION ABSTRACT

SYNTHESIS, FRACTIONATION, AND THIN FILM PROCESSING OF NANOPARTICLES USING THE

TUNABLE SOLVENT PROPERTIES OF CARBON DIOXIDE GAS EXPANDED LIQUIDS

Madhu Anand

Doctor of Philosophy, May 10, 2007
(B.E. Chem., Panjab University, 2001)

288 Typed Pages

Directed by Christopher B. Roberts

Nanoparticles have received significant attention because of their unusual characteristics including high surface area to volume ratios. Materials built from nanoparticles possess unique chemical, physical, mechanical and optical properties. Due to these properties, they hold potential in application areas such as catalysts, sensors, semiconductors and optics. At the same time, CO_2 in the form of supercritical fluid or CO_2 gas-expanded liquid mixtures has gained significant attention in the area of processing nanostructures. This dissertation focuses on the synthesis and processing of nanoparticles using CO_2 tunable solvent systems.

Nanoparticle properties depend heavily on their size and, as such, the ability to finely control the size and uniformity of nanoparticles is of utmost importance. Solution based nanoparticle formation techniques are attractive due to their simplicity, but they often result in the synthesis of particles with a wide size range. To

address this limitation, a post-synthesis technique has been developed in this dissertation to fractionate polydisperse nanoparticles ($\sigma = 30\%$) into monodisperse fractions ($\sigma = 8\%$) using tunable physicochemical properties of CO_2 expanded liquids, where CO_2 is employed as an antisolvent. This work demonstrates that by controlling the addition of CO_2 (pressurization) to an organic dispersion of nanoparticles, the ligand stabilized nanoparticles can be size selectively precipitated within a novel high pressure apparatus that confines the particle precipitation to a specified location on a surface. Unlike current techniques, this CO_2 expanded liquid approach provides faster and more efficient particle size separation, reduction in organic solvent usage, and pressure tunable size selection in a single process.

To improve our fundamental understanding and to further refine the size separation process, a detailed study has been performed to identify the key parameters enabling size separation of various nanoparticle populations. This study details the influence of various factors on the size separation process, such as the types of nanoparticles, ligand type and solvent type as well as the use of recursive fractionation and the time allowed for settling during each fractionation step.

This size selective precipitation technique was also applied to fractionate and separate polydisperse dispersions of CdSe/ZnS semiconductor nanocrystals into very distinct size and color fractions based solely on the pressure tunable solvent properties of CO_2 expanded liquids.

This size selective precipitation of nanoparticles is achieved by finely tuning the solvent strength of the CO_2/organic solvent medium by simply adjusting the applied CO_2

pressure. These subtle changes affect the balance between osmotic repulsive and van der Waals attractive forces thereby allowing fractionation of the nanocrystals into multiple narrow size populations. Thermodynamic analysis of nanoparticle size selective fractionation was performed to develop a theoretical model based on the thermodynamic properties of gas expanded liquids.

We have used the general phenomenon of nanoparticle precipitation with CO_2 expanded liquids to create dodecanethiol stabilized gold nanoparticle thin films. This method utilizes CO_2 as an anti-solvent for low defect, wide area gold nanoparticle film formation employing monodisperse gold nanoparticles. Dodecanethiol stabilized gold particles are precipitated from hexane by controllably expanding the solution with carbon dioxide. Subsequent addition of carbon dioxide as a dense supercritical fluid then provides for removal of the organic solvent while avoiding the dewetting effects common to evaporating solvents.

Unfortunately, the use of carbon dioxide as a neat solvent in nanoparticles synthesis and processing is limited by the very poor solvent strength of dense phase CO_2. As a result, most current techniques employed to synthesize and disperse nanoparticles in neat carbon dioxide require the use of environmentally persistent fluorinated compounds as metal precursors and/or stabilizing ligands. This dissertation presents the first report of the simultaneous synthesis and stabilization of metallic nanoparticles in carbon dioxide solvent without the use of any fluorinated compounds thereby further enabling the use of CO_2 as a green solvent medium in nanomaterials synthesis and processing.

The following publications were a product of this dissertation:

M.C. McLeod, M. Anand, C.L. Kitchens, C.B. Roberts, "Precise and Rapid Size Selection and Targeted Deposition of Nanoparticle Populations Using CO_2 Gas Expanded Liquids," *NanoLetters* (2005), 5(3), 461-465.

M. Anand, M. C. McLeod, P. W. Bell, C. B. Roberts, "Tunable Solvation Effects on the Size-Selective Fractionation of Metal Nanoparticles in CO_2 Gas-Expanded Solvents," *J. Phys. Chem.B* (2005), 109(48), 22852-22859.

P. W. Bell, M. Anand, X. Fan, R. M. Enick, C. B. Roberts, "Stable Dispersions of Silver Nanoparticles in Carbon Dioxide with Fluorine-Free Ligands," *Langmuir* (2005), 21(25), 11608-11613.

M. Anand, P. W. Bell, C. B. Roberts, "Synthesis and Stearic Stabilization of Silver Nanoparticles in Carbon dioxide Using Fluorine-Free Compounds," *J. Phys. Chem.B* (2006), 110(30), 14693-14701.

J. Liu, M. Anand, C. B. Roberts, "Synthesis and Extraction of β–D glucose Stabilized Au Nanoparticles Processed into Low Defect, Wide Area Thin Films And Ordered Arrays Using CO_2-Expanded Liquids," *Langmuir* (2006), 22(9), 3964-3971.

M. Anand, L. A. Odom, C. B. Roberts, "Finely Controlled Size Selective Precipitation and Separation of CdSe/ZnS Semiconductor Nanoparticles using CO_2 Gas Expanded Liquids," *Langmuir* (Submitted)

P. Dutta, M. Anand, M. S. Seehra, C. B. Roberts, "Characterization and Magnetic Properties of Gold Nanoparticles," in preparation for *Phys. Rev. Lett*.

M. Anand, C. B. Roberts, "Thermodynamic Analysis of Nanoparticle Size Selective Fractionation Using Gas Expanded Liquids," in preparation for *Industrial & Engineering Chemistry Research*.

Computer software used: Microsoft Office, ImageJ, Endnote 6.0, Omnic E., Hysys

TABLE OF CONTENTS

CHAPTER 1

INTRODUCTION

1.1 Introduction to Nanotechnology

The term 'Nanotechnology' is derived from the root 'nano', meaning one billionth. Its

area of study involves materials with feature of at least one dimension under the length of

100 nanometers. These nanoscale features or dimensions are often smaller than critical

length scales important to many material properties. Because of this, electrical, optical,

magnetic and mechanical properties of nanoscale materials are often completely different

from that of bulk scale materials (Poole and Owens 2003). As a result of this, natural and

manmade objects composed of nanoscale building blocks (Figure 1-1) can be controlled

at the molecular level, the level where basic properties are determined, in order to tailor

the properties (chemical, physical, optical etc.) of the material. In essence,

nanotechnology involves the understanding and manipulation of matter at the nanoscale

in order to exploit these novel and improved properties and to therefore effectively create

and utilize these nanostructures. Biology also works through the systematic coordinated

assemblies of nanoscale objects and nanotechnology helps to understand these life

processes in detail (Jaeger, Westhof et al. 2001; Henderson and Mosher 2002). The

application of nanoscale materials for the creation of powerful devices, materials and

systems can be successful only with knowledge of the underlying fundamental chemistry and physical phenomena from almost all the fields encompassing engineering and science. It is a broad and interdisciplinary research and development field which has spread rapidly throughout the science and engineering world in the past few years. While ample research has been performed in developing methods for creating materials and products at the nanoscale, there is still a great deal of work to be done in fully harnessing the complete potential that nanotechnology provides.

In 1960, Nobel laureate physicist Richard Feynman (Feynman 1993) delivered the famous speech (Feynman 1992) "There's Plenty of Room at the Bottom" and gave insight into the exciting new discoveries that can happen if one could fabricate things at the molecular level. Photography and catalysis are two examples of nanotechnologies where people have benefited from nanoscale systems, but with limited ability to truly control the systems at the nanoscale. It was not until the 1980's that instruments such as scanning tunneling microscope, atomic force microscope, near field microscope and transmission field microscope (Mukasa, Sueoka et al. 1995; Czajka, Polewska et al. 2002) were invented to more easily manipulate and measure material properties at micro and nano scales.

In 1996-98, the World Technology Evaluation Centre (WTEC) did a worldwide study on nanotechnology and organized this broad field according to the chart shown in Figure 1-2. The WTEC report has separate chapters focused on each major area as shown in Figure 1-2. As shown in the chart, nanostructures are made from nanoscale building blocks which are synthesized from atoms and molecules. This is why controlled synthesis of these building blocks and their subsequent assembly into nanostructures is a central

fundamental subject of nanotechnology.

1.1.1 Properties and applications of Nanoscale building blocks

According to the WTEC report, nanostructures are used in four broadly defined areas which are dispersions and coatings, high surface area materials, functional nanodevices and consolidated materials.

Dispersions and coatings utilize nanoscale properties for optical, thermal and electrical applications. Freedom from agglomeration and surface control is required for successful dispersions. Applications such as printing, sunscreens, photography, corrosion protection and pharmaceuticals are already commercialized. Targeted drug delivery, gene therapy, imaging enhancement, and information-recording layers are present research areas.

Nanoscale building blocks have a high surface area to volume ratio because they have more surface atoms than bulk atoms when compared to conventional materials. This high surface area quality can be used in applications like catalysis, adsorption/desorption materials, porous membranes, molecular sieves, sensors, drug delivery and for chemical and electrical energy storage. For instance, nanoscale catalysis can increase the efficiency of chemical reactions, thus affecting potential waste and pollution issues. As another example, many new useful medicines are not water soluble at the microscale but can be dispersed or even dissolved at the nanoscale, thus, nanostructuring can be used in finding new drugs. To improve the impact of high surface area on applications, critical dimensional control and stability of nanoscale building blocks are required to have high selectivity and high product yield.

Nanodevices are being used to expand the technological capabilities of electronic, magnetic, mechanical, and biological systems. In the information technology industry, nanoscale systems can increase the computer efficiency by a million times by reducing the area and volume needed per transistor on chips. Nanoscale systems with higher density of components than microscale systems allow the electrons to move faster between components and give rise to a million times more data storage capacity and increased processing speed as shown in Figure 1-3. Nanodevices will ultimately be utilized to reduce power consumption, enhance energy conversion, control pollution, and improve human health and longevity.

Consolidated materials are bulk size materials made of nanoscale building blocks. Nanostructuring can alter hardness, strength, magnetic and optical properties of materials. Nanoparticle fillers if used in metals, polymers matrices and ceramics can give rise to nanocomposites with unique properties. For example, carbon nanotubes are ten times stronger than steel even though carbon nanotubes are six times lighter in weight than steel. Nanoparticle-reinforced polymers can be used to manufacture lighter cars in the auto industry and thereby reduce fuel consumption and carbon dioxide emission. Nanocomposites also help in producing low-loss magnets, high-hardness and tough cutting tools, and nanocomposite cements.

So, in almost all fields, nanotechnology is useful in making products smaller, lighter and at the same time stronger. The goal is not to reduce the size but to change the properties which can enable breakthroughs in many fields. For example, efficient solar energy conversion and storage, energy efficient and brighter lightning systems, better sensors and process controls to increase efficiency in manufacturing and processing, and

4

stronger and lighter materials to increase transportation efficiency. Eric Drexler's (Drexler 1986) imagination in "Engines of Creation" about changing sand to computer chips or coal to diamond by rearranging the atoms is not possible yet. However, there are number of products incorporating nanomaterials are on the market, for example, metal particles are used in catalytic converters on vehicles, silver particles are used in photographic film and paper, and metal oxide particles are used in sunscreen to block ultraviolet rays. Research is ongoing in many other areas and a lot of new applications are predicted to happen in the near future as shown in Figure 1-4.

1.1.2 Nanoparticles and their Size-Dependent Properties and Applications

As shown in Figure 1-2, nanoparticles are the main building blocks for most nanostructures and controlled nanoparticle formation is the principal synthetic means of creating these building blocks. Nanoparticle size-selective synthesis, post-synthesis refinement techniques and assembly into nanostructures are the basis of this dissertation work. Nanoparticles, which are often smaller than the critical length scale associated with material properties, impart new properties to the nanostructures built from them (Poole and Owens 2003). Properties like conductivity, reactivity, melting temperature and mechanical properties change with the size of the particles and these properties can be tremendously different than the properties of the conventional bulk size materials. There is a huge potential for the applications of nanoparticles by designing the properties of the nanostructures with an exact control over the size and size distribution of the nanoparticles. There are many reasons for the changes in nanoparticle properties with their size such as the change in the number of surface atoms, variations in the density of the electronic energy levels, emergence of wave like transport, and predominance of

interfacial phenomena. Controlling the size and shape of nanoparticles can enhance the material properties and device functions more than what has already been accomplished. Some examples which require a precise and strict control over the nanoparticle size are illustrated below.

1. Uniform-size nanoparticles are required for the calibration of nanoscale property measuring instruments

2. The uniform size of quantum dots gives them their unique colors. Their exceptional optical properties can be utilized in many applications like biological staining and diagnosis (Bruchez, Moronne et al. 1998; Chan and Nile 1998). Electron confinement causes the quantization of bulk energy bands into discrete energy levels and these bands shift to higher energies with a decrease in size. This is called the quantum confinement effect and due to this, quantum dots have different colors corresponding to different dot sizes. Nakashima et.al. (Nakashima, Tsuzuki et al. 1999) have measured the volume plasmon energy in cadmium sulphide quantum dots and examined the shift in energy with particle size.

3. Liu and Zhang have shown that the saturation field and the saturation magnetization vary with the size of the $MnFe_2O_4$ nanoparticles (Liu and Zhang 2001). So superparamagnetic properties of Mn spinel ferrite nanoparticles are size dependent. Similarly, Drachev et.al. have done theoretical studies on size dependent susceptibility $\chi^{(3)}$ for conduction electrons in Ag nanoparticles (Drachev, Buin et al. 2004).

4. Pal et. al. (Pal, Torimoto et al. 2004) have shown the size dependent catalyst activity of silica coated cadmium sulfide nanoparticles for methanol dehydrogenation. Maillard et.al. (Maillard, Schreier et al. 2005) have found that in fuel cells, the reaction is quite sensitive

to the size of Pt nanoparticles and the reaction overpotential increases with a decrease in particle size below 3 nm. Similarly there are many articles in the literature that show the effect of particle size on the kinetics of various reactions (Haruta 1997; Valden, Lai et al. 1998; Arenz, Mayrhofer et al. 2005).

5. Stowell et. al. (Stowell and Korgel 2001) have formed self assembled networks of gold nanocrystals and found that the nanocrystal structures change from honeycomb to rings with an increase in nanoparticle polydispersity. They have also shown the dependence of surface tension in these structures due to particle size, distribution and particle concentration.

All of the above examples show that we need methods to either synthesize monodisperse particles or use post-synthesis techniques to size separate the polydisperse nanoparticle sample into monodisperse fractions.

1.1.3 Nanoparticle Synthesis

Applications of nanoparticles in optical, electronic, magnetic, sensor, superconducting, biological, catalytic and biomedical materials as well as coatings, films, and seeded growth of micro/macro scale materials require controlled synthesis and assembly of nanoparticles of various materials. Nanoparticles can be synthesized in solid, liquid or gaseous phase and then deposited using chemical or physical approaches. Nanoparticles are synthesized either by conventional top-down approaches or bottom-up techniques as shown in Figure 1-5. In the top-down methods, the dimension or dimensions of large-scale objects are gradually reduced by methods such as 'sculpting' from the bulk material, 'ball milling' through mechanical attrition, laser evaporation where a high energy laser beam is incident on a metal rod, causing the atoms of the metal to evaporate

and then subsequently cool into nanoparticles. The bottom up synthesis approach, on the other hand, is where individual atoms and molecules, typically achieved by one of the three chemical methods, acid/base reaction, precipitation, or reduction/oxidation reaction, are assembled into the final material (Poole and Owens 2003). Wu et. al. (Wu, Windeler et al. 1993) has also shown the powder compaction method where first powder components are formed through aerosol techniques and then compacted into the final material. The appropriate synthesis technique for a given application would be one that provides the best control over the size, composition, and distribution of the nanoscale building blocks in the final material.

Gas phase synthesis and solution based processing are contemporary techniques used to synthesize monodisperse nanoparticles with sizes between 1-10 nm and a relative standard deviation of ~25%. Nanoparticles obtained by these techniques also typically have a consistent crystal structure. Gas phase synthesis includes various aerosol techniques, for example combustion flame (Calcote and Keil 1997), plasma (Rao, Lee et al. 1997), laser ablation (Becker, Brock et al. 1998), chemical vapor condensation (Sadangi, Voronov et al. 1999), spray pyrolysis (Messing, Zhang et al. 1993), electrospray (Ahn, Anh et al. 2001) and plasma spray (Karthikeyan, Berndt et al. 1997). Solution based processing techniques include gelation, precipitation and hydrothermal treatment techniques (Kung and Ko 1996). Other techniques for nanoparticle synthesis include sonochemical, cavitation, and microemulsion processing.

This dissertation is focused primarily on metallic and semiconductor nanoparticles. Metallic nanoparticles have found applications in optics, electronics, magnetic materials, sensors, explosives, catalysts, pharmaceuticals, powder metallurgy,

thin films and coatings. There are numerous methods to produce metal nanoparticles, including simple solution based techniques such as reverse micelle synthesis (Cason and Roberts 2000) and two phase arrested precipitation methods (Brust, Walker et al. 1994). In these solution based methods, particles are capped with surfactant or ligand tails to quench nanocrystal growth and stabilize them against attractive van-der Waals forces between the particle cores while they are dispersed in a solvent. Solvent-ligand interaction provides enough repulsive force to disperse the particles in the solution. The balance of these forces can be manipulated to control the particle size and polydispersity of nanoparticles. Shah et. al. (Shah, Husain et al. 2002) proposed a model using a soft sphere approach to balance the attractive van der Waals force against the steric repulsive forces to determine the total interaction energy for dispersed particles in a solvent. The total interaction energy is the sum of attractive and repulsive forces and this should be maintained above the minimum threshold energy of -3/2kT in order to disperse the particles in the bulk solvent.

While these particular solution based synthesis and stabilization techniques are attractive due to their simplicity, they often result in the synthesis of particle sizes with a wide size range (e.g. 2 to 12 nm). As such, post synthesis processing is required to further refine the size distribution to the desired narrow monodisperse range for size-dependent nanoparticle applications. Herein we will use the relaxed definition of monodisperse particles as being samples that have a standard deviation of diameter, σ, less than 5% (Murray, Kagan et al. 2000). A variety of post-synthesis techniques have been developed to narrow size distributions. These include the use of liquid antisolvents (Murray, Norris et al. 1993; Korgel, Fullam et al. 1998; Sigman, Saunders et al. 2004) to

selectively control precipitation, isoelectric focusing electrophoresis (IEF) (Arnaud, Abid et al. 2005) and chromatography techniques (Siebrands, Giersig et al. 1993). As an example, Sigman et al. (Sigman, Saunders et al. 2004) used ethanol as an antisolvent and subsequent centrifugation to size selectively precipitate and separate a polydisperse dispersion of silver nanoparticles capped with dodecanethiol ligands into monodisperse particle fractions.

In these antisolvent nanoparticle precipitation techniques, ligand capped particles are first dispersed in solution where the interaction between the solvent and the ligand tails provides enough repulsive force to overcome the inherent van der Waals attraction between the particles that would otherwise result in agglomeration and precipitation. Through the addition of an antisolvent, the resultant poorer solvent mixture interacts less with the ligand tails than did the pure solvent, thereby reducing the ability of the solvent/antisolvent mixture to disperse the particles. Larger particles possess greater interparticle van der Waals attractions and therefore precipitate first upon worsening solvent conditions followed by subsequent precipitation of the smaller sized particles with further addition of antisolvent. Applying centrifugation then provides an external force to accelerate the precipitation process. Repetition of this antisolvent/centrifugation method on the separated particles can result in narrow particle size distributions, $\sigma < 5\%$, however, the whole process is both solvent and time intensive. It is also difficult to obtain an apriori desired particle size through this separation process in a repeatable manner simply by changing the composition of the liquid antisolvent/solvent pair.

1.1.4 Influence of Solvent on Nanoparticle Stabilization

In solution based techniques, the solvent plays an important role in affecting the size of nanoparticles synthesized and then dispersed in a given solvent. The interactions between the solvent and the particle stabilizing ligands play an important role in the dispersion and precipitation of nanoparticles (Shah, Holmes et al. 2002; Kitchens, McLeod et al. 2003). In general, a decrease in the solvent strength weakens the solvation of the ligand tails and results in stronger tail-tail interactions (Lee, Johnston et al. 2001) thereby decreasing the particle dispersibility. Sufficient solvation of the stabilizing ligand tails is necessary to provide enough repulsive force (osmotic and elastic repulsion) to overcome the van der Waals forces of attraction between the nanoparticles. Since solvent strength plays an important role in nanoparticle synthesis and dispersibility, tunable solvent media including supercritical fluids and gas expanded liquids hold potential for these nanoparticle processing strategies.

1.2 Tunable solvent systems

The solvent strength of compressed fluids can be easily varied by the simple tuning of variables like pressure and temperature of the system which thereby tunes the density of the solvent. These fluids have applications in areas like material processing, particle synthesis, drug formation, etc. Supercritical fluids and gas expanded liquids are two examples of tunable solvent systems which are discussed below.

1.2.1 Properties and Applications of Supercritical fluids (SCFs)

Over the past several years, scientists have been exploring the use of supercritical fluids (SCFs) for a variety of novel applications. A supercritical fluid (SCF) is any material

heated above its critical temperature and compressed above its critical pressure. The physicochemical properties (McHugh and Krukonis 1986) of supercritical fluids (SCFs), such as density, diffusivity, solubility parameter, heat capacity and others can be varied from gas-like to liquid-like as a continuum through simple variations in pressure (density) and temperature. This variation in physicochemical properties opened the door to many novel opportunities for processes based on tunable solvent systems. One major advantage of SCF solvents is that, depending on the temperature and pressure, liquid-like solvent strength (density) can be achieved at the same time when gas like viscosity and diffusivity can be achieved. SCFs also provide other advantages including zero to low surface tensions and higher compressibility than normal liquids. Regarding solubilities in SCFs, there is generally an increase in solubility with an increase in pressure but the effect of temperature depends on the solvent density and the solute vapor pressure. However, an increase in temperature always increases the solute solubility at constant SCF density.

Carbon dioxide is the most studied and used supercritical fluid solvent with almost 100 commercialized industrial plants that employ supercritical (SC) CO_2. CO_2 is generally used because it is green, cheap, relatively inert, nontoxic, readily available, non-flammable, highly miscible with many organic liquids and environmentally benign. In addition to these attributes, the critical temperature (304 K) and critical pressure (71 bar) of CO_2 are easily accessible. Eric Beckman (Beckman 2004) has written an excellent review on chemical synthesis and processing using compressed CO_2 that highlights many applications, advantages and disadvantages of using CO_2 as a solvent. Extraction, chromatography, electronic circuit cleaning and chemical reactions such as

hydrogenations and polymerizations are some examples where use of CO_2 has provided further improvement in a given process or product .

Supercritical CO_2 has also been used to generate microparticles through various solution based techniques where scientists are trying to control particle size, shape and distribution through simple tuning of system pressure. Different methods for particle formation in compressed fluids include spray techniques, aerosol solvent extraction system (ASES) (Bleich, Kleinebudde et al. 1994), gas antisolvent precipitation (GAS) (Randolph, Randolph et al. 1993), precipitation with a compressed fluid antisolvent (PCA) (Dixon, Johnston et al. 1993), supercritical antisolvent (SAS) (Yeo, Debenedetti et al. 1993) and solution-enhanced dispersion by supercritical fluids (SEDS) (Shekunov, Baldyga et al. 2001). In all of these techniques, a solution containing a dissolved solute is mixed with a compressed sometimes a supercritical fluid such as CO_2, which acts as an antisolvent. The solvent dissolves in the compressed fluid, in which the solute is insoluble, and thus precipitates from solution. Many review papers (Jung and Perrut 2001) have been written on all of these processes used to synthesize particles of various materials using supercritical fluids. Even though carbon dioxide has many applications as given above, its use as a solvent is limited due to its relatively poor solvent strength.

CO_2 being a feeble solvent, because of its very low dielectric constant (1.1 to 1.5) and zero dipole moment, cannot dissolve many organic and polymeric species. Although CO_2 has larger solubility parameter (Johnston, Peck et al. 1989) than propane, due to its large quadruple moment, the dispersion component of the solubility parameter is smaller than ethane. Another way of confirming solvent strength, polarizability per volume (refractive index) is also very low for CO_2 resulting in weaker van der Waals forces than

hydrocarbons, therefore making it more similar to a fluorocarbon with respect to solvent strength. This results in higher solubility of fluorinated compounds in CO_2 than in their hydrocarbon analogs. For example, hydrocarbon-chain surfactants are relatively insoluble in CO_2, while adding fluorine atoms into backbone can seriously enhance the solubility. Even though fluorine compounds can increase the CO_2 solubility, these compounds are both environmentally persistent and expensive. Since the two main reasons of using CO_2 is its low cost and environmentally benign nature, these aspects present drawbacks to their use in many processing applications. The disadvantages of poor solubility and high pressure can be overcome to some extent by adding a co-solvent (Dobbs, Wong et al. 1986; Peck, Mehta et al. 1989) or CO_2-philic compounds. These co-solvents are selected to interact more strongly with the solute than does the CO_2 solvent molecules and therefore increase the solubility. For example, solubility of salicylic acid can be increased by the addition of a small amount of methanol. Another option for increasing the solubility and reducing the pressure required in CO_2-based applications, such as precipitation, crystallization, and extraction, involves the use of gas expanded liquids (GELs).

1.2.2 Properties and Applications of Gas Expanded liquids (GELs)

The disadvantages of poor solubility and the requirement of high pressure in supercritical CO_2 operations can be addressed by the use of gas expanded liquid (GEL) systems (Jessop and Subramaniam 2006). GELs are liquids where an organic solvent is pressurized with a gas (e.g. CO_2) and these fluids have the characteristics intermediate to both the gas and the organic solvent. In these CO_2-expanded liquid systems, a liquid solvent is pressurized with CO_2 where CO_2 partitions (dissolves) into the liquid phase to

create a mixture at pressures greater than atmospheric but lower than the vapor pressure of the pure gas component (e.g. lower than 860 psi for CO_2). For example, when an organic solvent like hexane is slowly pressurized with carbon dioxide gas at low pressures, initially very little carbon dioxide dissolves into the liquid phase, but, with further increases in CO_2 pressure applied there is a tremendous increase in the volume of the liquid mixture due to further dissolution of CO_2 into the hexane rich phase and this process is commonly referred to as volume expansion. The composition and properties of GELs, such as surface tension, viscosity, diffusivity, density and solvent strength, can be easily tuned with simple changes in the pressure of the system. GELs work at much lower pressures than liquid and supercritical CO_2. The physicochemical properties of the GEL mixtures lie between the properties of the pure components such that it is easy to tune these properties with a change in the pressure of the gas. Interestingly, it has the best of both of the pure components, including better solvent strength than gases and at the same time, less surface tension and viscosity than normal liquids. The amount of organic solvent is reduced and these processes can be performed at much lower pressures than supercritical CO_2.

These GELs have found applications in gas antisolvent crystallization (Gallagher, Coffey et al. 1989; Eckert, Bush et al. 2000; Xie, Brown et al. 2002; Chen, Zhang et al. 2004), precipitation (Zhang, Han et al. 2002; Liu, Zhang et al. 2003; Zhang, Han et al. 2004; Zhang, Xiao et al. 2004), particle formation (Randolph, Randolph et al. 1993), forming reverse micelles (Zhang, Liu et al. 2002) and in tuning chemical reactions (Thomas, Bonilla et al. 2001; Wei, Musie et al. 2002; Xie, Liotta et al. 2004), etc. Eckert et. al. (Eckert, Bush et al. 2000) have written a detailed review on the applications of

tunable solvents in sustainable technology. The main advantage of this solvent system lies in the ability to tune solubility and the other physicochemical properties. Another distinct advantage involves the easy removal of the CO_2 gas by depressurizing the system thereby allowing complete recycle of both the gas and the liquid constituents. A few of the attributes of GELs are described below in the following examples.

1.2.2.1 GELs as Gas Antisolvent Systems

Gases at elevated pressures have enough solubility in organic liquids and they expand the organic liquids resulting in decrease in solvent strength of the solvent which causes precipitation of dissolved or suspended solid. This process is known as the gas antisolvent (GAS) process using compressed gases as the antisolvent. Researchers have been interested in producing micron size particles with controlled particle size and distribution using gas antisolvent (GAS) (Randolph, Randolph et al. 1993) and supercritical antisolvent (SAS) (Jung and Perrut 2001) process. CO_2 is often preferred for this high pressure process because of its properties, high solubility in organic liquids and that it can expand the liquids up to the vapor pressure of CO_2. Advantages of this process over conventional antisolvent process are the easy adjustment in pressure of CO_2, which can easily vary the solubilities and the mass transfer characteristics, hence affecting the growth of the particles. The solvent and antisolvent can be easily removed and recycled from the system, through decompression.

Han and coworkers have studied the recrystallization of cholesterol in acetone using CO_2 as an antisolvent (Liu, Wang et al. 2002). The solubility of cholesterol in the acetone-CO_2 mixture decreases with CO_2 pressure at pressures lower than 7.5 MPa and

increases with system temperature. This happens mainly due to the change in the CO_2 mole fraction in the mixture that therefore decreases the solvent strength. These researchers have studied the effect of CO_2 pressure on the size and morphology of the particles obtained. Similar effects were found while generating poly(ethylene teraphthalate) (PET) powder from PET/phenol solution using CO_2 as an antisolvent (Li, Liu et al. 2000).

1.2.2.2   GELs exhibit greater solvent strength than Supercritical CO_2

CO_2 has poor solvent strength and, as described earlier, fluorinated ligands are required for nanoparticle synthesis and processing. However, GELs have solvent strength comparable to organic solvents and Mcleod et.al. (McLeod, Kitchens et al. 2005) have shown an example of processing nanoparticles in GELs using conventional organic non-fluorinated ligands. Interestingly, Han and coworkers were able to form reverse micelle of polymer (P104) in p-xylene with the help of compressed CO_2 (Zhang, Liu et al. 2002). While, in the absence of CO_2, the polymer (P104) could not solubilize water in p-xylene.

GELs provide tunable solvation properties: Gas expanded liquids have been used as a switch for the reversible dissolution and recovery of fluorinated complexes and reagents (Jessop, Olmstead et al. 2002). These authors have described this new application of GELs for recrystallization. Here, CO_2 is used as a solvent to make the GELs temporarily fluorophilic so it is an inverse of the GAS process. Fluorinated complexes are insoluble or partially soluble in organic solvents but they are highly soluble in liquid or supercritical CO_2. Thus, the organic solvent is pressurized and expanded with CO_2 to help in dissolving the complexes and then depressurized to

17

precipitate and recover the relatively pure crystals for the purposes of X-ray crystallography.

1.2.2.3 GELs exhibit enhanced mass Transfer compared to conventional solvents

Almost twenty-five masking steps are required while fabricating the integrated circuit and each step requires a photoresist to generate patterns and then, subsequently, photoresist removal process (Spuller and Hess 2004; Spuller and Hess 2004). Commercial liquids have the disadvantages of limited mass transport and a problem of surface wetting because of their viscosity, surface tension and diffusivity of normal liquids. Gas phase processing overcomes these mass transfer and surface wetting limitations, however suffers from poor solubilities. On the other hand, supercritical carbon dioxide has the disadvantage of the high pressures required in its applications. GELs provide an opportunity to overcome these disadvantages due to their excellent mass transfer properties compared to normal liquids while maintaining the reasonable solvent strength.

In an another example, Han and coworkers have shown the variations in the polymerization rate and molecular weights of the polymers polystyrene and poly(methyl methacrylate) with an increase in volume expansion of an organic solvent via CO_2 (Liu, Han et al. 2003). They found an increase in the polymerization rate with the increased volume expansion; this enhanced rate was attributed to high diffusion of monomer into the precipitate in these GEL systems.

1.2.2.4 GELs provide unique reaction environment

Another application of GELs is found in increasing the yield of the desired product in

reactions and in separating those products (Xie, Liotta et al. 2004). In the heterogeneous hydrogenation reaction of benzonitrile and phenylacetonitrile to form primary amines as the major product, the yield is increased by protecting the primary amines in the form of carbamic acids and ammonium carbamates after reacting them with CO_2 in GELs. In homogeneous hydrogenation, the product is separated in the form of solid carbamic acids and ammonium carbamates from the catalyst.

1.3 Nanoparticle synthesis and processing in CO_2 Tunable Solvent Systems

Over the last several years there has been ongoing research in the developing area of processing nanoparticles and other nanomaterials in supercritical CO_2 in order to take advantage of its unique properties (Shah, Hanrath et al. 2004). This section provides a summary of examples of work on application of CO_2 tunable solvent systems in nanoparticles processing

Controlled Nanoparticle Synthesis: Shah et.al. (Shah, Husain et al. 2002) showed that good solvent conditions quenched the growth of silver nanocrystals in CO_2 in the presence of fluorinated thiols resulting in smaller nanocrystals than those synthesized under poor solvent conditions (lower densities). In this case, perfluorodecanethiol-stabilized silver nanocrystals were synthesized in supercritical CO_2 via hydrogen reduction of silver acetylacetonate. It was found that in the early stages of the growth process, metal core coagulation competes with thiol ligand adsorption. Under poor solvent conditions, particles grew to larger sizes (4nm at P < 250bar, T = 80°C compared to 2 nm at P > 250 bar, T = 80°C) before the coverage of capping ligand was sufficient to prevent coagulation of the metal particles illustrating a tunability of particle sizes that

19

could be synthesized through variations in solvent strength.

Tunable Nanoparticles Dispersion: Pressure and temperature tunable solvent properties of CO_2 can also be use for size-selective dispersion of nanoparticles. Shah et al. (Shah, Holmes et al. 2002) demonstrated the size-selective dispersion of dodecanethiol coated nanoparticles in supercritical ethane by density tuning (Shah, Holmes et al. 2002). They illustrated that with the change in solvent density, the dispersable particle size could be adjusted where the largest particle sizes were dispersed at the highest pressure. However, ethane is a feeble solvent and very high pressures of around 414 bar were required to disperse particles of only 3.7 nm in size. Efficient solvent based separation techniques for a wide range of nanoparticle sizes would require better solvent strength than these supercritical solvents are able to provide at significantly lower pressures.

Tunable Nanoparticle Precipitation: Gas expanded liquid systems provide a wide range of solvent properties (from liquid-like to gas-like) that are widely tunable with simple adjustments in gas pressure thereby providing further opportunity for nanoparticle precipitation and separation. For example, Han and coworkers (Zhang, Han et al. 2002) recently precipitated nanoparticles from AOT reverse micelles in liquid isooctane using pressurized CO_2 as an antisolvent.

Thin Film Formation: Unique wetting characteristics of CO_2 can be used in the deposition of metal films on surfaces and the deposition of nanoparticles on surfaces into uniform monolayers. Single phase SCFs eliminate the liquid-vapor interface and, hence, the interfacial forces associated with solvent evaporation. McLeod et. al. (McLeod, Kitchens et al. 2005) and Shah et. al. (Shah, Novick et al. 2003) used dispersions of

20

nanoparticles in supercritical CO_2 and compressed liquid CO_2, respectively, in the formation of thin films of Ag nanoparticles with wider surface area coverage and uniformity compared to the films obtained by simple solvent-evaporation techniques. These wetting characteristics can be used to synthesize high surface area catalysts and to obtain more uniform and ordered thin film assemblies for micro-electronic devices.

While CO_2 does offer certain processing advantages (e.g. tunable solvent strength and wetting characteristics), its use in nanoparticle synthesis, dispersion and processing is limited by the current need for fluorinated compounds resulting from its relatively poor solvent strength. Shah et. al. has written a descriptive review on nanoparticle synthesis and dispersibility in supercritical fluids (Shah, Hanrath et al. 2004). Nanoparticles are typically formed in CO_2 by water in CO_2 (W/C) microemulsions or by arrested precipitation techniques using fluorinated compounds. As explained earlier, fluorinated surfactants (Hoefling, Beitle et al. 1993) have shown high solubility in CO_2 and some of them have stabilized water in CO_2 microemulsions (Calcote and Keil 1997). Fluorinated surfactants and ligands have each been used to disperse particles in CO_2. Interactions between CO_2 and the fluorinated coating on the nanoparticles provide enough repulsive forces to counterbalance the attractive van der Waals forces between the particles. In W/C microemulsion systems, fluorinated surfactant supported aqueous cores act as nanoreactors to synthesize and then disperse the particles in a CO_2 phase due to strong fluorine-CO_2 interactions. Various types of particles have been prepared in W/C microemulsions including: Ag (Ji, Chen et al. 1999; McLeod, McHenry et al. 2003), Ag halide (Liu, Raveendran et al. 2005), Cu (Ohde, Hunt et al. 2001), and semiconductor nanoparticles (Holmes, Bhargava et al. 1999). Since fluorinated compounds are

environmentally persistent and expensive, researchers are also trying to develop CO_2-philic fluorine free compounds or surfactants to form stable microemulsions in CO_2. For non-fluorinated compounds, the disadvantages of poor solubilities and high cloud point pressures can be overcome by adding co-solvents or CO_2-philic compounds. These co-solvents interact more strongly with the solute than CO_2 and can increase their solubility. Zhang et. al. (Zhang, Liu et al. 2003) used p-Xylene as co-solvent and were able to form Au nanoparticles in CO_2 induced reverse micelles of non-fluorinated surfactants. One class of compounds that have shown high solubility in CO_2 are highly branched, methylated and stubby surfactants due to increased tail solvation and weak tail-tail interactions (Eastoe, Paul et al. 2001; da Rocha, Dickson et al. 2003; Stone, Da Rocha et al. 2003; Stone, Smith et al. 2004). Researchers synthesized stubby hydrocarbon surfactants (Liu, Han et al. 2001; Ryoo, Webber et al. 2003) to form microemulsions in CO_2 and ionic hydrocarbon surfactants (Dickson, Smith et al. 2005; Fan, Potluri et al. 2005), trisiloxane surfactants (da Rocha, Dickson et al. 2003) to stabilize macroemulsions in CO_2.

Researchers have also synthesized nanoparticles in supercritical CO_2 using arrested precipitation techniques and dispersing the particles in a single continuous CO_2 phase while eliminating the aqueous phase. Arrested precipitation is one of the most successful solution based techniques for nanoparticle synthesis in conventional solvents. In this technique, an organometallic precursor, soluble in a given solvent, is reduced in the presence of a capping ligand (Brust, Walker et al. 1994) to quench further growth. Shah (Shah, Husain et al. 2001; Shah, Husain et al. 2002) and Mcleod (McLeod, Gale et al. 2004) used this technique in supercritical CO_2 and capped the synthesized

nanoparticles with fluorinated thiol stabilizing ligands. Recently, Fan (Fan, McLeod et al.) was also successful in using a non-fluorinated precursor silver bis(3,5,5-trimethyl-1-hexyl)sulfosuccinate (Ag-AOT-TMH) and fluorinated thiols to stably disperse the particles in CO_2. They used a non-fluorinated organometallic compound, Ag-AOT-TMH, a highly methylated stubby compound with a very high solubility in CO_2, however, fluorinated ligands were still used. Even though fluorinated compounds generally have higher solubility in CO_2, the two main reasons for using CO_2 are its low cost and its environmentally benign nature. The cost and environmental problems of fluorinated compounds present drawbacks to their use in many processing applications.

Recently, Bell et. al. (Bell, Anand et al. 2005) used a stubby non-fluorinated compound, iso-stearic acid, to disperse Ag nanoparticles in compressed liquid CO_2. In this technique, nanoparticles were first made in a conventional organic solvent using sodium bis(2-ethylhexyl) sulfosuccinate (AOT) reverse micelles and then the capping agent was replaced by iso-stearic acid. When these iso-stearic acid capped particles were dispersed in CO_2, only a very small fraction of the synthesized particles were dispersed in CO_2 due to the difference between the solvent strength of CO_2 and the organic solvent in which the particles were synthesized.

1.4 Summary of Chapters in this Dissertation on Application of CO_2 Tunable Solvent Systems in Nanoparticles Processing

The following section provides a summary of the chapters given in this dissertation.

1.4.1 Chapter 2

The highly tunable solvent properties of CO_2 expanded organic solvents were utilized to

size selectively precipitate and separate ligand stabilized metal nanoparticle dispersions into narrow distributions through fine adjustments in CO_2 pressure in Chapter 2. By pressurizing an organic solution with CO_2, dodecanethiol stabilized silver nanoparticles were size selectively precipitated within a novel apparatus that confined the particles to specified locations on a surface allowing their separation. Accordingly, the solvent strength of the medium was tuned through successive CO_2 pressurization to provide sequential precipitation of increasingly smaller particles.

1.4.2 Chapter 3

A detailed study was performed to examine the factors influencing this nanoparticle size separation process using CO_2 as an antisolvent. Variations in ligand–solvent interactions were examined to demonstrate the effects of solvent strength and thiol length on the CO_2 pressure range required for particle size separation. The effect of temperature on this pressure range for precipitation was also studied. Recursive fractionation on particles collected at a given pressure range was performed to show that multiple fractionations further improve the CO_2 antisolvent size separation process, just as is observed in traditional liquid antisolvent processes.

1.4.3 Chapter 4

This Chapter demonstrates the rapid fractionation and separation of polydisperse dispersions of CdSe/ZnS semiconductor nanocrystals into very distinct size and color fractions based solely on the pressure tunable solvent properties of CO_2 expanded liquids. This highly precise, and less solvent intensive, size selective precipitation technique is achieved by directing semiconductor nanocrystal precipitation at specific locations within

24

a unique Archimedes screw type apparatus coupled with fine adjustment of the solvent strength of the CO_2/hexane medium. These subtle changes in solvent strength affect the balance between osmotic repulsive and van der Waals attractive forces in the nanoparticle dispersion, thereby allowing fractionation of the nanocrystals into multiple narrow size (color) populations.

1.4.4 Chapter 5

We have extended the general phenomenon of nanoparticle precipitation with CO_2 expanded liquids to an improved method for nanoparticle thin film deposition in Chapter 5. This is often performed by simply evaporating a liquid solution containing ligand stabilized nanoparticles to leave behind dry nanoparticles coated on a surface. However, solvent dewetting and capillary forces at the liquid/vapor interfaces can lead to film defects such as nanoparticle islands, percolating networks, ring-like particle arrays, and uneven particle concentration. We have developed a novel nanoparticle deposition technique which utilizes CO_2 as an anti-solvent for low defect, wide area metallic nanoparticle film formation employing monodisperse nanoparticles. Ligand stabilized metallic particles are precipitated from organic solvents by controllably expanding the solution with carbon dioxide. Subsequent addition of carbon dioxide as a dense supercritical fluid then provides for removal of the organic solvent while avoiding the dewetting effects common to evaporating solvents. These dewetting effects and interfacial phenomena can be very detrimental to nanoscale structures. Controllable expansion of the liquid solution via CO_2 injection allows for control over the physicochemical properties that govern this deposition and assembly process. Ordered thin film arrays of metal nanoparticles were successfully produced using this CO_2-

expanded liquid technique provided that the original dispersion of nanoparticles was fairly monodisperse.

1.4.5 Chapter 6

Ag nanoparticles were synthesized and dispersed in neat CO_2 using fluorine-free compounds in Chapter 6. This reduces the whole process of synthesis and dispersion of nanoparticles in CO_2 for nanoparticle processing to one step without using any harmful organic solvents. This chapter describes the first illustration of a one-step synthesis and stabilization of metallic nanoparticles in CO_2 using non-fluorinated compounds with a tremendous increase in the concentration of particles dispersed than previously achieved without fluorinated ligands.

1.4.6 Chapter 7

A thermodynamic model and related equations were developed to improve our understanding of the size selective fractionation of ligand stabilized nanoparticles using a CO_2 gas expanded liquid precipitation process. This size selective precipitation process is based on controlled reduction of the solvent strength of the organic solution through increases in the antisolvent CO_2 concentration via pressurization. A decrease in the solvent strength reduces the repulsive Osmotic contributions to the total interaction energy of the dispersion by weakening the interactions between the solvent and the ligand tails. Eventually, these repulsive forces in the dispersion are lowered to the point where they can no longer overcome the van der Waals forces of attraction between particles, thereby causing the particles to precipitate. This results in an ability to tune the size of the nanoparticles that are dispersed or precipitated simply by adjusting the CO_2 pressure. In

this chapter, Osmotic energy and Hamaker constant expressions were developed for CO_2 gas expanded solvent mixtures consisting of an organic solvent (e.g. hexane) and antisolvent (e.g. CO_2). These expressions, coupled with appropriate thermodynamic data, were used to estimate the maximum size of dodecanethiol capped Ag nanoparticles that could be dispersed at a given CO_2 pressure by equating the total interaction energy to the Boltzman threshold stabilization energy (-3/2 kT). A parameter sensitivity analysis was performed to determine which parameters most affect the predicted maximum particle size that could be dispersed at a given CO_2 pressure. It was found that the length of the ligand tail that interacts with the solvent medium had the most influence on these total interaction energy calculations. Assuming complete solvation of the entire ligand tail, the model always overpredicted the size of the particles that would be precipitated at a given CO_2 pressure compared to the experimental results. Consequently, we have proposed that the entire length of the dodecane chain is not accessible to the solvent medium. As such, three phenomenological model variations were developed that provide for differing abilities of the ligand tails to interact with the solvent.

Figure 1-1 Comparison of the size of nanoscale objects with the size of small everyday objects. Courtesy of the Office of Basic Energy Sciences, Office of Science, U.S. Department of Energy.

Building Blocks

Atoms

Synthesis

Nanoparticles

Assembly

Nanostructures

| Dispersions and Coatings | High Surface Area Materials | Functional Nanodevices | Consolidated Materials |
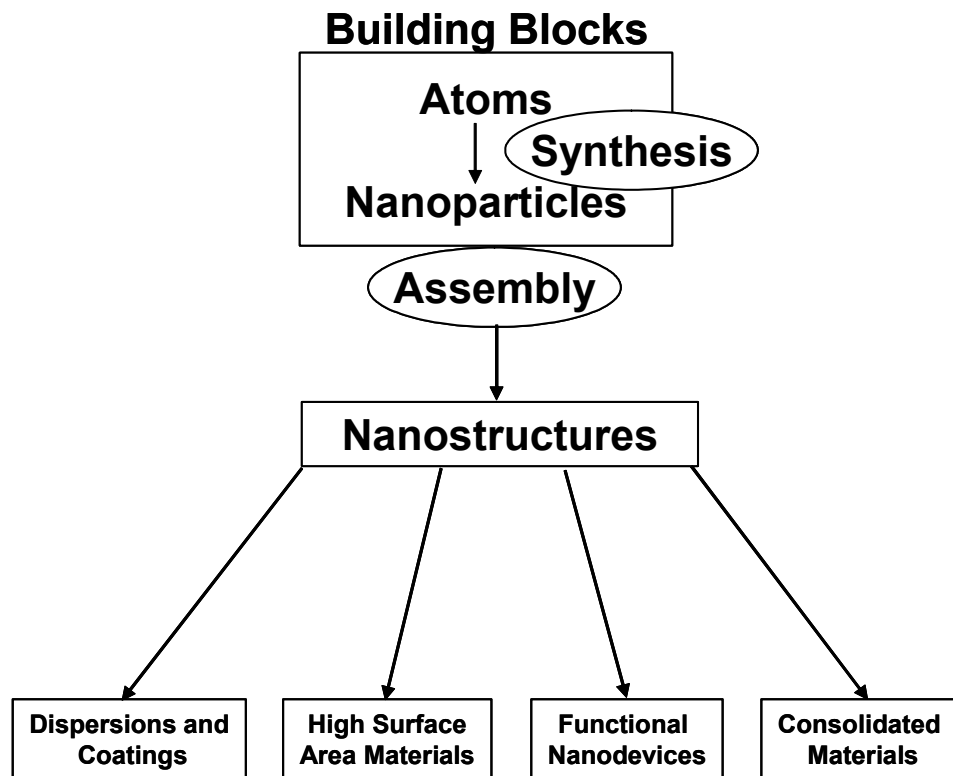
Figure 1-2 Nanostructures science and technology was described according to this chart in the WTEC study (adapted from WTEC study 1999, National Science and Technology Council, Interagency Working Group on Nano Science, Engineering and Technology (IWGN)).
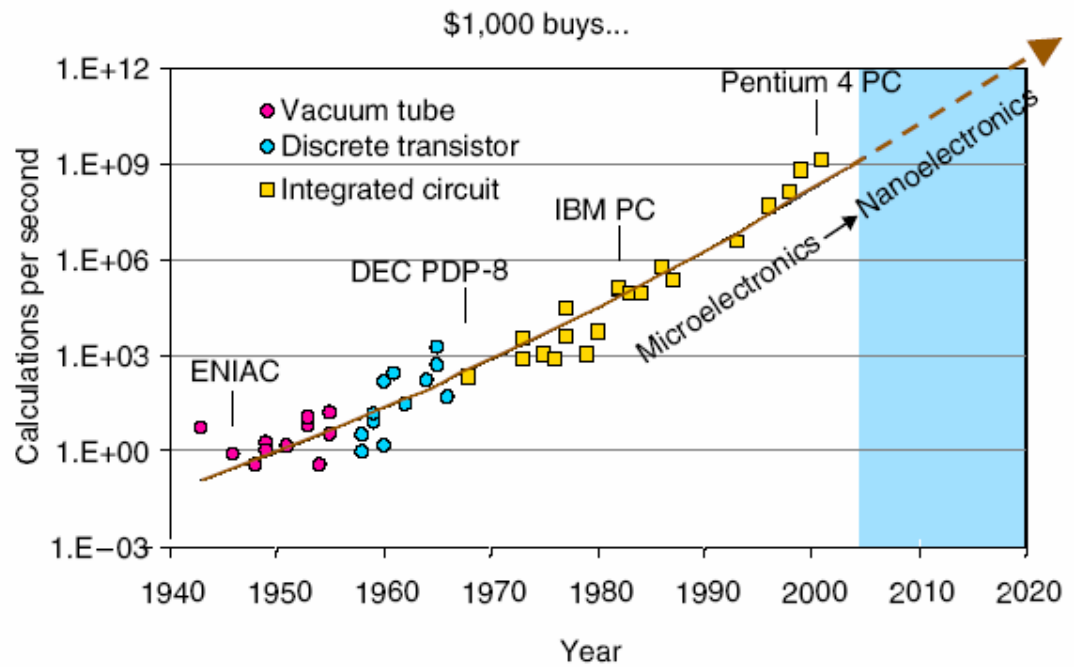
Figure 1-3 The increasing efficiency of components in computing and information technology due to decrease in size. (adapted from R. Kurzweil, The Age of Spiritual Machines, Penguin Books, 1999).
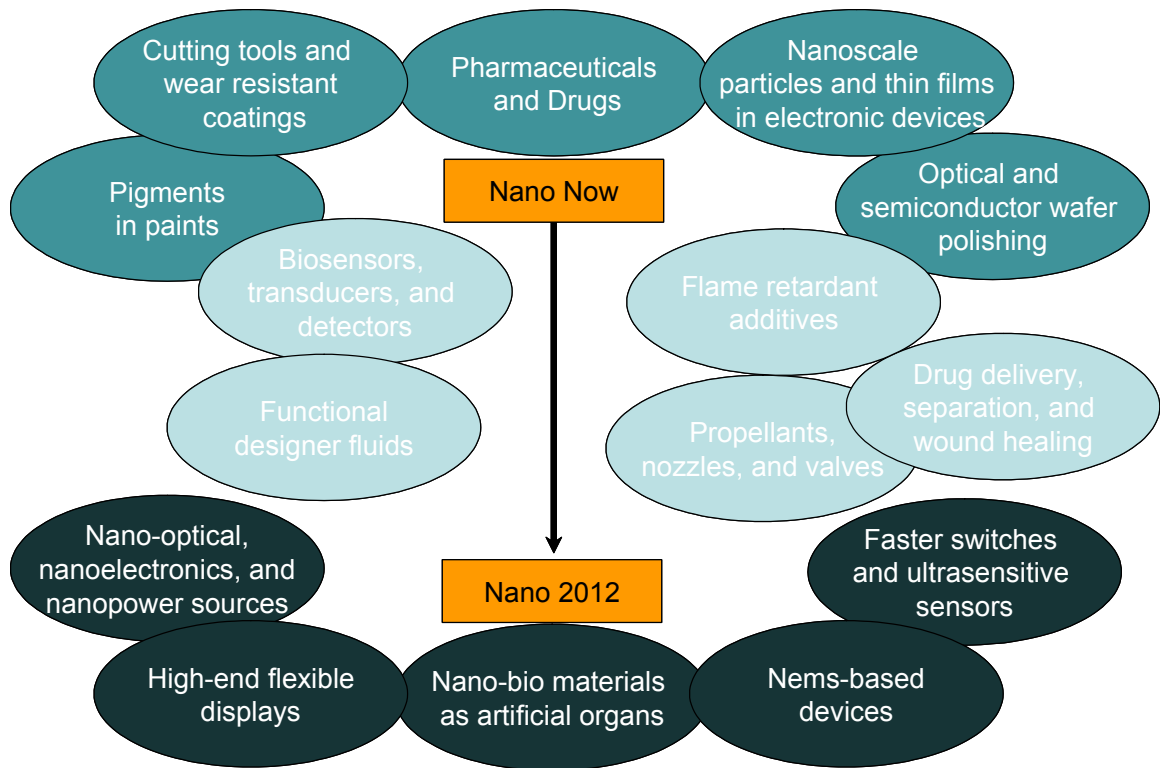
Figure 1-4 Recent and potential applications of nanotechnology and time line for anticipated advances (adapted from Small Wonders, Endless Frontiers, National Research Council Review of the NNI, 2002).

Nanostructured Material

Assemble from Nano- building Blocks

• powder/aerosol compaction
• chemical synthesis

'Sculpt' from Bulk

• mechanical attrition (ball milling)
• lithography/etching...
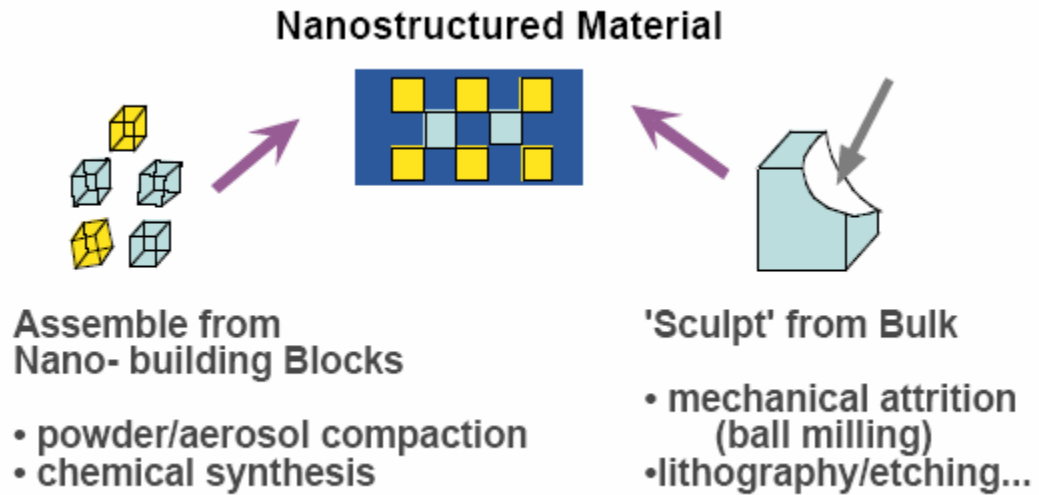
Figure 1-5 Representation of variety of nanostructure synthesis and assembly approaches. (adapted from WTEC study 1999, National Science and Technology Council, Interagency Working Group on Nano Science, Engineering and Technology (IWGN)).

CHAPTER 2

PRECISE AND RAPID SIZE SELECTION AND TARGETED DEPOSITION OF NANOPARTICLE

POPULATIONS USING CO_2 GAS EXPANDED LIQUIDS

This chapter demonstrates the rapid and precise size selection of nanoparticle populations using the pressure tunable solvent properties of CO_2-expanded liquids. Specifically, by pressurizing and expanding a single organic solution with carbon dioxide gas, ligand stabilized silver particles of desired mean size were size selectively precipitated at desired locations. Compared to current techniques, this CO_2-expanded liquid approach provides for faster and more efficient particle size separation, a reduction in organic solvent usage, and pressure tunable size selection.

2.1 Introduction

Many nanoscale materials manifest unusual mechanical, chemical, magnetic, and optical properties which can be utilized in applications demanding improved or specialized performance (Adair, Li et al. 1998). Not only do these properties arise on the nanoscale, but they are also often size dependent. Thus, controlling the size and size distribution can provide opportunities to tune the special characteristics of nanomaterials for chosen

applications. Spherical nanoparticles in particular have received considerable attention since they allow for an investigation of basic properties of nanomaterials. However, despite the widespread interest and investigation of ligand stabilized nanoparticles over the last decade, relatively little improvement has been made to the time consuming and solvent intensive techniques employed for isolating monodisperse particle populations of ligand stabilized particles (Fischer, Weller et al. 1989; Vossmeyer, Katsikas et al. 1994). We have developed a greatly improved method for obtaining monodisperse particle populations from an initially polydisperse solution of ligand capped metal nanoparticles. Our improved methodology utilizes gaseous CO_2 as the antisolvent to induce an organic/CO_2 liquid mixture often termed a gas-expanded liquid (Eckert, Bush et al. 2000) and in so doing allows for pressure tunable particle separation. The benefits of this implementation are four fold: 1) The use of CO_2 eliminates large quantities of organic liquid solvents and antisolvents required in the traditional technique. 2) By simply choosing the amount of CO_2 pressurization, the mean size of precipitated particles can be easily predetermined. 3) The degree of polydispersity can be determined simply by the pressure increment of fractionation. And lastly, 4) through creative implementation, multiple monodisperse particle populations can be rapidly fractionated by adjusting only the CO_2 pressure and liquid location on a surface.

Monodisperse particle populations are required in order to identify individual particle properties from the bulk population as well as to elucidate size dependent properties. Once the known characteristics and behavior of defined particle populations are known, the particles can be applied to specific needs. Two often cited examples of nanoscale size dependent behavior are the fluorescence of semiconductor nanoparticles

(quantum dots) when exposed to ultraviolet light and the unusual ultraviolet-visible absorbances of many metallic nanoparticles (Creighton and Eadon 1991; Bruchez, Moronne et al. 1998). For the case of quantum dots, narrowly sized populations are currently finding application as size tunable fluorescent probes in biological staining and diagnostics (Bruchez, Moronne et al. 1998).

The most commonly used technique for particle size selection uses liquid solvent/anti-solvent pairs combined with centrifugation to selectively precipitate the largest particles from solution (Murray, Norris et al. 1993). The method takes advantage of the inherent van der Waals attractions between particles which lead to the aggregation and subsequent precipitation of unstabilized particles from solution. Capping ligands which attach to the particle surface are often used to provide a barrier against particle aggregation and growth but they also facilitate particle dispersal in liquid solvents which solvate the tails. The solvent interaction with the capping ligands attached to the particle then determines particle dispersibility. Assuming a good solvent for the ligands, solvation of the capping agent tails provides a repulsive force of sufficient strength and range to overcome the interparticle attraction. In a poor solvent, the ligands are not sufficiently solvated by the solvent and are thus unable to prevent the interparticle attraction, agglomeration, and precipitation. Hence, gradual addition of antisolvent to the dispersed particle solution can induce a gradual reduction in solubility for the particles in solution. Since large particles possess greater interparticle van der Waals attractions, they precipitate first upon worsening solvent conditions. Centrifuging the particle solution can then accelerate precipitation of the larger particles from solution. Repetition of the size-selection procedure to the recovered particles can successfully narrow the particle

distribution to less than 5% standard deviation ($\sigma < 5\%$) (Murray, Norris et al. 1993). While monodispersity implies that nanoparticles be identical in size and shape, this definition is often relaxed to allow for a 5% or even a 10% standard deviation since many interesting behaviors such as crystalline nanoparticle organization into nanoparticle arrays and crystalline lattice superstructures occur at this level of size similarity (Collier, Vossmeyer et al. 1998; Murray, Kagan et al. 2000; Sigman, Saunders et al. 2004). Fractions of successively smaller sizes can be obtained by repeating the process with the remaining supernatant. In addition to being time consuming and solvent intensive, the technique can be somewhat subjective as it is often based on the observed opalescence of the solution upon antisolvent addition (Murray, Norris et al. 1993; Vossmeyer, Katsikas et al. 1994). Therefore, obtaining similar size fractions can be difficult if the particles are fractionated separately. Otherwise, solutions must be mixed in careful quantities to achieve desirable solvent conditions. Evidently, recursive application of this technique to obtain multiple monodisperse populations of different mean size is, by nature, time and solvent intensive (Vossmeyer, Katsikas et al. 1994). In addition to solvent/antisolvent size narrowing, size exclusion chromatography has also been utilized for size selection but, unfortunately, throughput with this method is limited (Fischer, Weller et al. 1989; Wilson, Szajowski et al. 1993).

Our method for improved size separation of nanoparticles relies on the phenomenon whereby gaseous CO_2 pressurized over an organic liquid can expand the liquid volume several fold (Gallagher, Coffey et al. 1989; Kordikowski, Schenk et al. 1995; de la Fuente Badilla, Peters et al. 2000). For this reason the resulting liquid CO_2/organic mixture is referred to as a gas-expanded liquid or GEL. By simply changing

the pressure of gaseous CO_2, the fraction of CO_2 liquid comprising the GEL can be altered and, accordingly, the solubility can be tuned between the solvent strength of the initial solvent and that of liquid carbon dioxide. For particle dispersibility, a threshold strength of interaction between the solvent mixture and ligand tails is necessary to sterically stabilize particles of a given size (Kitchens and Roberts; Shah, Hanrath et al. 2004). By adding CO_2 (pressurizing) to the solution, the solvent strength diminishes to below the threshold interaction value for that particle size, at which point the correspondingly sized particles precipitate. An especially attractive feature of the GEL for particle separation is that the pressures required are relatively low (typically below 800 psi) whereas the pressure tunable solubility offered by supercritical fluids requires pressures exceeding the fluid's critical point. Moreover, it has been shown that in order to attain dispersability of small particles in supercritical fluids, pressures must far exceed the critical pressure with further elevations in pressure necessary to disperse even larger particles (Kitchens and Roberts; Shah, Hanrath et al. 2004). For example, small 1.8 nm diameter gold crystals can be dispersed at 2000 psi in supercritical ethane while 6000 psi is required to disperse 4.2 nm particles (Shah, Hanrath et al. 2004). For the case of supercritical CO_2, which is attractive as an environmentally friendly and highly tunable solvent, particle dispersibility is even more challenging because of CO_2's weak solvent strength (Sarbu, Styranec et al. 2000). Nanoparticles have only been successfully dispersed in liquid and supercritical CO_2 through the use of fluorinated ligands (Shah, Hanrath et al. 2004) which are unfortunately both costly and environmentally persistent. In our methodology, however, the feeble solvent nature of carbon dioxide is harnessed for the benefit of effective particle separation. Since carbon dioxide is a notoriously weak

solvent having no dipole moment and little self interaction (Johnston, Harrison et al. 1996; Beckman 2003), it is an ideal antisolvent for separations. Yet, in spite of their obvious utility as tunable solvent systems, GEL's have been popularized only in the last few years, being so far implemented for purposes such as the tuning of reactions (Thomas, Bonilla et al. 2001; Wei, Musie Ghezai et al.), the switching of fluorous compound solubility (Jessop, Olmstead et al. 2002), and the separation of metallic nanoparticles from reverse micelles in isooctane (Zhang, Han et al. 2001). Until this time, however, gas expanded liquids have not been employed for the size selection and separation of nanoparticles.

2.2 Experimental

Fisher deionized water was used in particle synthesis and all other chemicals were used as supplied by Aldrich Chemical Co.

2.2.1 Silver Nanoparticle Synthesis

The hexane dispersed dodecanethiol coated silver particles used in this research were prepared by arrested precipitation methods (Brust, Walker et al. 1994; Sigman, Saunders et al. 2004). A Solution of silver ions (0.19g of $AgNO_3$ in 36 mL of H_2O) was combined with an organic solution containing a phase transfer catalyst, tetraoctylammonium bromide (2.7 g of tetraoctylammonium bromide in 24.5 mL of chloroform). After stirring this mixture for 1 hr, the aqueous phase was discarded. 240 μL of dodecanethiol was then added to the organic mixture and stirred for 5-10 min. An aqueous $NaBH_4$ reducing agent solution (0.5 g of $NaBH_4$ in 30 mL of H_2O) was then added and the mixture was stirred for 4-12 h before discarding the aqueous phase.

Figure 2-3A shows a transmission electron microscope image of the original unprocessed silver particles and Figure 2-4 shows the corresponding measured size distribution data (heavy line) for the unprocessed nanoparticle population. The particles exhibit a broad size distribution with particles ranging principally between 2 and 10 nm, having a mean size of 5.5 nm, and a 32% standard deviation. This concentrated hexane/particle mixture was then size-selectively fractionated using our GEL apparatus.

2.2.2 Size Selective Separation of Silver Nanoparticles

In order to achieve the physical separation of different sized particles from an initially polydisperse population, the precipitation apparatus shown in Figure 2-1 was developed which permits GEL antisolvent tuning and localized particle precipitation. The basis of the apparatus is comprised of an open-ended glass tube fabricated to include concentric spiral grooves placed into the tube and traversing from end to end. The glass tube was 12 cm long by 2 cm in diameter. The concentric spiral grooves are 6 mm deep and create a 2.5 cm wide by 6 mm deep spiral channel. These grooves create a spiral channel within the tube such that rotation of the tube can move the liquid/particle mixture to specific desired locations along the length of the channel The glass tube was 12 cm long by 2 cm in diameter. The concentric spiral grooves were 6 mm deep and created a 2.5 cm wide by 6 mm deep spiral channel. The spiral tube was placed in high-pressure stainless steel cylindrical view cell sealed on one end by a quartz window and on the opposite end with a Teflon fitting. The Teflon fitting allows an 1/8 in. stainless rod to enter the vessel and connect with the spiral tube through a Teflon interconnect. This interconnect allows rotation of the metal rod from outside the vessel while maintaining a dynamic high pressure seal. As such, the spiral tube can be manipulated to control the location of the

particle dispersion within the tube.

To start off the separation process, 700 µL of pure hexane was placed inside the high pressure vessel external to the glass tube and allowed to sit for ca. 10 minutes to facilitate vapor saturation. This was done as a precaution to prevent excessive hexane evaporation at the beginning of each experiment. Here it should be noted that, for the specific case of dodecanethiol coated silver particles, most particle precipitation was observed to occur between 400 and 700 psi by UV-vis spectroscopy as depicted in Figure 2-2. The figure shows the absorbance change of silver nanoparticles in hexane brought on by their reduced solubility in the CO_2 expanded liquid at various pressures. The original hexane/particle solution was then placed in the channel nearest the quartz window and the vessel was pressurized to an initial pressure. Once elevated to the starting pressure the system was allowed to reach GEL equilibrium over a 20 minute time period. During this time, the largest fraction of particles, which are no longer soluble in the expanded liquid, precipitate and affix to the glass surface of the tube through van der Waals attraction. The spiral tube is then rotated to move the liquid to the next location while leaving the precipitated particles behind, affixed on the glass surface. Increasing the pressure to the next chosen level drives the second fraction to precipitate. Such fractionation can be performed as many times as the length of the tube permits so long as the precipitation areas are separated, with pressure increments selected to achieve the desired level of particle dispersity.

This original polydisperse particle population was fractionated using GEL tuning as follows: 200 μL of hexane solution containing dispersed Ag-thiol particles was loaded into the starting section of the spiral tube. The pressure was then slowly elevated to 500

psi and allowed to equilibrate over 20 minutes. After the equilibration period, the spiral glass tube was rotated 180° to displace the particles remaining dispersed in the hexane from those which had precipitated and attached to the glass surface. This series of pressurization, equilibration, and displacement was repeated at pressures of 550 psi, 600 psi, 625 psi, and 650 psi. In total, six fractions were recovered when counting the 5 precipitated populations along with the particles remaining in solution after the final pressurization. Particles from each section were collected by redispersing the particles in hexane and then placing a small drop on a carbon coated copper TEM grid.

2.3 Results and Discussion

Figure 2-3 shows the unprocessed particles along with the particles collected from each section and allows for their close comparison. The largest particles were precipitated and recovered at 500 psi and successive precipitation of smaller particles continues at increasing pressures. The corresponding size distributions for each recovered fraction are portrayed in Figure 2-4 and give quantitative emphasis to the precise separation that can be achieved using this technique. Statistical analysis of the original solution and the fractionated populations is shown in Table 2-1 Statistical analysis of particle populations. The first six fractions following the original population were separated in a single experiment. The last two fractions were obtained in separate experiments about a common mean pressure of 600 psi. All silver particles precipitate from hexane by 700 psi, therefore the last ΔP is listed as < 50 psi. As expected, smaller pressure changes between precipitations provide even greater precision through more subtle adjustments to solvent strength. When the pressure change to induce precipitation is sequentially

41

lowered from a ΔP of 500 to 50 to 25 psi, the standard deviation falls from 20.7 to 15.8 to 10.1%, respectively. No further cleaning was performed on any of the fractionated particles but recursive processing should further narrow the size distribution in a manner similar to liquid/liquid size selection. All six particle populations were selected from the original distribution using only the initial hexane and gaseous CO_2 while taking no longer than 1.5 hours, a major improvement over current methods.

To further deduce the extent to which the size distribution can be narrowed by decreasing the increment of pressurization, two nanoparticle fractionations were performed about a common mean pressure of 600 psi. The first fractionation was performed as previously detailed but with pressurization to 575 psi followed by 625 psi. The particles precipitated then represent a 50 psi fractionation increment centered at 600 psi. Similarly, the second fractionation was performed between 597 and 603 psi, thus providing for a smaller 6 psi fractionation increment centered about the common 600 psi mean. The particles obtained from the 50 psi and the 6 psi pressure changes were collected from the vessel as before and placed on the TEM grid using a CO_2-antisolvent deposition technique. Grids were placed in a 10 mm deep by 6 mm diameter glass tube and filled with 25 μL dilute hexane/nanoparticle solution. The tubes were then placed in a high-pressure vessel and gradually pressurized with CO_2 to 800 psi to induce antisolvent deposition of particles on the grid. This technique circumvents interfacial tensions and size selective organization (Ohara, Leff et al. 1995) common to drying liquids that can potentially throw off size characterizations. Figure 2-5 shows the population distribution for the two separate pressure changes and demonstrates the size selection capable with both a large and small pressure increment to induce particle

deposition. A significant separation with a 16.1% standard deviation is achieved for the 50 psi deviation, whereas the 6 psi deviation achieves a visibly narrower size distribution with a 14.7% standard deviation. The size distribution of the 6 psi fraction has a narrowed distribution for the majority population but possesses an offset shoulder due to residual small particles. The separation achieved using this GEL technique is remarkable in that an initial polydisperse nanoparticle solution can be narrowed to populations with greater than 55 % of the population having $\sigma \leq 5\%$ in a single pressurization step. Traditional liquid size selective separations typically achieve less than 30 % of the particles with $\sigma \sim 5\%$ in one process step when starting with a population having $\sigma \leq 10\%$ (Murray, Kagan et al. 2000). Also of note in this series of experiments is the fact that the mean size of each recovered population is the same, attesting to the repeatability and ability to "tune" for a specific size by dialing in an appropriate pressure.

2.4 Conclusion

We have demonstrated that CO_2 can be used to dramatically improve the traditional liquid solvent/antisolvent size selective precipitation techniques employed for narrowing the size distribution of nanoparticles through pressure tunable gas-expanded liquids. Not only is the volume of required organic solvent reduced but multiple nanoparticle populations can be separated rapidly while obtaining greater monodispersity of the selected population all in a single step. Additionally, pressure can be used to select the precise nanoparticle size that is desired for recovery. For these reasons, this new utilization of CO_2 gas-expanded liquids provides the field of nanotechnology with a simple, yet powerful new tool for nanoparticle manipulation and selection.

2.5 Acknowledgements
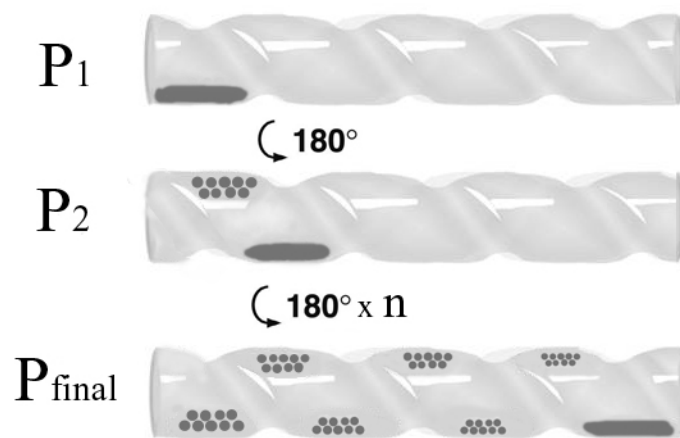
Figure 2-1 Nanoparticle size selection apparatus depicting recursive pressurization of organic liquid with CO_2 followed by 180° tube rotation to achieve multiple size selected populations. The high-pressure vessel which enclosed the glass tube is not shown in the figure.
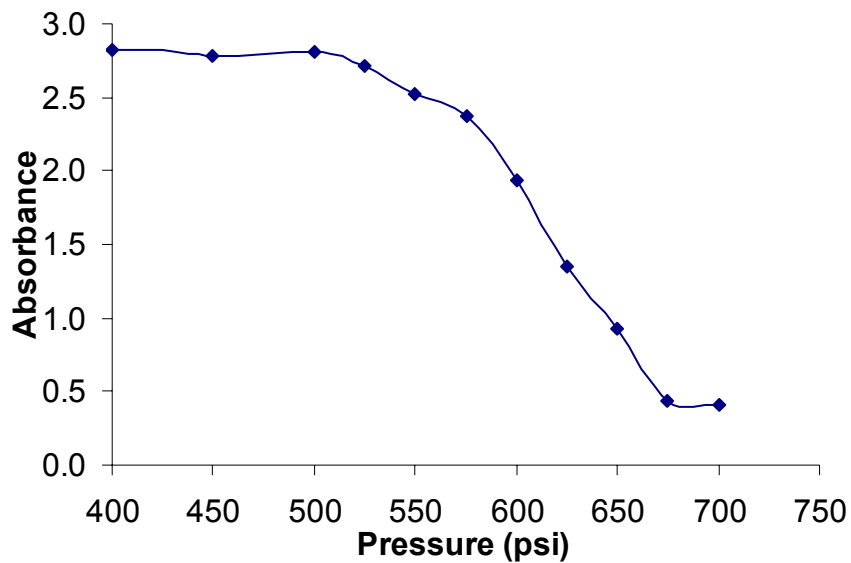
Figure 2-2 Change in UV-vis absorbance of polydisperse dodecanethiol stabilized silver nanoparticles at different CO_2 pressures. Absorption data has been corrected for the change which would occur due to volume expansion so that absorption change presented depicts particles falling from solution at different CO_2 pressurizations.
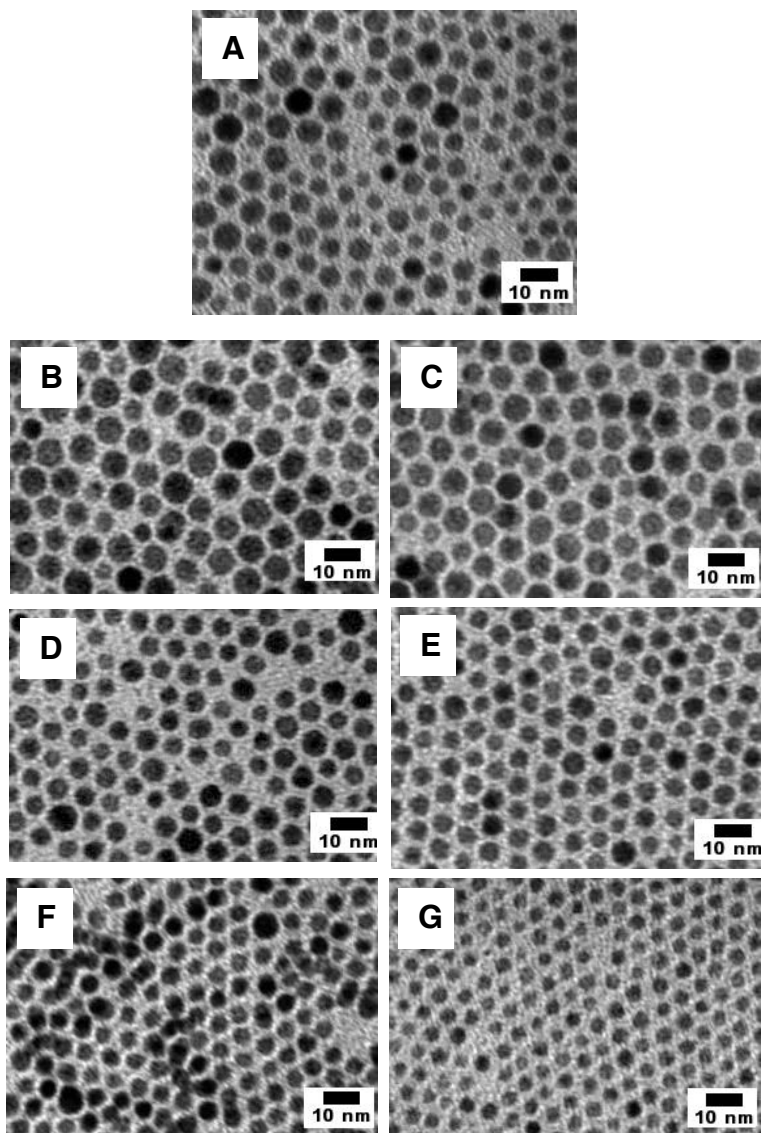
Figure 2-3 TEM micrographs of (A) unprocessed dodecanethiol silver particles and TEM micrographs of particles precipitated from hexane by CO_2 pressurization from (B) 0 to 500 psi, (C) 500 to 550 psi, (D) 550 to 600 psi, (E) 600 to 625 psi, (F) and 625 to 650 psi. (G) Particles remaining in solution after 650 psi CO_2 pressurization.
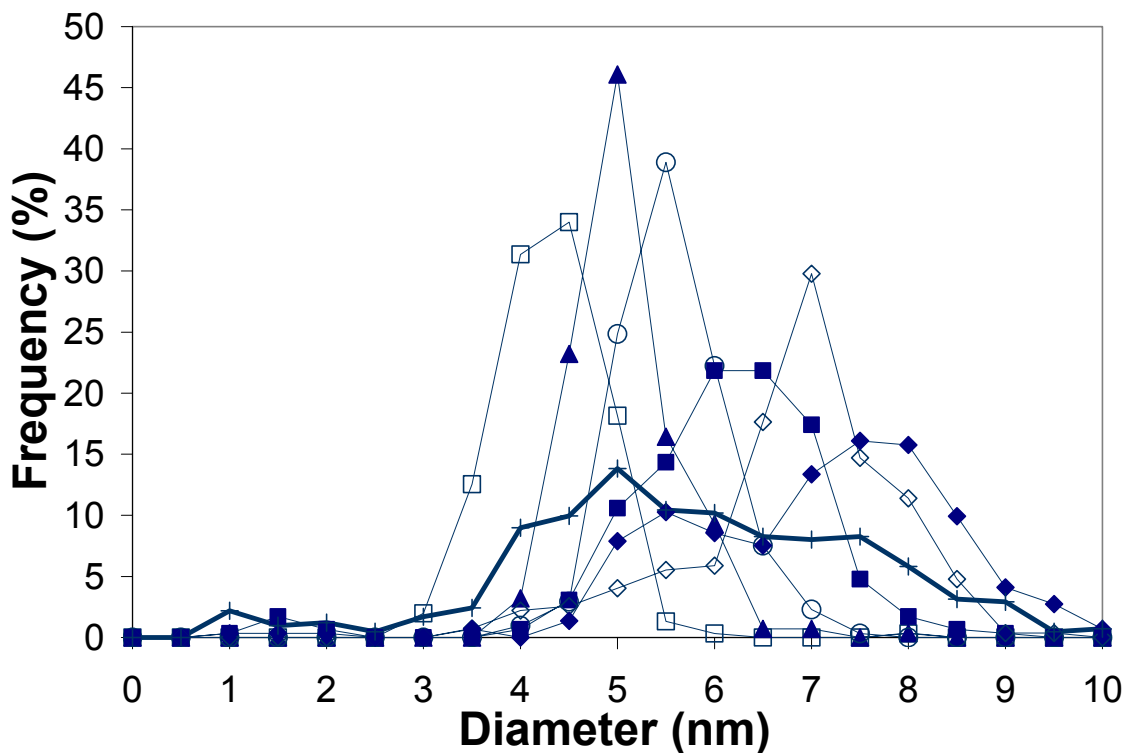
Figure 2-4 Size distribution of unprocessed particles (+, heavy line) and particles fractionated at CO_2 pressures of 500 psi (◆), 550 psi (◇), 600 psi (■), 625 psi (○), 650 psi (▲), and particles remaining in solution after 700 psi (□). Data points represent the percentage of particles of the total population found between the associated diameter and 0.5 nm less that diameter.

Table 2-1 Statistical analysis of particle populations. The first six fractions following the original population were separated in a single experiment. The last two fractions were obtained in separate experiments about a common mean pressure of 600 psi. All silver particles precipitate from hexane by 700 psi, therefore the last ΔP is listed as < 50 psi.

Fraction (psi)	ΔP of fraction (psi)	Mean Diameter (nm)	Std Dev (nm)	Relative Std Dev (%)	95% Confidence (nm)	Particle Count
Original	0	5.5	1.7	31.9	0.2	412
0 to 500	500.0	6.7	1.4	20.7	0.2	292
500 to 550	50.0	6.6	1.0	15.8	0.1	272
550 to 600	50.0	5.8	1.1	18.9	0.1	293
600 to 625	25.0	5.3	0.5	10.1	0.1	306
625 to 650	25.0	4.8	0.5	11.2	0.1	280
650 +	< 50	4.1	0.6	13.7	0.1	280
575 to 625	50	5.8	0.9	16.1	0.1	514
597 to 603	6	5.6	0.8	14.7	0.1	613

49
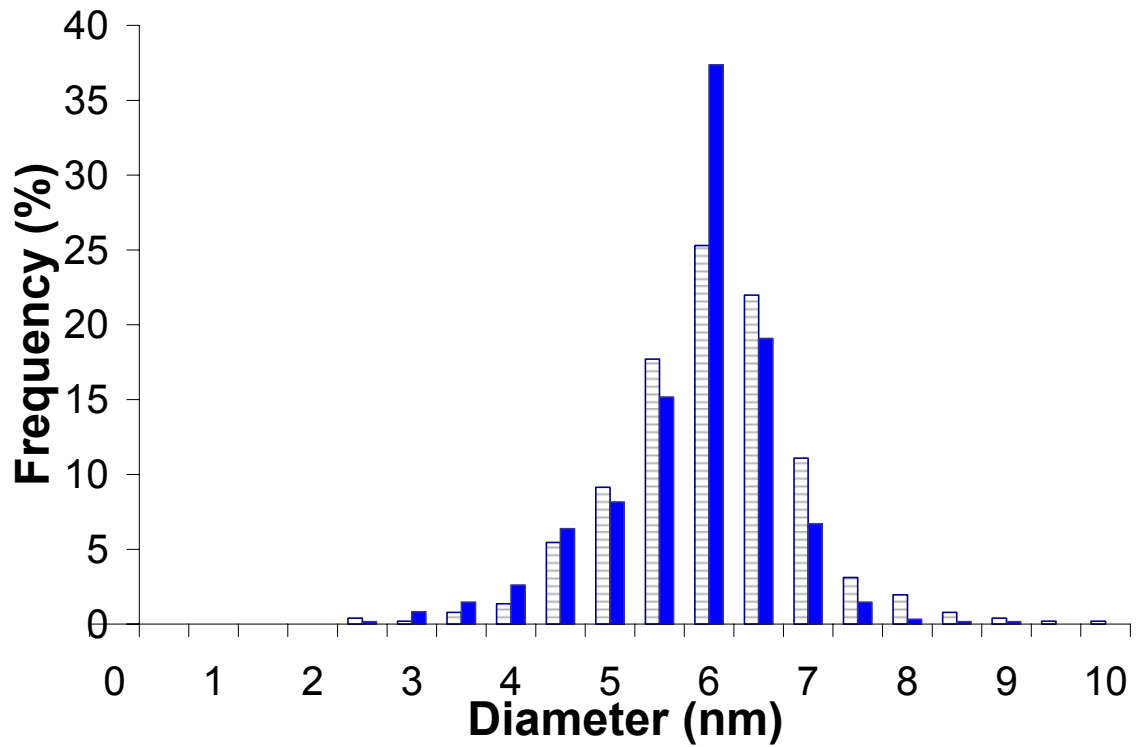
Figure 2-5 Size distribution of particles fractionated at mean pressures of 600 psi by pressurization from 575 to 625 psi ($\Delta P = 50$ psi) (light) and by fractionating from 597 to 603 psi ($\Delta P = 6$ psi) (dark).

CHAPTER 3

T̲UNABLE S̲OLVATION E̲FFECTS ON THE S̲IZE S̲ELECTIVE F̲RACTIONATION OF M̲ETAL

N̲ANOPARTICLES I̲N CO_2 G̲AS E̲XPANDED S̲OLVENTS

This chapter presents an environmentally friendly, inexpensive, rapid and efficient

process for size selective fractionation of polydisperse metal nanoparticle dispersions into

multiple narrow size populations. The dispersibility of ligand-stabilized silver and gold

nanoparticles is controlled by altering the ligand tails-solvent interaction (solvation) by

the addition of carbon dioxide (CO_2) gas as an antisolvent, thereby tailoring the bulk

solvent strength. This is accomplished by adjusting the CO_2 pressure over the liquid,

resulting in a simple means to tune the nanoparticle precipitation by size. This study also

details the influence of various factors on the size separation process, such as the types of

metal, ligand and solvent as well as the use of recursive fractionation and the time

allowed for settling during each fractionation step. The pressure range required for the

precipitation process is the same for both the silver and gold particles capped with

dodecanethiol ligands. A change in ligand or solvent length has an effect on the

interaction between the solvent and the ligand tails and therefore the pressure range

required for precipitation. Stronger interactions between solvent and ligand tails require

greater CO_2 pressure to precipitate the particles. Temperature is another variable that

impacts the dispersibility of the nanoparticles through changes in the density and the

51

mole fraction of CO_2 in the gas expanded liquids. Recursive fractionation for a given system within a particular pressure range (solvent strength) further reduces the polydispersity of the fraction obtained within that pressure range. Specifically, this work utilizes the highly tunable solvent properties of organic/CO_2 solvent mixtures to selectively size-separate dispersions of polydisperse nanoparticles (2 to 12 nm) into more monodisperse fractions (±2 nm). In addition to providing efficient separation of the particles, this process also allows all of the solvent and antisolvent to be recovered, thereby rendering it a green solvent process.

3.1 Introduction

Nanoparticle based technologies take advantage of the fact that materials built from particles less than a critical length (Poole and Owens 2003) display unique chemical and physical properties. These properties depend heavily on the size, shape and composition of the nanoparticles. The size dependent properties of nanoparticles allows one to engineer them to have a specific function such as in catalysts (Pal, Torimoto et al. 2004; Arenz, Mayrhofer et al. 2005; Maillard, Schreier et al. 2005), quantum dots for optical properties (Mahamuni 1999; Nakashima, Tsuzuki et al. 1999) and medical applications (Bruchez, Moronne et al. 1998). The preparation of monodisperse metal particles is also necessary to study the effects of size on their novel applications including size dependent conduction of electrons in Ag nanoparticles (Drachev, Buin et al. 2004) and size dependent oxidation with Au catalysts (Haruta 1997; Valden, Lai et al. 1998). Moreover, monodisperse nanoparticles are also critical in the production of high quality ordered arrays and ordered thin films (Korgel, Fullam et al. 1998; Stowell and Korgel 2001; Shah, Novick et al. 2003; Shah, Sigman et al. 2003).

There are numerous methods to produce metal nanoparticles, including simple solution based techniques such as reverse micelle synthesis (Cason and Roberts 2000; Kitchens, McLeod et al. 2003) and two phase arrested precipitation methods (Brust, Walker et al. 1994). While these particular solution based techniques are attractive due to their simplicity, they often result in the synthesis of particle sizes with a wide size range (e.g. 1 to 20 nm). As such, post synthesis processing is required to further refine the size distribution to the desired narrow monodisperse range. Herein we will use the relaxed definition of monodisperse particles as being samples that have standard deviation, σ, of diameter less than 5% (Murray, Kagan et al. 2000) to 10%. A variety of post-synthesis techniques have been developed to narrow size distributions including the use of liquid antisolvents (Murray, Norris et al. 1993; Korgel, Fullam et al. 1998; Sigman, Saunders et al. 2004) to selectively control precipitation, isoelectric focusing electrophoresis (IEF) (Arnaud, Abid et al. 2005) and chromatography techniques (Siebrands, Giersig et al. 1993). As an example, Sigman et al. (Sigman, Saunders et al. 2004) used ethanol as an antisolvent and centrifugation to size selectively precipitate and separate a polydisperse dispersion of silver nanoparticles capped with dodecanethiol ligands into monodisperse particle fractions.

In these antisolvent nanoparticle precipitation techniques, ligand capped particles are first dispersed in solution where the interaction between the solvent and the ligand tails provides enough repulsive force to overcome the inherent van der Waals attraction between the particles that would otherwise result in agglomeration and precipitation. Through the addition of an antisolvent, the resultant poorer solvent mixture interacts less with the ligand tails than did the pure solvent, thereby reducing the ability of the

solvent/antisolvent mixture to disperse the particles. Larger particles possess greater interparticle van der Waals attractions and therefore precipitate first upon worsening solvent conditions followed by subsequent precipitation of the smaller sized particles with further addition of antisolvent. Applying centrifugation then provides an external force to accelerate the precipitation process. Repetition of this antisolvent/centrifugation method on the separated particles can result in narrow particle size distributions, $\sigma < 5\%$, however, the whole process is both solvent and time intensive. It is also difficult to obtain an apriori desired particle size through this separation process in a repeatable manner simply by changing the composition of the liquid antisolvent/solvent pair. To overcome this limitation, and to provide improved control over size selective precipitation, McLeod et al. (McLeod, Anand et al. 2005) developed an antisolvent precipitation technique based on the pressure tunable solvent properties of gas expanded liquid mixtures (liquid solvents pressurized with CO_2) as described later in this chapter.

Research in the area of compressed and supercritical fluid solvents has shown that the pressure and temperature tunable solvent properties in these systems provides a means to control the size of nanoparticles that can be synthesized and/or dispersed (Clarke, Waters et al. 2001; Shah, Husain et al. 2002; Kitchens and Roberts 2004; Shah, Hanrath et al. 2004). Shah et al. demonstrated the size-selective dispersion of dodecanethiol coated nanoparticles in supercritical ethane by density tuning (Shah, Holmes et al. 2002). They illustrated that with the change in solvent density, the dispersable particle size could be adjusted where the largest particle sizes were dispersed at the highest pressure. However, ethane is a feeble solvent and very high pressures of around 414 bar were required to disperse particles of only 3.7 nm in size. Efficient

54

solvent based separation techniques for a wide range of nanoparticle sizes would require better solvent strength than these supercritical solvents are able to provide at significantly lower pressures.

Gas expanded liquid systems, on the other hand, provide a wide range of solvent properties (from liquid-like to gas-like) that are widely tunable with simple adjustments in gas pressure thereby providing further opportunity for nanoparticle precipitation and separation (McLeod, Anand et al. 2005). For example, Han and coworkers recently precipitated nanoparticles from AOT reverse micelles in liquid isooctane using pressurized CO_2 as an antisolvent (Zhang, Han et al. 2002; Liu, Zhang et al. 2003; Zhang, Han et al. 2004). This antisolvent effect with CO_2 is available because compressed gases such as CO_2 dissolve into organic liquids and expand the liquid volume significantly while also altering the liquid's solvation characteristics. These pressurized liquid solutions of organic solvent and CO_2 mixtures are commonly referred to as gas expanded liquids (GELs). Among their many applications, GELs have been used as tunable reaction media (Thomas, Bonilla et al. 2001; Wei, Musie et al. 2002; Xie, Liotta et al. 2004), as adjustable solvents for separations (Gallagher, Coffey et al. 1989; Eckert, Bush et al. 2000; Xie, Brown et al. 2002; Chen, Zhang et al. 2004), in the switching of fluorous compound solubilities (Jessop, Olmstead et al. 2002), and in gas antisolvent (GAS) precipitation techniques for organic and polymer microparticle formation (Randolph, Randolph et al. 1993). CO_2 is an excellent choice in these gas expanded liquids as it is a very weak solvent even at high pressures (Beckman 2003) and has no dipole moment and very low refractive index (Shah, Hanrath et al. 2004). As such, the solvent strength of CO_2 expanded organic liquid solutions can be varied from that of the pure organic to that

of liquid CO_2 at pressures below the vapor pressure of CO_2.

McLeod et al (McLeod, Anand et al. 2005) utilized the highly tunable solvent properties of CO_2 expanded organic solvents to size selectively precipitate and separate ligand stabilized metal nanoparticle dispersions into narrow distributions through fine adjustments in CO_2 pressure. By pressurizing an organic solution with CO_2, ligand stabilized nanoparticles were size selectively precipitated within a novel apparatus that confined the particles to specified locations on a surface allowing their separation. Accordingly, the solvent strength of the medium was tuned through successive CO_2 pressurization to provide sequential precipitation of increasingly smaller particles. A novel spiral tube apparatus was developed for separating polydisperse silver nanoparticles into different fractions of uniform sizes by regulating the CO_2 pressure (McLeod, Anand et al. 2005) and therefore altering the liquid's solvation of the particle ligand tails. The advantage of this apparatus is that it separates a polydisperse solution of nanoparticles into fairly monodisperse fractions in one contiguous process. This method has a number of advantages compared to traditional liquid based size selection methods and can be applied to a broader range of particle sizes as compared to SCF CO_2 particle processing while operating at much lower pressures. This method also avoids the use of expensive and environmentally persistent fluorinated molecules commonly used in SCF processing, while simultaneously allowing for the separation of particles from a minimum amount of organic liquid. These characteristics make it a green solvent process.

In this chapter, a detailed study was performed to examine the factors influencing this nanoparticle size separation process using CO_2 as antisolvent. Variations in ligand–solvent interactions were examined to demonstrate the effects of solvent strength and

thiol length on the CO_2 pressure range required for particle size separation. The effect of temperature on this pressure range for precipitation was also studied. Recursive fractionation on particles collected at a given pressure range was performed to show that multiple fractionations further improve the CO_2 antisolvent size separation process, just as is observed in traditional liquid antisolvent processes.

3.2 Experimental Section

3.2.1 Materials

Silver nitrate (99.8% purity) ($AgNO_3$) was obtained from Acros. Hydrogen tetrachloroaurate trihydrate (99.9%) ($HAuCl_4.3H_2O$), tetraoctylammonium bromide (98%), chloroform (99.8%), sodium borohydride (99%), dodecanethiol (98%), hexanethiol (95%), octanethiol (98.5%), tetradecanethiol (98%), hexane (99%), cyclohexane (99.5%), octane (99%) and heptane (99%) were obtained from Aldrich chemical Co. Pentane (99.6%), toluene (99%) and deionized water (D-H_2O) was obtained from Fisher. Ethanol (200 proof) was obtained from Florida Distillers. Carbon dioxide (SFC/SFE grade) was obtained from Airgas. All chemicals were used as supplied.

3.2.2 Nanoparticle Synthesis

Ligand stabilized silver and gold nanoparticles were synthesized by the two phase arrested precipitation method as developed by Brust et. al. (Brust, Walker et al. 1994). In short, a solution of 0.19g of $AgNO_3$ in 36 mL of D-H_2O was mixed with an organic solution of 2.7 g of tetraoctylammonium bromide in 24.5 mL of chloroform. The mixture was stirred for 1 hr, the aqueous phase was removed, and then 240μL of dodecanethiol

were added. A solution of 0.5 g of NaBH$_4$ in 30 mL of D-H$_2$O was added as a reducing agent after stirring the mixture for 5-10 min. The mixture was stirred for 4-12 h before discarding the aqueous phase. In addition to dodecanethiol, other thiols were used to examine the effect of thiol length on the size separation process. In each case, the mole percentage of thiol added was the same as that of the dodecanethiol described above. Gold nanoparticles were synthesized by replacing 0.19g of AgNO$_3$ with 0.38g of hydrogen tetrachloroaurate trihydrate (HAuCl$_4$·3H$_2$O), replacing chloroform with toluene, and adding thiol after 4-12 hours of stirring. The delayed addition of thiol was performed to accommodate the higher affinity of the ligands to gold particles.

Once the thiol coated metal particle dispersion was formed, ethanol was added as antisolvent. The dispersion of nanoparticles in the solvent/antisolvent mixture was then centrifuged (Fisher Centrific Model 228) to precipitate out the metallic nanoparticles. The particles were again washed with ethanol and centrifuged to remove any unbound ligands. This process of washing with ethanol was repeated 3 times to remove the phase transfer catalyst. The particles were then dispersed in hexane by sonication (Fisher). The remaining dispersion of nanoparticles in hexane was used for further experimentation.

3.2.3 UV-visible Absorbance Spectroscopy

The UV–visible absorbance spectrum of the particle dispersions in both neat solvent and in the CO$_2$ expanded solvents was measured in a high pressure view cell with a Varian 300E spectrophotometer to monitor the precipitation of gold particles with added CO$_2$ pressure. The cell had a stainless steel body with two O-ring sealed windows on opposite ends. The optical path length of the cell was 3 cm. A quartz cuvette of 10mm path length

was filled with 3mL of organic solvent and 200µL of the hexane solution of dispersed nanoparticles. A Teflon cuvette holder was then used to position the dispersion in a quartz cuvette at the centerline of the windows. The view cell was then pressurized with CO_2 using an ISCO 260D syringe pump and UV-Vis absorbance spectra were collected at each operating pressure until the maximum absorbance value reached a steady value. This was an indication of an equilibrium condition being reached in terms of particle dispersion.

3.2.4 Size Selective Precipitation Process

The spiral tube apparatus as shown in Figure 3-1 was fabricated to obtain monodisperse metal nanoparticle populations (McLeod, Anand et al. 2005) from an initially polydisperse population through precipitation at specific locations on a surface via CO_2 pressurization. This apparatus involves a 12 cm long, 2 cm diameter glass tube modified to include a concentric, spiral indentation on the surface of the tube from one end to the other. These indentations provide a 6mm deep, 2.5 cm wide spiral channel, or groove, inside of the tube that allows a liquid droplet of nanoparticle dispersion resting within the channel to be translated from one location to another by a simple rotation of the tube while keeping the length of the tube horizontal. The spiral tube is situated within a cylindrical high pressure stainless steel view cell equipped on one end with an O-ring sealed quartz window for observation. The other end is fitted with Teflon tapered high pressure fitting that allows entry of a 1/8 in. stainless steel rod attached to the spiral tube with a Teflon interconnect. This assembly allows radial rotation of the spiral tube within the high pressure vessel by simply turning the metal rod from outside the vessel while a

dynamic high pressure seal is maintained by the Teflon fitting. The location of a liquid droplet situated in the glass tube channel (inside the tube) can then be controlled by turning the steel rod. The process was initiated by introducing 700μL of pure hexane into the high pressure view cell in the annular space outside of the spiral tube and allowing it to sit for at least 10 min. This hexane was introduced to saturate the system with hexane vapor prior to introducing the nanoparticle dispersion sample. This was done in order to minimize evaporative losses of hexane from the dispersion droplet during the separation process. Next, 250μL of the hexane dispersion of thiol coated metal particles was introduced into the channel of the spiral tube at the horizontal position closest to the quartz window as shown in the top image in Figure 3-2. The vessel was then slowly pressurized to an initial pressure of 550 psi and allowed 20 min to equilibrate at location A in the spiral tube. Of the overall 950μL of hexane introduced into the 60 ml vessel (both inside and outside of the spiral tube), 15% of this hexane is dissolved into the CO_2 gaseous phase at equilibrium at 500 psi and 25°C, and this partitioning is increased to 22% of this hexane dissolved into the CO_2 at the highest pressure of 700 psi as determined by phase equilibrium calculations using the Peng Robinson equation of state. More importantly, the increased concentration of CO_2 in the solvent mixture (liquid phase) decreases the overall solvent strength such that particles too large to be stabilized by the now weakened CO_2/solvent mixture will precipitate during this 20 minute settling time. van der Waal's forces cause the particles to adhere to the surface on which they precipitate. To separate the remaining liquid dispersion from the precipitated particles, the tube was rotated by turning the rod 180°. This rotation moves the liquid dispersion to the next location B (180° around the tube, but further along axially) leaving behind the

precipitated particles affixed to the spiral groove A. The vessel was then pressurized to 600 psi with the suspension at the new location; the particles that precipitate at this pressure are, on average, smaller than those that precipitated at the lower pressure. The glass tube is then turned another 180° to take the dispersion to a new location C leaving this second fraction of affixed particles behind in the second location B. This process was continued to acquire fractions at 625 and 650 psi at positions C and D respectively. A final precipitation at 700 psi can induce the precipitation of the remaining particles from the hexane dispersion at location E in the spiral tube.

3.2.5   Sample Collection

After completing the final precipitation, the vessel was depressurized. There were 5 particle populations in the spiral tube at locations A, B, C, D and E. These 5 particle samples were recovered through redispersion in hexane, giving 5 size fractions. Sample grids were made by evaporative deposition and tested for particle size distribution on a Zeiss EM 10 Transmission Electron Microscopy (TEM).

3.3 Results and Discussion

3.3.1 Volume Expansion of the Solution

When a given organic dispersion of nanoparticles was pressurized with CO_2, the volume of the organic phase was increased by dissolution of CO_2 until equilibrium was reached. This increase in volume of the organic dispersion/CO_2 mixture can be characterized by the volume expansion coefficient, defined as, where   is the volume of the solution saturated with CO_2 at a given pressure and   is the volume of the CO_2 free solution (unpressurized). This volume expansion coefficient was estimated using the Peng-

Robinson equation of state (Peng and Robinson 1976) and compared well to measurements made by visual observation of volume expansion in a high pressure Jerguson site gage (less than 5% error between the experimental data and the equation of state in the pressure range of 500 to 700 psi). This volume expansion coefficient is necessary when interpreting UV-Visible spectra to compensate for the decrease in particle concentration that accompanies an increase in solution volume with CO_2 pressure. The volume expansion coefficient of hexane for a range of CO_2 pressures as determined by the Peng-Robinson equation of state, is shown in Figure 3-3 where increases in CO_2 pressure significantly increase the volume expansion coefficient as a result of CO_2 gas partitioning into the liquid phase. Interestingly, this dissolution of CO_2 in the organic solvent also increases the density of the solvent mixture as obtained from the Peng-Robinson equation of state, indicating that while these mixtures are referred to as gas expanded liquids, the resulting solution is a dense mixture of liquid CO_2 and organic solvent. However, CO_2 is a very poor solvent for the solvation of the ligand coated particles in the organic solvent mixture. Therefore, as the percentage of CO_2 increases in the expanded organic solvent, solvent-ligand interactions decrease and the dispersed particles will precipitate once a threshold solvent strength is passed.

3.3.2 UV-Visible Absorbance Spectroscopy

An increase in CO_2 pressure decreases the concentration of dispersed nanoparticles. This is due to a decrease in the solvent strength of the GEL. Here, a decrease in solvent strength means that CO_2 has a very poor interaction with the ligand tails attached to the nanoparticles as compared to the organic solvent. So, as the concentration of CO_2 in the GEL is increased, interactions between the ligand tails and the solvent is diminished such

that particles are no longer stabilized and start precipitating from the solvent. The precipitation of the nanoparticles from the organic solvent depends on many factors, such as ligand type, solvent type, temperature, and metal type. The effect of each of these variables on the nanoparticle precipitation process is examined in this chapter.

Figure 3-4 presents the UV-vis spectra of gold particles synthesized by arrested precipitation and dispersed in hexane (top line). This absorption band is attributed to the absorption of Au nanoparticles dispersed in hexane and is due to the excitation of plasma resonances or interband transitions (Creighton and Eadon 1991). The gold nanoparticles do not precipitate in the absence of CO_2 even after extended periods of time. However, the intensity of the UV absorbance band decreases when the nanoparticle dispersion was pressurized with CO_2. This decrease in intensity indicates that particles begin precipitating from solution and the absorbance maximum decreases with the increase in pressure. Correspondingly, the absorbance maxima of the UV-Visible spectra, after correcting for the volume expansion of the organic solvent with the addition of CO_2, was plotted against the CO_2 pressure as a measure of particle concentration that remains dispersed at a given CO_2 pressure. Figure 3-5 shows a decrease of the absorbance with an increase in the pressure of CO_2 and indicates that the gold nanoparticles primarily precipitate from the solution in the range of 500 to 700 psi of CO_2 pressure. At pressures higher than 700 psi, complete precipitation occurs. The gold particles used in this experiment had a mean particle size of 5.0 nm and a standard deviation of 26% as shown in Table 3-1. McLeod et al.(McLeod, Anand et al. 2005) also demonstrated a dramatic decrease in the UV absorbance band for dodecanethiol stabilized silver particles dispersed in hexane with similar increases in CO_2 pressure (also shown in Figure 3-5).

The mean particle size and standard deviation for these silver particles (McLeod, Anand et al. 2005) was 5.5 nm and 31.9%, respectively. Interestingly, the pressure range for the precipitation and the slope of this curve was very similar for both the gold and silver nanoparticles. This is consistent with the fact that both dodecanethiol stabilized gold (Prasad, Stoeva et al. 2002) and dodecanethiol stabilized silver (Korgel, Fullam et al. 1998) nanoparticles have Hamaker constants of 1.95 eV resulting similar inherent van der Waals forces of attraction.

3.3.3 TEM Characterization

The particle size precipitated at each pressure range was determined by analysis of TEM images using ImageJ software where each particle was bounded by a rectangle and the diameter was estimated by the average of length and width of the rectangle. Figure 3-6 (A) shows an example of the TEM micrographs of unprocessed dodecanethiol-coated gold particles prepared by the two phase arrested precipitation method as explained earlier. These images were analyzed to determine the size distribution of this original sample as shown in Figure 3-6(B). This original sample of polydisperse dodecanethiol-coated gold particles was fractionated in a spiral tube into 5 fractions corresponding to different pressure ranges at different locations in a spiral tube as shown by arrows in Figure 3-7. TEM images of these fractions given in Figure 3-7 illustrate that the particle size collected within each ΔP decreases with increased CO_2 pressure. Moreover, particles in these images are very monodisperse and significantly more ordered into arrays as a result of the size separation process. After analyzing these particles with ImageJ software, histograms were prepared for all 5 pressure ranges simultaneously as shown in Figure 3-8

to quantitatively compare the various fractions. Compared to the wide size distribution (Figure 3-6(B)) of the original sample ranging from (2-9 nm), the histograms of the distinct fractions obtained after the size separation process are sharp (±2 nm). The size separation process improves the quality of the particles by increasing the percentage of particles at the median particle size in a single experiment. For example, 30% of the original group of nanoparticles was 5 nm in diameter but after the size separation process, 70% of the particles in the 650 psi fraction were 5 nm. Table 3-1 shows a statistical analysis of the fractions obtained at different pressure ranges from the size selection process. The standard deviation of the original sample is 26%. At 550 psi, the standard deviation is 22.4% because the pressure range, ΔP for collection, is large (0 to 550 psi). The standard deviation was reduced to 15.9% for the particles precipitated from 550 to 600 psi with a ΔP of 50 psi. The standard deviation was further reduced to 12.5% at 625 psi and 11.0% at 650 psi with ΔP's of 25 psi in each of these fractionation steps. This illustrates that a smaller ΔP gives a more precise particle separation due to a more subtle change in solvent strength and the process can be manipulated to obtain a desired particle size. McLeod et. al. (McLeod, Anand et al. 2005) showed that pressure can be used as a parameter to obtain a desired particle size. McLeod et. al. also showed that smaller pressure ranges (ΔP) for precipitation can be used to further narrow the size distribution where a ΔP of 50 psi resulted in a standard deviation of 16.1% and a ΔP of 6 psi resulted in a standard deviation of 14.7% for silver particles.

3.3.4 Effect of Solvent Hydrocarbon Length on the Size Selective Precipitation Process

Kitchens et al (Kitchens, McLeod et al. 2003) explained that variations in bulk solvent strength can have a significant effect on the size of nanoparticles that can be sterically stabilized in a given solvent. For example, cyclohexane solvent was shown to disperse larger AOT stabilized copper nanoparticles than was hexane solvent at identical operating conditions as a result of stronger AOT-solvent interactions. Shah and coworkers also demonstrated that the dispersability of dodecanethiol stabilized gold and silver particles could be varied in liquid and supercritical ethane by altering the pressure and thereby tuning the solvent density (Shah, Holmes et al. 2002). Moreover, variations in solvent strength can play an important role in the precipitation and deposition (Sigman, Saunders et al. 2004; McLeod, Kitchens et al. 2005) processes of particles. For example, Sigman and coworkers examined the morphology of dodecanethiol stabilized gold and silver nanocrystal thin films that were deposited from various solvents and they attributed the morphology changes to the different interparticle attractions in the organic solvents (Sigman, Saunders et al. 2004). Rough superlattice films were obtained from hexane, while smooth films were deposited from chloroform. Each of these works demonstrate that the interactions between the solvent and the particle stabilizing ligands play an important role in the dispersion and precipitation of nanoparticles. In general, a decrease in the solvent strength weakens the solvation of the ligand tails and results in stronger tail-tail interactions (Lee, Johnston et al. 2001) thereby decreasing the particle dispersability. Sufficient solvation of the thiol stabilizing ligand tails is necessary to provide enough repulsive force (osmotic and elastic repulsion) to overcome the van der

Waals forces of attraction between the nanoparticles.

The effect of different solvents on the size selective precipitation and fractionation process was examined. Figure 3-9 presents maximum UV-visible absorbance values for dodecanethiol coated gold nanoparticles dispersed in different hydrocarbon length solvents pressurized with CO_2. These absorbance maxima were normalized to a common initial value for ease of comparison and zero absorbance simply denotes that all the particles were precipitated from solution at that pressure. In hexane, a large percentage of the particles remained dispersed up to 550 psi after which point more appreciable precipitation occurred (precipitation of successively smaller particles) with further increases in CO_2 pressure until all the particles had precipitated at 700 psi and beyond. In contrast to hexane, pentane is a slightly weaker solvent, and as such, appreciable precipitation was initiated at only 450 psi with complete precipitation as low as 600 psi. Given that pentane provides weaker solvation of the ligand tails than hexane, smaller amounts of CO_2 are necessary to bring the solvent/CO_2 mixture solvent strength below the threshold for dispersability of a given particle size. As a result, the pressure range required for precipitation is less in pentane than hexane. Interestingly, heptane and octane both exhibit stronger interactions with the ligand tails as compared to hexane resulting in more stable dispersions in the longer chain length solvents. Correspondingly, greater CO_2 pressure is required to reach the same weakened solvent strength of the solvent/CO_2 mixture to induce precipitation of nanoparticles of a given size. Figure 3-9 shows that the length of the organic solvent influences the gold nanoparticle precipitation process where the longer length solvent molecules have stronger interactions with the nanoparticle ligand tails compared to the shorter length solvent molecules. Additional

67

results of similar experiments performed with cyclohexane, decane, isooctane, and toluene are not shown here in Figure 3-9. In these solvent systems, particle dispersability remained quite high even at CO_2 pressures approaching the vapor pressure of CO_2 where the dodecanethiol coated gold particles remained dispersed in the solvent/CO_2 mixtures for several hours.

3.3.5 Effect of Thiol Length on the Size Selective Precipitation Process

Martin et al. (Martin, Wilcoxon et al. 2000) states that among all the alkyl thiols, dodecanethiol is more strongly bound to gold particles than hexanethiol or hexadecanethiol. Prasad et al. (Prasad, Stoeva et al. 2002) studied the effect of the alkyl chain lengths of thiol molecules on the formation of gold nanoparticle superlattices. These authors describe that there is a decrease in particle-particle attraction energy with an increase in the thiol hydrocarbon chain length. For example, particles aggregated into 3D superlattices with short chain lengths, i.e octanethiol and decanethiol (C8 and C10), due to particle-particle attraction. Longer chain length in hexadecanethiol resulted in weakly bound multilayers and hinders the development of 3D superlattices. These works have demonstrated the impact of thiol chain length on particle-particle attraction. It is important to note that in the current study, dispersion of particles in solution requires that these attractive interactions be finely balanced by the osmotic repulsion and an elastic contribution generated by interactions between the solvent and the thiol stabilizing ligands. As shown in the previous section of this chapter, modification of the solvent strength of the solution (i.e. CO_2 pressurization) can result in changes in these attractive and repulsive interactions thereby inducing precipitation. Changes in this fine balance can also be accomplished by altering the thiol chain length such that there is a

modification to the interaction between the solvent and the thiol ligand tails.   Here we present the influence of various thiol chain lengths on the CO_2 pressurization range required to induce precipitation. As shown in Figure 3-10 precipitation of the particles stabilized with octanethiol ligands occurs between 400 and 600 psi as compared to 500 to 700 psi for particle stabilized by dodecanethiol ligands. The precipitation of particles with hexanethiol ligands was similar to those with octanethiol ligands, and the curve was shifted to a lower pressure range (300-575 psi). Particles stabilized with tetradecanethiol ligands require a smaller CO_2 pressure for the precipitation of particles compared to dodecanethiol ligands, even though they have a longer tail length. The shorter tail length for octanethiol and hexanethiol ligands decreases the CO_2 pressure required for precipitation in a GEL compared to dodecanethiol ligand stabilized particles. This effect is because the shorter length ligands have smaller interactions with the solvent compared to the longer length ligands. Tetradecanethiol ligand stabilized particles also require less CO_2 pressure for the nanoparticle precipitation than dodecanethiol ligand stabilized particles because of larger tail - tail interactions. These results suggest that dodecanethiol ligands have the optimum length for strong ligand – solvent interactions (Prasad, Stoeva et al. 2002).

3.3.6 Effect of Temperature on the Size Selective Precipitation Process

Temperature also has a pronounced effect on nanoparticle stabilization and dispersibility (Kitchens, McLeod et al. 2003). As shown by Shah and coworkers (Shah, Holmes et al. 2002), temperature effects solvent density, which affects the nanoparticle dispersability in an organic solvent. Temperature affects on the precipitation of gold particles stabilized with dodecanethiol ligands in hexane are shown in Figure 3-11. At the lowest

temperature of 22 $^{\circ}$C, the nanoparticle precipitation occurs between 500 and 700 psi CO_2 pressure. At the highest temperature of 35 $^{\circ}$C, this pressure range for precipitation was shifted up to 650 to 800 psi, illustrating that an increase in pressure is required for precipitation with an increase in temperature. This variation is due in part to the CO_2 density change with temperature. As temperature is increased, the mole fraction of CO_2 in the organic liquid/CO_2 mixture is reduced resulting in a smaller volume expansion of the liquid dispersion at a given pressure. This, therefore, reduces the antisolvent effect in the nanoparticle precipitation process.

3.3.7 Recursive Fractionations

Korgel and coworkers used ethanol recursively as an antisolvent to improve the size separation process (Sigman, Saunders et al. 2004). In the current study, a set of size separation experiments were repeated on one of the recovered fractions (particles collected within a given pressure range at one location in the spiral tube) to further improve the size separation process using CO_2 as an antisolvent. The results of the recursive fractionation are summarized in Figure 3-12. The size separation process, shown in Figure 3-2, was done by placing the original polydisperse sample at location A in the spiral tube. The 1st fractionation sample, at location D, shown in Figure 3-12 was the sample of particles precipitated within the pressure range of 625-650 psi. In this recursive process, this 1st fractionation sample was collected at the end of the experiment and was returned to location A and the size separation process was repeated. The 2nd fractionation sample shown in Figure 3-12 was again obtained from position D within the same pressure range of 625-650 psi. In the same way, the 3rd fractionation was obtained by placing the 2nd fractionation sample at location A and collecting the particles

70

precipitated at location D within the same pressure range. The separation was improved during each successive processing step with a decrease in the standard deviation from 13% to 8% as shown in Table 3-2. This process is an improvement over the liquid antisolvent process where the desired size is controllably obtained as a function of pressure. For instance, keeping the solvent, thiol length and temperature the same, this process will always result in a ~5.0 nm sized fraction of gold particles collected at 650 psi since the precipitation is governed simply by the solvent strength. Therefore, this CO_2 antisolvent size separation process gives a predictable particle size at a given CO_2 pressure. On the other hand, the number of variables involved in the liquid antisolvent process including the specific amount of ethanol addition and the centrifugation time makes predictable size selection challenging.

3.3.8 Effect of Time on the Size Selective Precipitation Process

During this size selection process, the liquid droplet with dispersed nanoparticles is moved to a specific location on the surface of the spiral tube followed by an increase in pressure that initiates precipitation of particles within that pressure range. Once the desired pressure is reached, the system is allowed to sit for a specified period of time allowing precipitation of the particles, and this period of time is referred to as the holding time. Table 3-3 presents standard deviations for particles precipitated during three different holding times in the pressure range of 600-625 psi. The results shown earlier in this chapter were collected during a holding time of 20 min where a mean size of 4.7 nm and the standard deviation of 14.9% were obtained as given in Table 3-3. For holding time of 1 hr, the mean size and standard deviation were 4.7 nm and 16.9% respectively. It was found that a 5 min holding time resulted in a standard deviation of 14.6% with a

mean nanoparticle size of 5.1 nm. The experiments performed at different holding times suggest that there is little difference in the size distribution of the nanoparticles collected indicating that the system quickly reaches an equilibrium. This demonstrates that the size separation process using CO_2 as the antisolvent is a very rapid process compared to the liquid antisolvent process which requires several hours for the separation of the same quantity of particles.

3.4 Conclusions

A method for precise, rapid, pressure tunable, size selective nanoparticle precipitation and redispersion using tunable CO_2 gas-expanded liquids has been developed. This technique is a marked improvement over the current techniques of nanoparticle fractionation employing liquid antisolvent techniques. In this size separation process, dodecanethiol stabilized polydisperse gold nanoparticles dispersed in hexane were fractionated into monodisperse fractions using CO_2 pressurization in the range of 500-700 psi. The original sample of dodecanethiol stabilized gold particles of 26% polydispersity were successfully separated into fractions of as little as 11% polydispersity in a single step process. To understand the precipitation process in more detail, the effect of various parameters on the size separation process was studied. Variations in solvent length from five to eight hydrocarbon chains have a significant effect on the pressures required for precipitation of dodecanethiol coated gold nanoparticles. Experiments in which the thiol stabilizing ligand length was varied illustrated that dodecanethiol provides the best solvent - ligand tail interaction when hexane was the bulk solvent medium. It was also found that as the solvent temperature was increased an increase in CO_2 pressure is required to completely precipitate all the nanocrystals from solution.

Recursive fractionations on a sample collected within a given pressure range elicit the desired nanoparticles of a precise size. This new process is very fast, repeatable and reproducible requiring very short holding time at each precipitation stage.

3.5 Acknowledgements
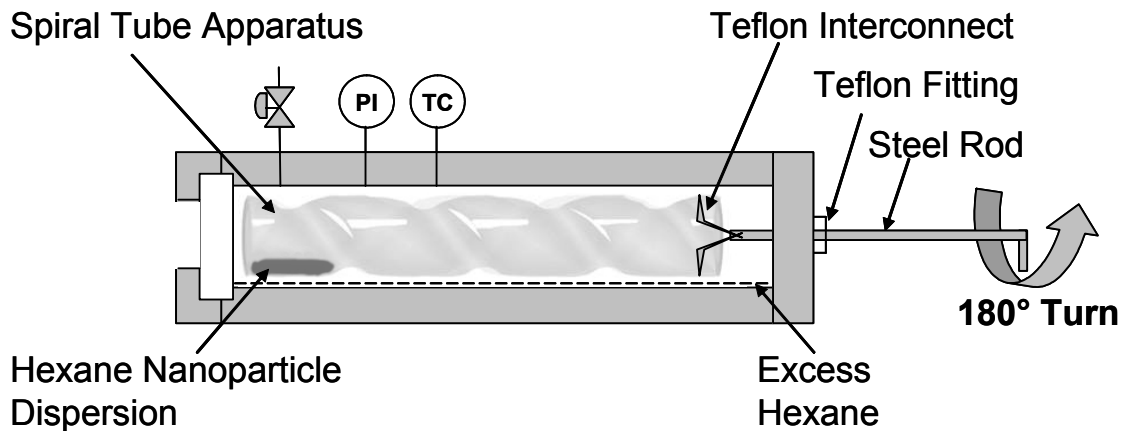
Figure 3-1 Nanoparticle size selection apparatus enclosed in a high pressure vessel shows loading of hexane nanoparticle dispersion. Excess hexane was loaded for saturating the high pressure vessel with hexane vapor. Teflon fitting allows the steel rod to enter into the vessel and maintains the high pressure seal while turning the steel rod 180° which rotates the spiral tube with the help of Teflon interconnect. PI and TC stand for pressure indicator and temperature controller respectively.
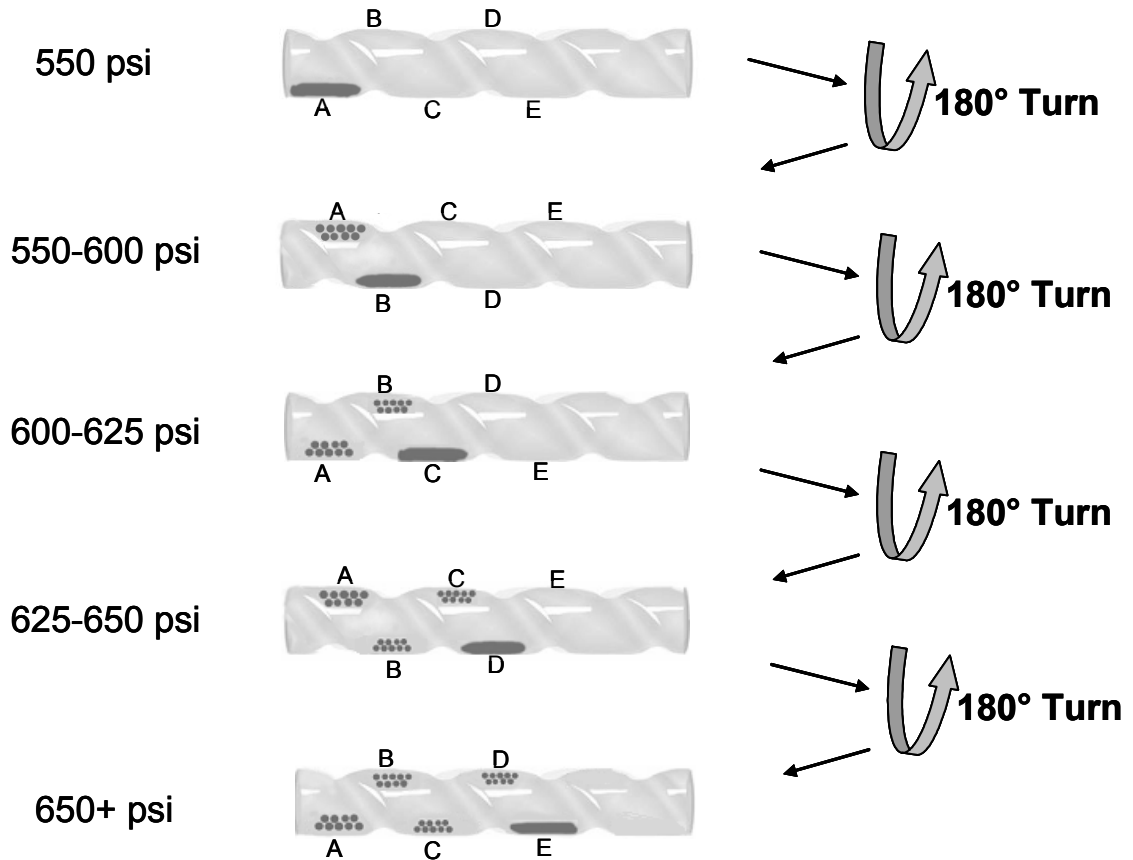
Figure 3-2 Nanoparticle size selection spiral tube apparatus depicting recursive pressurization of organic liquid with CO_2, followed by 180° tube rotations to achieve multiple size selected populations.
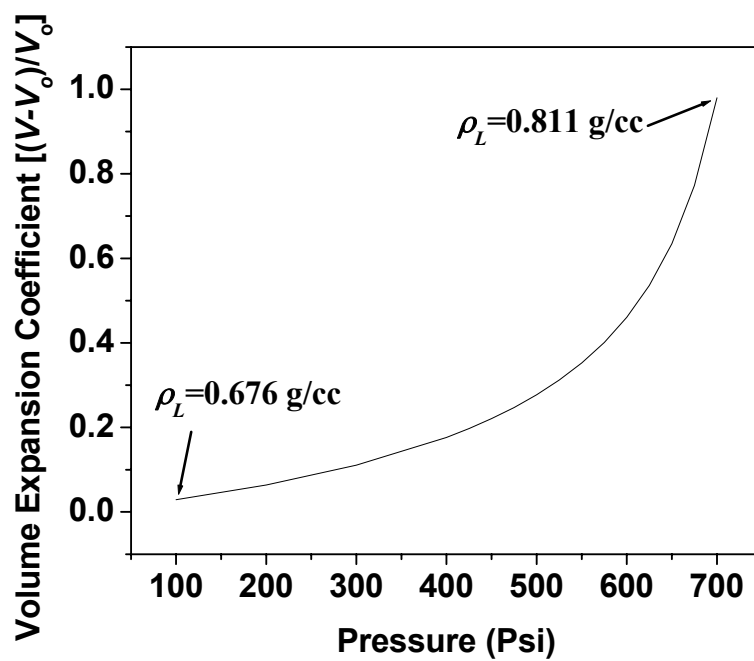
Figure 3-3 Volume expansion coefficient vs. system pressure for liquid hexane/CO_2 mixtures pressurized with gaseous CO_2 and modeled using the Peng-Robinson equation of state at 25°C.
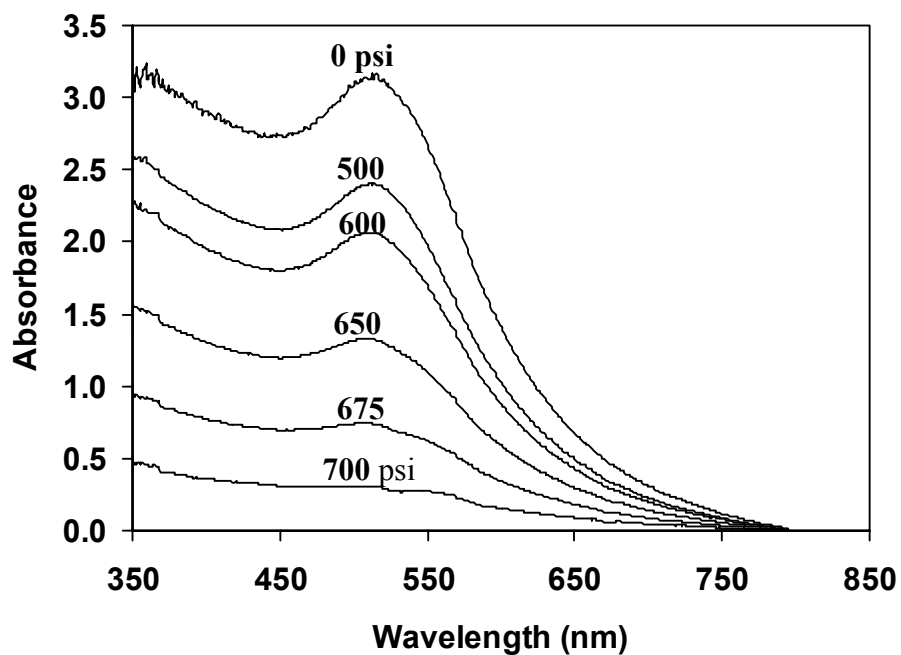
Figure 3-4 UV-visible absorbance spectra of gold particles dispersed in hexane/CO_2 liquid mixtures at increasing CO_2 pressures. The spectra were normalized to give zero absorbance at 800 nm wavelength. Decreased absorbance of gold particles after correcting for the volume expansion of hexane shows that particles are precipitating from hexane by increasing the CO_2 pressure.
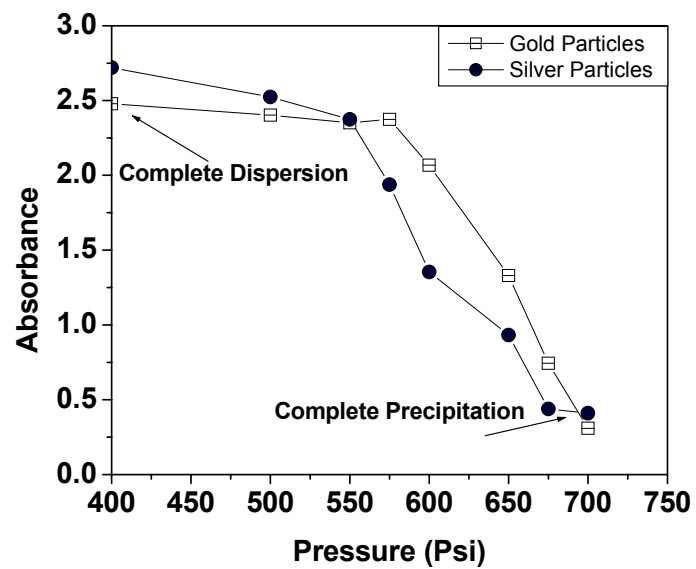
Figure 3-5 Maximum UV-visible absorbance of dodecanethiol coated silver (McLeod, Anand et al. 2005) and gold particles dispersed in liquid hexane/CO_2 mixtures vs. system pressure. Absorbance values obtained were corrected for the volume expansion of the liquid mixture.

(A)
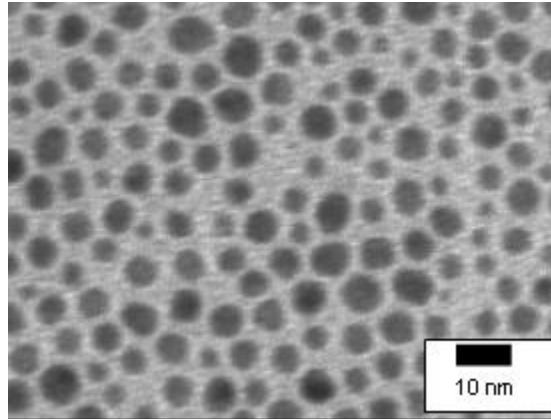
(B)
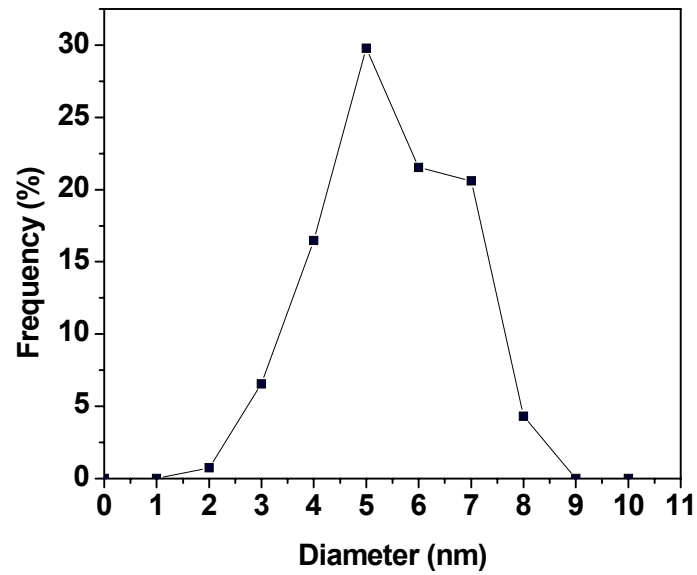
Figure 3-6 (A) TEM micrograph of unprocessed dodecanethiol-coated gold particles prepared by two phase arrested precipitation method. (B) Size distribution of unprocessed particles.
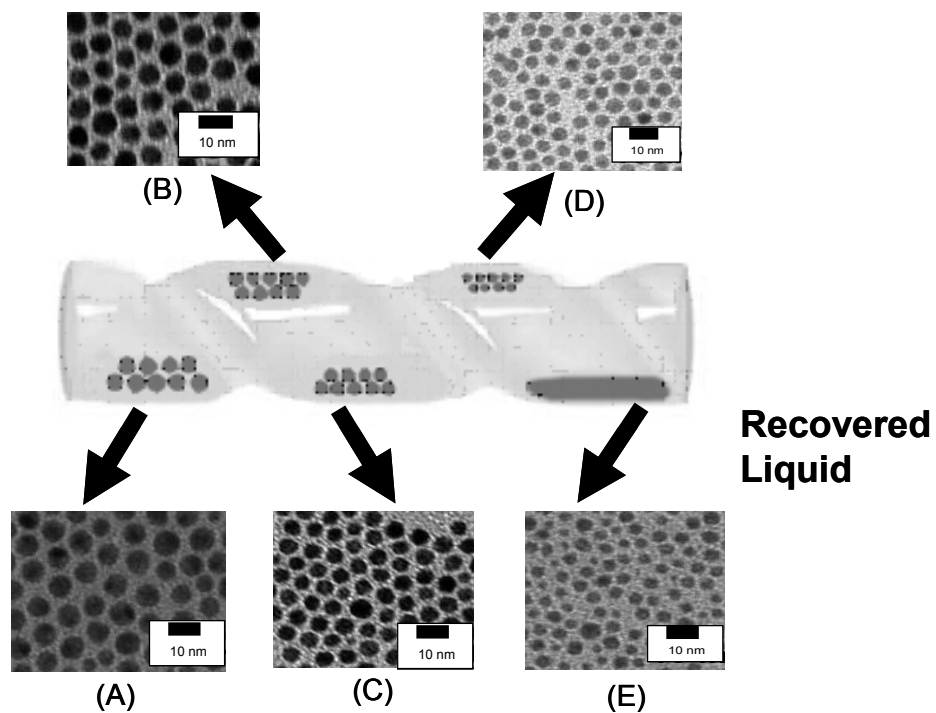
Figure 3-7 TEM micrographs of particles precipitated from hexane by CO_2 pressurization from (A) 0 to 550 psi, (B) 550 to 600 psi, (C) 600 to 625 psi, (D) 625 to 650 psi and (E) 700 psi CO_2 pressurization.
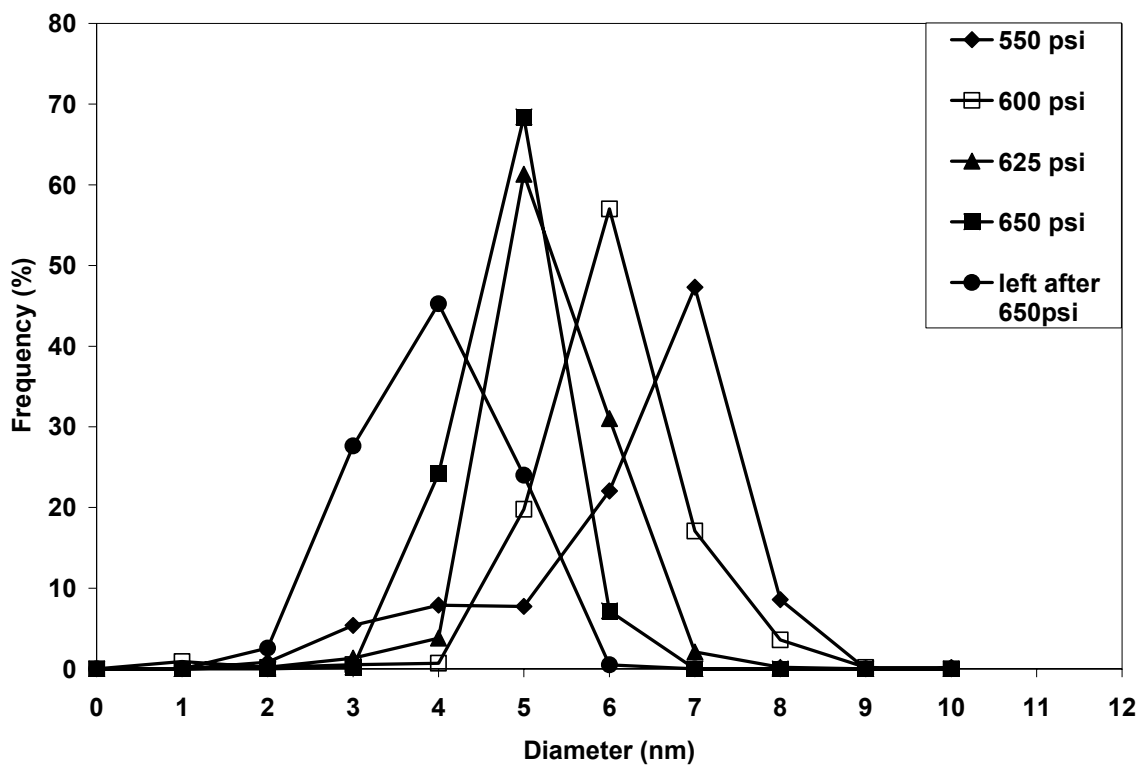
Figure 3-8 Size distributions of dodecanethiol-coated gold particles fractionated within the CO_2 pressure ranges of 0-550 psi (♦), 550-600 psi (□), 600-625 psi (▲), 625-650 psi (■), 700 psi (●). Data points represent the percentage of particles of the total population found between the associated diameter and <1nm less than that diameter.
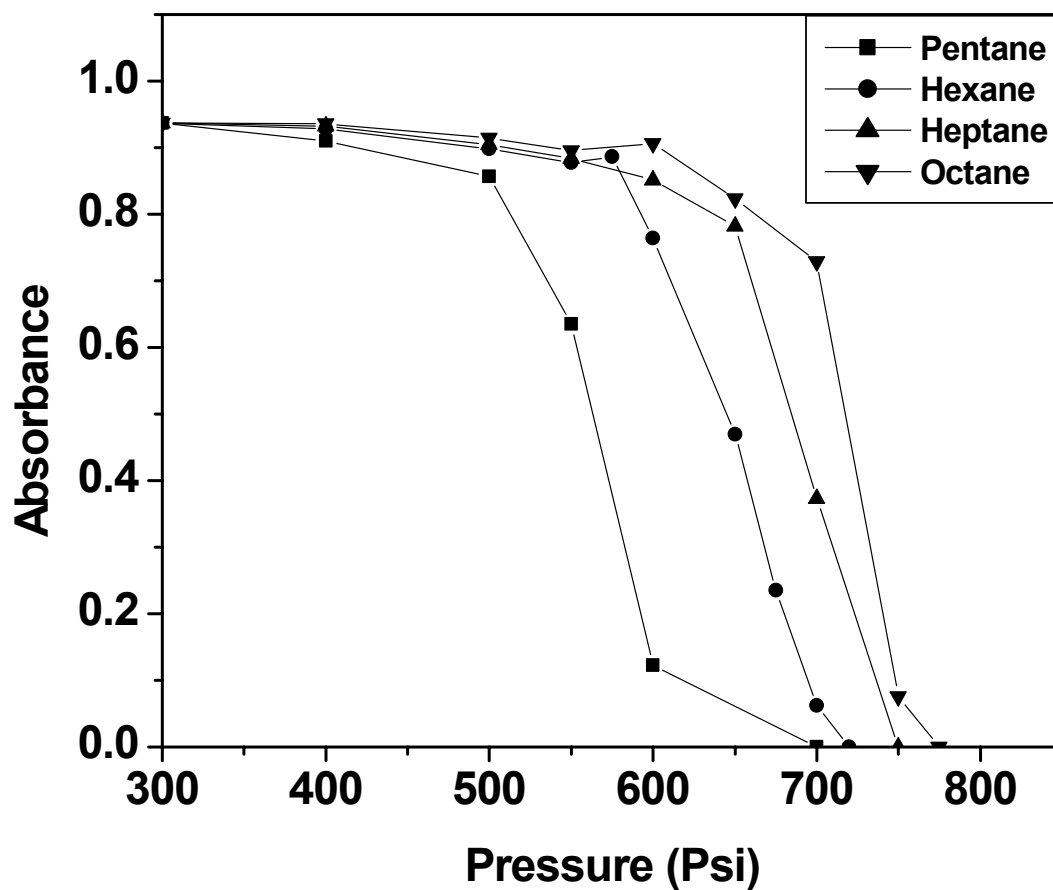
Figure 3-9 Maximum UV-visible absorbance values for dodecanethiol coated gold nanoparticles dispersed in different hydrocarbon length solvents pressurized with CO_2.
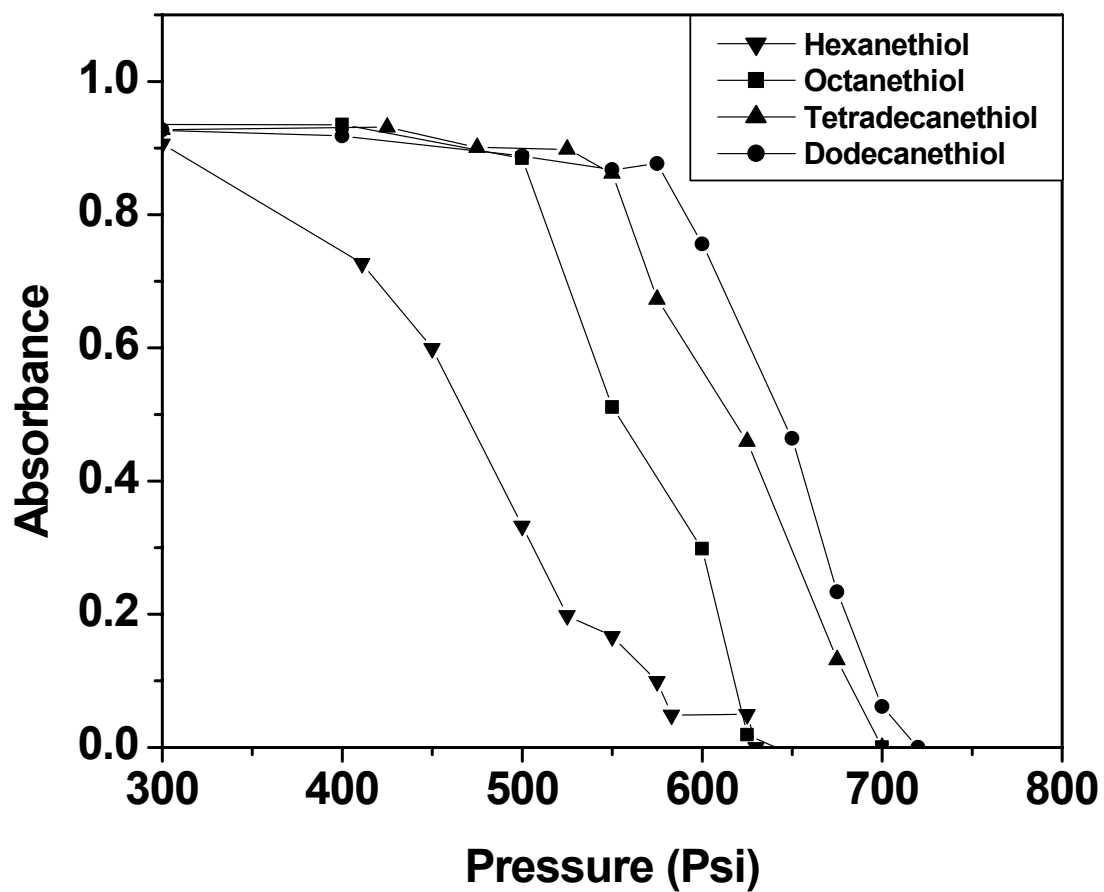
Figure 3-10 Maximum UV-Visible absorbance values for gold nanoparticles coated with different thiol length molecules dispersed in liquid hexane/CO_2 mixtures at increasing CO_2 pressure.
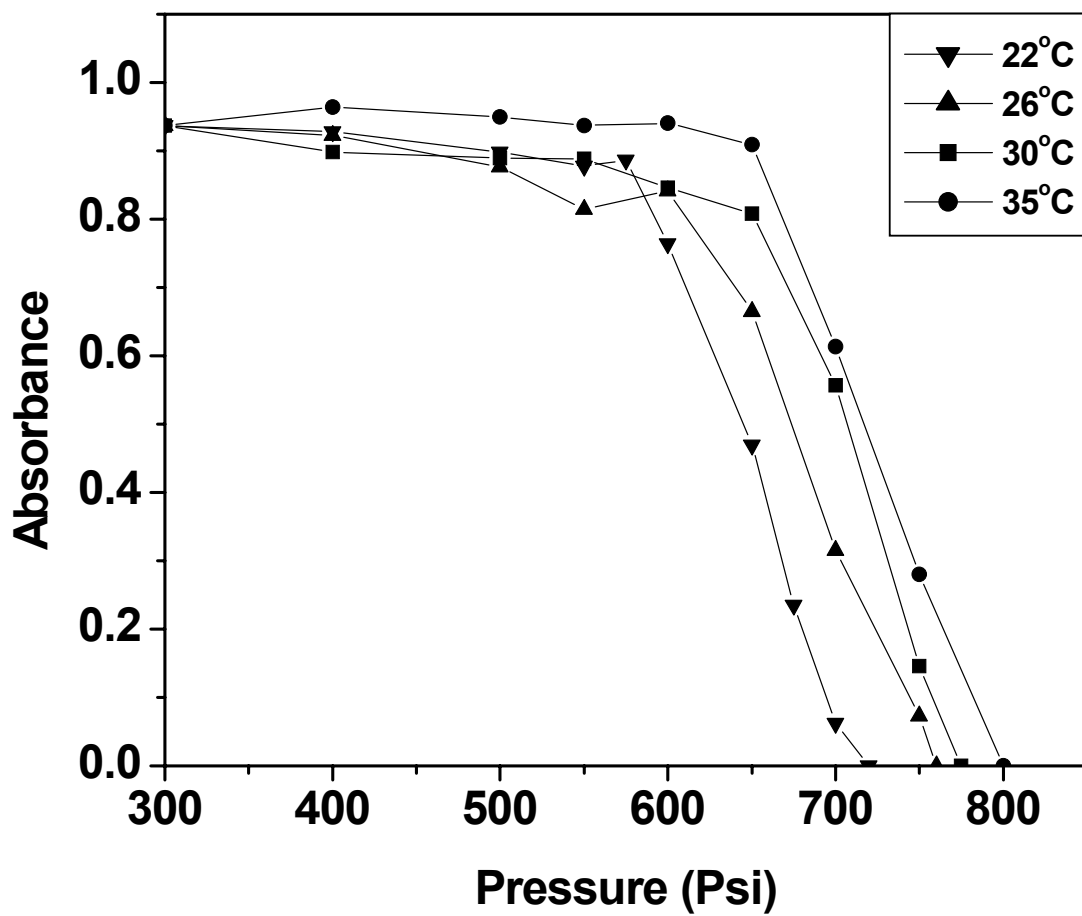
Figure 3-11 Maximum UV-Visible absorbance values for dodecanethiol coated gold nanoparticles dispersed in liquid hexane/CO_2 mixtures at various CO_2 pressures and system temperatures.
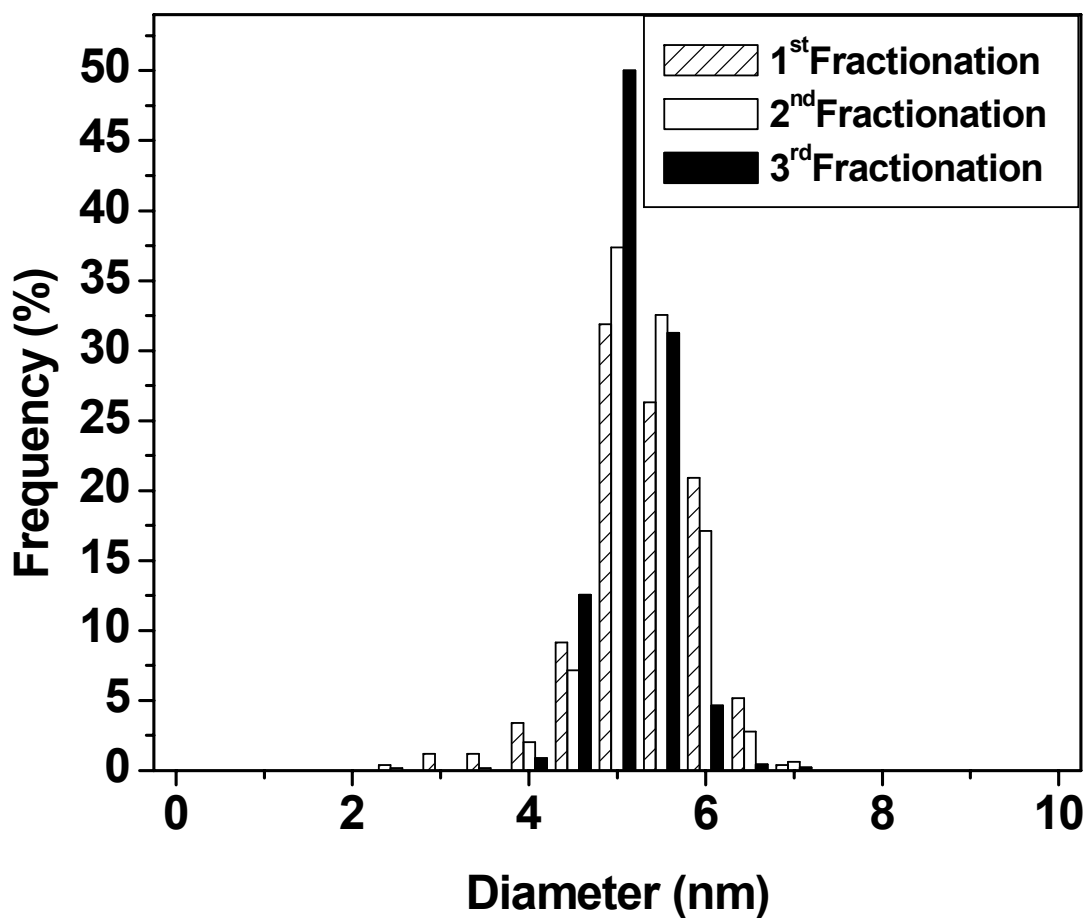
Figure 3-12 Comparison between the size distributions of gold particles collected in the pressure range of 625 to 650 psi after fractionation one, two or three times. Particles from the 1st fractionation were obtained from the location D in the spiral tube apparatus corresponding to pressure range of 625-650 psi. This 1st fractionation sample was returned to location A and the size separation process was repeated. The 2nd fractionation sample was again obtained from position D. In the same way, the 3rd fractionation was obtained by placing the 2nd fractionation sample at location A and collecting the particles precipitated at location D. Data points represent the percentage of particles of the total

population found between the associated diameter and <0.5 nm less that diameter.

Fraction (Psi)	ΔP of Fraction (Psi)	Mean Diameter (nm)	Std Dev (nm)	Relative Std Dev (%)	95% Confidence (nm)	Particle Count
Original	0	5.0	1.3	26.0	0.1	534
0 to 550	550.0	5.7	1.3	22.4	0.1	594
550 to 600	50	5.5	0.9	15.9	0.07	556
600 to 625	25	4.8	0.6	12.5	0.05	522
625 to 650	25	4.3	0.5	11.0	0.04	459
650 +	<50	3.4	0.7	20.6	0.06	579

Table 3-1 Statistical analysis of particle populations where the five fractions were separated in a single experiment from the original population. All gold particles are completely precipitated from the hexane at 700 psi.

Fractionation (Number)	Mean Diameter (nm)	Std Dev (nm)	Relative Std Dev (%)	Fraction (Psi)	95% Confidence (nm)	Particle Count
1	5.0	0.7	13.1	625-650	0.06	502
2	5.0	0.5	10.0	625-650	0.04	642
3	4.9	0.4	8.1	625-650	0.04	454

Table 3-2 Statistical analysis of particle populations for different numbers of fractionation steps.

Holding Time (min)	Mean Diameter (nm)	Std Dev (nm)	Relative Std Dev (%)	95% Confidence (nm)	Particle Count	Fraction (Psi)
5	5.1	0.75	14.6	0.06	464	600 to 625
20	4.7	0.70	14.9	0.07	309	600 to 625
60	4.7	0.79	16.9	0.06	591	600 to 625

Table 3-3 Statistical analysis of particle populations for different holding times at each step of fractionation.

CHAPTER 4

FINELY CONTROLLED SIZE SELECTIVE PRECIPITATION AND SEPARATION OF CdSe/ZnS

SEMICONDUCTOR NANOCRYSTALS USING CO_2 GAS EXPANDED LIQUIDS

A technique was developed to size selectively separate polydisperse dispersions of CdSe/ZnS nanocrystals into distinct color fractions using only the tunable solvent properties of CO_2 expanded hexane. This size selective precipitation of semiconductor nanoparticles is achieved by finely tuning the solvent strength of the CO_2/hexane medium by simply adjusting the applied CO_2 pressure. These subtle changes affect the balance between osmotic repulsive and van der Waals attractive forces thereby allowing fractionation of the nanocrystals into multiple narrow size populations.

4.1 Introduction

Semiconductor nanocrystals, also known as quantum dots, have unique electronic and optical properties due to the three dimensional confinement of charge carriers (Poole and Owens 2003). The change in properties for quantum dots, 10 nm or less in size, results from confinement of holes and electrons into a dimension which is close to a critical quantum measurement called exciton Bohr radius (Rossetti, Nakahara et al. 1983; Nenadovic, Rajh et al. 1985; Nakashima, Tsuzuki et al. 1999). Extensive research has been performed to study the size dependent quantum confinement of semiconductor

quantum dots (Alivisatos 1996). The valence–conduction band-gap increases in semiconductor nanocrystals with a decrease in the particle diameter (Viswanatha, Sapra et al. 2005; Li and Li 2006) and therefore provides an avenue for size-tunable nanodevices. The properties of semiconductor nanocrystals, such as their electronic states, light absorption, and emission, can be tuned with particle size and shape. As such, monodisperse semiconductor nanocrystals are employed in number of applications such as optoelectronic devices (Nakashima, Tsuzuki et al. 1999), sensors (Hansen, Mukhopadhyay et al. 2006; Shi, De Paoli et al. 2006), catalysis (Pal, Torimoto et al. 2004) and as fluorescent chemical labels in biomedicine (Bruchez, Moronne et al. 1998). CdSe is one the most widely used semiconductor nanocrystal materials due in part to the availability of highly efficient and high quality CdSe nanocrystal synthesis techniques and the fact that their optical gap is in the visible region. As an example, monodisperse CdSe quantum dots are used in obtaining electroluminescence which can also be tuned by varying the size of the nanocrystals (Dabbousi, Bawendi et al. 1995; Dabbousi, Onitsuka et al. 1995).

Much research has been done to develop efficient synthesis as well as post-synthesis processing techniques to produce semiconductor nanocrystals with narrow size distributions (Eychmueller 2000). A number of synthesis techniques for semiconductor nanocrystals have been reported including arrested precipitations (Murray, Norris et al. 1993), microemulsion methods (Hao, Sun et al. 1999),(Chandrasekharan and Kamat 2002), high-temperature pyrolysis (da Silva, Silva et al. 2001; Yosef, Schaper et al. 2005), and sonochemical methods (Zhu, Koltypin et al. 2000; Murcia, Shaw et al. 2006). One of the most efficient techniques to synthesize CdSe nanocrystals is through

kinetically controlled arrested precipitations where CdSe nanocrystals are stabilized with capping ligands such as trioctyl phosphine oxide (TOPO) (Peng, Wickham et al. 1998; Talapin, Rogach et al. 2001; Murcia, Shaw et al. 2006).

While several synthesis alternatives have been developed for semiconductor nanocrystals, post-synthesis purification and size-separation processing steps are commonly required to obtain nanocrystal fractions with the desired size and narrow size distributions. Various post-synthesis processing techniques such as liquid antisolvent precipitation (Murray, Norris et al. 1993; Vossmeyer, Katsikas et al. 1994; Korgel, Fullam et al. 1998; Rogach, Kornowski et al. 1999; Sigman, Saunders et al. 2004) and exclusion chromatography (Fischer, Weller et al. 1986; Fischer, Lilie et al. 1989) have been developed that improve control over semiconductor particle size and polydispersity (Murray, Norris et al. 1993; Vossmeyer, Katsikas et al. 1994; Rogach, Kornowski et al. 1999). Perhaps the most widely applied technique involves liquid antisolvent induced size-selective precipitations coupled with centrifugation (Murray, Norris et al. 1993; Vossmeyer, Katsikas et al. 1994; Rogach, Kornowski et al. 1999). This liquid antisolvent precipitation technique involves first dispersing ligand capped nanocrystals in an organic solvent. An antisolvent is then introduced dropwise to this stable nanocrystal dispersion until opalescence occurs upon stirring. This addition of antisolvent weakens the ligand-solvent interaction in solution and thus results in precipitation of nanocrystals where particles of decreasing size precipitate with the subsequent addition of the antisolvent. The solution is normally centrifuged after each addition of antisolvent to speed up the precipitation process for the unstabilized fraction of the particles from solution. This process of gradual antisolvent addition and centrifugation is repeated a number of times

on the precipitate or supernatant depending on how narrow a size distribution is required. Although this liquid antisolvent process is commonly employed, it is time consuming, solvent intensive, and requires multiple processing steps. This technique is also somewhat subjective in that the separation depends on the observation of opalescence during antisolvent addition. Improved size-selective precipitation techniques are required to address these limitations.

Our research group has recently developed a post-synthesis nanoparticle size-separation technique based on the tunable solvent strength of CO_2 gas expanded liquid mixtures. Polydisperse populations of metal (Au, Ag) nanoparticles capped with alkane thiol ligands were separated and fractionated into monodisperse size fractions using the adjustable solvent strength of CO_2 gas expanded alkane solvent mixtures by simply adjusting the applied CO_2 pressure (Anand, McLeod et al. 2005; McLeod, Anand et al. 2005). An expansion of the organic solution occurs upon increasing pressurization with CO_2 gas due to the condensation and miscibility of CO_2 with the organic solvent. The addition of CO_2 to the organic solution thereby acts as an antisolvent for the non-polar ligands and thus allows size selective precipitation of the nanocrystals with simple adjustments in CO_2 pressure. Particle dispersability in a solvent requires a sufficient solvent-ligand interaction in order to provide enough repulsive force to overcome the van der Waals forces of attraction between the particles in solution. Hence, the degree of solvent-ligand interaction is diminished upon the gradual addition of CO_2 antisolvent through pressurization and, since the larger particles in solution have greater van der Waals forces of attraction, the larger particles begin precipitating first upon worsening solvent conditions. CO_2 gas was chosen as an antisolvent in this case because it is a

feeble solvent with zero dipole moment and a low dielectric constant. Moreover, the physico-chemical properties of CO_2 gas expanded liquids can be finely tuned with simple adjustments in temperature and pressure (Eckert, Bush et al. 2000; Jessop and Subramaniam 2006). These systems allow the solvent-ligand interactions, and hence nanocrystals dispersability to be finely tuned with adjustments in CO_2 pressure (Zhang, Han et al. 2001; Anand, McLeod et al. 2005; McLeod, Anand et al. 2005; McLeod, Kitchens et al. 2005; Liu, Anand et al. 2006).

This method has a number of advantages over the liquid antisolvent precipitation technique. The first of these involves the ease to which the properties of the gas expanded liquid mixtures can be adjusted via simple pressure changes. In addition, CO_2 gas expanded liquids have higher diffusivities and lower viscosities than normal liquid solutions resulting in rapid mixing and precipitation such that time intensive centrifugation steps are not required to precipitate the nanocrystals from solution. This CO_2 gas expanded liquid precipitation process is also less solvent intensive where CO_2 is a benign antisolvent and the liquid solvent used can be recycled by removing the CO_2 antisolvent through simple depressurization. The CO_2 gas expanded liquid nanocrystals size separation process is rapid, highly precise and reproducible given that the solvent strength of the medium is simply a function of the applied CO_2 pressure. As such, multiple size fractionation steps can be achieved sequentially by subsequent increases in pressure in a single process (Anand, McLeod et al. 2005; McLeod, Anand et al. 2005) as opposed to the multiple mixing, separation and centrifugation steps required to achieve multiple fractionations using the traditional liquid antisolvent precipitations techniques.

This chapter presents the size separation of CdSe/ZnS core shell semiconductor

94

nanocrystals using a CO_2 gas expanded liquid approach. In short, aliquots of four CdSe/ZnS nanocrystal dispersions, each with different sized nanocrystals dispersed in toluene, were mixed to produce a CdSe/ZnS nanocrystal dispersion containing four different sized (colored) nanocrystals. These nanocrystals in this mixed dispersion were then size separated using the above mentioned CO_2 based technique to regain the original size fractions (colors) thus illustrating the effectiveness of this tunable separation process.

4.2 Experimental Section

4.2.1 Materials

The four different sized CdSe/ZnS core shell nanocrystals capped with TOPO and dispersed in toluene were purchased from Evident Technologies. Hexane (99%) was obtained from Aldrich Chemical Co. and carbon dioxide (SFC/SFE grade) was obtained from Airgas. All chemicals were used as received. CdSe/ZnS core shell quantum dots were chosen for investigation because the ZnS core shell improves stability, strength and fluorescent brightness of the CdSe quantum dots. The TOPO capped CdSe/ZnS core shell quantum dots which were dispersed in toluene were of four different colors; red, orange, yellow and green corresponding to average crystal diameters 5.2 nm, 3.2 nm, 2.4 nm, 1.9 nm, respectively, as reported by Evident Technologies. The mixture of these 4 different sized semiconductor nanocrystal dispersions in toluene was prepared using equivalent masses of CdSe/ZnS particles from each colored solutions.

4.2.2 Solvent Exchange Process

An earlier study on the CO_2 gas expanded liquid size precipitation process has demonstrated that the solvent used for the bulk medium has a significant impact on the

pressure range required for precipitation of metal nanocrystals capped with alkane thiol

ligand tails (Anand, McLeod et al. 2005). Stronger interactions between the solvent and

the hydrocarbon ligand tails required greater CO_2 pressure to precipitate the particles.

Previous studies indicate that toluene is a very good solvent for hydrocarbon ligand tails

and particle dispersability in this solvent medium remains quite high even at CO_2

pressures approaching the vapor pressure of CO_2 (Anand, McLeod et al. 2005). For

instance, dodecanethiol coated gold nanocrystals remain dispersed in toluene/CO_2

mixtures for several hours. Similarly, in the current study, TOPO capped CdSe/ZnS core

shell quantum dots remained dispersed in toluene even at the vapor pressure of CO_2 for

several hours rendering the toluene medium inappropriate for the CO_2 gas expanded

liquid precipitation process. The solvent medium for the mixed CdSe/ZnS core shell

quantum dot dispersions was changed from toluene to hexane by completely evaporating

toluene and subsequently dispersing the particles in hexane, as shown in the vial labeled

'original' in Figure 4-1. Hexane has a lower solvent strength than toluene and resulted in

significant CdSe/ZnS particle precipitation when the hexane medium was pressurized

with CO_2 up to its vapor pressure.

4.2.3 Size Selective Separation of CdSe/ZnS Semiconductor Nanocrystals

The mixed CdSe/ZnS core shell quantum dots were separated into distinct size fractions

(different colors) via CO_2 pressure induced size selective precipitation at specific

locations on the surface of a spiral tube apparatus as shown in Figure 4-2 (McLeod,

Anand et al. 2005). This spiral tube precipitation apparatus consists of an open ended

glass tube (2cm diameter, 12 cm long) modified to include a concentric, spiral

indentation on the surface of the tube from one end to the other. These spiral indentations

provide a spiral channel (6mm deep, 2.5 cm wide each) or groove inside of the tube that allows a liquid droplet of the nanocrystal dispersion resting within the channel to be translated from one location to another by a simple rotation of the tube while keeping the length of the tube horizontal. In short, the function of the spiral tube is like that of an Archimedes screw, where the liquid nanocrystal dispersion can be controllably moved from one location within the groove to the next by simple rotation of the tube. This spiral tube is located within a cylindrical stainless steel high pressure view cell equipped on one end with an O-ring sealed quartz window that allows observation of the liquid expansion and particle precipitation process. The other end of the high pressure cell is fitted with a Teflon high pressure fitting that allows the entry of a 1/8 in. stainless steel rod connected to the spiral tube with a Teflon interconnect. This interconnect assembly allows radial rotation of the spiral tube within the high pressure vessel by simply turning the metal rod outside the vessel while maintaining the dynamic high pressure seal with the Teflon fitting. Thus, the location of liquid droplet of nanocrystal dispersion in a spiral tube can easily be controlled by simply turning the steel rod from outside the vessel while maintaining the high pressure conditions within the vessel. The spiral groove within the tube also helps in separating the liquid nanocrystal dispersion from an already precipitated nanocrystal particle fraction by moving the remaining liquid dispersion to the next desired location along the length of the tube. Therefore, by placing a sample of the mixed nanocrystal dispersion at one end of the spiral tube, and by coordinating sequential increases in the CO_2 pressure along with movement of the liquid to the next location within the tube prior to each pressurization step, successively smaller sized nanocrystals can be precipitated at each subsequent location on the tube surface.

An experiment was started by placing $700\mu L$ of pure hexane in the annular space outside the spiral tube in the high pressure vessel and allowing it to sit for 10 minutes to saturate the vessel with hexane vapor. This prevents the excessive evaporative loss of hexane from the original hexane nanocrystal dispersion which was introduced later in the spiral tube within the high pressure vessel. Next, $250\mu L$ of the original mixed nanocrystal dispersion in hexane was placed in the spiral grove at location A closest to the quartz window, as shown in the top image of Figure 4-3. The vessel was then slowly pressurized to an initial pressure of 660 psi with CO_2 gas using an ISCO 260D syringe pump. Once the desired pressure was reached, the system was allowed to sit for 20 minutes to allow the largest size fraction of the CdSe/ZnS core shell nanocrystals to precipitate.

The increase in CO_2 pressure to 660 psi results in an increase in the concentration of CO_2 within the hexane nanocrystal dispersion (CO_2 expanded hexane solution) where the condensed CO_2 acts as an antisolvent thereby causing the largest fraction of the CdSe/ZnS core shell nanocrystals that are no longer stabilized in the weakened CO_2/hexane mixture to precipitate at location A as shown in Figure 4-3.

This precipitated fraction of the CdSe/ZnS nanocrystals adhered to the surface of the spiral tube at location A through van der Waals forces of attraction with the surface. To move the remaining dispersion away from affixed particles, the spiral tube was rotated by turning the metal rod 180°. This rotation of the spiral tube moved the liquid dispersion to the next location, B, leaving the largest size fraction of the particles, those that were precipitated at 660 psi, affixed to the spiral tube at location A. The residual liquid nanocrystal dispersion, now located at location B within the spiral tube, was further

subjected to the next higher CO_2 pressure, 680 psi, and allowed to sit for 20 minutes to allow additional condensed CO_2 to mix with the nanocrystal dispersion and, hence, induce the second largest size fraction to precipitate. This sequence of pressurization, precipitation and movement of the remaining liquid nanocrystal dispersion to the next location in the spiral tube, was repeated with CO_2 pressures of 700 and 800 psi resulting in nanocrystal precipitation of subsequently smaller size fractions at locations C & D in the spiral tube, respectively. After completing the final precipitation stage, the vessel was depressurized. The four fractions of the CdSe/ZnS core shell nanocrystals recovered at locations A, B, C and D were redispersed in hexane and displayed four distinct colors (red, orange, yellow and green), as shown in Figure 4-1, corresponding to the four samples used in making the original mixed nanocrystal dispersion.

4.3 Results and Discussion

In the end, four different colored fractions of the original CdSe/ZnS core shell quantum dot dispersion in hexane with TOPO as capping ligand were recovered using this CO_2 expanded liquid separation process. This result demonstrates that monodisperse fractions of CdSe/ZnS core shell quantum dots can be separated and recovered from a mixture of multiple sized CdSe/ZnS nanocrystals in a single process by using an efficient size separation technique based on the pressure tunable physicochemical properties of CO_2 gas expanded liquids. These redispersed CdSe/ZnS nanocrystals were further analyzed using UV-vis spectroscopy and Transmission Electron Microscopy (TEM).

4.3.1 UV-Vis Absorbance Spectroscopy

Figure 4-4 shows the UV–vis absorbance spectra of the four samples of TOPO capped

CdSe/ZnS core shell quantum dots dispersed in hexane before they were mixed and subsequently size-separated. A quartz cuvette of 10 mm path length was filled with $160\mu L$ of the dispersed nanocrystals in hexane and the UV-vis absorbance spectrum of each sample was collected using a Varian 300E spectrophotometer with absorbance measurements acquired at wavelength intervals of 1 nm over the range of 200 to 800 nm. It is clear from Figure 4-4 that the absorbance spectra of the CdSe/ZnS nanocrystals is a strong function of particle size. For example, the red line in Figure 4-4 corresponds to the sample with an average crystal diameter of 5.2 nm having a wavelength of maximum absorption of 594 nm (which also corresponds to a red colored dispersion). Similarly for the orange, yellow and green colored dispersions, corresponding to average crystal diameters of 3.2 nm, 2.4 nm, 1.9 nm, the wavelengths of maximum absorption were observed at 563, 522 and 475, respectively. Four dotted lines were added to Figure 4-4 corresponding to these wavelengths of maximum absorption for the four different sized CdSe/ZnS nanocrystals. Equal masses of the four CdSe/ZnS nanocrystal samples were combined to produce a mixed CdSe/ZnS nanocrystal dispersion in hexane consisting of four distinct nanocrystal size populations (average diameters ca. 5.2 nm, 3.2nm, 2.4nm, and 1.9 nm). This mixture of the CdSe/ZnS samples (now referred to as 'original' sample) was then subjected to particle separation (nanocrystal size fractionation) using the CO_2 gas expanded size separation technique. The UV-vis absorbance spectrum of this original sample is presented as a solid line in Figure 4-5. On the other hand, the dashed line in Figure 4-5 corresponds to the cumulative spectrum obtained by adding the absorbances at each wavelength from the four different spectra in Figure 4-4 corresponding to the four different colored dispersions (adjusted to zero absorbance at

800 nm). The primary absorbance bands in both the spectrum of the original sample mixture and cumulative spectrum correspond to the wavelengths of 594, 563, 522 and 475 nm indicating that there is no shift in the wavelengths of maximum absorption due to mixing, although the intensity of each band appears diminished due to the overlap of the other bands from the different sized particles. Figure 4-6 presents the UV-vis absorbance spectra of four different nanocrystal fractions (dispersions in hexane) that were obtained after performing the CO_2 expanded liquid size separation process on the original sample mixture along with four dotted lines corresponding to the wavelengths of maximum absorption of 594, 557, 516, and 467 nm. There is little variation between the wavelengths of maximum absorption before and after the size separation process coupled with a corresponding increase in the intensity of the respective absorption bands for each particle size compared to the original sample mixture, thereby indicating that this CO_2 expanded liquid size separation process is very effective in separating CdSe/ZnS nanocrystals by size into four different colored fractions. Table 4-1 shows a comparison of the UV-vis wavelengths of maximum absorption for the four fractions both before and after the CO_2 expanded liquid nanocrystal size separation process.

4.3.2 TEM Characterization

TEM grids were prepared for the original sample mixture (including all four sized CdSe/ZnS core shell quantum dots) as well as for each of the four individual nanocrystal fractions obtained after the size separation experiment. These grids were prepared by evaporative deposition by placing a small drop of the nanocrystal dispersion on a carbon coated copper TEM grid. These samples were examined using a Zeiss EM 10 Transmission Electron Microscopy (TEM) and the images obtained were further size

analyzed using ImageJ software where each particle in the image was bounded by a rectangle and the diameter was estimated by the average of length and width of the rectangle. Figure 4-7 shows an example of the TEM images obtained from the original (unprocessed) dispersion comprised of a mixture of 4 different sized CdSe/ZnS nanocrystals with average crystal sizes ranging from 5.2 to 1.9 nm. Figure 4-8 presents example TEM images obtained from each of the four CdSe/ZnS fractions recovered after the CO_2 expanded liquid size separation process corresponding to the red dispersion (obtained between P = 0 psi and 660 psi), orange dispersion (obtained between P = 660 psi and 680 psi), yellow dispersion (obtained between P = 680 psi and 700 psi) and green dispersion (obtained between P = 700 psi and 800 psi). The different sized CdSe/ZnS nanocrystal fractions precipitated and adhered to the spiral tube surface as illustrated in Figure 4-8 where the color of the recovered nanocrystal fraction changed from red, to orange, to yellow, to green with the increase in CO_2 pressure and droplet movement. After analyzing the TEM images of these fractions, it was observed that the average CdSe/ZnS crystal size collected from the different locations decreased with the increase in CO_2 pressure as shown in Table 4-1. The average particle sizes of these four fractions obtained after the size separation process are very similar to the sizes of the original quantum dots obtained from Evident Technology prior to mixing.   Both the UV-Vis spectral results and the particle sized obtained from the TEM images illustrate that CdSe/ZnS quantum dots can be rapidly (within 1 hour) separated by size using only hexane solvent and CO_2 as a anti-solvent in a CO_2 gas expanded liquid processing technique.

4.4 Conclusions

We have demonstrated that CO_2 can be use as an antisolvent to successfully size separate and fractionate the CdSe/ZnS core shell quantum dots through pressure tunable gas expanded liquids in a simple process. This is a rapid, precise, pressure tunable and green nanocrystal size separation technique.

4.5 Acknowledgements
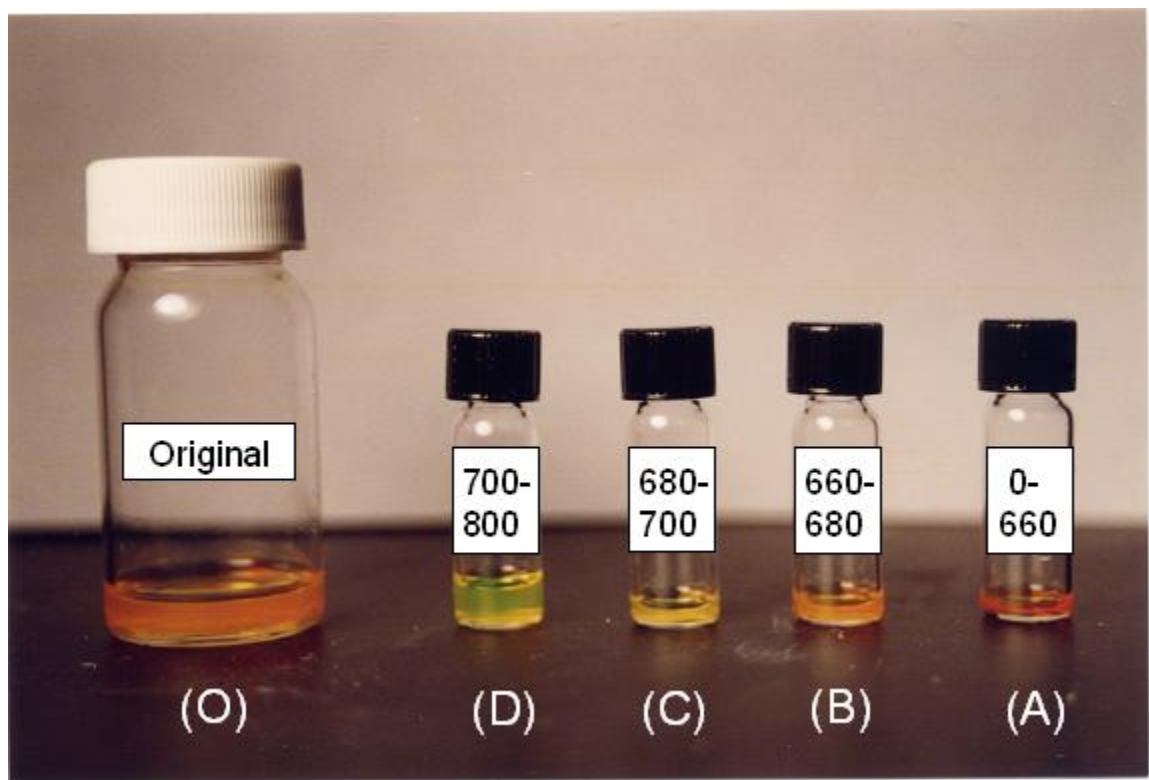
Figure 4-1 Image of CdSe/ZnS core shell nanocrystal dispersions in hexane before (O) and after (A, B, C, D) size separation using CO_2 gas expanded hexane where vial (O) contains the original mixture of four distinct sizes of CdSe/ZnS particles in hexane, and vials (A, B, C, D) contain the separate size fractions collected between (A) 0 to 660 psi, (B) 660 to 680 psi, (C) 680 to 700 psi and (D) 700 to 800 psi.
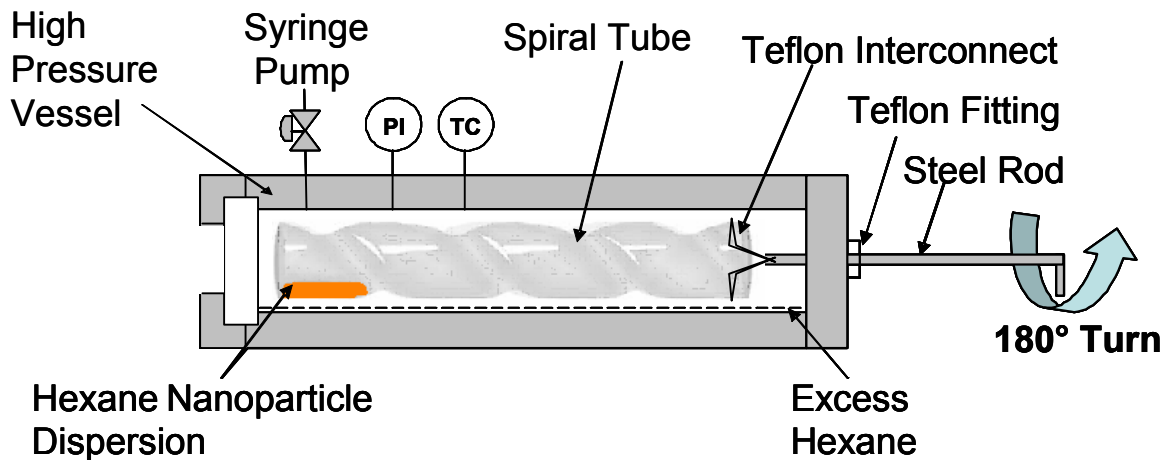
Figure 4-2 Nanocrystal size separation apparatus consisting of a glass open-ended tube, with a concentric spiral groove, enclosed within a high pressure vessel. The hexane nanocrystal dispersion is placed within the groove of the glass tube and excess hexane is loaded to saturate the high pressure vessel with hexane vapor. The teflon fitting allows the steel rod to enter into the vessel and maintains the high pressure seal. Turning the steel rod 180° rotates the open ended, glass spiral tube with the help of the Teflon interconnect thereby allowing translation of the liquid droplet. PI and TC stand for pressure indicator and temperature controller, respectively. CO_2 gas can be controllably introduced via a high pressure syringe pump.
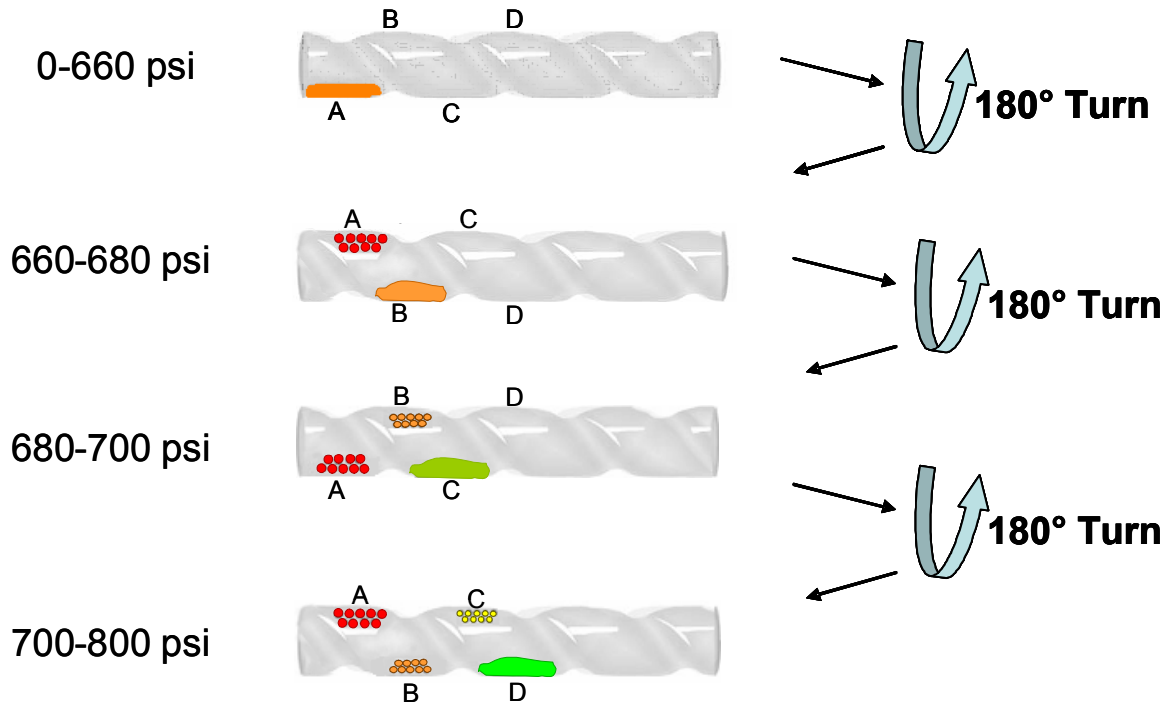
Figure 4-3 Nanocrystal size separation spiral tube apparatus depicting recursive pressurization of organic liquid with CO_2, followed by 180° tube rotations to achieve multiple size selected populations.
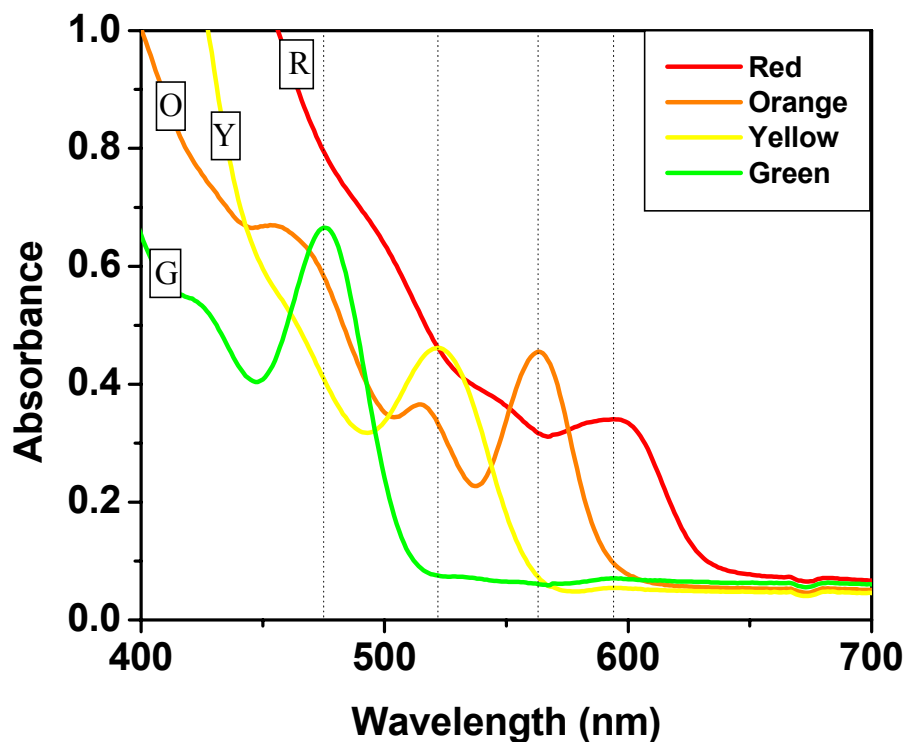
Figure 4-4 UV-visible absorbance spectra of CdSe/ZnS core shell nanocrystals capped with TOPO and dispersed in hexane (the as obtained nanocrystals from Evident Technology were dispersed in toluene and a solvent exchange was performed as described within to change the solvent medium to hexane). The spectra were normalized to give zero absorbance at 800 nm wavelength. Four dotted lines were drawn corresponding to the wavelength of the maximum absorption for the four different sized CdSe/ZnS nanocrystal dispersions. The R, O, Y and G lines correspond to the spectra obtained for the Red, Orange, Yellow and Green dispersions, respectively.
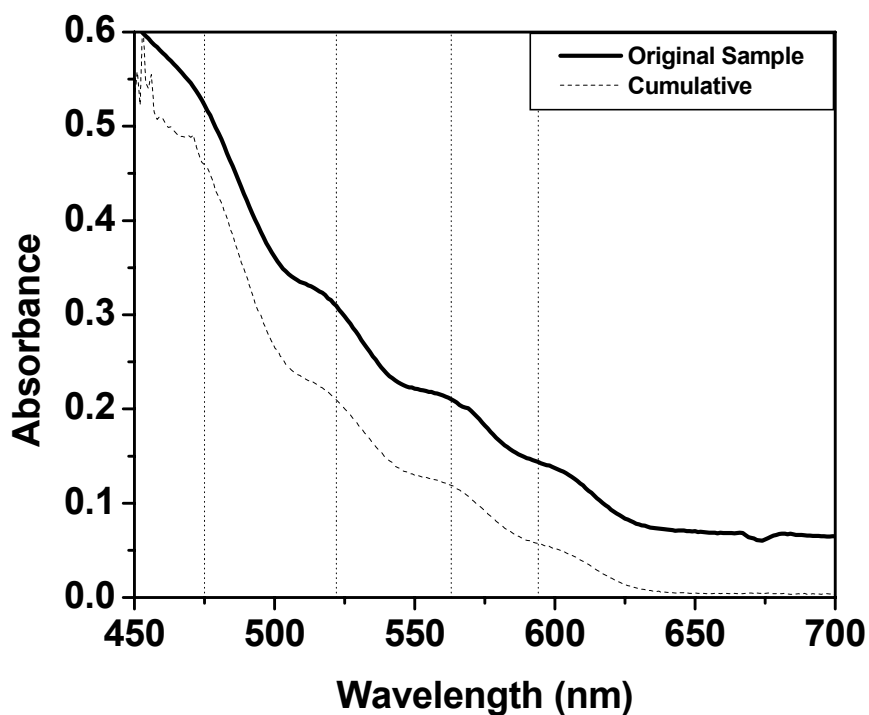
Figure 4-5 UV-visible absorbance spectra of a mixture of CdSe/ZnS core shell nanocrystals capped with TOPO and dispersed in hexane. The solid line spectrum was obtained by recording the UV-vis absorbance spectrum of the original mixture. The dashed line (cumulative spectrum) was obtained by adding the absorbances of the spectra of four different sizes of the CdSe/ZnS core shell nanocrystals from Figure 4-4. The spectra were normalized to give zero absorbance at 800 nm wavelength. Four dotted lines were drawn corresponding to the wavelength of the maximum absorbance for four different sized CdSe/ZnS nanocrystals. There is no shift in the wavelength of the maximum absorbance due to mixing of four different sized nanocrystals.
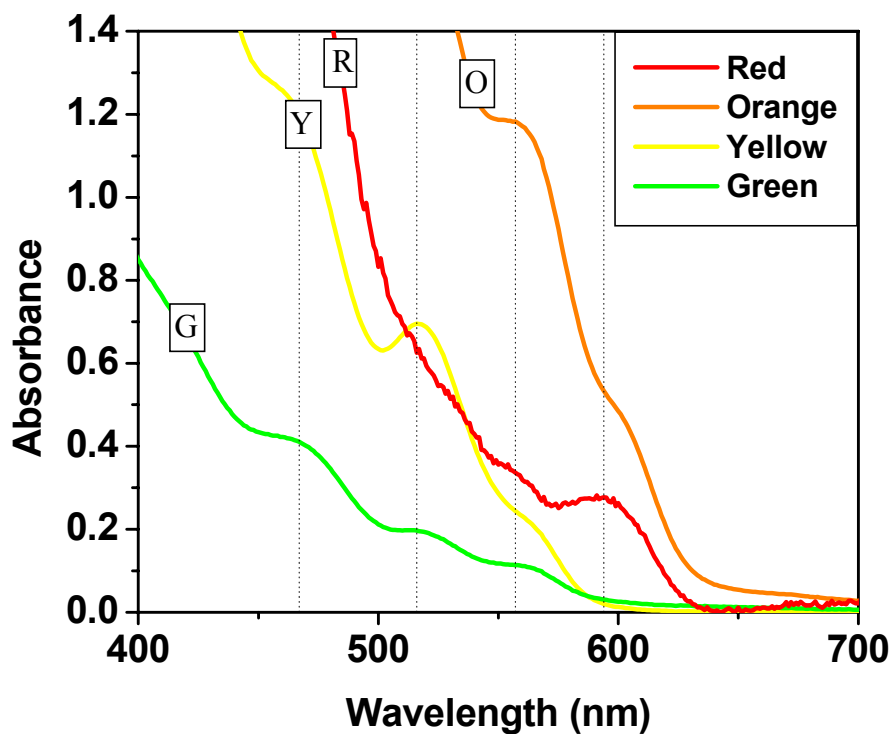
Figure 4-6 UV-visible absorbance spectra of CdSe/ZnS core shell nanocrystals obtained after the size separation of the original mixture in a spiral tube apparatus using CO_2 expanded liquid technique. These particles are capped with TOPO and dispersed in hexane. The spectra were normalized to give zero absorbance at 800 nm wavelength. Four dotted lines were drawn corresponding to the wavelength of the absorbance maximum for four different sized CdSe/ZnS nanocrystals. The wavelength of the maximum absorbance for four different spectra obtained after the size separation are similar to the spectra obtained before the size separation process.
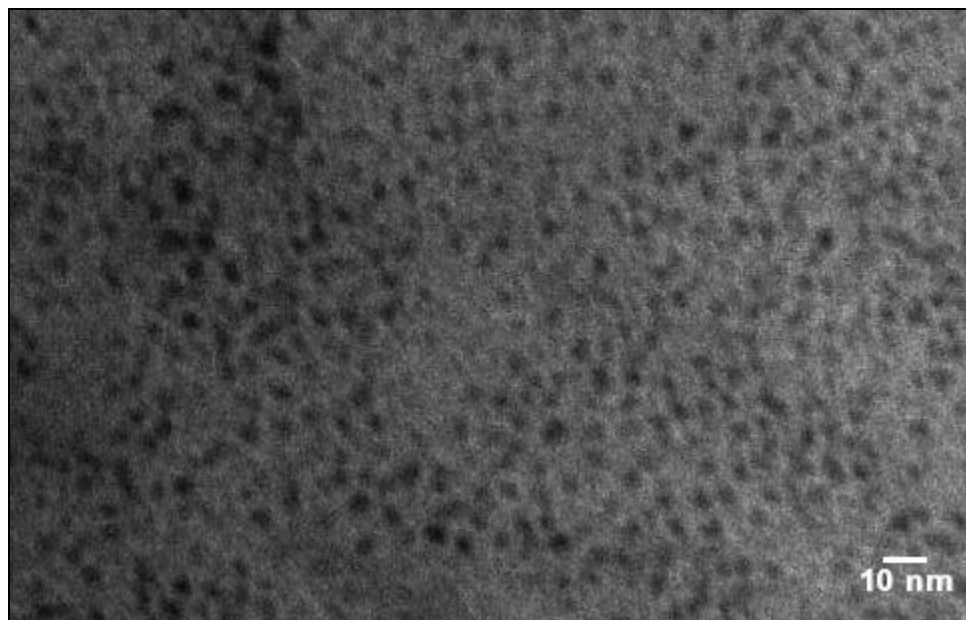
Figure 4-7 Example TEM image obtained from the original (unprocessed) dispersion comprised of a mixture of 4 different sized CdSe/ZnS nanocrystals with average crystal sizes ranging from 5.2 to 1.9 nm.
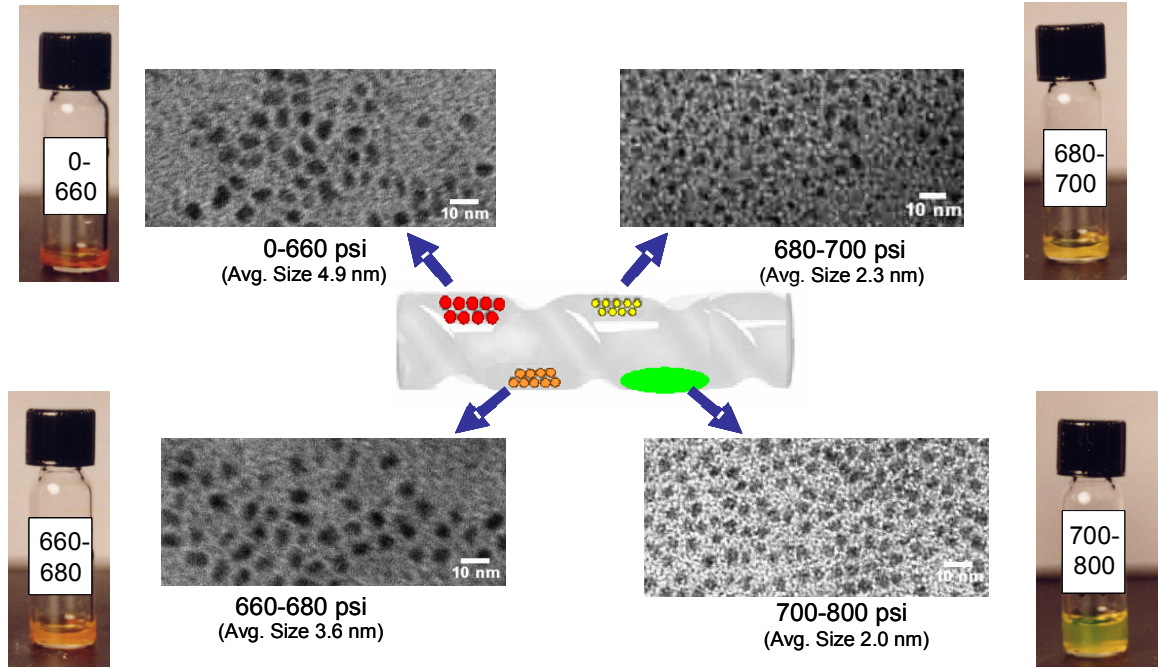
Figure 4-8 Example TEM images obtained from each of the four CdSe/ZnS fractions recovered after the CO_2 expanded liquid size separation process using the high pressure spiral tube apparatus. The four images correspond to the particles obtained from the recovered red, orange, yellow and green dispersions, corresponding to average CdSe/ZnS crystal sizes of 4.9, 3.6, 2.3 and 2.0, respectively.

Fraction	UV- vis Wavelength (nm)		Mean Crystal Diameter (nm)		Pressure (Psi)
	Before Separation	After Separation	Before Separation	After Separation	
Red	594	594	5.2	4.9	0 to 660
Orange	563	557	3.2	3.6	660 to 680
Yellow	522	516	2.4	2.3	680 to 700
Green	475	467	1.9	2.0	700 to 800

Table 4-1 Statistical analysis of particle populations where a polydisperse dispersion of TOPO (trioctyl phosphine oxide) capped CdSe/ZnS core shell nanocrystals were separated into four monodisperse fractions in a single experiment.

CHAPTER 5

SYNTHESIS AND EXTRACTION OF β-D GLUCOSE STABILIZED AU NANOPARTICLES

PROCESSED INTO LOW DEFECT, WIDE AREA THIN FILMS AND ORDERED ARRAYS USING

CO_2-EXPANDED LIQUIDS

This chapter presents a straightforward and economic strategy to create aqueous Au
nanoparticle dispersions using small amounts of β-D glucose as a "green" alternative to
the conventional phase transfer catalyst approach. Furthermore, this new process provides
for efficient extraction of these monodisperse Au nanoparticles into an organic phase
which was successfully processed into wide area, locally ordered nanoparticle arrays and
thin films using a precisely controlled CO_2-expanded liquid particle deposition technique.
This CO_2 based technique allows pressure tunable particle deposition while eliminating
the detrimental surface tension and dewetting effects common to normal solvent
evaporation techniques.

5.1 Introduction

The creation of nanometer-scale particles as stable building blocks for the assembly of
supramolecular structures such as nanoparticle thin films and ordered arrays has been an
area of significant interest (Blackburn, Long et al. 2001; Saunders, Shah et al. 2004).
Much of the recent interest in the assembly of nanoparticle thin films has been driven by

113

their prospective applications including electronic devices (Brust, Bethell et al. 1998; Shipway, Katz et al. 2000), optical materials (Freeman, Grabar et al. 1995; Brust, Bethell et al. 1998; Shipway, Katz et al. 2000; Lu, Liu et al. 2005), sensors (Wohltjen and Snow 1998; Evans, Johnson et al. 2000; Shipway, Katz et al. 2000), molecular catalysts (Dai and Bruening 2002; Sun and Crooks 2002) and others. Herein, we present a straightforward β-D glucose assisted aqueous phase process for the synthesis of Au nanoparticles followed by extraction of the particles into an organic phase via ligand exchange. This extraction process results in a Au nanoparticle dispersion with a narrow size distribution in an organic solvent. This organic nanoparticle dispersion was subsequently processed into close packed, wide area thin films and ordered arrays using a precisely controlled CO_2-expanded liquid particle deposition technique. This strategy has several technical advantages and attributes. First, it provides a facile and effective nanoparticle synthesis/extraction approach to produce relatively monodisperse nanoparticles without the need for elaborate post synthesis processing to narrow the particle size distribution. Notably, the process utilizes small amounts of β-D glucose as a "green" alternative to expensive phase transfer catalysts while also allowing complete recycle of the β-D glucose. Second, CO_2-expanded liquid and supercritical CO_2 ($scCO_2$) processes were implemented as a means to remove organic solvents thereby avoiding the detrimental dewetting effects and interfacial tensions that exist in conventional solvent evaporation techniques. This CO_2-based technique also allows for nanoparticle deposition with much greater focus since the particles settle directly onto the substrate without being carried to undesired locations by the liquid/vapor interface (McLeod, Kitchens et al. 2005). As a result, low defect and wide area nanoparticle thin films were formed with

114

local order. Additionally, the CO_2-expanded liquid process allows particle deposition to occur at mild conditions compared to the high pressures commonly required in $scCO_2$ based synthesis and assembly of Nanomaterials (Holmes, Johnston et al. 2000; Shah, Hanrath et al. 2004; Liu, Raveendran et al. 2005). Finally, the environmentally benign solvents of water and CO_2 were employed along with the "green" capping agent β-D glucose and a small amount of inexpensive dodecanethiol (as opposed to the expensive and environmentally persistent fluorinated compounds required in $scCO_2$ based processes).

Considerable effort has been directed towards the creation of close packed, ordered arrays and wide area nanoparticle thin films (Andres, Bielefeld et al. 1996; Whetten, Khoury et al. 1996; Kiely, Fink et al. 1998; Lin, Jaeger et al. 2001; Brust and Kiely 2002; McLeod, Kitchens et al. 2005). Unfortunately, few strategies (Lin, Jaeger et al. 2001) demonstrate the ability to generate nanoparticle thin films that have both the characteristics of wide area coverage and two dimensional order (ordered arrays). Lin et al. (Lin, Jaeger et al. 2001) have reported the formation of the long-range-ordered Au nanocrystal superlattices on silicon nitride substrates using a large amount of dodecanethiol prior to solvent evaporation in order to maintain a long lasting wetting layer. The availability of stable nanoparticle building blocks with uniform size and shape is a prerequisite to the assembly of these supramolecular films. For this purpose, alkanethiols have been shown to be effective capping ligands to passivate the surfaces and quench the growth of particles due to the well established chemical bonding between the SH functional group and the surface of the metallic nanoparticles (Brust, Walker et al. 1994; Templeton, Wuelfing et al. 2000). Brust et al. (Brust, Walker et al. 1994) first

reported a phase transfer approach for particle synthesis that has been very widely employed in the preparation of thiol-protected metal nanoparticles (Whetten, Khoury et al. 1996; Kiely, Fink et al. 1998; Shah, Holmes et al. 2000; Sigman, Saunders et al. 2004; McLeod, Anand et al. 2005; McLeod, Kitchens et al. 2005). The Brust-Schiffrin method utilizes a phase transfer catalyst in order to introduce metal ions into an organic solution thereby avoiding the use of expensive organic metallic compounds as reaction precursor. However, this approach requires the use of a significant amount of expensive phase transfer catalyst and organic solvent as well as elaborate and time-consuming post synthesis processing to narrow the size distribution of the product (Whetten, Khoury et al. 1996; Korgel, Fullam et al. 1998; Shah, Holmes et al. 2000; Sigman, Saunders et al. 2004). Recently, Crooks et al. reported that monodisperse metal nanoparticles could be extracted intact from dendrimer templates from an aqueous solution to an organic phase using n-alkanethiols (Garcia-Martinez, Scott et al. 2003; Garcia-Martinez and Crooks 2004; Wilson, Scott et al. 2004). Unfortunately, the high cost of these dendrimers makes them less promising as industrially viable capping agents. To date some polyhydroxylated molecules such as sugars and polymeric sugars have been successfully used for nanomaterial synthesis and self-assembly facilitated by inter- and intra-molecular hydrogen bonding (Raveendran, Fu et al. 2003; Huang, Li et al. 2004; Lu, Gao et al. 2004; Bae, Numata et al. 2005; Liu, Raveendran et al. 2005; Lu, Gao et al. 2005; Liu, Qin et al. 2006). Liu. et al. recently reported an interesting self-assembly of β-D glucose stabilized Pt nanocrystals into nanowire-like structures in aqueous solution (Liu, Raveendran et al. 2005). The work presented herein demonstrates that β-D glucose stabilized Au nanoparticles in aqueous solution can be effectively extracted into an

organic phase through an exchange of the capping agent from the β-D glucose to dodecanethiol. This strategy allows for the formation of 2-D Au nanoparticle superlattices upon the evaporation of organic solvent. Unfortunately, organic solvent evaporation results in dewetting effects, capillary forces and surface tensions that are detrimental to the supramolecular assembly of nanoparticles into low-defect and wide area nanoparticle thin films (Ohara and Gelbart 1998; Lin, Jaeger et al. 2001; Shah, Novick et al. 2003; McLeod, Kitchens et al. 2005). To overcome this limitation, this chapter further presents a nanoparticle deposition technique utilizing CO_2 as an antisolvent to target low-defect and wide area nanoparticle thin films without the detrimental dewetting effects inherent to the evaporation of normal liquid systems.

5.2 Experimental

5.2.1 Gold Nanoparticle Synthesis

The Au nanoparticles were first synthesized by the reduction of Au^{3+} ions in a β-D glucose aqueous solution using sodium borohydride ($NaBH_4$) as a reducing agent. In a typical preparation, a 200μL aliquot of a 0.05M aqueous $HAuCl_4.3H_2O$ solution was added to 50mL of a 0.05M β-D glucose aqueous solution. Subsequently, a freshly prepared 0.05M $NaBH_4$ aqueous solution (c.a. 600μL) was added to the system (leading to a pH value around 4.3), whereby the solution gradually changed its color to ruby red (see Figure 5-S1 in supporting information) visually indicating the initial formation of Au nanoparticles.

5.2.2 Gold Nanoparticle Extraction

Once the Au nanoparticles were formed in the β-D glucose aqueous solution the transfer

117

of the particles into an organic phase was examined using a liquid-liquid extraction process. While the β-D glucose stabilized Au nanoparticles could not be extracted directly from the aqueous phase (10mL) into a hexane phase (5mL), the addition of 100μL of dodecanethiol allows for fast and complete extraction of the Au nanoparticles from aqueous phase to the hexane phase upon vigorous shaking of the glass tube (see Figure 5-1 inset).

5.2.3 Gold Nanoparticle deposition

The apparatus used for the deposition/assembly of the Au nanoparticle thin films is depicted in Figure 5-2. A TEM copper grid was placed in a glass tube followed by the addition of 150 μL of the Au nanoparticle dispersion in hexane that was produced in the extraction experiments described above. The Au nanoparticle dispersion has a concentration adequate for a complete monolayer surface coverage on the TEM grid substrate ($\sim 3.5 \times 10^{-4}$ M Au in the hexane dispersion). The glass tube held by a Teflon sleeve was immediately put into a 50 mL stainless steel view cell for the thin film deposition experiments. In a typical experiment, the chamber was first gently charged with CO_2 gas up to 200 psi using an ISCO 260D high pressure syringe pump and the pump and the cell were allowed to equilibrate at this pressure. The vessel was then very slowly pressurized at room temperature with a constant CO_2 flow rate of 0.3 mL/min delivered from the syringe pump. Faster pressurization rates, on the other hand, lead to clustering and aggregation of particles in solution before settling thereby yielding regions of high nanoparticle concentrations and clusters of packed nanoparticles (McLeod, Kitchens et al. 2005). This slow pressurization was continued until a pressure of 800 psi was reached. Figure 5-7 presents the UV-vis absorption spectra of Au nanoparticles in the

118

CO$_2$-expanded hexane solution collected on a Cary 3 UV-vis spectrophotometer over a pressure range of 200-800 psi. The characteristic absorption band for dispersed Au nanoparticles centered at ca. 517 nm decreases in absorption intensity as the CO$_2$ pressure is increased indicating the controllable precipitation of the nanoparticles from solution with simple adjustments of system pressure (absorption maximum as a function of pressure is presented in the inset of Figure 5-7). At pressures of 800 psi and above, the particles are completely removed from CO$_2$-expanded hexane solution. This CO$_2$ pressurization process was then continued beyond this 800 psi threshold where more CO$_2$ was added until liquid CO$_2$ filled the high pressure vessel at the vapor pressure. Once the entire vessel was filled with a liquid CO$_2$/hexane mixture (with the nanoparticles deposited on the bottom of the glass vial), the system was elevated to the supercritical state by increasing the temperature to 40 ^{o}C and the pressure correspondingly increased to ca. 1700 psi facilitating the complete dissolution of the hexane into this supercritical phase. This transition to the supercritical state eliminates the surface tension at the liquid/vapor interface and the associated surface wetting instabilities that have detrimental effects on the assembly of nanoparticles into low defect thin films. The vessel was then slowly purged with pure CO$_2$ at 40 ^{o}C and a constant pressure of 1700 psi. After purging the vessel with 25ml of pure CO$_2$, the CO$_2$ was completely vented from the vessel and the TEM grid with gold nanoparticle deposition was collected.

5.3 Results and Discussion

5.3.1 Gold Nanoparticles Dispersion before Extraction

Figure 5-1 (curve a) presents the UV-vis surface plasmon absorbance spectrum of β-D

glucose capped Au nanoparticles in aqueous solution. The appearance of the characteristic absorption band of Au nanoparticles at 508 nm suggests that the β-D glucose is an effective capping agent for the formation and stabilization of these nanosized particles. The interaction between the Au nanoparticles and the β-D glucose hydroxyl groups was examined by comparing the Fourier Transform Infrared (FTIR) spectrum of neat β-D glucose (Figure 5-S2a in supporting information) and the FTIR spectrum of the β-D glucose capped Au nanoparticles (Figure 5-S2b in supporting information) recovered from the aqueous dispersion. A strong absorption peak at 3395 nm^{-1} indicates the attachment of the β-D glucose on the surface of the Au nanoparticles (Huang, Li et al. 2004). The –OH stretching vibration undergoes a significant high frequency shift from 3260 to 3395 nm^{-1} resulting from the association between the β-D glucose hydroxyl groups and the surface of the Au nanoparticles (Huang, Li et al. 2004). A typical TEM image of the β-D glucose capped Au nanoparticles is presented in Figure 5-3 along with the corresponding histogram of the particle size distribution. Au nanoparticles with an average diameter of 6.9 nm (standard deviation, SD = 1.6 nm) were observed. This further confirms that β-D glucose effectively passivates the surface of the Au particles thus suppressing their growth. Centrifugation (6000/rpm) of the aqueous β-D glucose- stabilized Au nanoparticle dispersion results in a significant precipitation of the Au nanoparticles. These β-D glucose-stabilized Au nanoparticles can be completely re-dispersed in the aqueous phase by simply shaking the centrifuge tube. It is important to note that this cycle of precipitation and re-dispersion can be readily repeated without irreversible aggregation or decomposition.

5.3.2 Gold Nanoparticles Dispersion after Extraction

Larger amounts of the reducing agent $NaBH_4$ and highly basic environments were found to have negative effects on the extraction. UV-vis absorption spectra of the Au nanoparticles dispersed in hexane (curve b) and the residual aqueous phase (curve c) after extraction are also presented in Figure 5-1 illustrating the successful extraction of Au nanoparticles into the hexane phase. After extraction, the hexane phase exhibited a characteristic UV-vis absorption band for dispersed Au nanoparticles at 515 nm (comprising a red shift of 7 nm upon extraction). The increased absorption intensity of curve (b) compared to the intensity of curve (a) stems from the increase in concentration of particles in the smaller volume of the hexane phase upon extraction. The absence of any peak in curve (c) quantitatively indicates the complete extraction of the Au nanoparticles from the aqueous phase into the hexane phase. It is worth noting that highly concentrated Au nanoparticle dispersions in hexane can also be achieved upon extraction utilizing a minimum amount of organic solvent (e.g. a 10 fold increase in concentration, see Figure 5-S3 in supporting information) and hence providing another "green" virtue of this strategy.

Figure 5-4 shows a comparison of the FT-IR spectra for neat dodecanethiol (a) and Au nanoparticles collected from the organic phase after extraction (b). The common features in the FT-IR spectra confirm the presence of thiol on the Au nanoparticles. The dodecanethiol alkyl tails allow for the extraction of the Au nanoparticles into the alkyl solvent hexane. Slight shifts were observed for the CH_2 antisymmetric stretch (from 2925 to 2918 cm^{-1}) and the symmetric stretch (from 2855 to 2849 cm^{-1}), suggesting that the hydrocarbon chains in the monolayer surrounding the Au nanoparticles are in a close-

packed state (Korgel, Fullam et al. 1998). Figure 5-4b also shows the C-C twisting, wagging and rocking vibrations in the broad region of 1200-800 cm^{-1}. The increase in intensity and sharper nature of the spectra can be ascribed to the capping effect (Khomane, Manna et al. 2002). Importantly, the disappearance of the –OH stretching band in the range of 3000-3500 cm^{-1} in Figure 5-4b (after extraction) indicates the complete substitution of the β-D glucose with dodecanethiol. The energy dispersive spectroscopy (EDS) spectrum presented in Figure 5-5 was also used to identify the composition of the nanoparticles after extraction where both Au and sulfur atoms were present in the EDS spectra while oxygen was not. The EDS results further indicate the complete substitution of β-D glucose with dodecanethiol thereby enabling the extraction of the Au nanoparticles from the aqueous β-D glucose solution into the organic hexane phase. The β-D glucose remaining in the aqueous phase after extraction can therefore be recycled. The low cost and the ability to recycle the β-D glucose provides for a "green" and economically attractive approach. The nanoparticle extraction principle is shown in Scheme 1.

Figure 5-6 presents a typical TEM image of the Au nanoparticles obtained after extraction along with a corresponding particle size distribution histogram. The sample for TEM analysis was prepared by evaporating hexane from a droplet of Au nanoparticle dispersion. This evaporation process results in the self-assembly of a close-packed and ordered array (or 2-D superlattice) of relatively monodisperse spherical Au nanoparticles (average diameter = 6.8 nm, SD = 1.1 nm). The extracted Au nanoparticles exhibit nearly the same average particle diameter compared to those analyzed before extraction with a more narrow size distribution. These Au nanoparticle self-assemblies are characterized

by hexagonal arrangements of parallel rows of Au nanoparticles separated by a distance of 1-2 nm. Unfortunately, the high interfacial tensions, capillary forces and dewetting effects inherent to the evaporating vapor/liquid interface inevitably lead to areas of high local particle concentration and random voids preventing wide area coverage of nanoparticle superlattices (Ohara and Gelbart 1998; Lin, Jaeger et al. 2001; Shah, Novick et al. 2003; McLeod, Kitchens et al. 2005). This is clearly shown in the low magnification TEM image presented later in Figure 5-8b. The elimination of these detrimental effects is important in the assembly of nanoparticles with narrow size distribution into low defect and wide area nanoparticle thin films (McLeod, Kitchens et al. 2005).

5.3.3 Gold Nanoparticle Thin Film Formation

Compressed CO_2 has been used as an alternative solvent to overcome these dewetting instability issues due to its vanishingly low interfacial tension and excellent surface wetting properties (Shah, Novick et al. 2003). For example, Shah et al. utilized CO_2 as a solvent medium for the stabilization of fluorinated-ligand coated Ag nanoparticles (Shah, Holmes et al. 2000). Furthermore, Shah and coworkers used liquid CO_2 as a means of depositing fluorinated ligand stabilized gold nanocrystals with controllable solvent evaporation rates while overcoming the thin film instabilities and dewetting effect common to normal liquid solvents (Shah, Novick et al. 2003). However, much of the focus on CO_2 as a solvent for nanoparticle processing has relied heavily on environmentally suspect and expensive fluorinated ligands/surfactants (Ji, Chen et al. 1999; McLeod, McHenry et al. 2003; Shah, Hanrath et al. 2004) due to the weak solvent strength of CO_2 for conventional hydrocarbon ligands and surfactants (Ryoo, Webber et

123

al. 2003; Bell, Anand et al. 2005). CO_2 gas expanded liquid systems (i.e. CO_2/organic solvent mixtures) provide a tunable alternative to compressed CO_2 with a wider range of solvent properties available (i.e. from that of pure organic solvent to that of liquid CO_2 below the vapor pressure of CO_2) (Jessop, Olmstead et al. 2002; Wei, Musie Ghezai et al. 2002). This wider range of available solvent strength allows for the stabilization and controllable deposition of nanoparticles in these CO_2 tunable solvent systems with conventional hydrocarbon stabilizing ligands (Anand, McLeod et al. 2005; McLeod, Anand et al. 2005; McLeod, Kitchens et al. 2005) rather than fluorinated compounds. This methodology utilizes compressed CO_2 as an antisolvent to create an organic/CO_2 liquid mixture (often termed as a CO_2 gas-expanded liquid) of variable solvent strength where an increase in CO_2 pressure results in a decrease in the liquid mixture solvent strength. Ligand capped nanoparticles will be dispersed in a solution when the interaction between the solvent and the ligand tails (solvation) provides enough repulsive force to overcome the inherent van der Waals attraction between the particles that would otherwise result in agglomeration and precipitation. The poorer solvent mixture that results from the addition of the CO_2 antisolvent interacts less with the ligand tails than does the pure solvent. Therefore, this reduces the ability of the solvent/antisolvent mixture to disperse the particles and hence nanoparticle precipitation can be achieved through application of CO_2 pressure to the organic solvent. Han and coworkers (Zhang, Han et al. 2001; Zhang, Han et al. 2002) have recently demonstrated the ability to employ CO_2 as a gas antisolvent to recover metal and semiconductor nanoparticles from reverse micelles in isooctane. More recently, our group has reported on the precise size selection and targeted deposition of nanoparticle populations (Anand, McLeod et al. 2005;

124

McLeod, Anand et al. 2005) and the deposition of wide area silver nanoparticle thin films (McLeod, Kitchens et al. 2005)   utilizing CO_2-expanded liquid particle deposition techniques. While this CO_2-expanded liquid particle deposition technique did produce wide area nanoparticle thin films, the particles were randomly distributed without local order due in part to the relatively high CO_2 pressurization rates employed (McLeod, Kitchens et al. 2005). The low pressurization rates employed in this work should allow formation of thin films with both local order and wide area coverage. Wide area, close-packed arrays can be achieved through the elimination of dewetting effects (Shah, Novick et al. 2003; McLeod, Kitchens et al. 2005) and the use of relatively monodisperse particle populations (Murray, Kagan et al. 1995; Andres, Bielefeld et al. 1996; Murray, Kagan et al. 2000).

Figure 5-7 presents the UV-vis absorption spectra of Au nanoparticles in the CO_2-expanded hexane solution collected on a Cary 3 UV-vis spectrophotometer over a pressure range of 200-800 psi. The characteristic absorption band for dispersed Au nanoparticles centered at ca. 517 nm decreases in absorption intensity as the CO_2 pressure is increased indicating the controllable precipitation of the nanoparticles from solution with simple adjustments of system pressure (absorption maximum as a function of pressure is presented in the inset of Figure 5-7). At pressures of 800 psi and above, the particles are completely removed from CO_2-expanded hexane solution. The entire vessel was then filled with liquid CO_2 and elevated to the supercritical state. This transition to the supercritical state eliminates the surface tension at the liquid/vapor interface and the associated surface wetting instabilities that have detrimental effects on the assembly of nanoparticles into low defect thin films. Purging with pure CO_2 provides displacement of

the hexane from the system leaving the vessel with supercritical CO_2 above the nanoparticle thin film. Transition from the supercritical state to the gas phase can be achieved by simply lowering the pressure while keeping the temperature above the critical temperature of the mixture. As such, the supercritical CO_2 was gently vented from the vessel at this elevated temperature as a single phase reducing the detrimental impact of a phase transition or surface tension effects on the nanoparticle assembly that was deposited on the TEM grid at the bottom of the glass vial.

Figure 5-8c&d present TEM images of the assembly of dodecanethiol coated Au nanoparticles deposited using the CO_2-expanded hexane technique. It should be noted that the dodecanethiol capped Au nanoparticle dispersion used in this CO_2 expanded liquid process was the same as that used in the solvent evaporation process shown in Figure 5-6 and Figure 5-8b. Figure 5-8c&d demonstrate that close packed, ordered arrays of Au nanoparticles can be deposited/assembled into wide area thin films on the TEM grid successfully using this CO_2-expanded hexane technique. These CO_2 processed films are superior in their structural arrangement and wide area coverage compared to the Au nanoparticle assemblies created from the evaporation of the aqueous solution (Figure 5-8 a) or the organic solvent hexane (Figure 5-8 b). Even though these Au nanoparticles are not assembled into long range parallel arrangements, the particles are densely packed into hexagonal microarrays as shown in the high magnification TEM images (Figure 5-8d). Figure 5-8 (c) presents an image of a portion of a Au nanoparticle film covering an area of 0.84 μm^2. The low defect Au nanoparticle thin film actually extends over an even greater area encompassing the entire TEM grid (see Figure 5-S4 with an area of 4.2 μm^2 in supporting information) or other substrate such as the quartz window shown in Figure

5-10a. Au nanoparticle thin films having the characteristics of both wide area coverage and structural regularity of this type have seldom been reported. The electron diffraction (ED) pattern in Figure 5-8e corresponds to the standard crystalline planes of a face-centered-cubic (fcc) structure of Au nanocrystals indicating that the nanoparticle thin film created in this work has crystalline structural properties. In addition, ordered 3-D multilayer thin films with wide area coverage can also be achieved by simply controlling the quantity of the Au nanoparticle/hexane dispersion prior to CO_2 expansion (Figure 5-9 and Figure 5-S5 in supporting information). Apparently, this tunable CO_2 based deposition technique has allowed the assembly of Au nanoparticles into low defect ordered arrays through the elimination of dewetting effects common to simple solvent evaporation.

The UV-vis optical properties of Au nanoparticle thin films and ordered arrays are of current interest. In this context, Au nanoparticle thin films were prepared on the surface of a 11.40 cm^2 quartz window by placing it on the bottom of a glass vial (containing 2 mL of a 3.5×10^{-4} M Au in hexane dispersion) and then placing the vial inside a 50mL stainless steel high-pressure vessel. The Au nanoparticles were then deposited on the surface of the quartz window following the same CO_2 processing procedures described above. A uniform and wide area Au nanoparticle thin film was achieved over the entire surface of the quartz window (Figure 5-10a) where the film exhibited a light purple color significantly different than that of the unprocessed quartz window (Figure 5-10 b). Figure 5-10c presents the UV-vis absorption spectrum of the Au nanoparticle film on the quartz window. Interestingly, a significant UV-vis absorption band centered at 570 nm was observed. This represents a significant red shift of about 55

nm compared to that of the Au nanoparticles dispersed in hexane. This red shift is attributed to the collective contributions of the individual nanoparticles within the close packed, ordered arrays.

5.4 Conclusion

In summary, a straightforward and effective nanoparticle synthesis/extraction strategy was developed based on aqueous β-D glucose solutions to yield Au nanoparticle dispersions with narrow size distribution. These Au nanoparticle dispersions were successfully processed using CO_2 tunable solvent systems into wide area, close packed nanoparticle assemblies. This new nanoparticle synthesis and deposition strategy presents economic, environmental and processing opportunities in the bottom-up development of nanoscale devices that require nanoparticle arrays.

5.5 Acknowledgment

5.6 Supporting Information Available

We present digital images of an aqueous β-D glucose capped Au nanoparticle dispersion and the effective extraction process of the particles to create a highly concentrated Au nanoparticle dispersion in hexane, FTIR spectra of neat β-D glucose and β-D glucose capped Au nanoparticles along with low magnification TEM images of the wide area

monolayer and multilayer Au nanoparticles films.
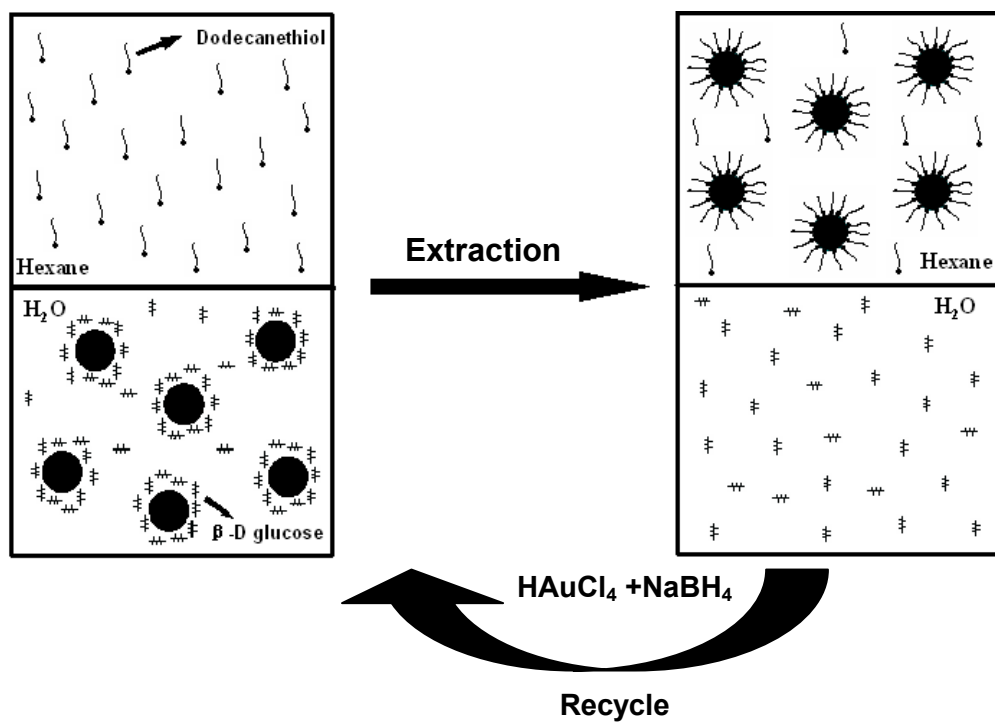
Scheme 1 Extraction of Au nanoparticles from aqueous phase to organic phase

via exchange of capping agent.
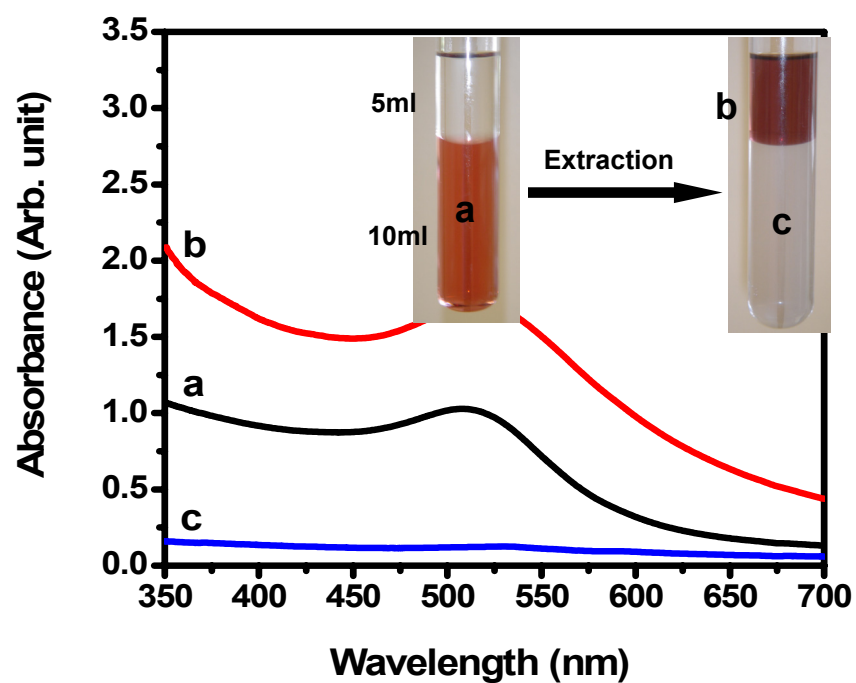
Figure 5-1 The surface-plasmon absorption spectra of Au nanoparticles before and after extraction; (a) aqueous phase β-D glucose capped Au nanoparticles before extraction, (b) dodecanethiol capped Au nanoparticles dispersed in hexane after extraction, (c) residual β-D glucose aqueous phase after extraction. The inset presents digital images of the Au nanoparticle extraction process.
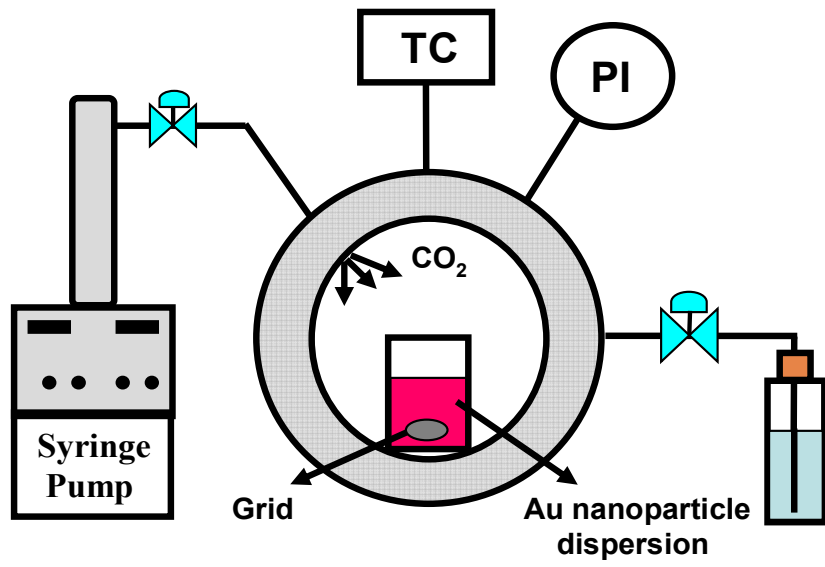
Figure 5-2 Schematic drawing of the experimental setup for the CO_2-expanded liquid deposition/ assembly of the Au nanoparticles into thin films.
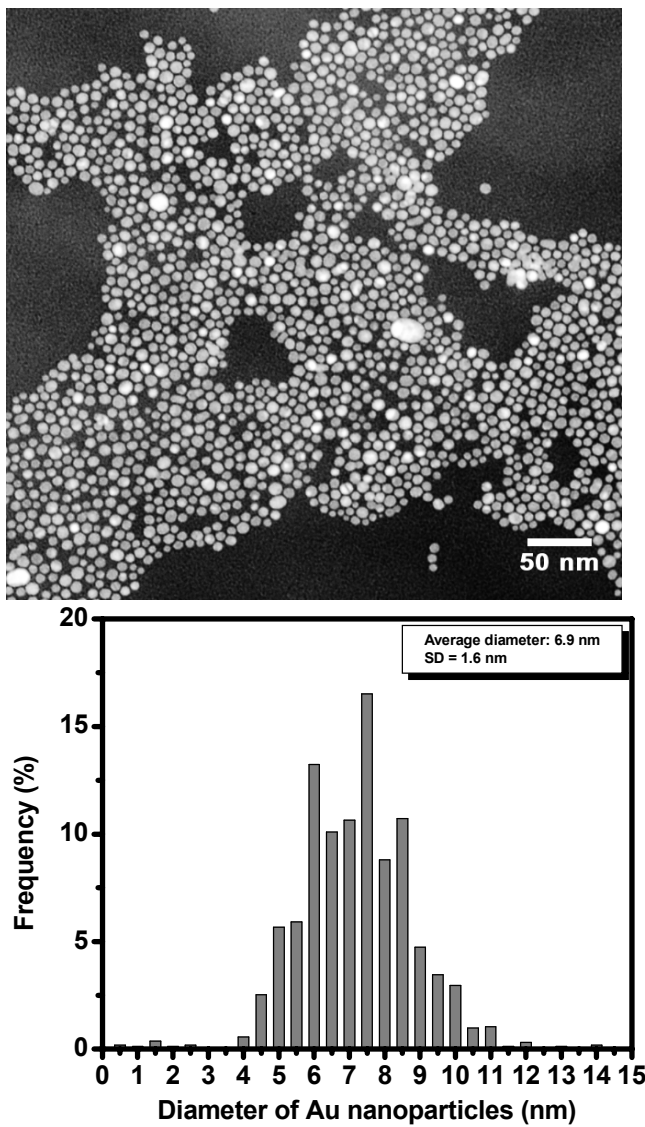
Figure 5-3 TEM image of β-D glucose capped Au nanoparticles along with the corresponding particle size distribution histogram. The sizes of 1620 particles were determined using Image J software to create the histogram.
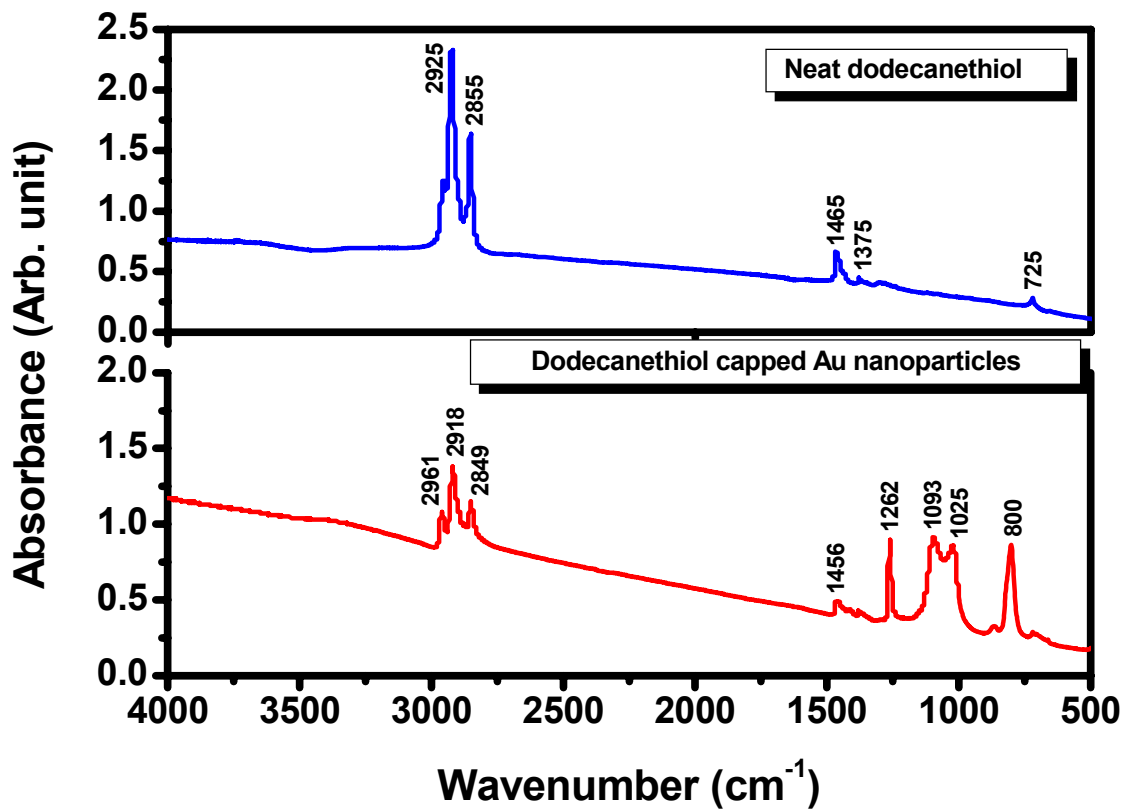
Figure 5-4 FT-IR spectra of (a) neat dodecanethiol and (b) dodecanethiol coated Au nanoparticles.
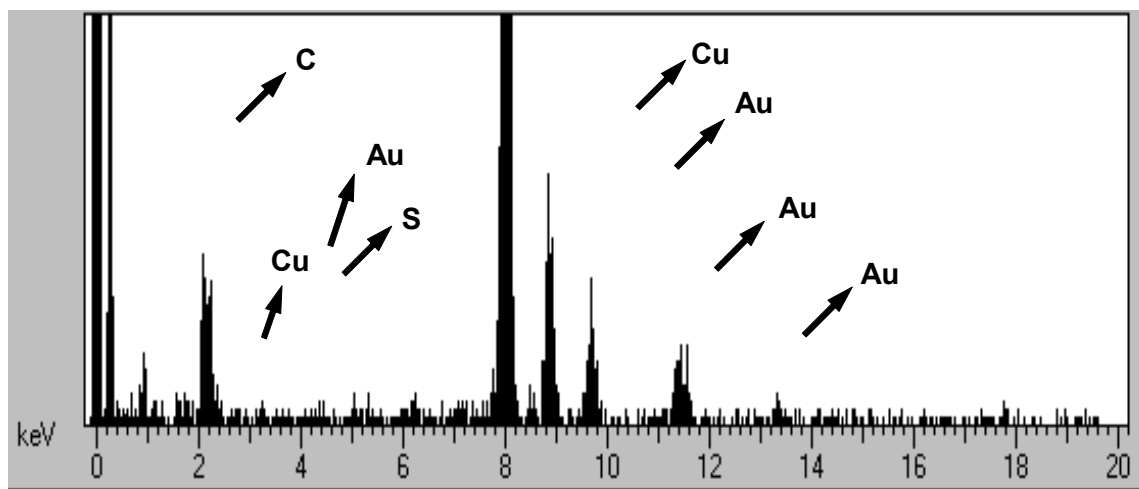
Figure 5-5 EDS spectrum of the dodecanethiol capped Au nanoparticles obtained after extraction.
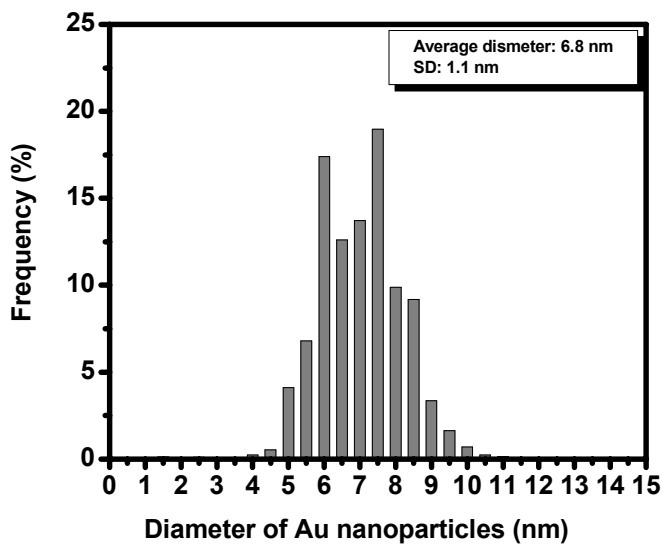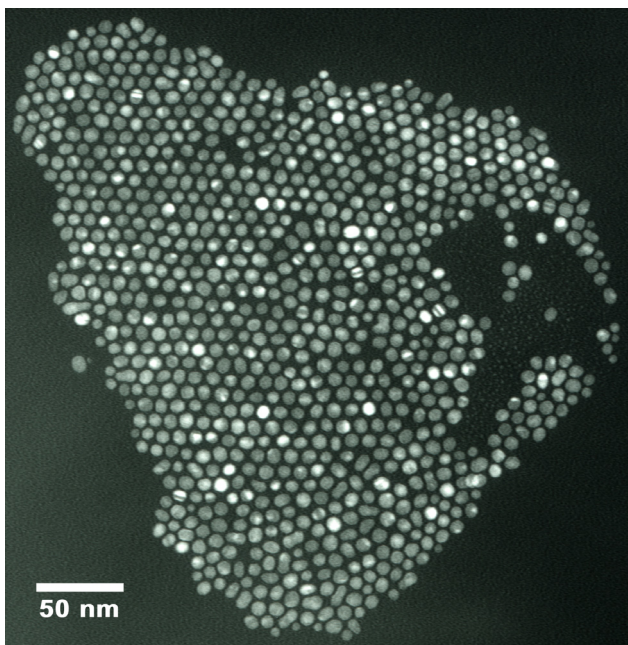
Figure 5-6 TEM image of dodecanethiol capped Au nanoparticles obtained after extraction along with the histogram of the particle size distribution. The sizes of 4524 particles were determined using Image J software to create the histogram.
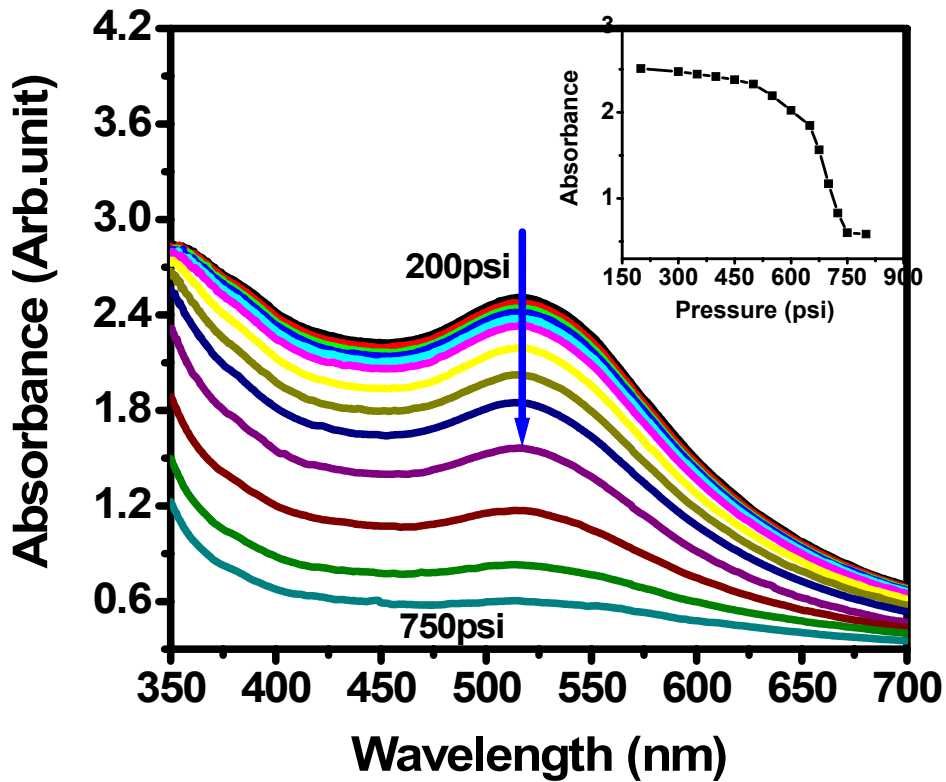
Figure 5-7 UV-vis absorption spectra of Au nanoparticles in the CO_2-expanded hexane at various pressures. The inset presents the effect of the system pressure on the absorption intensity of the Au nanoparticles at 517 nm wavelength.
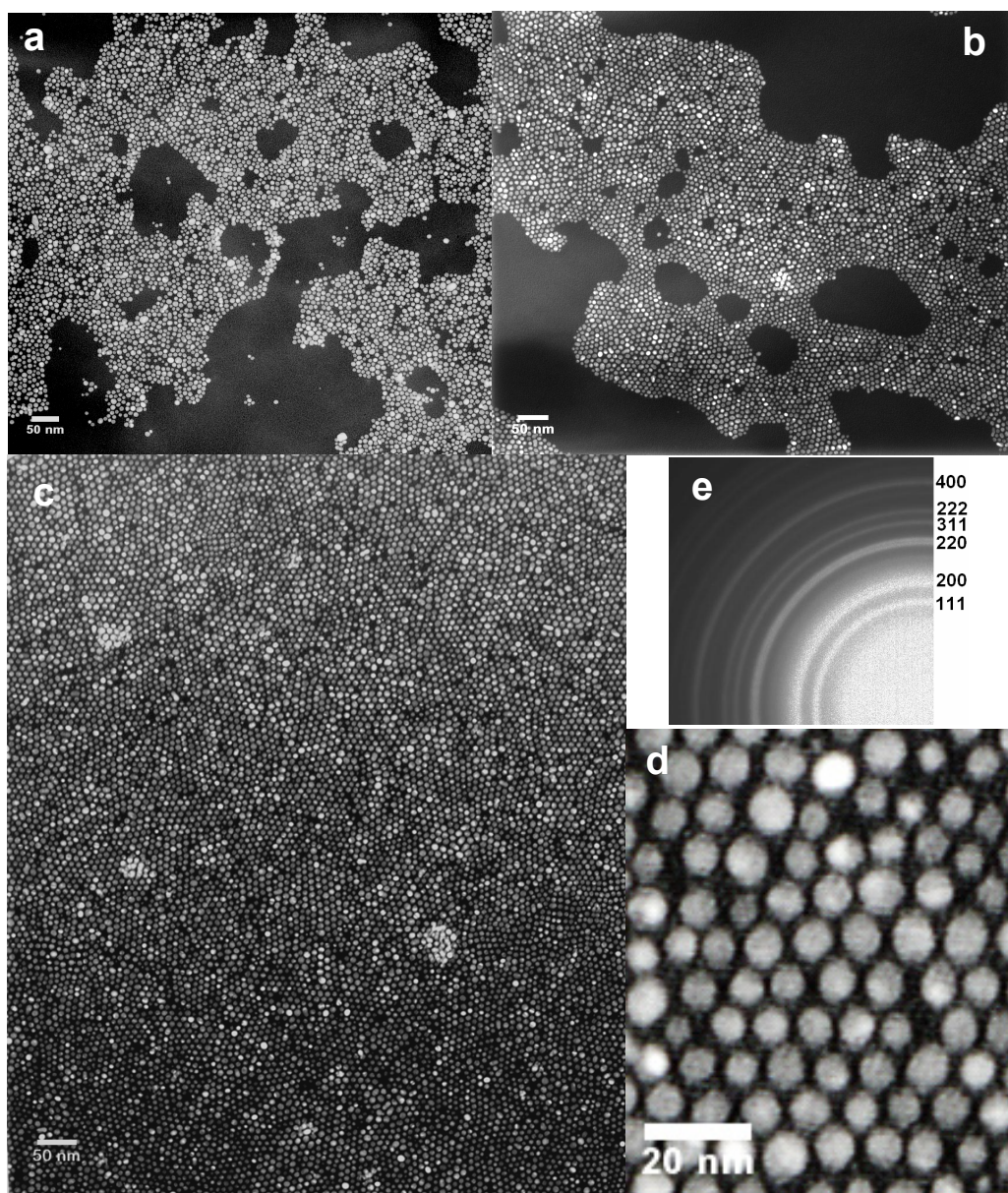
Figure 5-8 TEM images of Au nanoparticles deposited on carbon coated copper TEM grid using three different approaches: (a) β-D glucose capped Au nanoparticles deposited on the TEM grid by evaporation of aqueous solution. (b) dodecanethiol capped Au nanoparticles deposited on a TEM grid by evaporation of hexane solvent (particles were initially synthesized in aqueous β-D glucose solution and extracted into hexane phase via

ligand exchange). (c) dodecanethiol capped Au nanoparticles deposited on a TEM grid using the CO_2 expanded hexane particle deposition technique (particles were initially synthesized in aqueous β-D glucose solution and extracted into hexane phase via ligand exchange prior to CO_2 processing). (d) higher magnification image of Au nanoparticles. (e) electron diffraction pattern of Au nanoparticles within the thin film presented in (c).
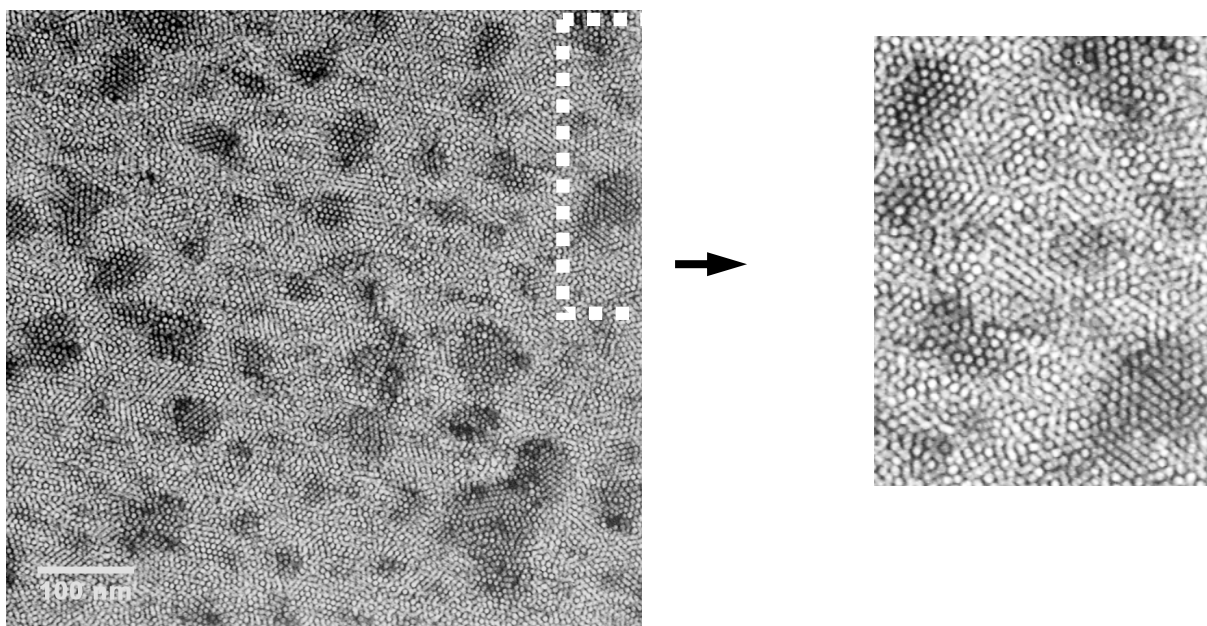
Figure 5-9 TEM images of multilayer Au nanoparticle thin film deposited by the CO_2 expansion of 250μL of 3.5×10^{-4} M Au in hexane dispersion.
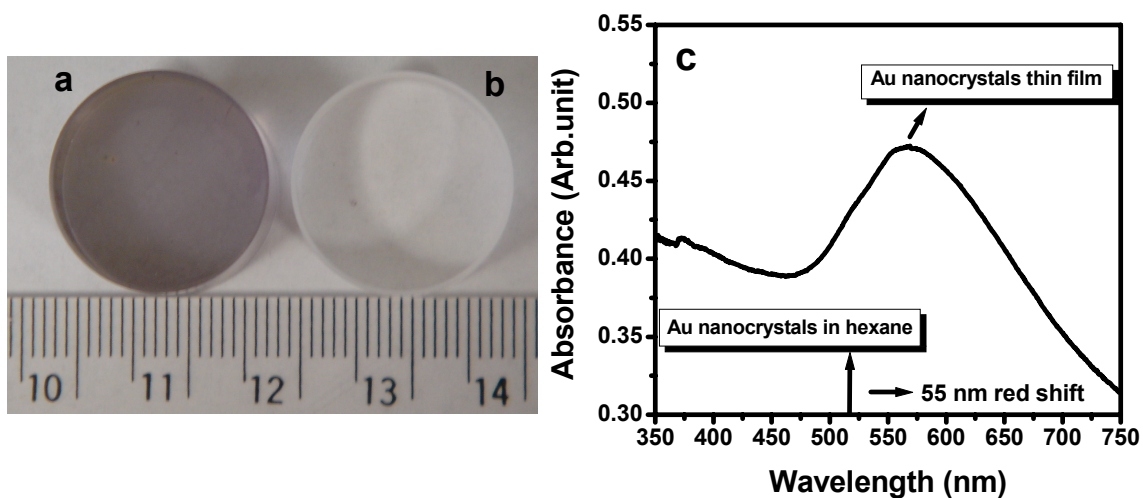
Figure 5-10 (a) Image of a Au nanoparticle thin film coated quartz window. (b) Image of an unprocessed quartz window. (c) UV-vis absorption spectrum of the Au nanoparticle thin film shown in image (a) corrected for the baseline absorption of the unprocessed window. The thin film was prepared on the quartz surface through CO_2 expansion of 2 ml of a 3.5×10^{-4} M Au in hexane dispersion.

SYNTHESIS AND EXTRACTION OF B-D GLUCOSE STABILIZED AU NANOPARTICLES

PROCESSED INTO LOW DEFECT, WIDE AREA THIN FILMS AND ORDERED ARRAYS USING

CO$_2$-EXPANDED LIQUIDS

Figure 5-S1 Digital image of an aqueous dispersion of β-D glucose stabilized Au nanoparticles.
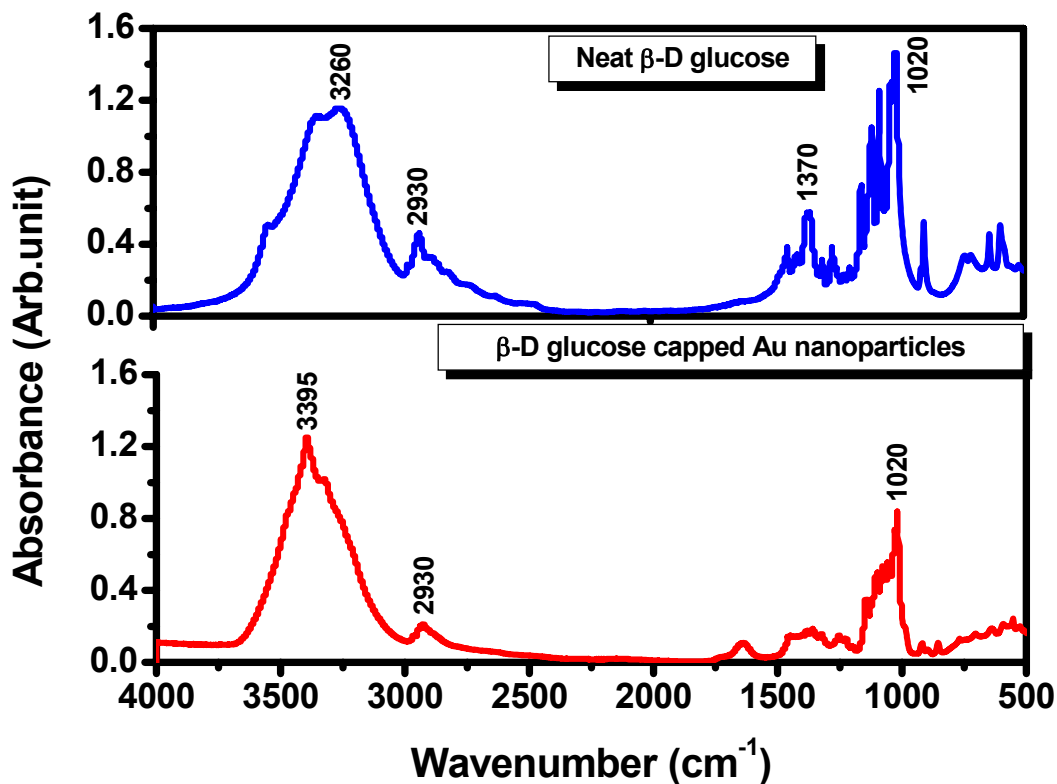
Figure 5-S2 FT-IR spectra of neat β-D glucose (a) and β-D glucose coated Au nanoparticles (b).

Preparation of FT-IR sample: Initially, an aqueous Au nanoparticle dispersion was centrifuged for 15 minutes at a speed of 6000/rpm where a significant portion of the Au nanoparticles were precipitated on the bottom of the centrifuge tube. A polyethylene transfer pipette was used to withdraw the highly concentrated Au nanoparticle aqueous solution from the bottom of the centrifuge tube. This process of centrifugation and withdrawal was repeated three times to remove the Au nanoparticles from the bulk phase thereby leaving most of the unbound β-D glucose and isolated ions in the upper solution. A centrifugal membrane with a molecular weight cutoff of 3000 (PALL Life Science) was subsequently employed to further remove excess glucose and isolated ions. Freeze-

drying under vacuum was then applied overnight to obtain a dry Au nanoparticle composite. Finally, the FT-IR samples were obtained by forming a thin pellet of transparent KBr (95 mg) and Au nanoparticles (1 mg). Figure 5-S2 (a) presents the pure β-D glucose IR spectrum where a broad band centered at 3260 cm^{-1} was observed, undoubtedly resulting from the -OH stretch of the β-D glucose molecules.

Extraction

Figure 5-S3: Digital images illustrating the effective extraction of Au nanoparticles from an aqueous β-D glucose solution into a hexane phase via ligand exchange from β-D glucose to dodecanethiol. These images display the generation of highly concentrated dodecanethiol capped Au nanoparticle dispersions in hexane.
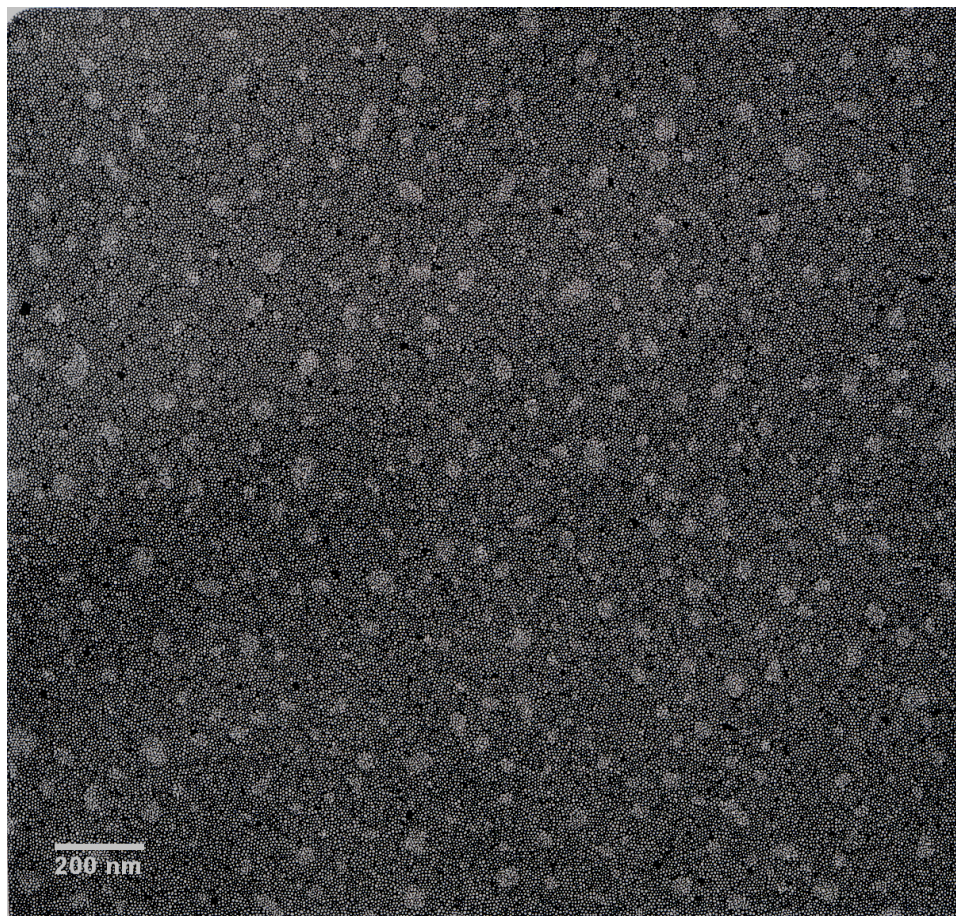
Figure 5-S4 Low magnification TEM image of a closed packed and locally ordered Au nanoparticles thin film over a wide area of 4.2 μm^2 (150μL of 3.5×10^{-4} M Au in hexane dispersion was employed).
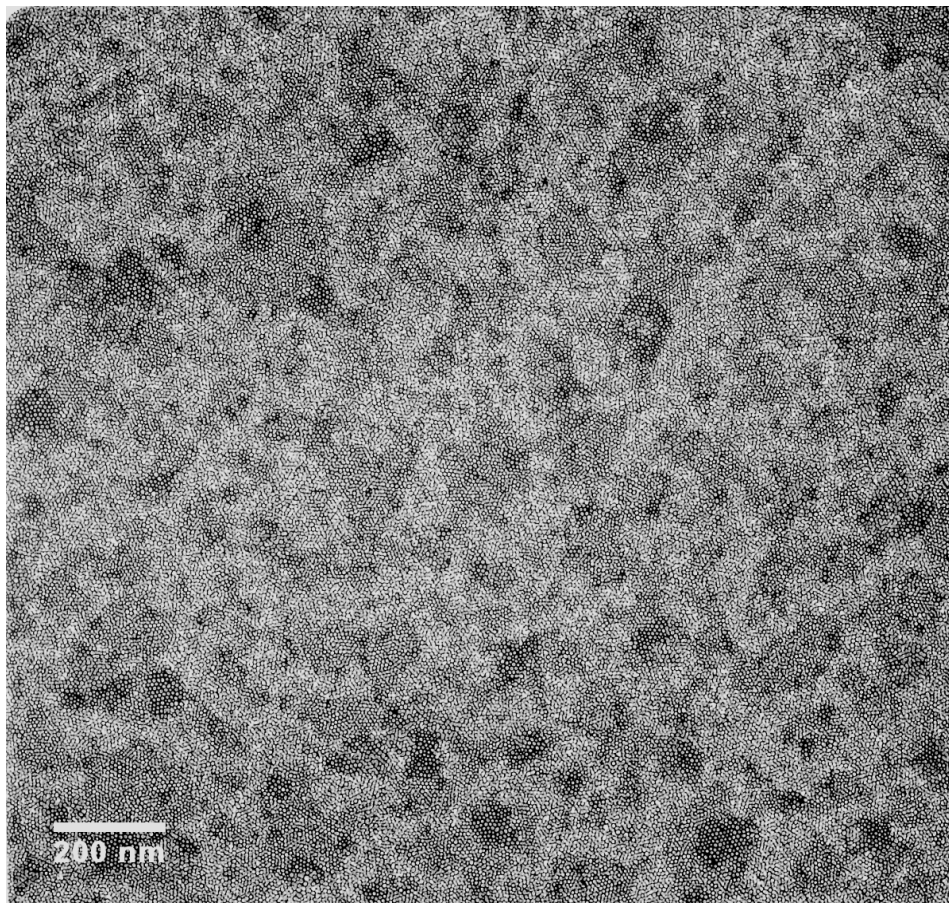
Figure 5-S5 TEM image demonstrating the generation of a wide-area Au nanoparticle multilayer film (3.0 μm^2 and 250µL of 3.5×10^{-4} M Au in the hexane dispersion was employed).

CHAPTER 6

SYNTHESIS AND STERIC STABILIZATION OF SILVER NANOPARTICLES IN NEAT CARBON

DIOXIDE SOLVENT USING FLUORINE-FREE COMPOUNDS

The adjustable solvent properties, vanishingly low surface tensions and environmentally green characteristics of supercritical carbon dioxide present certain advantages in nanoparticles synthesis and processing. Unfortunately, most current techniques employed to synthesize and disperse nanoparticles in carbon dioxide use environmentally persistent fluorinated compounds as metal precursors and/or stabilizing ligands. This chapter illustrates a one-step process for synthesis and stabilization of silver nanoparticles in carbon dioxide using only fluorine-free compounds. Iso-stearic acid coated silver nanoparticles were formed and stably dispersed through arrested precipitation. Silver bis(3,5,5-trimethyl-1-hexyl)sulfosuccinate (Ag-AOT-TMH) was reduced in the presence of iso-stearic acid as a capping ligand in carbon dioxide solvent to form silver nanoparticles. The addition of cyclohexane as co-solvent or an increase in carbon dioxide solvent density enhances the dispersibility of the particles due to an increase in solvent strength. The dispersibility of the iso-stearic acid capped silver nanoparticles diminished with time until a stable dispersion was achieved due to the precipitation of a fraction of particle sizes too large to be stabilized by the solvent medium, thereby leaving a smaller size fraction of nanoparticles stably dispersed in the CO_2 mixtures. This chapter presents

the first report of one-step synthesis and stabilization of metallic nanoparticles in neat carbon dioxide without the aid of any fluorinated compounds.

6.1 Introduction

Supercritical fluids (SCFs) have received a great deal of attention in the area of nanomaterial synthesis and processing due to their unique characteristics of tunable physicochemical properties, vanishingly low surface tensions and excellent wetting properties. Physicochemical properties like density, diffusivity, and solubility parameter can be readily altered by varying the pressure and temperature, creating opportunities for use in a number of processes (McHugh and Krukonis 1986). Carbon dioxide (CO_2) is the most commonly used supercritical fluid because it is cheap, relatively inert, nontoxic, readily available, non-flammable, miscible with many organic liquids, and environmentally benign. In addition to these attributes, the critical temperature (304 K) and the critical pressure (73.8 bar) of CO_2 are easily accessible.

The unique tunable solvent properties of CO_2 have been successfully used in the controlled synthesis of metal nanoparticles using a variety of fluorinated precursors, ligands and surfactants (Fan, McLeod et al.; Holmes, Bhargava et al. 1999; Ji, Chen et al. 1999; Shah, Holmes et al. 2000; Ohde, Hunt et al. 2001; Shah, Husain et al. 2001; Dong, Potter et al. 2002; Shah, Husain et al. 2002; McLeod, McHenry et al. 2003; Yu, Steele et al. 2003; Esumi, Sarashina et al. 2004; McLeod, Gale et al. 2004; Saunders, Shah et al. 2004; Liu, Raveendran et al. 2005). For example, Shah et al. (Shah, Husain et al. 2002) studied the effects of CO_2 density on the synthesis of perfluorodecanethiol-stabilized silver Ag nanoparticles in CO_2. They found that higher CO_2 densities yielded 2 nm Ag

nanoparticles compared to 4 nm particles at lower CO_2 densities. The tunable solvent properties of supercritical fluids have also been used to control the size selective dispersion of nanoparticles. Shah et al. (Shah, Holmes et al. 2002) demonstrated the size-selective dispersion of dodecanethiol coated nanoparticles in supercritical ethane by density tuning where the largest particle sizes were dispersed at the highest pressure and vice-versa. CO_2 solvent systems also offer unique wetting characteristics that can be used to improve the deposition of metal films on surfaces (Watkins, Blackburn et al. 1999; Blackburn, Long et al. 2001) and the deposition of nanoparticles on surfaces into uniform monolayers (Shah, Novick et al. 2003; McLeod, Kitchens et al. 2005). McLeod et. al. (McLeod, Kitchens et al. 2005) and Shah et. al. (Shah, Novick et al. 2003) used dispersions of nanoparticles in supercritical CO_2 and compressed liquid CO_2, respectively, in the formation of thin films of Ag nanoparticles with wider surface area coverage and uniformity compared to the films obtained by simple solvent-evaporation techniques. While CO_2 does offer certain processing advantages (e.g. tunable solvent strength and wetting characteristics), its use in nanoparticle synthesis, dispersion and processing is limited by the current need for fluorinated compounds resulting from its relatively poor solvent strength.

CO$_2$ is a feeble solvent because of its very low dielectric constant (1.1 to 1.5) and zero dipole moment, resulting in low solubility of many organic species. The very low polarizability per unit volume and low refractive index of CO_2 results in weaker van der Waals forces than hydrocarbon solvents, making CO_2 more similar to fluorocarbons with respect to solvent strength (Johnston, Harrison et al. 1996). Fluorinated surfactants (Hoefling, Beitle et al. 1993) have shown high solubility in CO_2 and some of them have

stabilized water in CO_2 microemulsions (Johnston, Harrison et al. 1996; Clarke, Harrison et al. 1997). Nanoparticles have been formed in CO_2 within water in CO_2 (W/C) microemulsions or by arrested precipitation techniques using fluorinated compounds. Shah et. al. (Shah, Hanrath et al. 2004) has written a descriptive review on nanoparticle synthesis and dispersibility in supercritical fluids. Both fluorinated surfactants and fluorinated ligands have been used to disperse particles in CO_2. Interactions between the CO_2 solvent and the fluorinated coating on the nanoparticles provide enough repulsive forces to counterbalance the attractive van der Waals forces between the particles. In W/C microemulsion systems, fluorinated surfactant supported aqueous cores act as nanoreactors to synthesize and then disperse the particles in a CO_2 phase due to strong interactions between CO_2 and the fluorinated surfactant tails. Various types of particles have been prepared in W/C microemulsions including: Ag (Ji, Chen et al. 1999; McLeod, McHenry et al. 2003) Ag halide (Liu, Raveendran et al. 2005), Cu (Ohde, Hunt et al. 2001), and semiconductor (Holmes, Bhargava et al. 1999) nanoparticles. Because fluorinated compounds are environmentally persistent and expensive, researchers are also trying to develop CO_2-philic fluorine free compounds or surfactants to form stable microemulsions in CO_2. For non-fluorinated compounds, the disadvantages of poor solubilities and high cloud point pressures can be overcome by adding co-solvents or CO_2-philic compounds. These co-solvents interact more strongly with the solute than CO_2 and can increase their solubility. Zhang et. al. (Zhang, Liu et al. 2003) produced Au nanoparticles in CO_2 induced reverse micelles of non-fluorinated surfactants using a mixture of p-Xylene and CO_2. One class of compounds that have shown high solubility in CO_2 are highly branched, methylated and stubby surfactants due to increased tail

solvation and weak tail-tail interactions (Eastoe, Paul et al. 2001; da Rocha, Dickson et al. 2003; Stone, Da Rocha et al. 2003; Stone, Smith et al. 2004). Researchers utilized stubby hydrocarbon surfactants (Liu, Han et al. 2001; Ryoo, Webber et al. 2003), ionic hydrocarbon surfactants (Dickson, Smith et al. 2005; Fan, Potluri et al. 2005) and trisiloxane surfactants (da Rocha, Dickson et al. 2003) to stabilize both microemulsions and macroemulsions in CO_2.

Nanoparticles have also been synthesized in supercritical CO_2 using arrested precipitation techniques where the particles are dispersed in a single continuous CO_2 phase while eliminating the aqueous phase. Arrested precipitation is one of the most successful solution based techniques for nanoparticle synthesis in conventional solvents. In this technique, an organometallic precursor soluble in a given solvent is reduced in the presence of a capping ligand (Brust, Walker et al. 1994) used to stabilize the particle and to quench further growth. Shah (Shah, Husain et al. 2001; Shah, Husain et al. 2002) and Mcleod (McLeod, Gale et al. 2004) used this technique in supercritical CO_2 and capped the synthesized nanoparticles with fluorinated thiol stabilizing ligands. Recently, Fan (Fan, McLeod et al.) was also successful in using a non-fluorinated precursor silver bis(3,5,5-trimethyl-1-hexyl)sulfosuccinate (Ag-AOT-TMH) and fluorinated thiols to stably disperse the particles in CO_2. They used a non-fluorinated organometallic compound, Ag-AOT-TMH, a highly methylated stubby compound with very high solubility in CO_2, but fluorinated ligands were still used. Even though fluorinated compounds generally have higher solubility in CO_2, the cost and environmental problems of fluorinated compounds present drawbacks to their use in many processing applications.

Recently, Bell et. al. (Bell, Anand et al. 2005) used a stubby non-fluorinated compound, iso-stearic acid, to disperse Ag nanoparticles in compressed liquid CO_2. In this technique, nanoparticles were first made in a conventional organic solvent using sodium bis(2-ethylhexyl) sulfosuccinate (AOT) reverse micelles and then the capping agent was replaced by iso-stearic acid via ligand exchange. When these iso-stearic acid capped particles were introduced into CO_2, only a very small fraction of the synthesized particles were dispersed in CO_2 due to the difference between the solvent strength of CO_2 and the organic solvent in which the particles were synthesized.

This chapter presents the first synthesis and subsequent stable dispersion of metal nanoparticles in neat CO_2 solvent without the use of any fluorinated compounds. The process described herein utilizes non-fluorinated iso-stearic acid as a nanoparticle stabilizing ligand and Ag-AOT-TMH as a non-fluorinated metal precursor where the whole process of Ag nanoparticle synthesis and dispersion is reduced to one step in neat CO_2 solvent. Cyclohexane was examined as a non-fluorinated co-solvent to further enhance the solvent strength of the CO_2 mixtures and hence the dispersibility of the iso-stearic acid capped nanoparticles.

6.2 Experimental Section

6.2.1 Materials

Silver nitrate (99.8%) was purchased from Acros. Iso-stearic acid (100%) was received from Nissan Chemical America Corporation. Sodium bis(3,5,5-trimethyl-1-hexyl)sulfosuccinate (AOT-TMH) was provided by Julian Eastoe of the University of Bristol. Cyclohexane (99.5%) and hexane (99+%), were obtained from Aldrich. Sodium

borohydride (NaBH4) (ReagentPlus, 99%) and anhydrous ether (99+%) were acquired from Sigma. Ethanol (200 proof) was obtained from Florida Distillers. Deionized water used in the Ag-AOT-TMH synthesis was obtained from Fisher Scientific. Carbon dioxide (SFC/SFE grade) was obtained from Airgas. All materials were used as received.

6.2.2 Ag-AOT-TMH Synthesis

The CO_2-soluble silver salt, Ag-AOT-TMH, was synthesized by an ion-exchange of the AOT-TMH compound. The AOT-TMH synthesis has been described elsewhere (Nave, Eastoe et al. 2000). The technique followed for the ion exchange was adapted from that given by Fan et al. (Fan, McLeod et al.). The procedure is briefly described here. 5.025 g AgNO3 (29.58 mmol) was dissolved in 10 mL of deionized water. 0.8297 g AOT-TMH (1.8 mmol) was dissolved in 5 mL of ethanol. The two solutions were mixed for 6 hours. 6 mL of ether was added to form two phases. The two phases were separated and the upper phase containing Ag-AOT-TMH was dried in a vacuum oven at room temperature. The remaining solid was re-dissolved in isooctane and centrifuged to remove any solid contaminants. The solid dissolved in isooctane was again dried in a vacuum oven at room temperature, resulting in a yellowish-brown solid, Ag-AOT-TMH.

6.2.3 Ag Nanoparticle Synthesis in CO_2

Ag-AOT-TMH was directly reduced in dense CO_2 to produce silver nanoparticles which were capped with iso-stearic acid ligands. The particle synthesis experiments were initiated by loading 0.0516 g Ag-AOT-TMH (0.06 wt%), 0.175 g iso-stearic acid (0.19 wt%), either 0, 2, or 10 mL cyclohexane co-solvent, and a Teflon coated magnetic stir bar into a 96 mL stainless steel vessel equipped with opposing quartz windows to allow

passage of a UV-vis beam. The vessel was then pressurized with CO_2 to 207 bar at 295 K. The contents were stirred for 1 hour to fully dissolve all solutes and achieve a single-phase mixture. 540 uL of a 0.8 M $NaBH_4$ in ethanol solution was added using a 6 port injection valve. The reducing agent was forced in by additional CO_2, increasing the total pressure to 276 bar. The silver nanoparticles formed by the reduction were monitored with UV-vis spectroscopy on a Varian 300E spectrophotometer. The vessel was depressurized and the particles were collected from the bottom of the vessel in hexane.

6.2.4 Ag Nanoparticle Imaging

A Zeiss EM 10 transmission electron microscope (TEM) was used to image the particles. TEM grids of the particles that were dispersed in CO_2 were prepared by directly spraying the CO_2 nanoparticle dispersion from the high pressure cell through a needle valve onto a carbon coated TEM grid. Once the TEM grids of the dispersed particles were collected through this spray technique, the vessel was completely depressurized as described in the section above to allow precipitation of the dispersed particles. A small amount of hexane was then added to the vessel to redisperse all of the particles synthesized. To analyze all of the particles synthesized in CO_2 (both those that were dispersed in CO_2 and those that were not), a TEM grid was prepared by evaporating the hexane from a droplet of dispersion collected from the bottom of the vessel directly on a carbon coated copper grid. Sizing of the silver nanoparticles from the TEM images was performed using ImageJ software, where each particle was bounded by a rectangle and the diameter was approximated by the average of the length and width.

6.2.5 Infrared Spectroscopy of Ag Nanoparticles

Fourier transform infrared (FTIR) spectroscopy was performed using a Nicolet Avatar 360 FT-IR spectrometer to investigate the nature of the chemical interaction between the iso-stearic acid ligands and the silver nanoparticles. The resolution used was 2 cm^{-1} and the number of scans were 64.

To prepare the nanoparticles for FTIR analysis, the hexane nanoparticle dispersion obtained after the depressurization of the vessel was mixed with ethanol as an antisolvent. The dispersion of nanoparticles in the solvent/antisolvent mixture was then centrifuged (Fisher Centrific Model 228) to precipitate out the Ag nanoparticles. The particles were again washed with ethanol and centrifuged to remove any free iso-stearic acid molecules from the precipitate. This process of washing with ethanol was repeated 3 times and then the silver particles were dried in an oven (> 60 ^{o}C) under vacuum overnight. Finally, to obtain the transmission spectra, pellets were made by mixing these particles (1 mg) with KBr powder (100 mg).

6.3 Results and Discussion

6.3.1 Ag Nanoparticle Synthesis and Stabilization in Neat CO$_2$

Ag-AOT-TMH and iso-stearic acid, shown in Figure 6-1, were chosen as silver organometallic precursor and stabilizing ligand, respectively, for the synthesis and subsequent dispersion of silver nanoparticles in CO$_2$ due to their highly methylated, branched tails. Values from the pressure-composition diagram for the Ag-AOT-TMH-CO$_2$ mixture (Fan, McLeod et al.) and iso-stearic acid-CO$_2$ mixture (Bell, Anand et al. 2005) obtained through phase behavior measurements demonstrate that these compounds

are highly soluble in CO_2. Branched, methylated tails in these compounds result in effective CO_2-tail solvation and weak tail-tail interactions (Eastoe, Paul et al. 2001; Johnston, Cho et al. 2001; Bell, Anand et al. 2005). These effects lead to high CO_2 solubility. Iso-stearic acid is completely miscible with CO_2 at pressures above 138 bar at 295 K as shown in the phase behavior studies done by Bell et.al (Bell, Anand et al. 2005).

AOT-TMH and Ag-AOT-TMH have similar solubilities (Fan, McLeod et al.) in CO_2 because the only difference between the two structures is a change in the cation. These compounds are soluble in dense CO_2 because of the branched methylated tails, and as expected, the cloud point pressure at low weight percentages is low. This phase behavior data was collected at 313 K, while our experiments were conducted at 295 K. Figure 6-S1 in the supplementary data shows that the cloud point pressure decreases with a decrease in temperature for AOT-TMH. The phase behavior experiments at different temperatures were not performed for Ag-AOT-TMH due to the limited quantity of material available. Due to the similarity between the structure of the two surfactants and their phase behavior data, it is expected that less pressure is required to dissolve Ag-AOT-TMH at 295K than 313K. It is clear from the phase behavior studies for Ag-AOT-TMH performed by Fan et.al. (Fan, McLeod et al.) that less than 100 bar is required to dissolve the 0.06 wt% Ag-AOT-TMH used in our experiments at 313 K. To dissolve the solid, the vessel was pressurized to 206 bar at 295 K. No solid was observed in the vessel after mixing and silver nanoparticles were formed, indicating that the Ag-AOT-TMH was sufficiently soluble in CO_2 at the experimental conditions used.

The one-step process for synthesis and stabilization of silver nanoparticles in pure CO_2 takes advantage of the solubility of Ag-AOT-TMH and iso-stearic acid in CO_2. The

UV-vis absorbance spectrum for silver nanoparticles synthesized in pure CO_2 is shown in Figure 6-2. The absorbance band centered at a wavelength of 419 nm is attributed to the absorption of silver nanoparticles dispersed in neat CO_2 (Petit, Lixon et al. 1993). A single distinct absorption band in this wavelength range reflects the presence of spherically shaped silver particles. The UV-vis absorbance in this range is due to the excitation of plasmon resonances or interband transitions. This absorbance band decreased with time as the larger particles were unable to remain dispersed in the pure CO_2 phase. After 3 days, the absorbance ceased to change, indicating a stable dispersion of silver nanoparticles. The fraction of particles that remain dispersed after three days can be roughly estimated from the decrease in the intensity of the UV-vis absorbance band since absorbance is proportional to the particle concentration in solution. Based on this rough estimate, 23% of the particles remained dispersed after three days. The effect of time on the absorption intensities of the nanoparticle dispersions is discussed in detail later in this chapter. Figure 6-3 shows a TEM image of the silver nanoparticles synthesized in neat CO_2. Samples of these particles were prepared using both of the collection methods described above. Figure 6-3(a) shows a TEM image of particles synthesized in pure CO_2 that were collected from the bottom of the vessel after 3 days by depressurizing the vessel and subsequent redispersion in hexane solvent for grid preparation (this sample includes both particles that were dispersed in CO_2 and those that were not). Figure 6-3(b) shows a TEM image of particles synthesized and successfully dispersed in pure CO_2 at 295 K and 276 bar. This sample was collected 3 days after synthesis by simply spraying the CO_2 nanoparticle dispersion directly onto a TEM grid surface. These images clearly illustrate that Ag nanoparticles can be synthesized and

stabilized in neat CO_2 without the need for fluorinated ligands. It is clear from these images that only the smaller fraction of particles synthesized could be dispersed in CO_2. Figure 6-4 presents the size distributions of the particles obtained using both collection methods. The average size and standard deviation of the particles synthesized in pure CO_2 (collected on the bottom of the vessel after depressurization) are 3.4 nm and ±1.3 nm (Relative standard deviation 39%) respectively. On the other hand, the average size and standard deviation of the particles synthesized and then dispersed in CO_2 (collected from spray process) are 2.6 nm and ±1.2 nm (Relative standard deviation 45%) respectively. While larger particles were formed in the synthesis and subsequent growth process in CO_2, only the smallest particles were sufficiently solvated by the CO_2 solvent to be stably dispersed. This was also illustrated by a decrease in the magnitude of the UV-vis absorbance peak as the larger fraction of particles precipitated over time, as discussed later in this chapter. These results are the first successful synthesis and dispersion of metallic nanoparticles in pure CO_2 without the use of any fluorinated compounds. Additionally, no organic solvents were required during the synthesis or dispersion.

6.3.2 Infrared Spectroscopy of Iso-stearic Acid Coated Ag Nanoparticles

FTIR spectroscopy analysis was performed to verify the presence of the acid on the surface of the Ag nanoparticles and to study the nature of the adsorption of the capping material on the silver nanoparticles surface. Figure 6-5 shows the FTIR spectrum of (a) neat iso-stearic acid and (b) Ag nanoparticles capped with iso-stearic acid as synthesized in CO_2. These particles were collected in hexane after depressurizing the high-pressure vessel and further washed with ethanol to remove any free iso-stearic acid using the washing process described in the experimental section above. Figure 6-5 (a) shows the

158

FTIR spectra of neat iso-stearic acid, where the broad band between 3400 and 2500 cm^{-1} corresponds to the O-H stretch of the carboxylic acid. (Bellamy 1975) Bands superimposed on the O-H stretch correspond to the asymmetric (2955 cm^{-1}) and symmetric (2868 cm^{-1}) CH$_2$ stretch respectively (Wu, Fu et al. 2004). The peak at 1704 cm^{-1} corresponds to the C=O stretch. Carboxylic acids (COOH) typically have a characteristic C=O stretching vibration at ~1750 cm^{-1}, however, extensive hydrogen bonding in the liquid state between the hydroxyl and carbonyl groups, can lower the frequency corresponding to the C=O stretch to ~1700 cm^{-1} (Petroski and El-Sayed 2003). Figure 6-5 (b) corresponds to the FTIR spectrum of Ag nanoparticles coated with iso-stearic acid. Slight shifts were observed for the CH$_2$ stretches towards the lower frequencies indicating that the adsorbed hydrocarbon chains on the silver nanoparticles are in a close-packed, crystalline state (Wu, Fu et al. 2004). The carbonyl stretch has shifted to 1722 cm^{-1} which represents a significant blue shift (~30 cm^{-1}) compared to the acid (~1750 cm^{-1}). This blue shift can be due to the bonding between the hydroxyl oxygen and the silver metal surface resulting in the C=O bond having less electron density and therefore causing a frequency shift (Petroski and El-Sayed 2003). El-Sayed and coworkers have referred to this bonding as an ester-like linkage between the capping material and the nanoparticle surface (Petroski and El-Sayed 2003). A new peak at 1603 cm^{-1} which is characteristic of the carboxylate asymmetric stretch (COO$^{-}_{(a)}$) was also present in the FTIR spectrum of the iso-stearic acid capped particles (Nakamoto 1997). The region between 1377 and 1460 cm^{-1} results from the backbone vibrations (CH$_2$ deformation and wagging) overlapping with the symmetric vibration (COO$^{-}_{(s)}$) (Petroski and El-Sayed 2003). It is well known from the literature on IR data for surface

carboxylate bonding that there may exist two types of binding when the the carboxylate ion coordinates to a metal (Shafi, Ulman et al. 2001). In one of the binding types, the carboxylate is connected symmetrically with equivalent oxygen atoms to the surface of the metal and only the symmetric stretch ($COO^-_{(s)}$). is present (Ahn, Son et al. 1994). But, in the other binding type, the carboxylate is connected to the metal through only one oxygen atom and both the symmetric ($COO^-_{(s)}$) as well as asymmetric ($COO^-_{(a)}$) stretches were observed (Tao 1993). Wu et. al. has also mentioned that when the carboxylate is chemisorbed on the metal surface through inequivalent oxygen atoms, then a C=O band (1700~1730 cm^{-1}) is still present (Wu, Fu et al. 2004). The decrease in intensity of the C=O band in the spectrum for the iso-stearic acid capped particles compared to the spectrum for the iso-stearic acid further verifies the formation of the bond (Petroski and El-Sayed 2003). The symmetric ($COO^-_{(s)}$) and asymmetric ($COO^-_{(a)}$) stretches as well as the carbonyl stretch is present in the FTIR spectrum of the iso-stearic acid capped silver particles. This suggests that iso-stearic acid is connected to the Ag particles through one oxygen atom.

6.3.3 Effect of Co-solvent on Ag Nanoparticle Dispersion in CO_2

The addition of organic co-solvents can have a significant impact on nanoparticle dispersion in CO_2 solvent systems. While dodecanethiol-coated silver nanocrystals could not be dispersed in supercritical CO_2 alone, Shah et.al. (Shah, Holmes et al. 2000) found that they were able to disperse dodecanethiol-coated silver nanocrystals by adding 50% (volume fraction) hexane as co-solvent. Recently, Anand et.al (Anand, McLeod et al. 2005) showed that solvent strength in various CO_2/co-solvent mixtures has a significant impact on dodecanethiol-coated Au nanoparticle dispersibility where an increase in the

alkyl tail length of the co-solvent increased dispersibility. Cyclohexane has been shown to have stronger interactions with hydrocarbon ligand tails than other alkane solvents allowing larger sized metallic nanoparticles to be dispersed in both liquid and supercritical solvent/co-solvent systems (Cason, Miller et al. 2001; Kitchens, McLeod et al. 2003; Kitchens and Roberts 2004).

Cyclohexane was examined as a co-solvent in the synthesis of iso-stearic acid coated silver nanoparticles in CO_2 in an effort to increase dispersibility without the addition of fluorinated compounds. Figure 6-6 shows a comparison of the UV-vis absorbance spectra of iso-stearic acid coated Ag nanoparticles synthesized and dispersed in CO_2 with 0, 2, and 10% cyclohexane co-solvent by volume at 295 K and 276 bar. The dotted line corresponds to the UV-vis absorbance spectrum collected 5 days after silver nanoparticles were synthesized in CO_2 with 10% cyclohexane co-solvent by volume, the dashed line corresponds to the UV-vis absorbance spectrum collected 3 days after particles were synthesized with 2% cyclohexane co-solvent by volume, and the solid line corresponds to the UV-vis absorbance spectrum collected 3 days after silver nanoparticles were synthesized in pure CO_2. These UV-vis absorbance spectra were acquired after each system had reached a stable dispersion. Although a stable dispersion of silver nanoparticles was obtained in pure CO_2, the addition of a small amount of cyclohexane co-solvent (up to 10% by volume) significantly enhanced the concentration of dispersed iso-stearic acid coated silver nanoparticles in CO_2. Cyclohexane solvates the ligand tails much better than does CO_2, greatly increasing the solvent strength, and consequently the number of particles that can be stably dispersed in the mixture. These results indicate that the interactions between the iso-stearic acid ligand tails and the

alkane co-solvent play a critical role in the dispersion of nanoparticles in CO_2.   A disadvantage to using alkane co-solvents to increase the dispersibility of these nanoparticles, on the other hand, is that the critical point of the mixture is increased above that of pure CO_2. Therefore, a higher temperature is required to operate within the critical regime of the mixture to take full advantage of the unique properties that supercritical solvents offer in nanomaterial processing.

The UV-vis absorbance spectrum of the iso-stearic acid coated Ag nanoparticles dispersed in CO_2 with 10% cyclohexane co-solvent has a single absorbance band centered at 437 nm indicating the presence of spherical silver nanoparticles. The UV-vis spectra of the nanoparticle dispersions in CO_2 with 2% and 0% cyclohexane co-solvent, on the other hand, have multiple absorbance bands. These multiple absorption bands have been attributed to the stabilization of silver nanoparticle intermediates and silver clusters composed of small numbers of atoms (McLeod, McHenry et al. 2003). For example, the UV-vis spectrum for the 2% cyclohexane system has absorbance bands at 250 nm, 340 nm, and 450 nm. The band at 250 nm corresponds to the presences of Ag_4^{2+} (Henglein and Tausch-Treml 1981; McLeod, McHenry et al. 2003) whereas the band at 340 nm may be attributed to a wider range of intermediates including metal silver atom (Ag^0) and its oligomeric clusters (Dimitrijevic, Bartels et al. 2001) including Ag_9^+ and Ag_8^{2+} (Ershov and Henglein 1998). These oligomeric clusters could then proceed to the formation of colloidal metallic silver nanoparticles as indicated by the band at 450 nm. Metallic silver nanoparticles are commonly characterized by an absorption in the range of 400 to 450 nm depending upon the size, shape and surrounding environment in which the nanoparticle is situated (Henglein and Tausch-Treml 1981; Petit, Lixon et al. 1993;

Zhang, Patel et al. 2000). Similarly for 0% cyclohexane, the absorbance bands at 273 nm and 419 nm show the presence of Ag_4^{2+} intermediates and silver nanoparticles respectively. The addition of 10% cyclohexane causes a diminution of the absorbance bands corresponding to silver intermediates and results in a single absorbance band at 437 nm indicative of stabilized silver nanoparticles.

TEM images of the particles synthesized in CO_2 using 0, 2% and 10% cyclohexane co-solvent are shown in Figure 6-7. Samples of these particles were again prepared using both of the collection methods described above. Figure 6-7(i) presents TEM images of iso-stearic acid coated Ag nanoparticles synthesized and successfully dispersed in the CO_2/cyclohexane mixtures at 295 K and 276 bar where the samples were collected 24 hours after synthesis by simply spraying the CO_2 nanoparticle dispersions directly onto a TEM grid surface. Figure 6-7(ii) shows TEM images of the particles collected from the bottom of the vessel by depressurizing the vessel and subsequently redispersing the particles in hexane solvent for grid preparation. Please note that these samples include both particles that were dispersed in the CO_2/cyclohexane mixtures as well as those that were not dispersed after synthesis. These particles shown in Figure 6-7(ii) were collected after stable dispersions were achieved (3 days for 0% and 2% cyclohexane and 5 days for 10% cyclohexane) as indicated by unvarying UV-vis absorption spectra in the CO_2/cyclohexane mixtures. The TEM images in Figures 6-7(i) and 4.7(ii) indicate that while a range of particle sizes could be synthesized in the CO_2/cyclohexane mixtures, only the smaller particles could be dispersed in the CO_2/cyclohexane mixtures after more than 24 hours. The particles that were synthesized at each cyclohexane concentration in CO_2 shown in Figure 6-7(ii) were larger in each

163

case than the particles dispersed at the corresponding CO_2/cyclohexane mixture shown in Figure 6-7(i). This signifies that even the addition of 10% (volume fraction) cyclohexane as a co-solvent in the CO_2/cyclohexane mixture did not provide enough solvent strength to stabilize all of the synthesized particles. Moreover, it is also visible from these pictures that particles synthesized in CO_2 with 2% volume fraction of cyclohexane are bigger than the particles synthesized in pure CO_2 but further addition of cyclohexane to 10% by volume has an adverse effect on particle size determined from both collection techniques shown in Figures 6-7(i) & (ii). Figure 6-8(i) presents the particles size distributions of the iso-stearic acid coated silver nanoparticles that were both synthesized and successfully dispersed in each of the CO_2/cyclohexane mixtures at 295K and 276 bar. The average size of the particles synthesized and then dispersed in pure CO_2 (collected from the spray process) as mentioned in an earlier section is 2.6 nm. With the addition of 2% (vol) cyclohexane to CO_2, the mean particle size increases to 3.4 nm, an increase of almost 0.8 nm. Interestingly, with the further addition of cyclohexane to 10% by volume in CO_2 the mean particle size decreases to 1.6 nm. Similar trends were observed from the particles collected after depressurization. Figure 6-8(ii) presents the size distributions of the iso-stearic acid coated silver particles (both those that were dispersed in the mixture and those that were not) in each of the CO_2/cyclohexane mixtures at 295K and 276 bar. The average size of the particles synthesized in pure CO_2 (collected from the bottom of the vessel after depressurization) is 3.4 nm and this size is larger than the particles which were actually dispersed (2.6 nm), indicating that the CO_2 solvent was only able to disperse a smaller size fraction of the particles that were synthesized. The addition of 2% cyclohexane to CO_2 increases the mean particle size to 4.2 nm, again a

difference of 0.8 nm. For 10% cyclohexane in the CO_2/cyclohexane mixture the size of the particles synthesized was reduced to 2.3 nm. In each of the CO_2/cyclohexane mixtures, the synthesized particles are larger than those that were successfully dispersed. Interestingly, the mean particle size did not increase monotonically with an increase in mixture solvent strength through the addition of the co-solvent (as observed in both means of particle collection). There seems to be an optimum amount of cyclohexane that would need to be added, between 0% to 10% by volume, to synthesize and/or disperse larger particles. Shah et.al. (Shah, Husain et al. 2002) showed that good solvent conditions quenched the growth of silver nanocrystals in CO_2 in the presence of fluorinated thiols resulting in smaller nanocrystals than those synthesized under poor solvent conditions (lower densities). In this case, perfluorodecanethiol-stabilized silver nanocrystals were synthesized in supercritical CO_2 via hydrogen reduction of silver acetylacetonate. It was found that at earlier stages in the growth process, metal core coagulation competes with thiol ligand adsorption. Under poor solvent conditions, particles grew to larger sizes (4 nm at $P < 250$ bar, $T = 80^oC$ compared to 2 nm at $P > 250$ bar, $T = 80^oC$) before the coverage of capping ligand was sufficient to prevent coagulation of the metal particles illustrating a tunability of particle sizes that could be synthesized through variations in solvent strength. On the other hand, Kitchens et. al. (Kitchens, McLeod et al. 2003; Kitchens and Roberts 2004) examined the effects of solvent strength on the synthesis of copper nanoparticles within (AOT) reverse micelles in liquid and compressed alkane systems. In this case, the AOT surfactant molecule more weakly adsorbs to the metal nanoparticle surface than a fluorinated thiol counterpart, and hence prevents coagulation to a lesser extent. With the use of AOT as a capping agent,

particles that are larger than 8 nm in size were synthesized and sterically stabilized in these liquid and compressed alkane systems. For example, the mean size of copper nanoparticles synthesized within AOT reverse micelles was increased from 8.6 nm to 12.6 nm by changing the solvent from pentane to cyclohexane, where cyclohexane better solvates the AOT surfactant tails. Similarly, an increase in the solvent strength by tuning the pressure from 400 bar to 550 bar resulted in an increase in copper nanoparticle size from 8.6 nm to 9.3 nm in compressed ethane solvent at $20^{\circ}C$. These examples illustrate that several factors can influence the particle size that can be synthesized and sterically stabilized in solution including particle-particle interactions, the ligand adsorption on the metal nanoparticle, and the solvation of the ligand by the solvent medium.

6.3.4 Effect of Pressure on Ag Nanoparticle Dispersion in CO_2

Another factor that was examined was the effect of pressure (or density) at constant temperature on the dispersability of iso-stearic acid coated Ag nanoparticles formed by reduction in CO_2/cyclohexane mixtures. Shah et. al. (Shah, Holmes et al. 2002) varied the dispersability of dodecanethiol stabilized gold and silver nanoparticles in liquid and supercritical ethane by altering the pressure and thereby tuning the solvent density. They were able to increase the particle dispersibility at higher pressure due to an increase in solvent density. Saunders et. al. (Saunders, Shah et al. 2004) performed small-angle X-ray scattering (SAXS) studies on interparticle interactions between perfluoropolyether (PFPE) coated gold nanocrystals in $scCO_2$. They observed an increase in interparticle attraction and, hence, particle aggregation at lower CO_2 density which indicates that particle dispersability is a strong function of solvent density.

UV-vis absorbance spectra for dispersions of iso-stearic acid coated silver nanoparticles at different pressures (or densities) at 295 K are shown in Figure 6-9. These particles were synthesized by reduction of Ag-AOT-TMH in CO_2 with 10% cyclohexane co-solvent by volume at 295 K and 276 bar. This system was chosen because it had the largest concentration of dispersed particles, making changes in the concentration of dispersed particles easier to distinguish. After particle synthesis at 295 K and 276 bar, the high pressure vessel was depressurized to 106 bar (0.10 g/ml). Once a stable dispersion was achieved, the pressure (or density) of the mixture was then increased by adding more CO_2. At each pressure, the system was given enough time for the UV-vis absorbance to not change appreciably. This time was typically less than one hour. The UV-vis absorbance was then recorded and the pressure was increased. This process was repeated for 6 pressures until the mixture was returned to the initial condition of 276 bar (0.96 g/ml). As the pressure (or density) of the system was increased, the absorbance peak also increased, presumably resulting from the re-dispersion of the larger particles that had precipitated once the pressure was reduced to 106 bar. This increase in absorbance corresponds to an increase in the concentration of dispersed particles with an increase in density. By increasing the density at a constant temperature, the solvent strength of the system improves as CO_2 more effectively solvates the iso-stearic acid ligand tails and hence has the capacity to disperse larger particles that add to the concentration of dispersed particles in solution.

6.3.5 Effect of Temperature on Ag Nanoparticle Dispersion in CO_2

The results presented to this point involve nanoparticle dispersions in liquid phase CO_2 at 295K and 276 bar. In order to harness the full potential of the processing advantages that

CO_2 can offer (e.g., high diffusivities and low surface tensions) it is necessary to retain the Ag nanoparticle dispersions under supercritical CO_2 conditions at elevated temperatures. Once a stable dispersion of nanoparticles was produced in neat CO_2 at 295 K and 276 bar, the temperature of the system was sequentially increased from 295K, to 298 K, 303 K, and 308 K at a constant density of 0.96 g/ml and held at each of these temperatures for 1 hour. No change was observed in the UV-vis absorbance spectrum with these sequential changes in temperature (data not shown). Since there was no observable change in the UV-vis absorbance spectra at these different temperatures with constant CO_2 density, the silver nanoparticles can therefore be synthesized in liquid CO_2 and then processed in the supercritical phase by a simple increase in temperature.

6.3.6 Effect of Time on Ag Nanoparticle Dispersion in CO_2

The influence of time on the dispersion of Ag nanoparticles in pure CO_2 and in each of the CO_2/cyclohexane mixtures was examined. UV-vis absorbance spectra were collected immediately after reduction of the Ag-AOT-TMH (defined as t = 0) and at regular time intervals until a stable dispersion was achieved. Immediately upon reduction, at t = 0, a strong UV-vis absorbance band with wavelength between 400 to 450 nm was observed in each of the CO_2/cylclohexane mixtures as shown in Figure 6-10. This strong absorbance at t = 0 corresponds to the rapid synthesis and dispersion of silver nanoparticles. In each CO_2/cyclohexane mixture, this absorbance band deceases in intensity with time corresponding to the precipitation of those synthesized particles that could not be sterically stabilized (i.e. thermodynamically dispersed) in that particular solvent strength medium, again indicating that not all of the particles that were synthesized could be stably dispersed in the CO_2 mixtures. This UV-vis absorption intensity decreased with

time until a stable dispersion was achieved in each solvent mixture after several days. In the case of neat CO_2, this absorption band rapidly dropped to a low absorbance value of ~0.2 absorbance units (a.u.) after 24 hours and remained effectively unchanged within 0.05 a.u. after 3 days (within the experimental error of these measurements). It should be noted that while there was a significant decrease in absorption in neat CO_2 at steady state (i.e. after 3 days) compared to that obtained immediately upon reduction, a fraction of the particles remain dispersed in neat CO_2 without the aid of fluorinated compounds or co-solvents. The addition of cyclohexane co-solvent resulted in both an increase in the initial absorbance intensity at t = 0 as well as an increase in the steady state absorbance corresponding to an increase in the concentration of Ag nanoparticles that were both synthesized and stably dispersed in these non-fluorinated CO_2 mixtures.

6.4 Conclusion

Silver nanoparticles capped with iso-stearic acid were synthesized and stabilized in a one-step process in pure CO_2 for the first time without the use of fluorinated surfactants or capping ligands. These dispersions are stabilized by molecular interactions between the iso-stearic acid ligand tails and CO_2. The synthesis and dispersion of the iso-stearic acid capped Ag nanoparticles can be significantly enhanced by the addition of small amounts of cyclohexane co-solvent. Increases in pressure (or density) at a constant temperature also increase the concentration of dispersed particles. By a simple increase in temperature, the particles synthesized and dispersed in the liquid CO_2 phase can be processed in the supercritical phase without affecting their dispersion. This study indicates that nanoparticle processing in CO_2 solvent can be advanced without the need for environmentally persistent fluorinated compounds.

169

6.5 Acknowledgements

6.6 Supporting Information Available

We present the experimental procedure used to obtain the cloud point pressures of AOT-TMH in carbon dioxide and its variation as a function of temperature.

Iso-Stearic Carboxylic Acid, C₁₇H₃₅COOH (Mn=284g/mol)
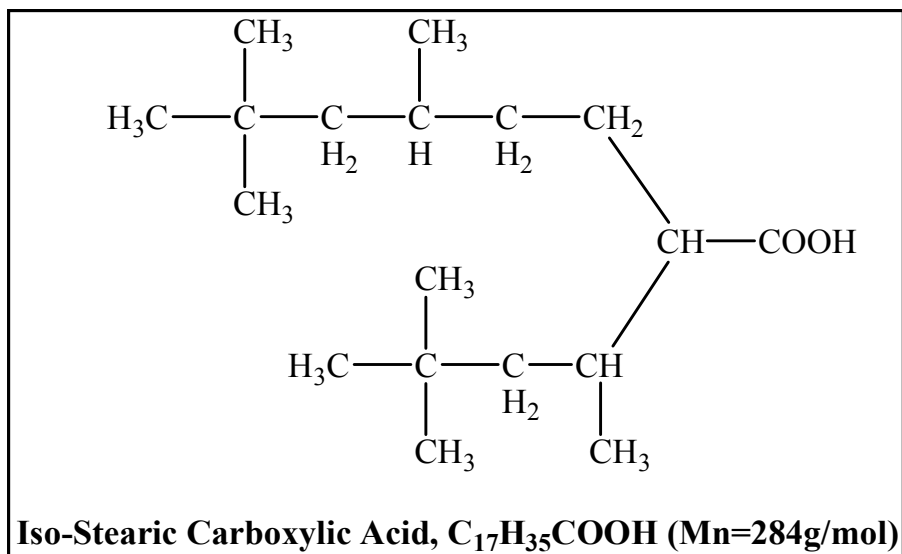
(a)
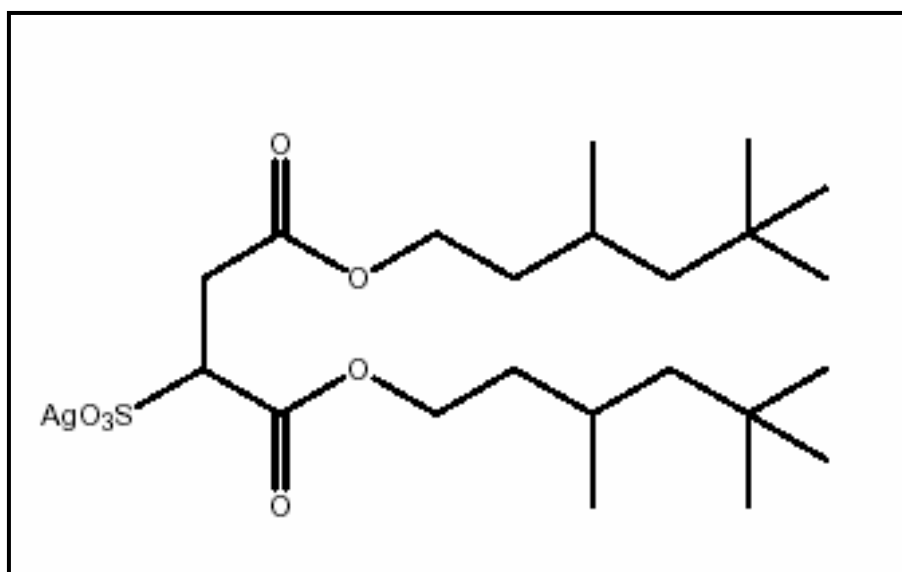
(b)

Figure 6-1 (a) Molecular structure of iso-stearic acid (Bell, Anand et al. 2005) (b)

Molecular structure of Ag-AOT-TMH (Fan, McLeod et al. 2006).
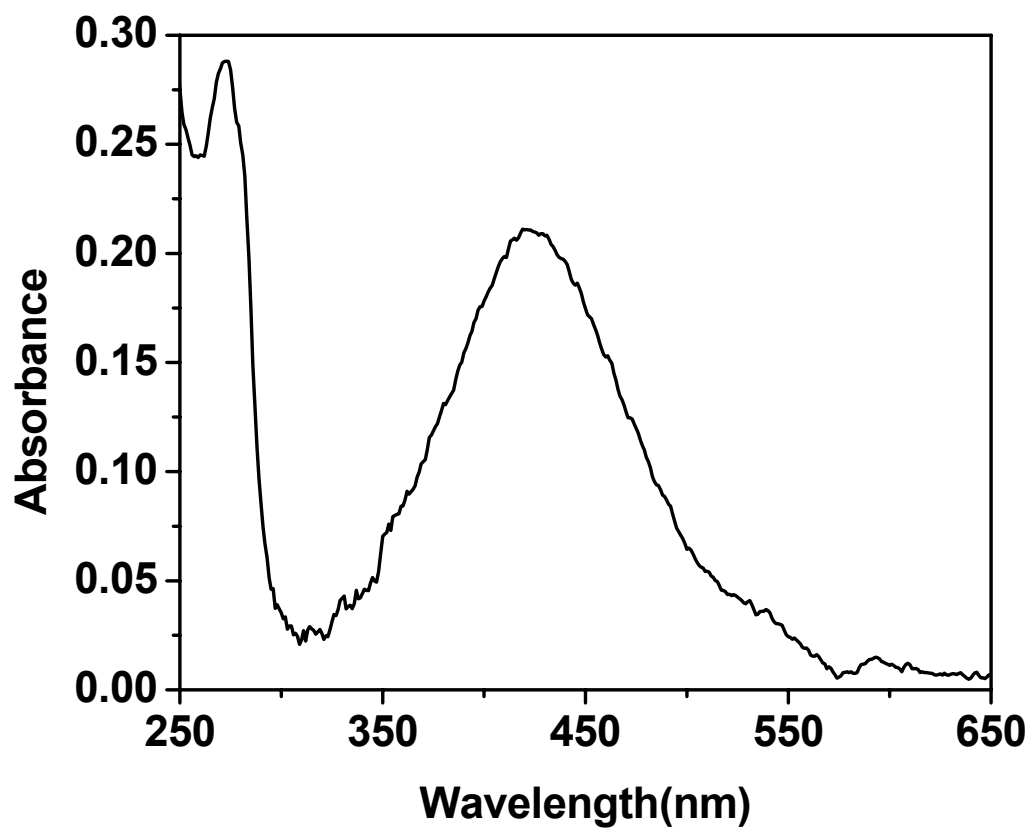
Figure 6-2 UV-vis absorbance spectrum of iso-stearic acid coated Ag nanoparticles synthesized and successfully dispersed in neat CO_2 collected after 3 days at 295 K and 276 bar.
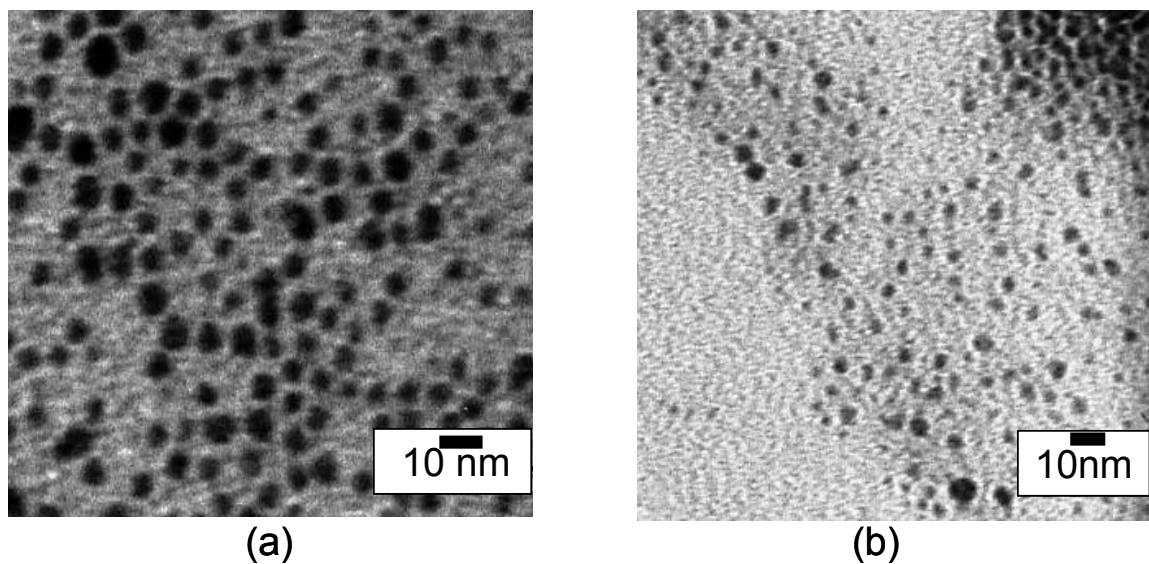
Figure 6-3 TEM images of iso-stearic acid coated silver nanoparticles synthesized in pure CO_2 at 295 K and 276 bar. (a) Particles recovered from the bottom of the vessel after 3 days by depressurizing the vessel and subsequent redispersion in hexane solvent for grid preparation. This sample includes both particles that were dispersed in CO_2 and those that were not. (b) Particles collected 3 days after synthesis by simply spraying the CO_2 nanoparticle dispersion directly onto a TEM grid surface. This sample shows a TEM image of particles synthesized and successfully dispersed in CO_2.
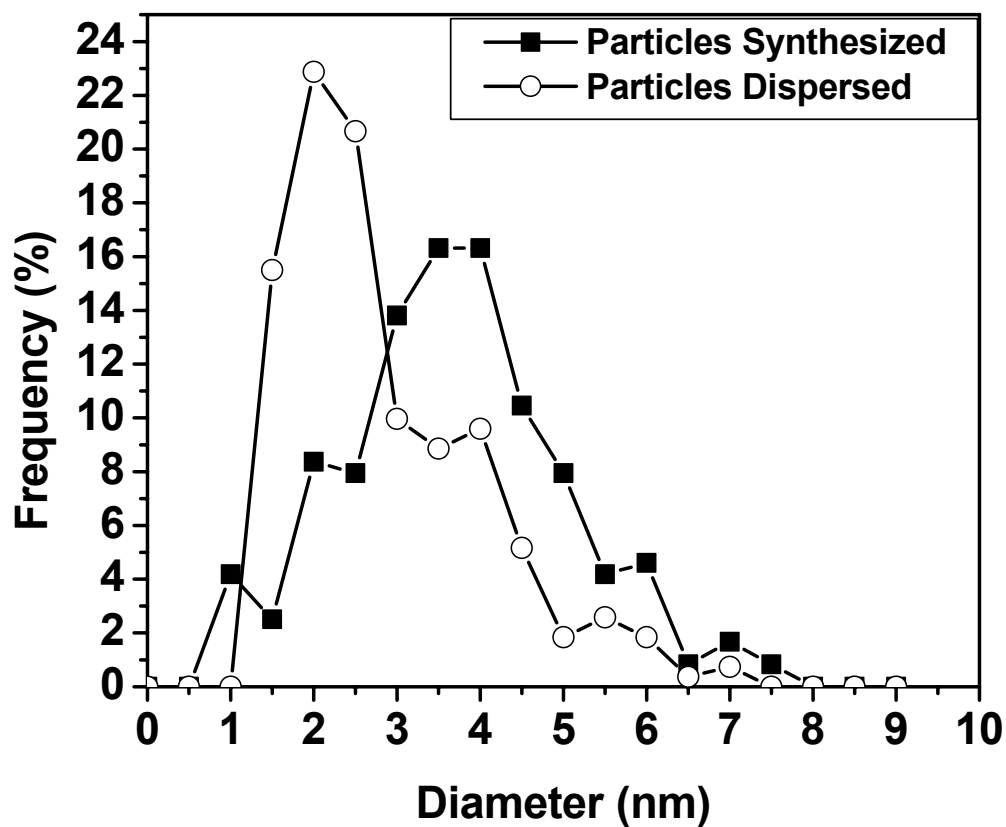
Figure 6-4 Size distributions of iso-stearic coated Ag nanoparticles (■) synthesized or (○) synthesized and successfully dispersed in pure CO_2 at 276 bar and 295 K.
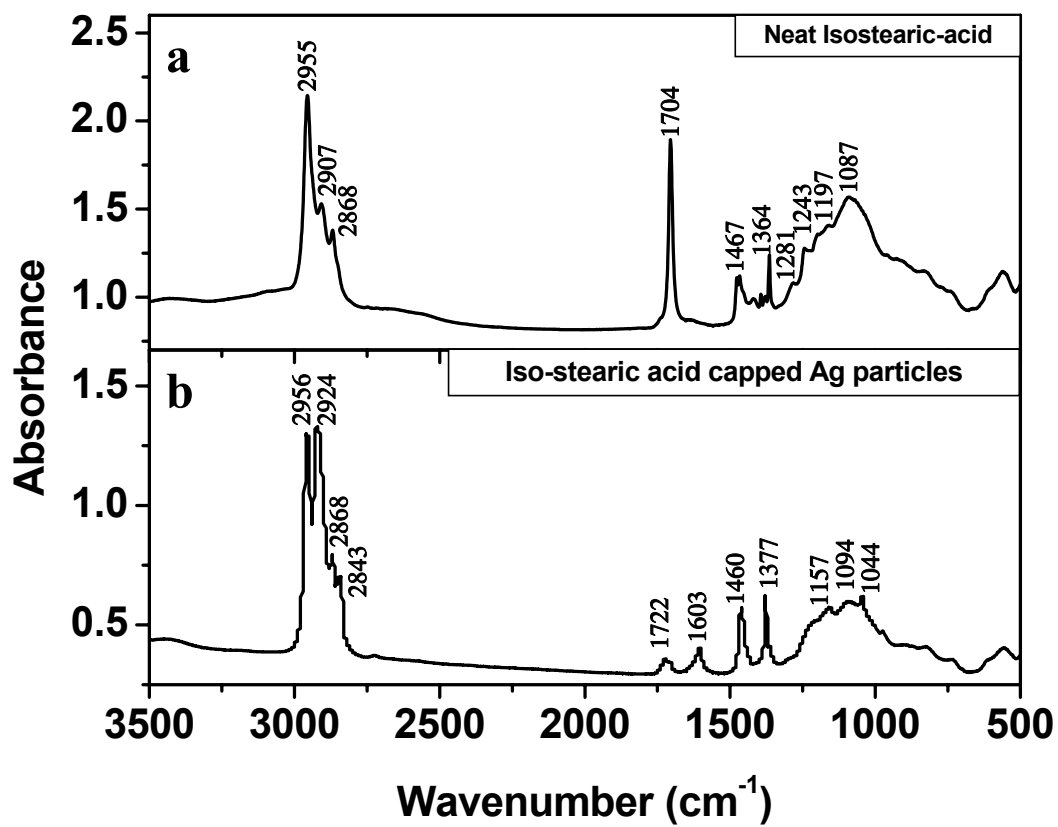
Figure 6-5 FTIR spectra of (a) neat iso-stearic acid and (b) iso-stearic acid coated silver nanoparticles.
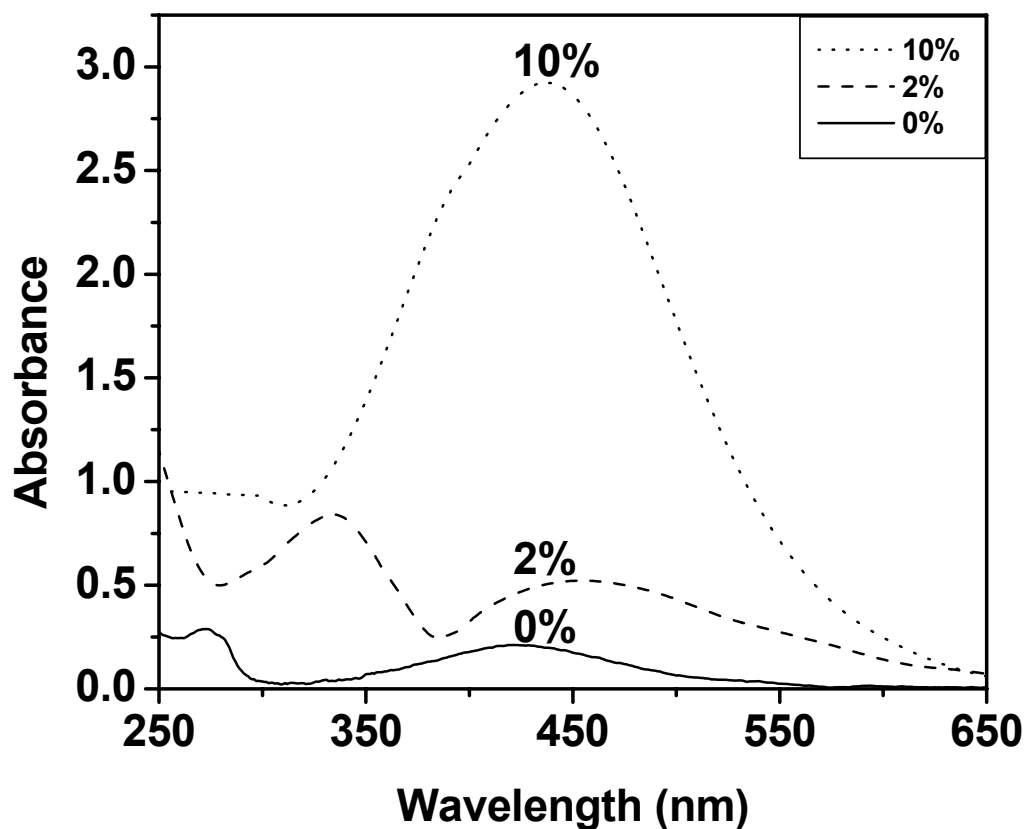
Figure 6-6 UV-vis absorbance spectra of iso-stearic acid coated Ag nanoparticles synthesized and dispersed in CO_2 with 0, 2, and 10% cyclohexane co-solvent by volume at 295 K and 276 bar. The dotted line corresponds to the UV-vis absorbance spectrum collected 5 days after silver nanoparticles were synthesized in CO_2 with 10% cyclohexane co-solvent by volume, the dashed line corresponds to the UV-vis absorbance spectrum collected 3 days after particles were synthesized with 2% cyclohexane co-solvent by volume, and the solid line corresponds to the UV-vis absorbance spectrum collected 3 days after silver nanoparticles were synthesized in pure CO_2. These UV-vis absorbance spectra were acquired after each system had reached a stable dispersion. The spectra have been scaled to have an absorbance of 0 at 700 nm for comparison.

176

(a)   (b)   (c)
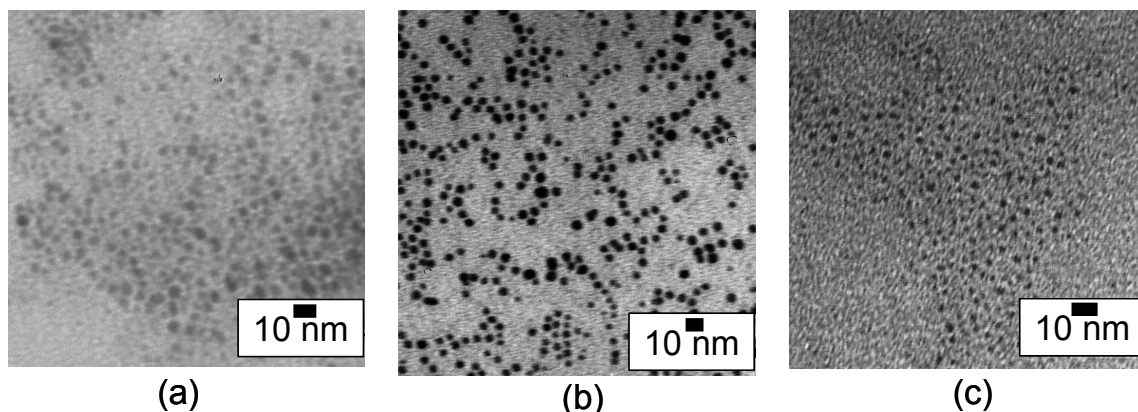
Figure 6-7(i) TEM images of iso-stearic acid coated silver nanoparticles synthesized and successfully dispersed in the CO_2/cyclohexane mixtures at 295 K and 276 bar with (a) no co-solvent (b) 2% cyclohexane (c) 10% cyclohexane. These particles were collected 24 hours after synthesis by spraying the CO_2 nanoparticle dispersions directly onto a TEM grid surface.

(a)   (b)   (c)
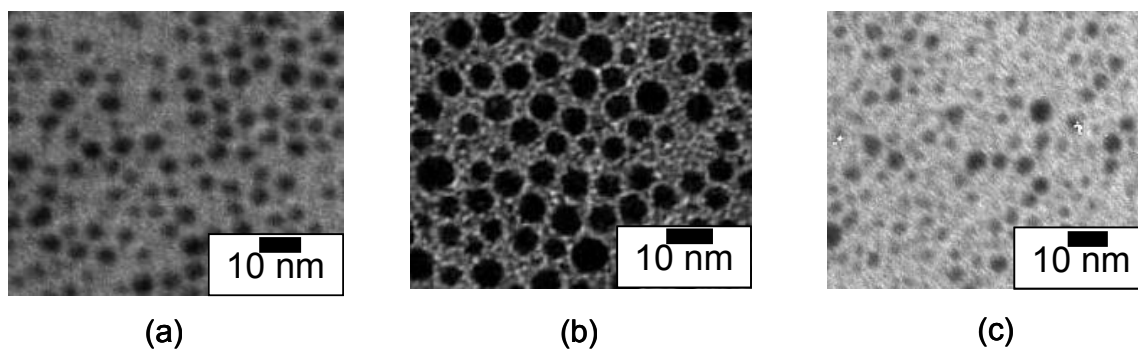
Figure 6.7(ii) TEM images of iso-stearic acid coated silver nanoparticles synthesized in the CO_2/cyclohexane mixtures at 295 K and 276 bar with (a) no co-solvent (b) 2% cyclohexane (c) 10% cyclohexane. These samples include both particles that were dispersed in the CO_2/cyclohexane mixtures as well as those that were not dispersed after synthesis. These particles were recovered from the bottom of the vessel in hexane after

depressurizing the vessel. The hexane dispersion was then allowed to evaporate on the TEM grid.
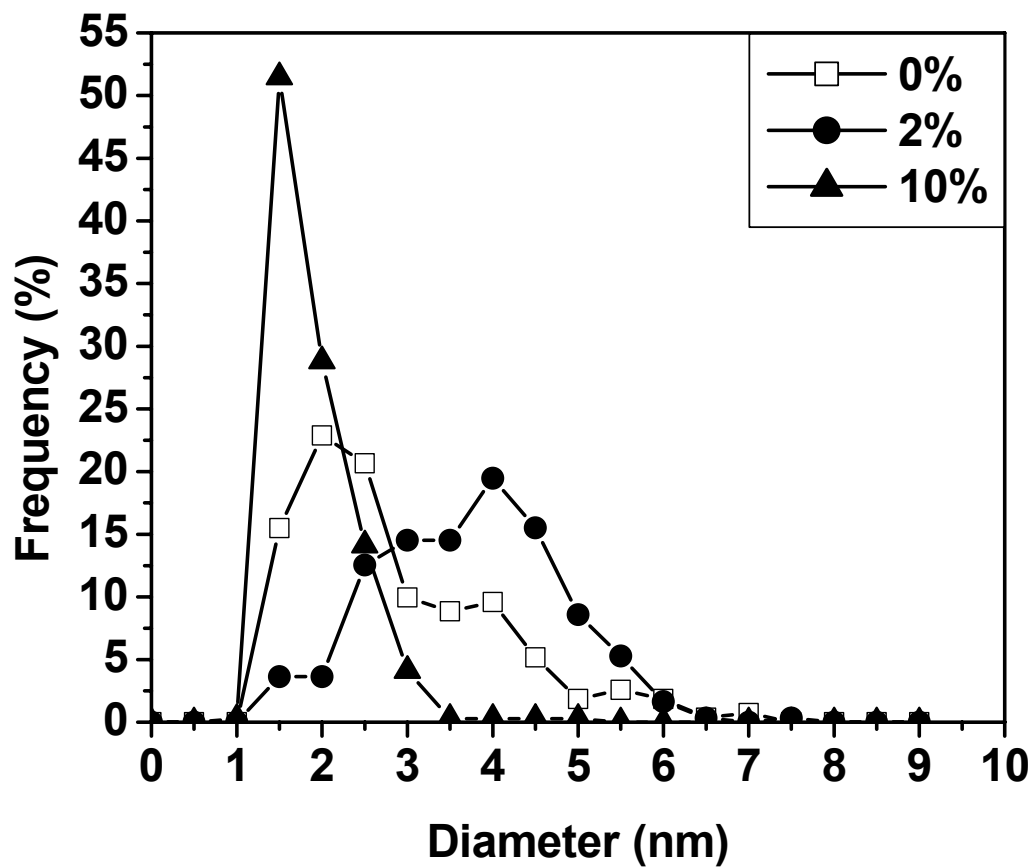
Figure 6-8(i) Size distribution of iso-stearic acid coated silver nanoparticles synthesized and dispersed in CO_2 at 295 K and 276 bar with (□) no co-solvent (●) 2% cyclohexane (▲) 10% cyclohexane. These particles were collected 24 hours after synthesis by spraying the CO_2 nanoparticle dispersions directly onto a TEM grid surface.

.
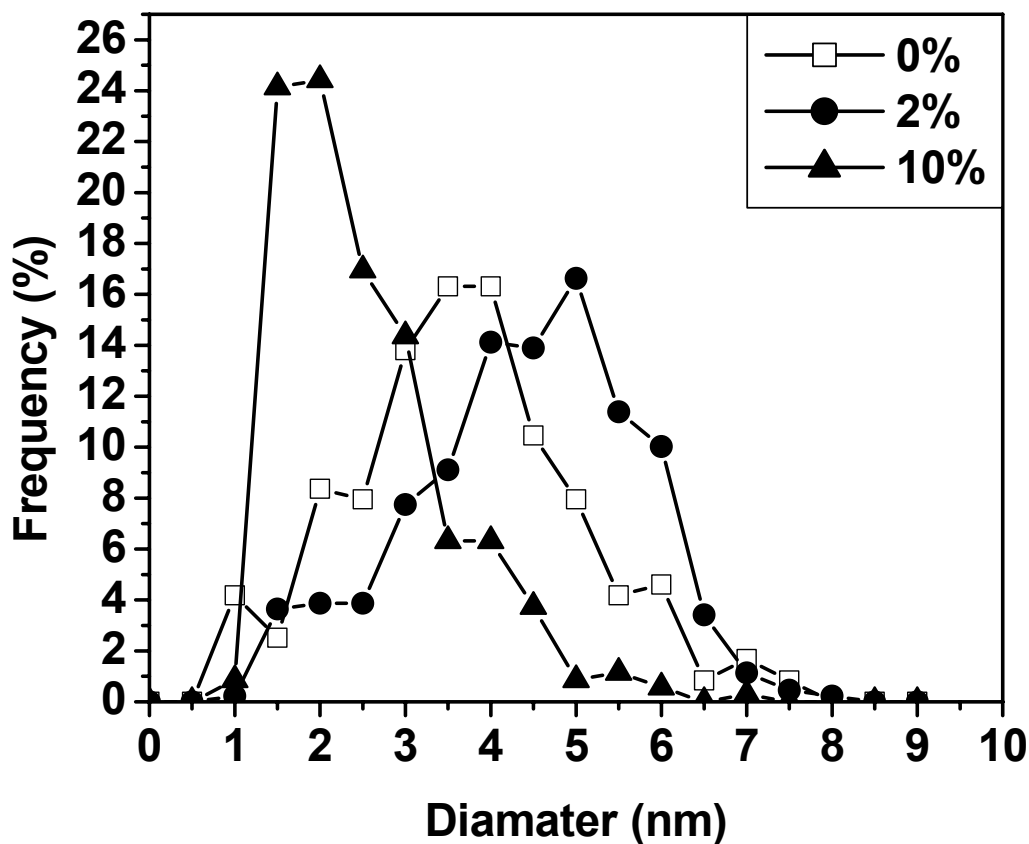
Figure 6.8(ii) Size distribution of iso-stearic acid coated silver nanoparticles synthesized in CO_2 at 295 K and 276 bar with (□) no co-solvent (●) 2% cyclohexane (▲) 10% cyclohexane. These particles were recovered from the bottom of the vessel in hexane after depressurizing the vessel and then the hexane dispersion was allowed to evaporate on the TEM grid. These samples include both particles that were dispersed in the CO_2/cyclohexane mixtures as well as those that were not dispersed after synthesis.
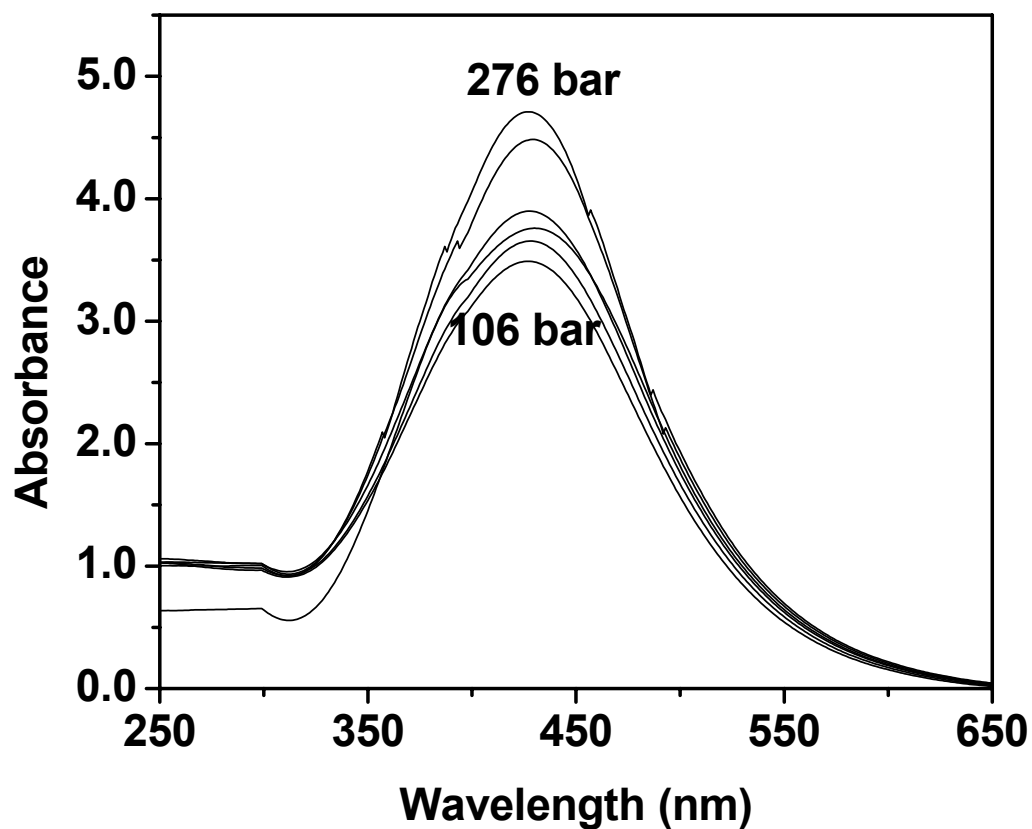
Figure 6-9 UV-vis absorbance spectra for iso-stearic acid coated silver nanoparticles dispersed in CO_2 at 295 K and various CO_2 pressures with 10% cyclohexane co-solvent by volume. Each curve corresponds to a different pressure going from the bottom curve (106 bar) to the top curve (276 bar). The spectra have been scaled to have an absorbance of 0 at 700 nm for comparison.
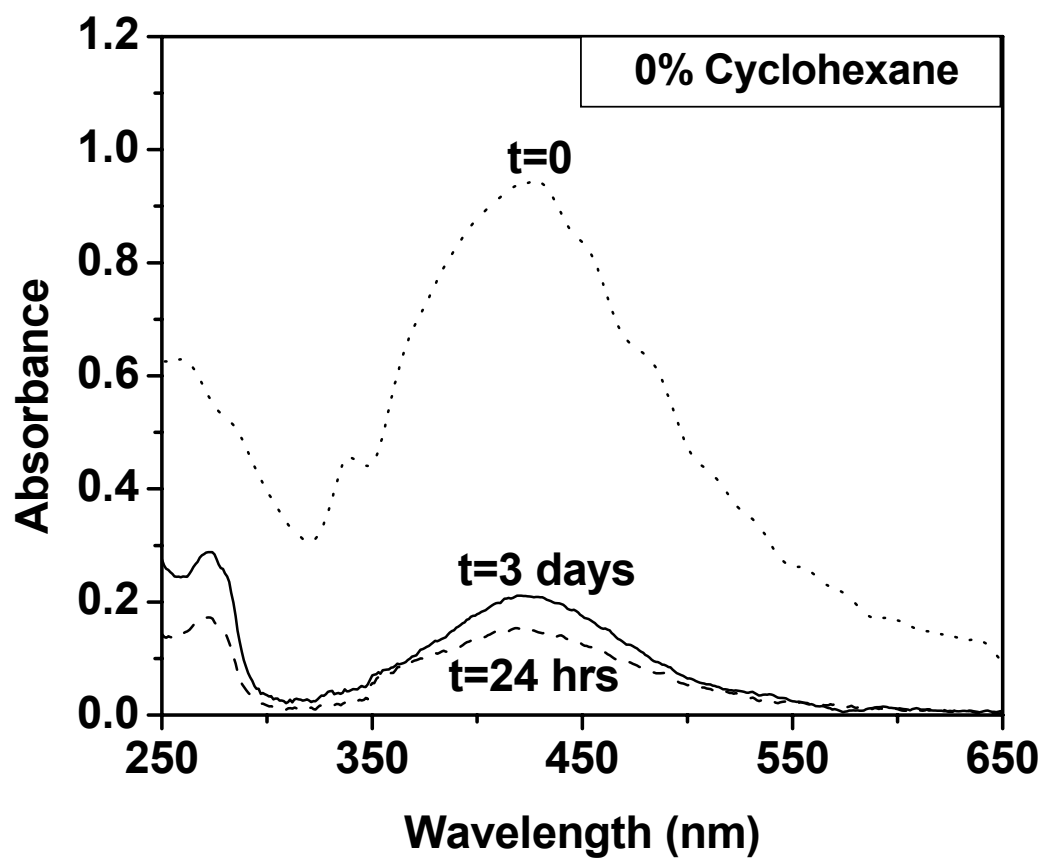
(a)
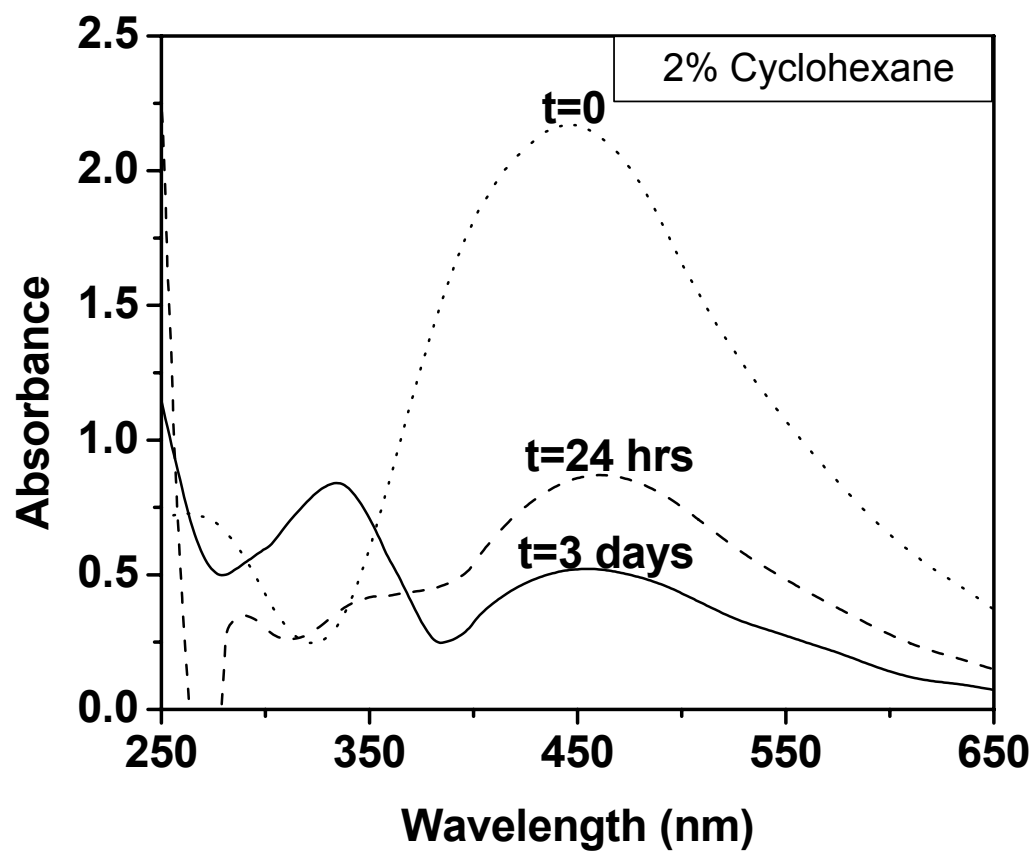
(b)
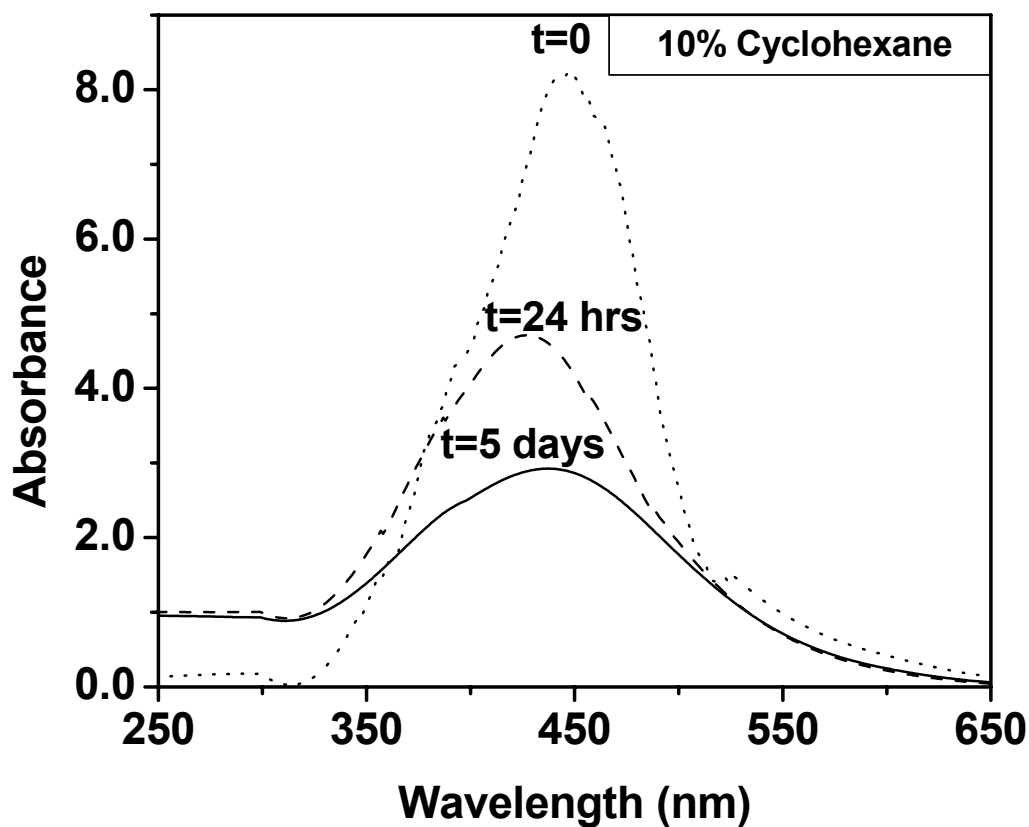
(c)

Figure 6-10 UV-vis spectra of iso-stearic acid coated silver nanoparticles synthesized in CO_2 at 295 K and 276 bar were taken at various time intervals with (a) no co-solvent (b) 2% cyclohexane (c) 10% cyclohexane. The spectra have been scaled to have an absorbance of 0 at 700 nm for comparison. The dotted line corresponds to the initial absorbance, the dashed line to the absorbance after 24 hours, and the solid line to the stable absorbance achieved after 3 days with 0% and 2% cyclohexane and after 5 days with 10% cyclohexane.

SYNTHESIS AND STEARIC STABILIZATION OF SILVER NANOPARTICLES IN

NEAT CARBON DIOXIDE SOLVENT USING FLUORINE-FREE COMPOUNDS

This supplementary information provides data on the cloud point pressures of AOT-TMH in carbon dioxide as a function of temperature and the experimental procedure used to obtain this information. Figure 6-S1 presents the variation in the cloud point pressure of 0.05 wt% AOT-TMH in carbon dioxide solvent as a function of temperature where pressures greater than the reported cloud point pressure at a given temperature resulted in a single homogeneous phase and pressures lower than the cloud point pressure resulted in phase separation of the AOT-TMH.
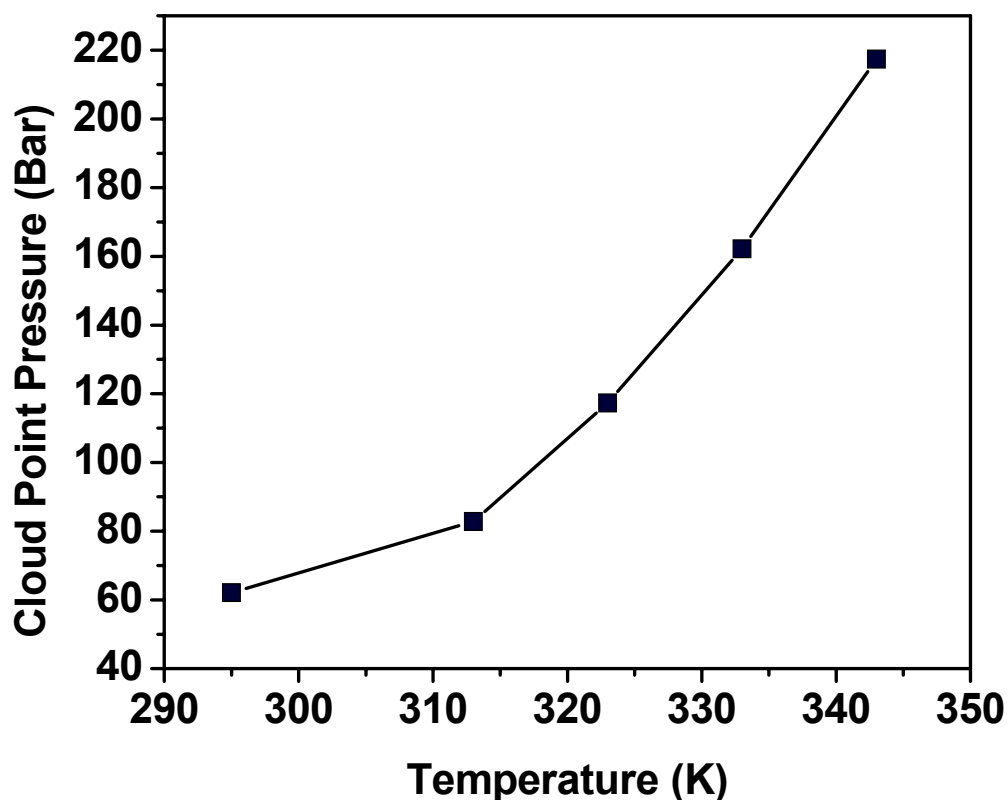
Figure 6-S1 Cloud point pressures of 0.05 wt% AOT-TMH in carbon dioxide as a function of temperature.

6.7 Cloud Point Measurement Procedure

A known amount of AOT-TMH was loaded into the sample volume of a high pressure, windowed, stirred, variable-volume view cell (DB Robinson & Assoc., 3.18 cm ID, ~120 mL working volume). In this cell, the sample volume is separated from the overburden fluid by a steel cylinder (floating piston) that retains an O-ring around its perimeter. The O-ring permits the cylinder to move while retaining a seal between the sample volume

and the overburden fluid. After purging with carbon dioxide at 0.2 MPa, the sample volume was minimized by displacing the floating piston to the highest possible position within the cell that did not result in the compaction of the surfactant. High pressure liquid carbon dioxide (295 K, 138 bar) was then introduced to the sample volume as the silicone oil overburden fluid was withdrawn at the equivalent flow rate using a dual-proportioning positive displacement pump (DB Robinson). This technique facilitated the isothermal, isobaric addition of a known volume of CO_2 into the sample volume. The mass of CO_2 introduced was determined from the displaced volume, temperature, and pressure using an accurate equation of state for carbon dioxide. Based on the uncertainties associated with the measurement of temperature, pressure, and volume, and the precision of the equation of state, compositions are estimated to be accurate to within 1% of the specified value (e.g.,0.05 ± 0.0005 wt%).

The (AOT-TMH/CO_2) mixture was compressed to high pressure (e.g., 500 bar) and mixed thoroughly using a magnetic stirrer (DB Robinson, max. 2500 rpm). If the solute didn't completely dissolve at these conditions, additional CO_2 was added to the system until a single transparent phase could be attained. Cloud points were determined by standard non-sampling techniques; the slow, isothermal expansion of the sample volume until the cloud point was attained and the solution became opaque. Cloud points were reproduced two or three times to within approximately ± 5 bar. Temperatures were measured with a type K thermocouple to an accuracy of ± 0.2 K

CHAPTER 7

THERMODYNAMIC ANALYSIS OF THE GAS EXPANDED LIQUID NANOPARTICLE SIZE

SEPARATION PROCESS

A thermodynamic model and related equations were developed to improve our understanding of the size selective fractionation of ligand stabilized nanoparticles using a CO_2 gas expanded liquid precipitation process. This size selective precipitation process is based on controlled reduction of the solvent strength of the organic solution through increases in the antisolvent CO_2 concentration via pressurization. A decrease in the solvent strength reduces the repulsive Osmotic contributions to the total interaction energy of the dispersion by weakening the interactions between the solvent and the ligand tails. Eventually, these repulsive forces in the dispersion are lowered to the point where they can no longer overcome the van der Waals forces of attraction between particles, thereby causing the particles to precipitate. This results in an ability to tune the size of the nanoparticles that are dispersed or precipitated simply by adjusting the CO_2 pressure. In this chapter, Osmotic energy and Hamaker constant expressions were developed for CO_2 gas expanded solvent mixtures consisting of an organic solvent (e.g. hexane) and antisolvent (e.g. CO_2). These expressions, coupled with appropriate thermodynamic data, were used to estimate the maximum size of dodecanethiol capped Ag nanoparticles that could be dispersed at a given CO_2 pressure by equating the total interaction energy to the

Boltzman threshold stabilization energy ($-3/2$ k_BT). A parameter sensitivity analysis was performed to determine which parameters most affect the predicted maximum particle size that could be dispersed at a given CO_2 pressure. It was found that the length of the ligand tail that interacts with the solvent medium had the most influence on these total interaction energy calculations. Assuming complete solvation of the entire ligand tail, the model always overpredicted the size of the particles that would be precipitated at a given CO_2 pressure compared to the experimental results. Consequently, we have proposed that the entire length of the dodecane chain is not accessible to the solvent medium. As such, three phenomenological model variations were developed that provide for differing abilities of the ligand tails to interact with the solvent including an Extended Ligand Length Solvation Model, a Condensed Phase Model, and a Limited Ligand Length Solvation Model with the best fit of the experimental size separation data coming from the Limited Ligand Length Solvation Model. Equations for a surface fraction model based on UNIQUAC parameters and its viability for this process is also discussed.

7.1 Introduction

Carbon dioxide gas expanded liquids have received a great deal of attention in various applications such as adjustable solvents for separations, in gas antisolvent crystallization, precipitation, organic and polymer microparticle formation as well as in tuning chemical reactions. These gas expanded liquids have garnered attention such that Jessop and Subramanium (Jessop and Subramaniam 2006) have recently written a thorough review on gas expanded liquids and Eckert et. al. (Eckert, Bush et al. 2000) has written a detailed review on the applications of tunable solvents in sustainable technology. The main advantage of this solvent system lies in the ability to tune solubility as well as other

189

physicochemical properties. Another distinct advantage involves the easy removal of the CO_2 gas from the solvent mixture by depressurizing the system thereby allowing complete recycle of both the gas and the liquid constituents.

Over the last several years there has been ongoing research in the developing area of processing nanoparticles and other nanomaterials in CO_2 gas expanded liquids in order to take advantage of their unique properties. Our group has used the highly tunable solvent properties of CO_2 gas expanded liquids to vary the solvent strength of nanoparticle dispersions thus resulting in precipitation and deposition of particles (McLeod, Kitchens et al. 2005; Liu, Anand et al. 2006) by using CO_2 as an antisolvent. Han and coworkers have also used CO_2 as an antisolvent in gas expanded liquids to precipitate ZnS nanoparticles from AOT reverse micelles in liquid isooctane (Zhang, Han et al. 2001).

As described in previous chapters, we have used CO_2 as an antisolvent to size selectively precipitate and separate ligand stabilized metal nanoparticle dispersions into narrow distributions through fine adjustments in CO_2 pressure (Anand, McLeod et al. 2005; McLeod, Anand et al. 2005). The dodecanethiol thiol capped polydisperse populations of silver (Ag) nanoparticles in hexane, with a mean diameter of 5.5 nm and a standard deviation of 31.9%, were size separated and fractionated into monodisperse size fractions by finely tuning the solvent strength of the CO_2 gas expanded alkane solvent mixtures by simply adjusting the applied CO_2 pressure. The organic solution expands upon increasing pressurization with CO_2 gas due to the condensation and miscibility of CO_2 with the organic solvent. CO_2 acts as an antisolvent for the non-polar ligands and thus its addition to the organic solution allows gradual size selective precipitation of the

nanoparticles with simple adjustments in CO_2 pressure. Particle dispersability in a solvent requires a sufficient solvent-ligand interaction in order to provide enough osmotic repulsive force to overcome the van der Waals forces of attraction between the particles in solution. Hence the degree of solvent-ligand interaction is diminished upon the gradual addition of CO_2 antisolvent through pressurization and since the larger particles in solution have greater van der Waals forces of attraction, the larger particles begin precipitating first upon worsening solvent conditions. Therefore, the particle dispersability and precipitation can be easily controlled by simply tuning the applied CO_2 pressure, which results in precise and controlled particle size separation and fractionation. In this chapter, a thermodynamic model is developed to analyze these experimental results presented in chapter 2 (McLeod, Anand et al. 2005).

7.2 Theoretical Section

In this chapter, a theoretical model based on total interaction energy was developed for the size selective fractionation process using the thermodynamic properties of CO_2 gas expanded liquids to predict the maximum particle size that can be dispersed as a function of CO_2 pressure (particles smaller than this maximum size will disperse and those larger than this maximum size will precipitate). Previously, studies have been done to predict the particle size that can be stabilized at given conditions in conventional liquid solvents (Kitchens, McLeod et al. 2003), supercritical ethane (Shah, Holmes et al. 2002), compressed propane (Kitchens and Roberts 2004) and supercritical CO_2 (Shah, Husain et al. 2002). Shah et. al. (Shah, Holmes et al. 2002) initiated this soft sphere modeling approach, where stabilization of nanoparticles in a given solvent depends on the balance between the van der Waals attractive forces with steric repulsive forces. Shah et. al.

(Shah, Holmes et al. 2002) and Kitchens et. al. (Kitchens, McLeod et al. 2003) have employed a total interaction energy model to correlate the solvent-ligand interaction with the maximum size of a ligand stabilized nanoparticle that can be dispersed within a given solvent system. Unfortunately, the maximum particle sizes predicted through this model are larger than the particle sizes obtained through experimental studies. The total interaction energy is the sum of attractive and repulsive terms as shown in equation (1) and depends on particle size, distance between the particles, ligand length, ligand composition and its density as well as solvent parameters. The van der Waals attractive force (Hamaker 1937), Φ_{vdW}, between two particles increases with an increase in particle radius R or with a decrease in center to center separation distance between the particles d. Φ_{vdW} is directly proportional to the Hamaker constant, A_{131}. A_{131} is a proportionality factor that accounts for the interaction between two nanoparticles of the same material (component 1) across a solvent (component 3) and depends on A_{11} and A_{33}, where A_{11} is a constant value for metallic nanoparticles with $A_{11} = 2.185$ eV for silver (Shah, Husain et al. 2002) and A_{33} for the solvent is calculated by an equation of state based on Lifshitz theory (Israelachvili 1985). A_{33} depends on the refractive index n, and dielectric constant ε of the solvent as given in equation (4) where k_B is Boltzmann's constant, h is Plancks's constant, v_e is the main electronic UV absorption frequency, generally assumed to be 3×10^{15} s^{-1} and T is temperature. Values of the refractive index and dielectric constant for CO_2 (Sun, Shekunov et al. 2003) and organic solvents (Lide 1994; Lide 1995) at 25°C are given in Table 7.1 and values of n_{vacuum} and ε_{vacuum} are taken as 1.

$$\Phi_{total} = \Phi_{vdW} + \Phi_{osm} + \Phi_{elas} \tag{1}$$

$$\Phi_{vdW} = -\frac{A_{131}}{6}\left[\frac{2R^2}{d^2-4R^2} + \frac{2R^2}{d^2} + \ln\left(\frac{d^2-4R^2}{d^2}\right)\right] \tag{2}$$

$$A_{131} \approx \left(\sqrt{A_{11}} - \sqrt{A_{33}}\right)^2 \tag{3}$$

$$A_{33} = \frac{3}{4}k_BT\left(\frac{\varepsilon_3 - \varepsilon_{vacuum}}{\varepsilon_3 + \varepsilon_{vacuum}}\right)^2 + \frac{3hv_e}{16\sqrt{2}}\frac{\left(n_3^2 - n_{vacuum}^2\right)^2}{\left(n_3^2 + n_{vacuum}^2\right)^{3/2}} \tag{4}$$

The above expression (equation 3) for A_{131} applies to a binary system with one solvent (component 3) and one nanoparticle material (component 1). But, gas expanded liquids are mixtures of two solvent components (in this case, CO_2 and hexane), so a new mathematical expression was developed to calculate the Hamaker constant where 3' represents one of the solvent components (in this case CO_2) and 3" represents the other solvent component (e.g. hexane). In equation (5), $\tilde{\phi}_{3'}$ is the CO_2 volume fraction in the solvent mixture excluding the ligand, and $A_{(33)'}$ is the Hamaker constant for CO_2. Similarly, $\tilde{\phi}_{3''}$ is the volume fraction of hexane in the solvent mixture excluding the ligand, and $A_{(33)''}$ is the Hamaker constant for hexane. The complete derivation of the equation (5) is given in supporting information.

$$A_{131} \approx \left[\sqrt{A_{11}} - \left(\tilde{\phi}_{3'}\sqrt{A_{(33)'}} + \tilde{\phi}_{3''}\sqrt{A_{(33)''}}\right)\right]^2 \tag{5}$$

For the repulsive contribution, Vincent et. al. (Vincent, Luckham et al. 1980) proposed the osmotic and elastic repulsive terms where the osmotic term is related to the solvation of the ligand tails between the colliding nanoparticles. The osmotic term

depends on the free energy of the solvent-ligand tail interactions. On the other hand, the elastic term results from the entropy loss due to the compression of ligand tails present between two metal cores. Shah et. al. (Shah, Holmes et al. 2002) introduced these two repulsive terms, originating from "soft sphere" theory, to the total interaction energy to balance the van der Waals forces of attraction between nanoparticles. These repulsive contributions, as given in equation (6-8), depend largely on the ligand length and solvent parameters as well as on the particle radius, R, and center to center particle distance, d. v_{solv} is the molar volume of the solvent and Avogadro's number (N_{av}) was used to convert this into molecular volume of the solvent. h is the separation distance from the particle surfaces calculated using equation (9). The elastic term, given by equation (8), depends on the ligand density (ρ) and its molecular weight (MW_2).

$$\Phi_{osm} = \frac{4\pi R k_B T}{(v_{solv}/N_{av})} \phi^2 \left(\frac{1}{2} - \chi\right)\left(l - \frac{h}{2}\right)^2 \qquad l < h < 2l \qquad (6)$$

$$\Phi_{osm} = \frac{4\pi R k_B T}{(v_{solv}/N_{av})} \phi^2 \left(\frac{1}{2} - \chi\right)\left[l^2\left(\frac{h}{2l} - \frac{1}{4} - \ln\left(\frac{h}{l}\right)\right)\right] \qquad h < l \qquad (7)$$

$$\Phi_{elas} = \frac{2\pi R k_B T l^2 \phi \rho}{MW_2}\left\{\frac{h}{l}\ln\left[\frac{h}{l}\left(\frac{3-h/l}{2}\right)^2\right] - 6\ln\left(\frac{3-h/l}{2}\right) + 3\left(1 - \frac{h}{l}\right)\right\} \qquad h < l \qquad (8)$$

$$h = d - 2R \qquad (9)$$

χ is the Flory-Huggins interaction parameter in the osmotic repulsion term and is a function of the Hilderbrand solubility parameter of the solvent (component 3) and ligand (component 2), as given in equation (10), where v_3 is the molar volume of the solvent and R is the ideal gas constant.

$$\chi_{32} = \frac{v_3}{RT}(\delta_3 - \delta_2)^2 \tag{10}$$

This osmotic repulsive term given above applies to one solvent (component 3) interacting with the ligand tails but in the case of the two solvents in the gas expanded liquid, a new mathematical expression was developed as given in the equation below. The complete derivation of the osmotic repulsive energy term for several solvent components interacting with the ligand tails is given in the supporting information.

$$\Phi_{osm} = \frac{4\pi R k_B T}{(v_M/N_{av})}\phi^2\left[x_{3'}\left(\frac{1}{2} + \tilde{\phi}_{3''}r_{3'}\chi_{(3'3'')} - r_{3'}\chi_{(3'2)}\right) + x_{3''}\left(\frac{1}{2} - r_{3''}\chi_{(3''2)}\right)\right]\left(l - \frac{h}{2}\right)^2$$

$$\text{When } l < h < 2l \tag{11}$$

$$\Phi_{osm} = \frac{4\pi R k_B T}{(v_M/N_{av})}\phi^2\left[x_{3'}\left(\frac{1}{2} + \tilde{\phi}_{3''}r_{3'}\chi_{(3'3'')} - r_{3'}\chi_{(3'2)}\right) + x_{3''}\left(\frac{1}{2} - r_{3''}\chi_{(3''2)}\right)\right]\left[l^2\left(\frac{h}{2l} - \frac{1}{4} - \ln\left(\frac{h}{l}\right)\right)\right]$$

$$\text{When } h < l \tag{12}$$

Where *3'* represents one of the solvent components (in this case, CO_2) and *3"* represents the other solvent component (e.g. hexane), and v_M in this case represents the molar volume of the solvent mixture of CO_2 and hexane excluding the ligand. As can be seen from these equations and from Figure 7.1, the repulsive energies do not contribute to the total interaction energy until the separation distance is less than twice the ligand length *l*. $r_{3'}$ and $r_{3''}$ are the segment lengths of molecules of CO_2 and hexane and their values are assumed to be $r_{3'} = 1$ and $r_{3''} = v_{3''}/v_{3'}$, respectively. $x_{3'}$ and $x_{3''}$ are mole fractions of CO_2 and hexane, respectively, in the solvent mixture of CO_2 and hexane excluding the ligand, as given in Table 7.2, where molar compositions and molar

volumes of the liquid phase for CO_2 gas expanded hexane at $25^{\circ}C$ were calculated using the Peng-Robinson Equation of State with the binary interaction parameter set as 0.125 (k_{12} = 0.125 for CO_2 and hexane). $\widetilde{\phi}_{3"}$ is the volume fraction of hexane in the CO_2 and hexane solvent mixture excluding the ligand. ϕ is the ligand volume fraction within the volumetric shell of one extended ligand length from the particle surface (i.e. local volume fraction of the ligand coating the particle surface), and it was calculated by modeling the ligand as a cylindrical structure extending from the particle surface. It is given in the literature that the ligand surface coverage varies with particle size from 30% for small nanocrystals (< 4 nm) to 60% for nanoparticles with a larger size range (Saunders and Korgel 2004). It was measured by Korgel et. al. that thiols have a surface coverage of 75% on silver nanoparticle surfaces for particles of 4 to 7 nm in size (Korgel, Fullam et al. 1998). The following expression for ligand volume fraction assumes a surface coverage of 75%.

$$\phi = 0.75\left(\frac{3R^2l}{(R+l)^3 - R^3} \right) \tag{13}$$

7.3 Results and Discussion

7.3.1 Total Interaction Energy Calculations

All of the forces which contribute to the total interaction energy were calculated for CO_2 gas expanded hexane at various pressures below the CO_2 vapor pressure (860 psi). As an example, the contributions of these forces are shown in Figure 7.1 as a function of the separation distance, h, at a CO_2 pressure of 500 psi. Also shown in Figure 7.1 is a dotted line, drawn at $-3/2\ k_BT$, that represents the minimum threshold energy for Brownian

motion necessary to disperse the particles of a given size within the bulk solvent. The total interaction energy for a given particle size should be above this minimum threshold energy at the given conditions in order to stabilize the particles. Due to van der Waals forces of attraction, particles approach each other, and if not sufficiently solvated and stabilized in the medium, they will flocculate and precipitate. If particles are larger than a threshold size, the minima in the total interaction energy curve for those sized particles drops below -3/2 k_BT and those particle will precipitate from solution. The sum of the elastic and repulsive forces thereby counteracts these van der Waals forces of attraction and result in an increase in particle dispersibility. The elastic term, which is due to tail-tail interactions, depends on thiol density and its volume fraction. It has a very small contribution to the total interaction energy except at very close separation distances. On the other hand, the osmotic force strongly counteracts the van der Waals forces of attraction and depends on the solvent molar volume, ligand length, ligand volume fraction and solvent-ligand interaction (given as χ in this model). Stabilized particles can therefore be induced to precipitate with the addition of an antisolvent, thereby decreasing the solvent strength and reducing the solvent-ligand interaction below the value necessary to disperse a given sized particle. In the example shown in Figure 7.1, the maximum size of the particles that can be stabilized at these conditions can be obtained by equating the total interaction energy with the Boltzmann threshold stabilization energy (-3/2 k_BT). To improve the CO_2 gas expanded liquid nanoparticle precipitation process, it would be important to be able to predict the threshold particle size where particles larger than this threshold size are precipitated and particles smaller than this threshold size are dispersed at a given set of conditions. In this study, threshold particle size for

precipitation/dispersion has been calculated at various operating conditions in the CO_2 gas expanded mixtures. In the example in Figure 7.1, a hexane/CO_2 mixture with a CO_2 pressure of 500 psi results in a threshold size of 12.6 nm for dodecanethiol stabilized silver nanoparticle. This model helps in finding the threshold nanoparticle size which can be precipitated/dispersed at various conditions as a function of the solvent, ligand, temperature and antisolvent CO_2 pressure.

In this chapter, we have considered three basic phenomenological variations on this total interaction energy model based on the nature of the interaction between the ligand tails and the solvent. A schematic of these three models is given in Figure 7.2 that illustrates the ligand tail arrangement and position within the solvent environment to depict differences in tail solvation and ligand length accessibility by the solvent. In the Extended Ligand Length Solvation Model (ELLSM), ligand tails are considered to be fully extended and the entire length of the thiol's alkyl tail is available to interact with the solvent. In the Condensed Phase Model (CPM), the ligand tails are considered to be condensed on the particle surface due to poor solvent strength and effective ligand lengths available for solvation were calculated by assuming the ligand volume fraction as unity. In Limited Ligand Length Solvation Model (LLLSM), effective ligand lengths available for interaction with solvent were determined by matching the model predicted particle size to the size obtained from the size fractionation experiments at a given set of conditions using the ligand length as an adjustable parameter. Hence effective ligand lengths were fit to the experimental data.

7.3.2 Extended Ligand Length Solvation Model (ELLSM)

In this model, it was assumed that the whole alkyl ligand tail is extended from the particle surface and solvated by the solvent as shown in Figure 7.2(a). The threshold particle size which can be precipitated/dispersed at a set of given solvent conditions was calculated by balancing the total interaction energy with the Boltzmann threshold stabilization energy ($-3/2\ k_BT$) by considering that the entire ligand length (dodecane length 15 Å) interacts with the solvent. Similarly, threshold particle sizes were calculated at various CO_2 pressures (see Table 7.3) that correspond to conditions used in the CO_2 expanded hexane particle precipitation experiments presented in chapter 2. Comparing the calculated threshold particle sizes to the experimental results, these calculated threshold particle sizes are always much larger than experimental and there was not much change in the calculated particle size with the corresponding changes in the CO_2 pressure as shown in Figure 7.4. Unfortunately, the ELLSM model is unable to predict both the threshold size and the effect of pressure on this threshold size. To improve these calculations it is important to understand which parameters have the greatest influence on the stabilization threshold size and the effect of CO_2 pressure on this size as measured experimentally. As such, we performed a sensitivity analysis on various parameters to understand which variables most affect these modeling results.

7.3.3 Parameter Sensitivity Analysis

The physicochemical properties of CO_2 gas expanded liquids are difficult to determine because the CO_2 in the liquid hexane/CO_2 mixture behaves as a hypothetical liquid despite the fact that the system pressure is below its vapor pressure, making it different to

determine pure component CO_2 "liquid" properties at these operating conditions. Liquid volumes and solubility parameters for CO_2 as a solute in hexane mixtures were obtained from the reports in the literature. Given the nonideality of these CO_2 expanded hexane mixtures, and the uncertainty of thermodynamic mixing rules in this case, sensitivity analysis was performed on these literature obtained CO_2 properties in order to determine the impact of potential measurement errors on these predicted threshold particle sizes. Sensitivity analysis was performed to analyze the effects of these properties of CO_2 as well as the influence of other model parameters such as ligand length solvation, surface coverage of the ligands on the particle surface, solvent mixture volume and the Hamaker constant of the metallic Ag particles on the over predicted threshold particle size. Sensitivity analysis was performed on the property values of the hypothetical liquid CO_2 and the other model parameters by increasing or decreasing the parameters by 30% from the baseline parameter values in order to determine the variation in the threshold particle size obtained. Note that, at CO_2 pressure of 500 psi using the ELLSM model the base parameter values yielded a threshold size of 12.6 nm, and the sensitivity to these parameters is determined by comparing the increased and decreased values to this base case of 12.6 nm. Also note that the experimental particle size at these conditions is 6.7 nm. As indicated above, the ELLSM model predicted a threshold particle size at the base conditions of 12.6 nm compared to this experimentally obtained size of 6.7 nm. The sensitivity analysis on the model parameters will allow us to determine which parameters most influence particle dispersability.

Van der Waals forces depend on the refractive index and dielectric constant of CO_2 as well as the Hamaker constant of the silver metal surface. The value of the CO_2

dielectric constant used in the ELLSM model was 1.483. With a 30% increase (1.928) or 30% decrease (1.038) in this base value of CO_2 dielectric constant, there was not a significant change in the threshold particle diameter from the 12.6 nm value obtained at the base parameter values as shown in Table 7.4. On the other hand, a 30% increase (1.54) in the CO_2 refractive index from its base value (1.185) results in a large increase in particle size (12.6 nm to 14.1 nm). However, a 30% decrease (0.829) in the CO_2 refractive index did not result in a large change in particle size. The base value of the Hamaker constant of the silver nanoparticle surface was taken as 2.185 eV. A 30% increase in the Hamaker constant value (2.84 eV) decreases the threshold particle size to 10.7 nm while a 30% decrease in the Hamaker value (1.53 eV) increases the particle size to 16.2 nm. While this increase in the Hamaker constant does reduce the predicted threshold size (10.7 nm) towards the experimental result (6.7 nm), Eichenlaub et. al. (Eichenlaub, Chan et al. 2002) have shown that the Hamaker constant for Ag-Ag interaction cannot be more than 3.12 eV (a maximum value reported), which results in a threshold size of 10.1 nm. It should be noted that Eichenlaub et. al. reported a range of possible Hamaker constant values for Ag ranging from 1.02 eV to 3.12 eV with an average value of similar to the value of 2.185 eV (Shah, Holmes et al. 2002) used in this study.

Osmotic forces depend on the solubility parameters of the solvent components as well as the ligand, solubility parameter, the ligand length and the ligand surface coverage as well as the solvent volumes. The properties of the pure hexane and pure ligand alkyl tail are well known in the literature and we are not investigating in the parameter sensitivity analysis. As shown in Table 7.4, among all the parameters investigated the

ligand length (actual value = 15 Å) has the greatest influence on the threshold particle size, where the particle size increased to 16.4 nm from 12.6 nm with a 30% increase (19.5 Å) in the ligand length. The threshold particle size was also changed to 8.8 nm from 12.6 nm with a 30% decrease (10.5 Å) in the ligand length. It is reasonable, based on discussions below, that the entire ligand length would not be available for complete solvation by the solvent medium. Therefore, the effective ligand length in the model could be decreased more than the 30% used in this sensitivity analysis in order to finely tune the threshold particle size to match the experimental obtained results. The effect of the degree of ligand solvation accounted for in the model by adjusting the "effective" ligand length is more clearly demonstrated in Figure 7.3 which shows the total interaction energy for three different ligand lengths (15, 19.5, 10.5 Å). Due to this sensitivity analysis, we find that the ligand length has the most pronounced affect on the threshold particle size predicted in the ELLSM. As such, we have developed two other variations of this model to explain our experimental results based on differing degrees of tail solvation and "effective" ligand lengths for this solvation.

7.3.4 Condensed/Collapsed Phase Model (CPM)

After performing the sensitivity analysis, it was observed that ligand length is the variable that has the most impact on the threshold particle size predicted in the ELLSM model. Indeed, the degree to which the solvent has access to the ligand tail length decides the magnitude of the ligand-solvent interaction and hence the effective ligand length being solvated impacts the repulsive energy. We considered two variations of the model based on different ligand lengths being able to interact with the solvent base on physical phenomena constraints.

De gennes (De Gennes 1976; De Gennes 1976; Brochard and De Gennes 1977) has shown that for a poor solvent, a polymer chain interacts more with itself than with the solvent and makes knots on itself. In other words, the polymers repel each other and extend more in a good solvent (interact more with the solvent) whereas the polymer collapses and condenses in a poor solvent. For example, In one of De gennes articles (Brochard and De Gennes 1977), he has shown that the polymer coil diameter is proportional to the polymerization index raised to a ½ power in poor solvent compared to a ⅗ power in good solvent. In the current study, the addition of antisolvent CO_2 decreases the solvent strength of the solvent mixture thereby reducing the ligand length interacting with the now poorer solvent. As an alternative to the ELLSM model, we have considered the scenario where the solvent strength would be low enough that the ligand tails are completely condensed on the particle surface. Figure 7.2 (b) shows the condensed phase arrangement of thiol tails with a ligand volume fraction considered to be unity. This model is referred to as the Condensed Phase Model (CPM) since it is considered that all the thiol tails are collapsed and condensed. The effective ligand length which is available for interaction is thus calculated by setting the ligand volume fraction in equation (13) equal to 1 and solving for l, for a given particle diameter, R obtained experimentally. The value of the ligand length which was obtained was 8.8 Å for a 6.7 nm particle diameter, as given in Table 7.5. The effective ligand length has reduced from 15 Å (in ELLSM) to 8.8 Å (in CPM) for a 6.7 nm particle diameter. The effective ligand lengths at different CO_2 pressures were calculated by setting the ligand volume fraction in equation (13) to a value of 1 with a ligand surface coverage of 75% (Korgel, Fullam et al. 1998) for each experimental particle size obtained at a particular CO_2 pressure. At this

point, all the calculations of the forces were performed with these new effective ligand lengths and the respective ligand solubility parameters that correspond to these alkyl tail lengths. The predicted threshold particle size obtained from the CPM model is much lower than the ELLSM model and closer to the experimental data as shown in Figure 7.4. Unfortunately, these results still slightly over predict the threshold particle diameters at the lowest pressure of 500 psi and do not demonstrate the significant effect of pressure on the threshold particle diameter as observed experimentally although a slight decrease in diameter is observed with increasing CO_2 pressure. While the CPM model does not capture the effect of CO_2 pressure compared to the experimental data, it does illustrate that limited tail solvation likely accounts for the differences in the ELLSM model and the experimental results.

In an effort to account for the difference between the threshold particle diameters obtained from the Condensed Phase Model (with constant surface coverage) and the experimental data, the degree of surface coverage, in the CPM model, was adjusted from the literature value of 75% (Korgel, Fullam et al. 1998). These results for this CPM model with variable surface coverage model are shown in Table 7.5. These results again indicate that a small variation in surface coverage from 69.3% to 58.3% can account for the change in particle size precipitated at the various experiment pressures. These results again indicate that the degree of ligand tail solvation is the most important parameter for controlling particle dispersability. In this case the model was fit to the experimental data at each pressure by adjusting the surface coverage and determining the corresponding effective length according to equation (13). It has been shown in literature that ligand surface coverage does not remain constant for all particle sizes (Saunders and Korgel

204

2004) Ligand surface coverage on the gold particles was found to vary with particle size from 30% for small nanocrystals (< 4 nm) to 60% for nanoparticles with a larger size range. However, the ligand surface coverage measured by Korgel et. al. for dodecanethiol coated Ag particles in the range of 4 to 7 nm, is a constant value of 75%. One major concern with the CPM model involves the dichotomy of the concept of the ligand tails being completely condensed on the particle surface while also being able to interact with the solvent through tail solvation. There is experimental evidence that thiol tails on a metal surface are in the extended mode. For example, using IR spectroscopic and ellipsometric data, Porter et. al. (Porter, Bright et al. 1987) have shown that thiol tails with hydrocarbon group ($-CH_2$) greater than 9 assemble on gold surfaces in a densely packed manner with fully extended alkyl chains tilted from the surface normal by 20-30°. This suggests that the Condensed Phase Model may not be the correct phenomenological model for our experimental system.

7.3.5 Limited Ligand Length Solvation Model (LLLSM)

Another model which was considered is shown in Figure 7.2 (c) where the ligand tails are fully extended yet the entire length is not accessible to the solvent, such that the effective ligand length which is interacting with the solvent is smaller than the total ligand length. This effective ligand length decreases with an increase in the antisolvent CO_2 concentration (pressure) due to the weaker solvent mixture being less able to solvate the ligand tails. In other words, the total ligand length is extended but only part of it is interacting with the solvent because only a portion of the ligand length is coming in contact with the solvent. As shown in Figure 7.2(c) if the ligand tails are densely packed (assume surface coverage 75%) then it would be very difficult for hexane solvent

205

molecules, which are half the length of dodecanethiol ligand molecules, to penetrate the tortuous path between the ligand tails and solvate the entire ligand length. Effective ligand lengths were obtained by matching the threshold particle size predicted from the total interaction energy model with the experimental results at constant ligand surface coverage of 75%. Ligand Solubility parameters were also adjusted according to the effective alkyl tail length in this model. The results from this Limited Ligand Length Solvation Model are given in Table 7.5. The effective ligand length required to disperse a threshold particle size of 6.7 nm at a CO_2 pressure of 500 psi is 8.2 Å compared to the total length of the dodecanethiol ligand which is 15 Å. Similarly, effective ligand lengths were calculated at each of the antisolvent CO_2 pressures by fitting the threshold particle size from the model to our experimental data at each of these CO_2 pressures. Considering limited ligand length solvation, the total interaction energy model indicates that the effective ligand length of the dodecane alkyl tail which is available to the solvent decreases from 8.2 Å to 5.9 Å corresponding to the Ag particle sizes of 6.7 nm to 4.1 nm, and CO_2 pressures from 500 psi to 700 psi, respectively. These results indicate that changes in the effective ligand length, due to solvation changes, can account for both the dispersed particle size as well as the effect of CO_2 pressure.

7.3.6 Surface Fraction Model

Another model was developed based on the surface area of the solvent and the ligand molecules. It was decided to find the effective surface area of the ligand instead of effective length interacting with the solvent. The van der Waals attractive force and elastic force would remain the same as in the volume fraction model, however, the osmotic term will take the surface area of the components into account instead of the

volume fractions of the components. The derivation of the osmotic term for a multicomponent system (several solvents and one ligand molecule) is given in the supporting information. In the case of CO_2 gas expanded hexane, the osmotic equation is given in equation (14) and (15), where s_j is the ratio of the surface area (q_j) and the segment number (r_j) of component j. $\Delta\varepsilon_{jk}$ is the interaction parameter, analogous to the Flory- Huggins parameter (χ_{jk}), given by equation (16) and $\widetilde{S}_M = \sum_i^n s_j\phi_j$ for solvents CO_2 and hexane excluding ligand.

$$\Phi_{osm} = \frac{4\pi R k_B T}{(v_M/N_{av})}\phi^2\frac{s_2^2}{\overline{S}_M^2}\left[\frac{1}{2}+x_3 r_3 s_3\left(s_{3''}\widetilde{\phi}_{3''}\frac{\Delta\varepsilon_{(3'3'')}}{\overline{S}_M}-\Delta\varepsilon_{(3'2)}\right)+\left(\frac{1}{2}-x_{3''}r_{3''}s_{3''}\Delta\varepsilon_{(3''2)}\right)\right]\left(l-\frac{h}{2}\right)^2$$

$$\text{When } l < h < 2l \qquad (14)$$

$$\Phi_{osm} = \frac{4\pi R k_B T}{(v_M/N_{av})}\phi^2\frac{s_2^2}{\overline{S}_M^2}\left[\frac{1}{2}+x_3 r_3 s_3\left(s_{3''}\widetilde{\phi}_{3''}\frac{\Delta\varepsilon_{(3'3'')}}{\overline{S}_M}-\Delta\varepsilon_{(3'2)}\right)+\left(\frac{1}{2}-x_{3''}r_{3''}s_{3''}\Delta\varepsilon_{(3''2)}\right)\right]\left[l^2\left(\frac{h}{2l}-\frac{1}{4}-\ln\left(\frac{h}{l}\right)\right)\right]$$

$$\text{When } h < l \qquad (15)$$

$$h = d - 2R$$

$$\Delta\varepsilon_{jk} = \chi_{jk}\left(\frac{s_j\phi_j + s_k\phi_k}{s_j s_k}\right) \qquad (16)$$

After performing the calculations with this surface fraction model, it was determined that the ligand length still needed to be reduced in order to fit the experimental data. Since, however, not all of the ligand length is accessible to interact with the solvent, as we have discussed so far in this chapter, the calculation of the van der Waals attractive force could be improved by basing it on the radius of the particle including the part of the condensed ligand that surrounds the particle surface. However,

in both manners, it is clear that part of the ligand is either condensed on the particle surface or inaccessible to the solvent such that only the remaining part is available to interact with the solvent.

7.4 Conclusions

A model was developed on the basis of total interaction energy to predict the threshold Ag nanoparticle size which can be precipitated/dispersed in CO_2 gas expanded liquids at various antisolvent CO_2 pressures. After deriving expressions for the osmotic energy term and the Hamaker constant that account for multiple solvent systems, the model was successfully applied to the CO_2 gas expanded liquid size separation process using the thermodynamic properties of CO_2 gas expanded liquids. However, allowing complete solvation of the ligand length in the model results in threshold particle sizes too large compared to the experimental results. Thus, three phenomenological variations of this total interaction energy model were considered where the Limited Ligand Length Solvation Model provided the best match of the threshold predicated particle sizes with the experimental results. This model shows that the degree of tail solvation strongly impacts the particle sizes and that limited ligand solvation is occurring and is a function of CO_2 pressure. Very subtle changes in solvent strength result in a fine tuning of dispersed particle size and this modeling study improves our understanding of particle dispersibility at various conditions alleviating the need for extensive experimentation.

7.5 Acknowledgements

DE-FG26-06NT42685, and CTS 0207781, respectively.

7.6 Supporting Information Available

We present the complete derivations of Hamaker constant and repulsive energies for a multi component system (several solvents and one ligand).
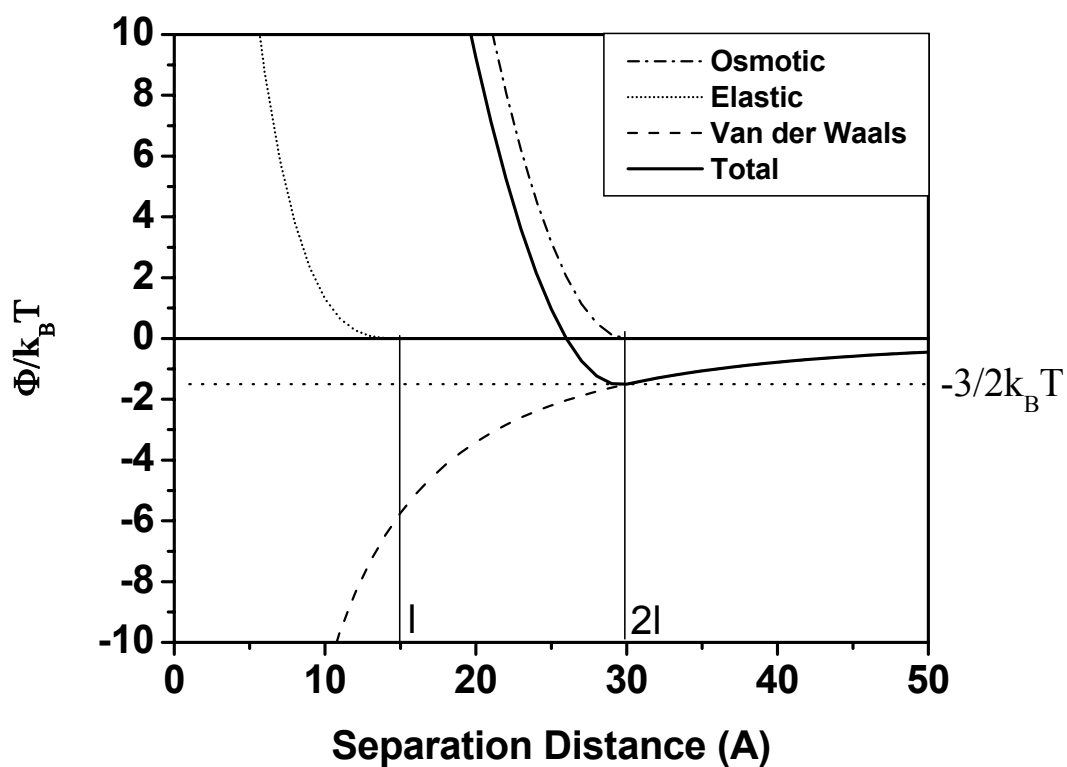
Figure 7-1 Representation of the attractive (van der Waals) and repulsive forces (osmotic and elastic) contributing to the total interaction energy for 12.6 nm dodecanethiol coated silver nanoparticles dispersed in CO_2 gas expanded hexane at a CO_2 pressure of 500 psi and system temperature 25^oC.
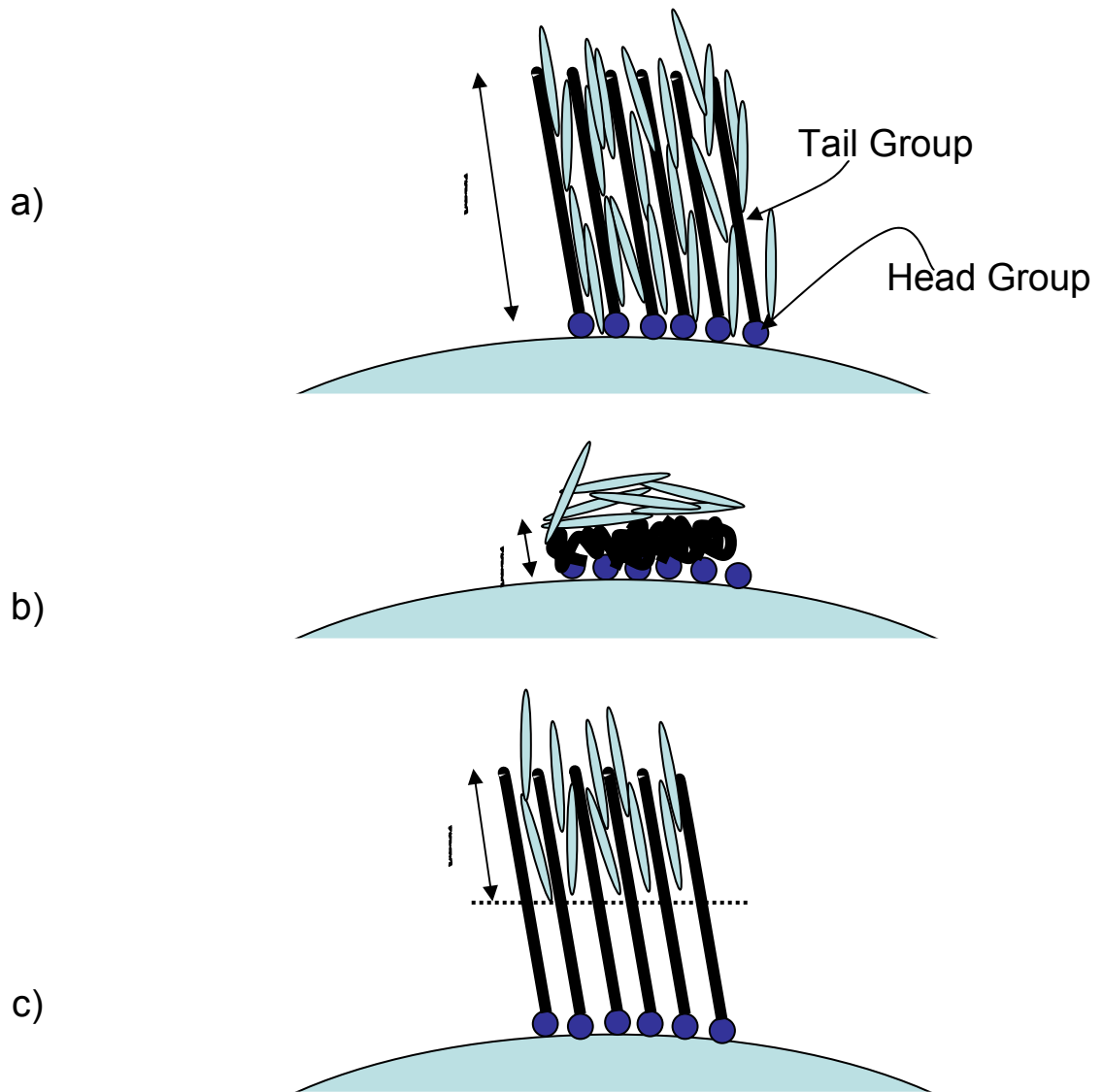
Figure 7-2 Schematic of three phenomenological models used to estimate the threshold

particle size for precipitation/dispersion in CO_2 expanded size separation process. In the

Extended Ligand Length Solvation Model (ELLSM), the ligand tails are extended

completely and the whole length of the ligand alkyl tail interacts with the solvent. In the Condensed Phase Model (CPM), the ligand tails are condensed and effective ligand lengths were calculated by assuming the volume fraction as unity. In Limited Ligand Length Solvation Model (LLLSM), effective ligand lengths available for interaction with solvent were determined by matching the model predicted particle size to the size obtained from the size fractionation experiments at a given set of conditions using the ligand length as an adjustable parameter.
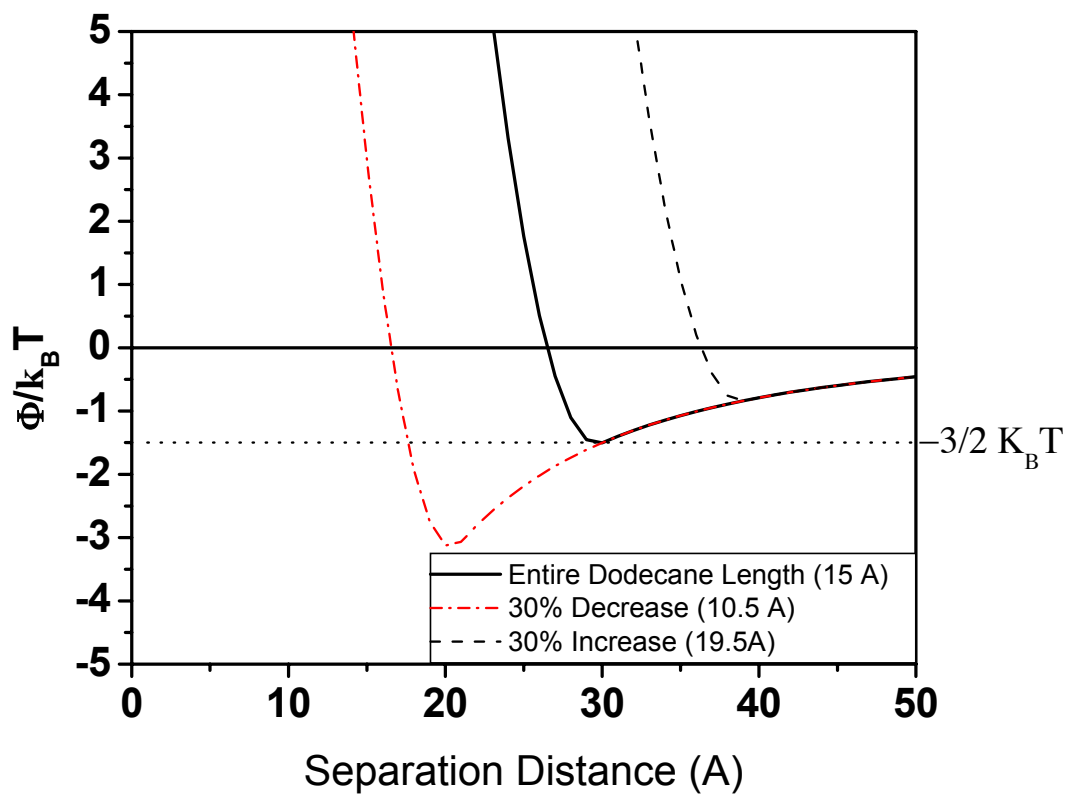
Figure 7-3 Demonstration of the effect of the degree of ligand solvation on the total interaction energy with a 30% increase and 30% decrease in the effective dodecanethiol ligand length
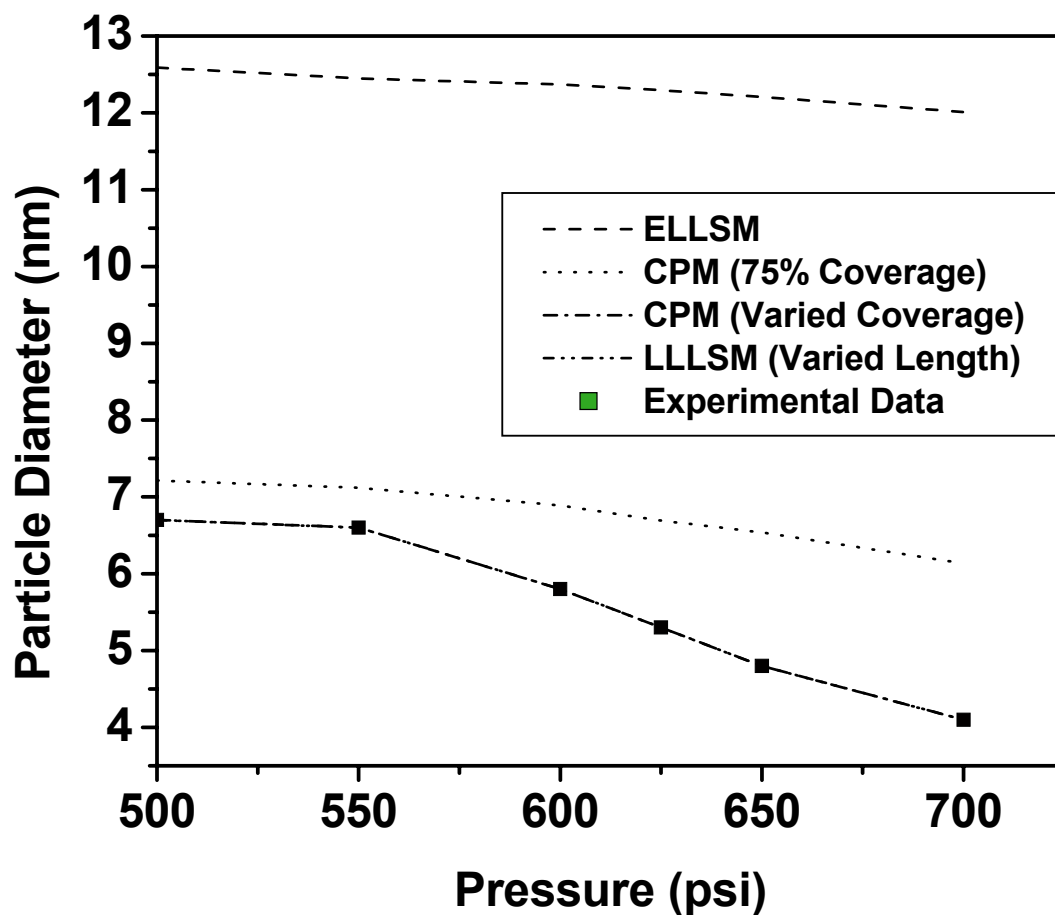
Figure 7-4 Comparison of Ag particle diameters precipitated in CO_2 gas expanded hexane experiments and threshold particle diameters predicted using the Extended Ligand Length Solvation Model (ELLSM), the Condensed Phase Model (CPM), and the Limited Ligand Length Solvation Model (LLLSM) as a function of CO_2 pressure. The experimental results are presented for dodecanethiol coated silver particles precipitated from hexane/CO_2 mixtures.

Compound	v_L (cm³/mol)	δ (J/cm³)$^{1/2}$	Dielectric Constant (ε)	Refractive Index (n)
CO_2	55	12.3	1.483	1.185
Hexane	132	14.9	1.882	1.372
Pentane	116	14.5	1.836	1.355
Heptane	147	15.2	1.917	1.385
Octane	164	15.3	1.942	1.393

Table 7-1 Physical properties of various solvents. The values for hexane and CO_2 were used to model the size fractionation process of dodecanethiol stabilized silver nanoparticles using CO_2 gas expanded liquids at 25°C.

Pressure (Psi)	Volume Fraction		Mole Fraction		Molar Volume (cm³/mol)
	Hexane	CO_2	Hexane	CO_2	
0	1	0	1	0	131
500	0.732	0.268	0.529	0.471	88
550	0.670	0.330	0.460	0.540	84
600	0.634	0.366	0.416	0.584	79
625	0.600	0.400	0.380	0.620	76
650	0.560	0.440	0.350	0.650	74
700	0.468	0.532	0.265	0.735	68

Table 7-2 Compositions and Molar volumes of the liquid phase for CO_2 gas expanded hexane at 25°C calculated using the Peng-Robinson Equation of State with the k_{12} binary interaction parameter set as 0.125 ($k_{12} = 0.125$ for CO_2 and Hexane).

Experimental Section		Theoretical Section			
Pressure Range (Psi)	**Mean Diameter (nm)**	**Pressure (Psi)**	**Threshold Particle Diameter (nm)**		
			ELLSM	**CPM**	**LLLSM**
0 - 500	6.7	500	12.6	6.7	6.7
500 - 550	6.6	550	12.5	6.6	6.6
550 - 600	5.8	600	12.4	5.8	5.8
600 - 625	5.3	625	12.3	5.3	5.3
625 - 650	4.8	650	12.2	4.8	4.8
650 - 700	4.1	700	12.0	4.1	4.1

Table 7-3 Comparison of experimental Ag particle diameters obtained at different pressures in the CO_2 gas expanded liquid particle size separation process and predicted particle diameters using three models based on total interaction energy. The experimental section shows the mean diameter of dodecanethiol-coated silver particles precipitated within the corresponding CO_2 pressure ranges. The theoretical section provides predictions of the threshold particle diameter that can be precipitated/dispersed using three phenomenological variations of the total interaction energy model based on a soft sphere approach. In the Extended Ligand Length Solvation Model (ELLSM), ligand tails are extended completely and the whole length of thiol molecule interacts with the solvent. In the Condensed Phase Model (CPM), ligand lengths are condensed on the particle surface and are calculated by assuming the volume fraction as unity. In the Limited Ligand Length Solvation Model (LLLSM), only a part of entire ligand length is solvated and is calculated by matching the predicted particle size with the size obtained from size fractionation experiments.

Parameter	Base Parameter Values Used	Threshold Particle Diameter (nm)	
		30% increase	30% decrease
Carbon Dioxide			
Dielectric Constant	1.483	12.6	12.6
Refractive Index	1.185	14.1	12.6
Solubility Parameter $(J/cm^3)^{1/2}$	12.3	12.6	12.6
Molar Volume (cm^3/mol)	55	12.4	12.9
Other Parameters			
Hamaker Constant (eV)	2.185	10.7	16.2
Surface Coverage	75%	12.6	12.5
Mixture Volume (cm^3/mol)	87	12.6	12.6
Length Of Ligand (Å)	15	16.4	8.8

Table 7-4 Results of sensitivity analysis performed at CO_2 pressure of 500 psi for analysis of the parameters affecting the threshold particle size obtained from the Extended Ligand Length Solvation Model. A 12.6 nm threshold size is obtained using the base parameter values of 500 psi CO_2 pressure. This table shows the change in the predicted threshold particle size using a 30% increase and a 30% decrease in various parameters relative to the threshold particle size obtained using the base values of the parameters.

Pressure (Psi)	Condensed Phase Model (75% Surface Coverage)		Condensed Phase Model (Variable Surface Coverage)			Limited Ligand Length Solvation Model (75% Surface Coverage)	
	Effective Ligand Length (Å)	Threshold Particle Size (nm)	Surface Coverage (%)	Effective Ligand Length (Å)	Threshold Particle Size (nm)	Effective Ligand Length (Å)	Threshold Particle Size (nm)
500	8.8	7.2	69.3	8.2	6.7	8.2	6.7
550	8.7	7.1	69.2	8.2	6.6	8.1	6.6
600	8.5	6.9	63.2	7.4	5.8	7.3	5.8
625	8.4	6.7	60.3	7.0	5.3	6.8	5.3
650	8.2	6.5	60.2	6.9	4.8	6.3	4.8
700	7.9	6.1	58.3	6.5	4.1	5.9	4.1

Table 7-5 Effective ligand lengths and threshold Ag particle sizes as a function of CO_2 pressure obtained from the Condensed Phase Model using 75% surface coverage, the Condensed Phase Model with surface coverage as an adjustable parameter, and the Limited Ligand Length Solvation Model.

This supporting information provides the derivations of the Hamaker constant and the osmotic repulsive energy term for a mixture of solvents and one polymer (i.e. ligand tails).

7.7 Derivation of Hamaker constant for mixed solvent (mixture of more than one solvent component) interacting with one polymer component
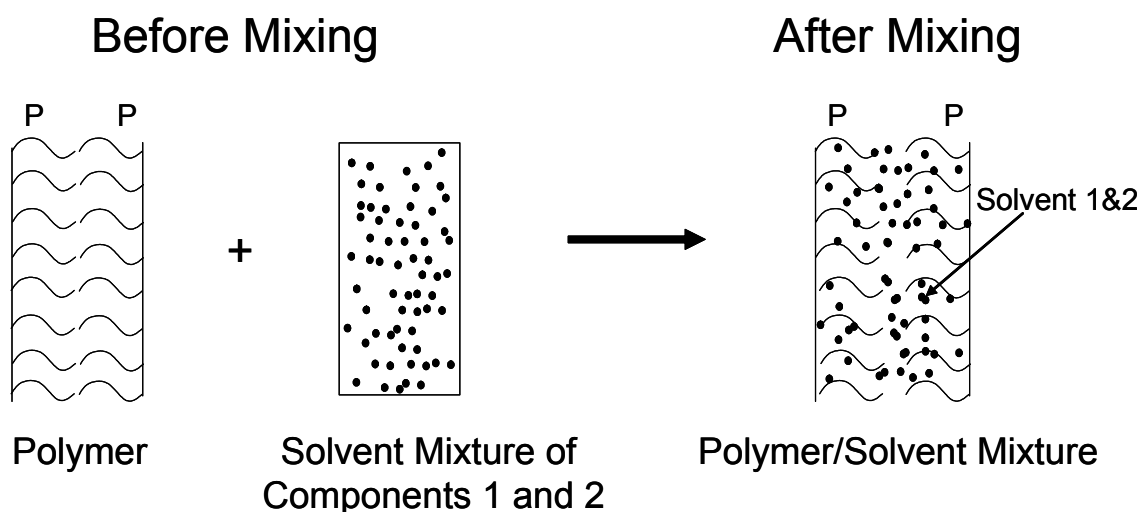
The summation of the components interactions before mixing of the polymer (P) with the solvent mixture of components 1 and 2 is given by (1)

$$k \, (\text{P-P}) + \alpha \, (\text{1-1}) + \beta \, (\text{2-2}) + \gamma \, (\text{1-2}) + \gamma \, (\text{2-1}) \tag{1}$$

where k, α, β, and γ denote coefficients of interaction for dispersion forces. Since we have assumed random mixing, the coefficients α, β, and γ are proportional to the product of the volume fractions of the species involved. This means that the contact probability of (1-1) would be $\widetilde{\phi_1}^2$, the contact probability of (1-2) would be $\widetilde{\phi_1} \, \widetilde{\phi_2}$ and the contact probability of (2-2) would be $\widetilde{\phi_2}^2$, where $\widetilde{\phi_1}$ and $\widetilde{\phi_2}$ represent the volume fractions of the solvent components 1 and 2 excluding the polymer.

So that $\alpha = k \widetilde{\phi_1}^2$, $\beta = k \widetilde{\phi_2}^2$, $\gamma = k \widetilde{\phi_1} \, \widetilde{\phi_2}$ and (1) becomes

$$k \, \{(\text{P-P}) + \widetilde{\phi_1}^2 \, (\text{1-1}) + \widetilde{\phi_2}^2 \, (\text{2-2}) + 2 \, \widetilde{\phi_1} . \widetilde{\phi_2} \, (\text{1-2})\} \tag{2}$$

Since we are taking as the basis 2 polymer chains, the proportionality constant 'k' in (B) is equal to 1, such that (2) becomes (3)

$$(\text{P-P}) + \widetilde{\phi_1}^2 \, (\text{1-1}) + \widetilde{\phi_2}^2 \, (\text{2-2}) + 2 . \widetilde{\phi_1} . \widetilde{\phi_2} \, (\text{1-2}) \tag{3}$$

After mixing the polymer (P) with the solvent mixture of components 1 and 2, the summation of the components interactions is given by (4).

$$2x \, (\text{P-1}) + 2y \, (\text{P-2}) \tag{4}$$

where x and y are unknown coefficients of contact probabilities with x +y equal to 1. Applying a component balance for solvent 1 before and after mixing using (3) and (4) yields

$$2\widetilde{\phi_1}^2 + 2 \, \widetilde{\phi_1} . \widetilde{\phi_2} = 2x \tag{5}$$

and since $\widetilde{\phi_1} + \widetilde{\phi_2} = 1$, simplifying (5) results in

$$\widetilde{\phi_1} = x \tag{6}$$

Similarly, applying the component balance on solvent 2 will result in $\tilde{\phi}_2 = y$.

Now, the expression for the Hamaker Constant for a mixed solvent – polymer interaction, A_{PMP}, can be derived by subtracting the Hamaker constants of component interactions of equation (3) from the Hamaker constants of component interactions of equation (4), yielding (7) where P denotes the polymer and M denotes the mixed solvent.

$$A_{PMP} = -\left[A_{PP} + \tilde{\phi}_1^2 A_{11} + 2\tilde{\phi}_1\tilde{\phi}_2 A_{12} + \tilde{\phi}_2^2 A_{22} - 2\tilde{\phi}_1 A_{P1} - 2\tilde{\phi}_2 A_{P2}\right]$$

$$A_{PMP} = -\left[A_{PP} - 2\tilde{\phi}_1 A_{P1} - 2\tilde{\phi}_2 A_{P2} + \left(\tilde{\phi}_1\sqrt{A_{11}} + \tilde{\phi}_2\sqrt{A_{22}}\right)^2\right]$$

Assuming $A_{12} = \sqrt{A_{11}}\sqrt{A_{22}}$

$$A_{PMP} = -\left[\sqrt{A_{PP}} - \left(\tilde{\phi}_1\sqrt{A_{11}} + \tilde{\phi}_2\sqrt{A_{22}}\right)\right]^2 \tag{7}$$

The expression (7) for the Hamaker constant can be obtained for a mixed solvent-polymer interaction. Since the negative sign is already taken into account in van der Waals attractive force term in the total interaction energy, the negative sign in front of Hamaker constant can be neglected. Therefore,

$$A_{PMP} = \left[\sqrt{A_{PP}} - \left(\tilde{\phi}_1\sqrt{A_{11}} + \tilde{\phi}_2\sqrt{A_{22}}\right)\right]^2$$

7.8 Derivation of the Osmotic repulsion term for mixed solvent (mixture of more than one solvent) interacting with one polymer in the volume fraction model

The Gibbs free energy change for mixing, ΔG_M, in a volume element, δV, is given by equation (8)

$$\delta(\Delta G_M) = \delta(\Delta G^C) + \delta(\Delta G^R) \qquad (8)$$

where G^C is the combinatorial free energy and G^R is the residual free energy (Napper

1983

For the combinatorial free energy, which is purely entropic in nature, we assume that the

polymer amount can be neglected in the bulk solvent system since its concentration is

very low compared to the solvent concentration. The combinatorial free energy can be

expressed as the following.

$$\delta(\Delta G^C) = k_B T \sum \delta n_i \ell n \phi_i \cong k_B T \sum_j^s \delta n_j \ell n \phi_j \qquad (9)$$

where i represents component i in the system, j represents components j in the solvent

mixture excluding the polymer, and s is the number of solvent components. Considering

the mixture of one polymer (in this case 'ligand') and a mixture of s solvent components.

The volume fraction, ϕ_j of component j in the system is given by

$$\phi_j = \widetilde{\phi}_j (1 - \phi_p) \qquad (10)$$

where $\widetilde{\phi}_j$ is a volume fraction of component j excluding polymer, ϕ_p is a volume fraction

of polymer p in the entire solvent-polymer system.

The number of molecules, δn_j of component j in the system is given by.

$$\delta n_j = \frac{x_j (1 - \phi_p) \delta V}{v_M} \qquad (11)$$

where x_j is the mole fraction of component j in the solvent mixture and v_M represents the molar volume of the solvent mixture excluding the polymer ($v_M = \sum x_j v_j$ where v_j is molar volume of component j in solvent mixture excluding polymer) and V is the total volume of the system.

Substituting equations (10) and (11) into equation (9) and using the expression for the logarithmic term in the Taylor's series expansion at the limit of ϕ_p approaching 0 yields the following expression for the combinatorial Gibbs free energy.

$$\delta(\Delta G^C) = k_B T \sum_j^s x_j (\ln \tilde{\phi}_j - \phi_p - \frac{\phi_p^2}{2})(\frac{1-\phi_p}{v_M})\delta V \tag{12}$$

The residual free energy, which is the free energy arising from contact dissimilarities, is given by the following expression

$$\delta(\Delta G^R) = k_B T \sum_{j<}^s \sum_k^s \chi_{jk} \delta(r_j n_j)\phi_k \tag{13}$$

where r_j is the segment length of the molecule j, ϕ_k is a volume fraction of component k, n_j is number of molecules and χ_{jk} is the Flory-Huggins interaction parameter. The residual free energy is the sum of the excess free energies associated with the interaction of solvent component j to the other solvent component k with volume fraction ϕ_k and polymer component p with volume fraction ϕ_p.

After substituting relation (11) into equation (13), the following expression is obtained

$$\delta(\Delta G^R) = k_B T \left[\sum_j^s \sum_{k>j}^s \chi_{jk} r_j x_j \phi_k + \sum_j^k \chi_{jp} r_j x_j \phi_p \right](\frac{1-\phi_p}{v_M})\delta V \tag{14}$$

Substituting equation (10) for ϕ_k into (14) yields the following expression for the residual Gibbs free energy

224

$$\delta(\Delta G^{R}) = k_{B}T\left[\sum_{j}^{s}\sum_{k>j}^{s}\chi_{jk}r_{j}x_{j}\widetilde{\phi}_{k}(1-\phi_{p}) + \sum_{j}^{k}\chi_{jp}r_{j}x_{j}\phi_{p}\right](\frac{1-\phi_{p}}{v_{M}})\delta V \tag{15}$$

The repulsive potential energy

According to Napper (Napper 1983), it is assumed that the free energy of attachment of the polymer chains is independent of the separation distance, d, of the plates, and the repulsive potential energy, ΔG_R, is

$$\Delta G_{R} = \Delta G_{M_{d}} - \Delta G_{M_{\infty}} \tag{16}$$

Assuming that $\{x_j\}$ and $\{\widetilde{\phi}_k\}$ are independent of the distance of the separation, substituting $\phi_{p} = v_{s}\rho_{p}(d)$ into equation (12) and (15) yields

$$\Delta G_{R} = k_{B}T\left[\sum_{j}^{s}x_{j}\left(\frac{1}{2} + r_{j}\sum_{k>j}\widetilde{\phi}_{k}\chi_{jk} - r_{j}\chi_{jp}\right)\right]\frac{v_{s}^{2}}{v_{M}}\left[\int_{V}\rho_{p}^{2}(d)\,dV - \int_{V}\rho_{p}^{2}(\infty)\,dV\right] \tag{17}$$

where, ρ_p (d) is the number density of the polymer, and v_s is the segment volume of the molecule.

As in Napper's derivation for a binary system, all terms except $\rho_{p}^{2}(d)$ terms vanish.

Assuming constant segment density and that the particles are equivalent spheres, we can obtain the expression of the osmotic interaction energy by applying Derjaguin approximation.

$$\Phi_{osm} = \frac{4\pi Rk_{B}T}{(v_{M}/N_{av})}\phi^{2}\left[\sum_{j}^{s}x_{j}\left(\frac{1}{2} + r_{j}\sum_{k>j}\widetilde{\phi}_{k}\chi_{jk} - r_{j}\chi_{jp}\right)\right]\left(l - \frac{h}{2}\right)^{2} \qquad l < h < 2l$$

$$\Phi_{osm} = \frac{4\pi Rk_{B}T}{(v_{M}/N_{av})}\phi^{2}\left[\sum_{j}^{s}x_{j}\left(\frac{1}{2} + r_{j}\sum_{k>j}\widetilde{\phi}_{k}\chi_{jk} - r_{j}\chi_{jp}\right)\right]\left[l^{2}\left(\frac{h}{2l} - \frac{1}{4} - \ln\left(\frac{h}{l}\right)\right)\right] \qquad h < l$$

$$h = d - 2R$$

7.9 Derivation of the Osmotic repulsion term for mixed solvent (mixture of more than one solvent) interacting with one polymer in the Surface Fraction Model

In the surface fraction model, the Gibbs free energy change for mixing is again given by equation (8)

where $\delta(\Delta G^C)$ is the same as in Equation (12) and $\delta(\Delta G^R)$ is given by the equation below

$$\delta(\Delta G^R) = k_B T \sum_j^s \sum_{k>j}^s \Delta\varepsilon_{jk} \delta(q_i n_i) \theta_k \tag{18}$$

$\Delta\varepsilon_{jk}$ is the interaction parameter analogous to the Flory- Huggins parameter (χ_{jk}), q_i is the surface area of component i, θ_i is the surface fraction of component i, and n_i is the number of molecules of component i.

Therefore, fraction, θ_k, is given by

$$\theta_k = \frac{q_k n_k}{\sum_i^n q_j n_j} = \frac{s_k \phi_k}{S_M}$$

$$where \quad S_M = \sum_i^n s_j \phi_j$$

$$and \quad s_k = \frac{q_k}{r_k} \tag{19}$$

$$and \quad \phi_k = \frac{r_k n_k}{\sum_j^n r_j n_j}$$

r_j is the segment number of component j, s_j is the ratio of surface area and segment number of component j.

The Taylor series expansion of θ_k and θ_p at the limit of ϕ_p approaching 0 yields

$$\theta_k = \frac{s_k \overline{\phi}_k}{\overline{S}_M} - \frac{s_k s_p \overline{\phi}_k}{\overline{S}_M^{\ 2}} \phi_p + \frac{s_k s_p \overline{\phi}_k (s_p - \overline{S}_M)}{\overline{S}_M^{\ 3}} \phi_p^{\ 2}$$

$$\theta_p = \frac{s_p}{\overline{S}_M} \phi_p + \frac{s_p (\overline{S}_M - s_p)}{\overline{S}_M^{\ 2}} \phi_p^{\ 2}$$

As in equation (16) the repulsive potential energy, ΔG^R, given by

$$\Delta G_R = \Delta G_d - \Delta G_\infty$$

Substituting the above expressions in an analogous manner to that of the development of equation (17), the following expression for the repulsive potential energy for the surface fraction model is given by

$$\Delta G_R = k_B T \frac{s_p^{\ 2}}{\overline{S}_M^{\ 2}} \left[\frac{1}{2} + \sum_j^s r_j s_j x_j \left[\sum_j^s s_k \overline{\phi}_k \frac{\Delta \varepsilon_{jk}}{\overline{S}_M} - \Delta \varepsilon_{jp} \right] \right] \frac{v_s^{\ 2}}{\overline{v}_{solv}} \left[\int_V \rho_p^{\ 2}(d)\, dV - \int_V \rho_p^{\ 2}(\infty)\, dV \right]$$

Assuming constant segment density and that the particles are equivalent spheres, we can obtain the expression of the osmotic interaction energy by applying Derjaguin approximation.

$$\Phi_{osm} = \frac{4\pi R k_B T}{(v_M / N_{av})} \phi^2 \frac{s_p^{\ 2}}{\overline{S}_M^{\ 2}} \left[\frac{1}{2} + \sum_j^s r_j s_j x_j \left[\sum_{k>j}^s s_k \widetilde{\phi}_k \frac{\Delta \varepsilon_{jk}}{\overline{S}_M} - \Delta \varepsilon_{jp} \right] \right] \left(l - \frac{h}{2} \right)^2 \qquad l < h < 2l$$

$$\Phi_{osm} = \frac{4\pi R k_B T}{(v_M / N_{av})} \phi^2 \frac{s_p^{\ 2}}{\overline{S}_M^{\ 2}} \left[\frac{1}{2} + \sum_j^s r_j s_j x_j \left[\sum_{k>j}^s s_k \widetilde{\phi}_k \frac{\Delta \varepsilon_{jk}}{\overline{S}_M} - \Delta \varepsilon_{jp} \right] \right] \left[l^2 \left(\frac{h}{2l} - \frac{1}{4} - \ln\left(\frac{h}{l} \right) \right) \right] \qquad h < l$$

$$h = d - 2R$$

CHAPTER 8

FUTURE WORK

8.1 Scaling-up of size selection process

8.1.1 Objective

With the current size fractionation apparatus, we can separate approximately 20 milligrams of metallic (Au, Ag, Pd, Pt) or semi-conductor nanoparticles (CdSe/ZnS) into seven different size-specific fractions. In order to show that this process is commercially viable, it is decided to scale-up the apparatus in order for it to be able to handle an initial sample on the gram or kilogram scale.

8.1.2 Apparatus Set Up

A batch apparatus would consist of two identical high pressure cylindrical vessels connected by a valve. Each vessel would have access ports for a temperature probe, a pressure transducer as well as a valve to connect a syringe pump. The vessels (with the valve connected in-line between the vessels) would need to be mounted on a bracket such that the vessels can be rotated end-over-end. This rotation needs to be able to occur very smoothly as not to loosen any already precipitated particles or to cause any trauma to the pressure vessels. The ends of each vessel would need to be easily removable such that samples can be easily inserted and removed.

.

8.1.3 Procedure

To begin an experimental run, the vessels would me aligned horizontally and a large sample of a polydisperse nanoparticle dispersion introduced into one vessel with the isolation valve in the closed position. Separately, each vessel is pressurized to a predetermined initial pressure using a CO_2 syringe pump. The assembly is then allowed to sit for a specific settling time required to precipitate the first fraction of the largest nanoparticles. The isolation valve is then opened and the system allowed to equilibrate at the initial pressure. The assembly is then rotated 90 degrees allowing the remaining nanoparticle dispersion to flow into the lower vessel via gravity. The particles were precipitated in the horizontal position of the first vessel so that they do not hinder the flow of the remaining nanoparticle dispersion into the second vessel. Once the remaining nanoparticle dispersion is in the second vessel, the isolation valve will be closed. The system is rotated back 90 degrees such that the assembly is in the horizontal position. At this point, the first vessel will be depressurized and opened in order to remove the largest sized nanoparticle fraction by redispersing it in hexane. With the first fraction removed, the first vessel can be sealed and both vessels brought to the next predetermined pressure. The isolation valve can then be opened and the system allowed to equilibrate. During the second settling time interval, the next largest size nanoparticles are precipitated in the horizontal position, the assembly is then rotated to the vertical position to move the remaining liquid dispersion to the first vessel. Again, the isolation valve will be closed, the second vessel will be depressurized and opened and the second fraction of nanoparticles will be removed by redispersing in hexane. This procedure can be repeated a number of times depending on the number of fractions desired.

229

The major advantage of this double high pressure vessel apparatus has over the smaller spiral tube is the use of larger volume per fraction inside the vessel. With the spiral tube apparatus, the volume was divided into seven locations for seven respective fractions. This was due to the need of having control over the location of the nanoparticle dispersion inside the spiral tube. Different fractions were located in different locations on the spiral tube. Rather than having different locations within one vessel for each fraction, this double-vessel apparatus allows us to precipitate each fraction of a much larger original dispersion in an individual vessel and clean as well as recover a fraction during one experimental run.

One possible foreseen problem with this apparatus could be thick layers of precipitated particles forming on the wall of the vessel. A thick layer could potentially break loose and block flow into the other vessel. Rather than creating thick layers along the walls, it is possible to fill each vessel with glass wool. The glass wool offers much more contact surfaces area and a removable support for which the particles can be precipitated onto. The glass wool covered with precipitated particles could be easily removed, after the depressurization following each precipitation, from the vessel and washed with an organic solvent to remove all the precipitated particles.

BIBLIOGRAPHY

Adair, J. H., T. Li, et al. (1998). "Recent developments in the preparation and properties of nanometer-size spherical and platelet-shaped particles and composite particles." Materials Science & Engineering R- Reports **23**(4-5): 139-242.

Ahn, K. H., J. H. Anh, et al. (2001). Apparatus for manufacturing ultra-fine particles using electrospray device and method thereof. PCT Int. Appl. Wo, (Kang, Seog Joo, S. Korea). 24 pp.

Ahn, S. J., D. H. Son, et al. (1994). "Self-assembled and Langmuir-Blodgett stearic acid monolayers on silver: a comparative reflection-absorption Fourier transform infrared spectroscopic study." Journal of Molecular Structure **324**(3): 223-31.

Alivisatos, A. P. (1996). "Perspectives on the physical chemistry of semiconductor nanocrystals." Journal of Physical Chemistry **100**(31): 13226-13239.

Anand, M., M. C. McLeod, et al. (2005). "Tunable Solvation Effects on the Size-Selective Fractionation of Metal Nanoparticles in CO2 Gas-Expanded Solvents." Journal of Physical Chemistry B **109**(48): 22852-22859.

Andres, R. P., J. D. Bielefeld, et al. (1996). "Self-assembly of a two-dimensional superlattice of molecularly linked metal clusters." Science (Washington, D. C.) **273**(5282): 1690-1693.

231

Arenz, M., K. J. J. Mayrhofer, et al. (2005). "The Effect of the Particle Size on the Kinetics of CO Electrooxidation on High Surface Area Pt Catalysts." Journal of the American Chemical Society **127**(18): 6819-6829.

Arnaud, I., J.-P. Abid, et al. (2005). "Size-selective separation of gold nanoparticles using isoelectric focusing electrophoresis (IEF)." Chemical Communications (Cambridge, United Kingdom)(6): 787-788.

Bae, A.-H., M. Numata, et al. (2005). "1D arrangement of Au nanoparticles by the helical structure of schizophyllan: A unique encounter of a natural product with inorganic compounds." Angewandte Chemie, International Edition **44**(13): 2030-2033.

Becker, M. F., J. R. Brock, et al. (1998). "Metal nanoparticles generated by laser ablation." Nanostructured Materials **10**(5): 853-863.

Beckman, E. J. (2003). "Green Chemical Processing Using CO2." Industrial & Engineering Chemistry Research **42**(8): 1598-1602.

Beckman, E. J. (2004). "Supercritical and near-critical CO2 in green chemical synthesis and processing." Journal of Supercritical Fluids **28**(2-3): 121-191.

Bell, P. W., M. Anand, et al. (2005). "Stable Dispersions of Silver Nanoparticles in Carbon Dioxide with Fluorine-Free Ligands." Langmuir **21**(25): 11608-11613.

Bellamy, L. J. (1975). The Infra-red Spectra of Complex Molecules. New York, John Wiley & Sons.

Blackburn, J. M., D. P. Long, et al. (2001). "Deposition of conformal copper and nickel films from supercritical carbon dioxide." Science (Washington, DC, United States) **294**(5540): 141-145.

Bleich, J., P. Kleinebudde, et al. (1994). "Influence of Gas Density and Pressure on

Microparticles Produced with the ASES Process." <u>Int. J. Pharm.</u> **106**: 77.

Bradley, J. S. (1994). "Synthesis and characterization of nearly monodisperse CdE (E = S, Se, Te) semiconductor nanocrystals." <u>Chemtracts: Inorganic Chemistry</u> **6**(4): 283-8.

Brochard, F. and P. G. De Gennes (1977). "Dynamical scaling for polymers in theta solvents." <u>Macromolecules</u> **10**(5): 1157-61.

Bruchez, M., Jr., M. Moronne, et al. (1998). "Semiconductor Nanocrystals as Fluorescent Biological Labels." <u>Science</u> **281**: 2013-2016.

Brust, M., D. Bethell, et al. (1998). "Self-Assembled Gold Nanoparticle Thin Films with Nonmetallic Optical and Electronic Properties." <u>Langmuir</u> **14**(19): 5425-5429.

Brust, M., J. Fink, et al. (1995). "Synthesis and reactions of functionalized gold nanoparticles." <u>Journal of the Chemical Society, Chemical Communications</u>(16): 1655-6.

Brust, M. and C. J. Kiely (2002). "Some recent advances in nanostructure preparation from gold and silver particles: a short topical review." <u>Colloids and Surfaces, A: Physicochemical and Engineering Aspects</u> **202**(2-3): 175-186.

Brust, M., M. Walker, et al. (1994). "Synthesis of thiol-derivatized gold nanoparticles in a two-phase liquid-liquid system." <u>Journal of the Chemical Society, Chemical Communications</u>(7): 801-2.

Bungert, B., G. Sadowski, et al. (1998). "Separations and Material Processing in Solutions with Dense Gases." <u>Industrial & Engineering Chemistry Research</u> **37**(8): 3208-3220.

Calcote, H. F. and D. G. Keil (1997). "Description of a combustion flame for the

production of silicon carbide." <u>Chemical and Physical Processes in Combustion</u>: 309-312.

Cason, J. P., M. E. Miller, et al. (2001). "Solvent effects on copper nanoparticle growth behavior in AOT reverse micelle systems." <u>Journal of Physical Chemistry B</u> **105**(12): 2297-2302.

Cason, J. P. and C. B. Roberts (2000). "Metallic copper nanoparticle synthesis in AOT reverse micelles in compressed propane and supercritical ethane solutions." <u>Journal of Physical Chemistry B</u> **104**(6): 1217-1221.

Chan, W. C. W. and S. Nile (1998). "Quantum dot bioconjugates for ultrasensitive nonisotopic detection." <u>Science (Washington, D. C.)</u> **281**(5385): 2016-2018.

Chandrasekharan, N. and P. V. Kamat (2002). "Tuning the properties of CdSe nanoparticles in reverse micelles." <u>Research on Chemical Intermediates</u> **28**(7-9): 847-856.

Chen, J., J. Zhang, et al. (2004). "Investigation on the precipitation, microenvironment and recovery of protein in CO2-expanded reverse micellar solution." <u>Colloids and Surfaces, B: Biointerfaces</u> **33**(1): 33-37.

Clarke, M. J., K. L. Harrison, et al. (1997). "Water in Supercritical Carbon Dioxide Microemulsions: Spectroscopic Investigation of a New Environment for Aqueous Inorganic Chemistry." <u>Journal of the American Chemical Society</u> **119**(27): 6399-6406.

Clarke, N. Z., C. Waters, et al. (2001). "Size-Dependent Solubility of Thiol-Derivatized Gold Nanoparticles in Supercritical Ethane." <u>Langmuir</u> **17**(20): 6048-6050.

Collier, C. P., T. Vossmeyer, et al. (1998). "Nanocrystal superlattices." <u>Annual Review of</u>

Physical Chemistry **49**: 371-404.

Creighton, J. A. and D. G. Eadon (1991). "Ultraviolet-visible absorption spectra of the colloidal metallic elements." Journal of the Chemical Society, Faraday Transactions **87**(24): 3881-91.

Czajka, R., W. Polewska, et al. (2002). "Scanning probe microscopy methods in studies of crystal surface structure." Prace ITME **57**: 92-109.

da Rocha, S. R. P., J. Dickson, et al. (2003). "Surfactants for Stabilization of Water and CO_2 Emulsions: Trisiloxanes." Langmuir **19**(8): 3114-3120.

da Silva, M. C., A. C. B. Silva, et al. (2001). "Production of nanometric particles of SnS semiconductors from organometallic precursors." Ciencia & Engenharia **10**(1): 10-13.

Dabbousi, B. O., M. G. Bawendi, et al. (1995). "Electroluminescence from CdSe quantum-dot/polymer composites." Applied Physics Letters **66**(11): 1316-18.

Dabbousi, B. O., O. Onitsuka, et al. (1995). "Size dependent electroluminescence from CdSe nanocrystallites (quantum dots)." Materials Research Society Symposium Proceedings **358**(Microcrystalline and Nanocrystalline Semiconductors): 707-12.

Dai, J. and M. L. Bruening (2002). "Catalytic Nanoparticles Formed by Reduction of Metal Ions in Multilayered Polyelectrolyte Films." Nano Letters **2**(5): 497-501.

De Gennes, P. G. (1976). "Dynamics of entangled polymer solutions. I. The Rouse model." Macromolecules **9**(4): 587-93.

De Gennes, P. G. (1976). "Dynamics of entangled polymer solutions. II. Inclusion of hydrodynamic interactions." Macromolecules **9**(4): 594-8.

De la Fuente Badilla, J. C., C. J. Peters, et al. (2000). "Volume expansion in relation to

the gas-antisolvent process." Journal of Supercritical Fluids **17**(1): 13-23.

Dickson, J. L., B. P. Binks, et al. (2004). "Stabilization of Carbon Dioxide-in-Water Emulsions with Silica Nanoparticles." Langmuir **20**(19): 7976-7983.

Dickson, J. L., P. S. Shah, et al. (2004). "Steric Stabilization of Core-Shell Nanoparticles in Liquid Carbon Dioxide at the Vapor Pressure." Langmuir **20**(21): 9380-9387.

Dickson, J. L., P. G. Smith, Jr., et al. (2005). "Interfacial Properties of Fluorocarbon and Hydrocarbon Phosphate Surfactants at the Water-CO2 Interface." Industrial & Engineering Chemistry Research **44**(5): 1370-1380.

Dimitrijevic, N. M., D. M. Bartels, et al. (2001). "Radiolytically Induced Formation and Optical Absorption Spectra of Colloidal Silver Nanoparticles in Supercritical Ethane." Journal of Physical Chemistry B **105**(5): 954-959.

Dimitrov, S., V. Kemenska, et al. (2004). "Predicting the biodegradation products of perfluorinated chemicals using CATABOL." SAR and QSAR in Environmental Research **15**(1): 69-82.

Dixon, D. J., K. P. Johnston, et al. (1993). "Polymeric Materials Formed by Precipitation with a Compressed Fluid Antisolvent." AIChE J. **39**(1): 127.

Dobbs, J. M., J. M. Wong, et al. (1986). "Nonpolar co-solvents for solubility enhancement in supercritical fluid carbon dioxide." Journal of Chemical and Engineering Data **31**(3): 303-8.

Dong, X., D. Potter, et al. (2002). "Synthesis of CuS Nanoparticles in Water-in-Carbon Dioxide Microemulsions." Industrial & Engineering Chemistry Research **41**(18): 4489-4493.

Doty, R. C., M. B. Sigman, Jr., et al. (2004). "Synthesis and fabrication of metal

nanocrystal superlattices." Optical Engineering (New York, NY, United States) **87**(Semiconductor and Metal Nanocrystals): 387-419.

Drachev, V. P., A. K. Buin, et al. (2004). "Size Dependent c(3) for Conduction Electrons in Ag Nanoparticles." Nano Letters **4**(8): 1535-1539.

Drexler, E., K. (1986). Engines of Creation:The Coming Era of Nanotechnology. New York, Anchor Books Editions.

Dupont, A., J. Eastoe, et al. (2004). "Hybrid Fluorocarbon-Hydrocarbon CO2-philic Surfactants. 2. Formation and Properties of Water-in-CO2 Microemulsions." Langmuir **20**(23): 9960-9967.

Eastoe, J., A. Dupont, et al. (2003). "Design and performance of surfactants for carbon dioxide." ACS Symposium Series **860**(Supercritical Carbon Dioxide): 285-308.

Eastoe, J., A. Dupont, et al. (2003). "Micellization of economically viable surfactants in CO2." Journal of Colloid and Interface Science **258**(2): 367-373.

Eastoe, J., A. Paul, et al. (2001). "Micellization of Hydrocarbon Surfactants in Supercritical Carbon Dioxide." Journal of the American Chemical Society **123**(5): 988-989.

Eastoe, J., A. Paul, et al. (2003). "Water-in-carbon dioxide microemulsions stabilized by fluorosurfactants." Surfactant Science Series **109**(Adsorption and Aggregation of Surfactants in Solution): 299-325.

Eckert, C. A., D. Bush, et al. (2000). "Tuning Solvents for Sustainable Technology." Industrial & Engineering Chemistry Research **39**(12): 4615-4621.

Eichenlaub, S., C. Chan, et al. (2002). "Hamaker Constants in Integrated Circuit Metalization." Journal of Colloid and Interface Science **248**(2): 389-397.

Ershov, B. G. and A. Henglein (1998). "Reduction of Ag+ on Polyacrylate Chains in Aqueous Solution." Journal of Physical Chemistry B **102**(52): 10663-10666.

Esumi, K., S. Sarashina, et al. (2004). "Synthesis of Gold Nanoparticles from an Organometallic Compound in Supercritical Carbon Dioxide." Langmuir **20**(13): 5189-5191.

Evans, S. D., S. R. Johnson, et al. (2000). "Vapour sensing using hybrid organic-inorganic nanostructured materials." Journal of Materials Chemistry **10**(1): 183-188.

Eychmueller, A. (2000). "Structure and Photophysics of Semiconductor Nanocrystals." Journal of Physical Chemistry B **104**(28): 6514-6528.

Fan, X., M. C. McLeod, et al. "Preparation of Silver Nanoparticles via Reduction of a Highly CO2-Soluble Hydrocarbon-Based Metal Precursor." Industrial & Engineering Chemistry Research: ACS ASAP.

Fan, X., V. K. Potluri, et al. (2005). "Oxygenated Hydrocarbon Ionic Surfactants Exhibit CO2 Solubility." Journal of the American Chemical Society **127**(33): 11754-11762.

Feynman, R. (1992). "There's Plenty of room at the Bottom." Journal of Microelectromechanical Systems **1**(1): 60-66.

Feynman, R. (1993). "Infinitesimal Machinery." Journal of Microelectromechanical Systems **2**(1): 4-14.

Fischer, C. H., J. Lilie, et al. (1989). "Photochemistry of colloidal semiconductors. 29. Fractionation of cadmium sulfide sols of small particles by exclusion chromatography." Berichte der Bunsen-Gesellschaft **93**(1): 61-4.

238

Fischer, C. H., H. Weller, et al. (1986). "Photochemistry of colloidal semiconductors. 10. Exclusion chromatography and stop flow experiments on the formation of extremely small cadmium sulfide particles." Berichte der Bunsen-Gesellschaft **90**(1): 46-9.

Fischer, C. H., H. Weller, et al. (1989). "Photochemistry of colloidal semiconductors. 30. HPLC investigation of small CdS particles." Langmuir **5**(2): 429-32.

Freeman, R. G., K. C. Grabar, et al. (1995). "Self-assembled metal colloid monolayers: an approach to SERS substrates." Science (Washington, D. C.) **267**(5204): 1629-31.

Fremgen, D. E., E. S. Smotkin, et al. (2001). "Microemulsions of water in supercritical carbon dioxide: an in-situ NMR investigation of micelle formation and structure." Journal of Supercritical Fluids **19**(3): 287-298.

Gallagher, P. M., M. P. Coffey, et al. (1989). "Gas antisolvent recrystallization: new process to recrystallize compounds insoluble in supercritical fluids." ACS Symposium Series **406**(Supercrit. Fluid Sci. Technol.): 334-54.

Gallagher, P. S., M. P. Coffey, et al. (1989). Gas antisolvent recrystallization: new process to recrystallize compounds insoluble in supercritical fluids. Supercritical Fluid Science and Technology. K. P. Johnston and M. L. Penninger. **406:** 334-54.

Gao, M., C. Lesser, et al. (2000). "Electroluminescence of different colors from polycation/CdTe nanocrystal self-assembled films." Journal of Applied Physics **87**(5): 2297-2302.

Garcia-Martinez, J. C. and R. M. Crooks (2004). "Extraction of Au Nanoparticles Having Narrow Size Distributions from within Dendrimer Templates." Journal of the

American Chemical Society **126**(49): 16170-16178.

Garcia-Martinez, J. C., R. W. J. Scott, et al. (2003). "Extraction of Monodisperse Palladium Nanoparticles from Dendrimer Templates." Journal of the American Chemical Society **125**(37): 11190-11191.

Hamaker, H. C. (1937). "The London-van der Waals attraction between spherical particles." Physica (The Hague) **4**: 1058-72.

Hansen, J. A., R. Mukhopadhyay, et al. (2006). "Femtomolar Electrochemical Detection of DNA Targets Using Metal Sulfide Nanoparticles." Journal of the American Chemical Society **128**(12): 3860-3861.

Hao, E., H. Sun, et al. (1999). "Synthesis and Optical Properties of CdSe and CdSe/CdS Nanoparticles." Chemistry of Materials **11**(11): 3096-3102.

Haruta, M. (1997). "Size- and support-dependency in the catalysis of gold." Catalysis Today **36**(1): 153-166.

He, R. and H. Gu (2004). "Synthesis and characterization of nearly monodisperse CdSe quantum dots at lower temperature." Oz Nano 03, Proceedings of the Asia Pacific Nanotechnology Forum, Cairns, Australia, Nov. 19-21, 2003: 59-62.

Henderson, E. and C. Mosher (2002). Nanoscale sensor. PCT Int. Appl. Wo, (Bioforce Laboratory, Inc., USA). 25 pp.

Henglein, A. and R. Tausch-Treml (1981). "Optical absorption and catalytic activity of subcolloidal and colloidal silver in aqueous solution: a pulse radiolysis study." Journal of Colloid and Interface Science **80**(1): 84-93.

Hoefling, T. A., R. R. Beitle, et al. (1993). "Design and Synthesis of Highly CO_2-Soluble Surfactants and Chelating Agents." Fluid Phase Equilibria **83**: 203.

Hoefling, T. A., R. M. Enick, et al. (1991). "Microemulsions in Near-Critical and Supercritical CO_2." J. Phys. Chem. **95**: 7127.

Holmes, J. D., P. A. Bhargava, et al. (1999). "Synthesis of Cadmium Sulfide Q Particles in Water-in-CO2 Microemulsions." Langmuir **15**(20): 6613-6615.

Holmes, J. D., K. P. Johnston, et al. (2000). "Control of thickness and orientation of solution-grown silicon nanowires." Science (Washington, D. C.) **287**(5457): 1471-1473.

Huang, Y., D. Li, et al. (2004). "b-Cyclodextrin controlled assembling nanostructures from gold nanoparticles to gold nanowires." Chemical Physics Letters **389**(1-3): 14-18.

Israelachvili, J. N. (1985). Intermolecular and surface forces: with applications to colloidal and biological systems, London, Orlando [FL].

Jaeger, L., E. Westhof, et al. "TectoRNA: modular assembly units for the construction of RNA nano-objects." Nucleic Acids Res FIELD Full Journal Title:Nucleic acids research FIELD Publication Date:2001 **29**(2): 455-63. FIELD Reference Number: FIELD Journal Code:0411011 FIELD Call Number:.

Jaeger, L., E. Westhof, et al. (2001). "TectoRNA: modular assembly units for the construction of RNA nano-objects." Nucleic Acids Research **29**(2): 455-463.

Jessop, P. G., M. M. Olmstead, et al. (2002). "Carbon Dioxide as a Solubility "Switch" for the Reversible Dissolution of Highly Fluorinated Complexes and Reagents in Organic Solvents: Application to Crystallization." Inorganic Chemistry **41**(13): 3463-3468.

Jessop, P. G., M. M. Olmstead, et al. (2002). "Carbon Dioxide as a Solubility \"Switch\"

for the Reversible Dissolution of Highly Fluorinated Complexes and Reagents in Organic Solvents: Application to Crystallization." <u>Inorganic Chemistry</u> **41**(13): 3463-3468.

Jessop, P. G. and B. Subramaniam (2006). "Gas-Expanded Liquids." <u>Chemical Reviews</u>: Submitted.

Ji, M., X. Chen, et al. (1999). "Synthesizing and dispersing silver nanoparticles in a water-in-supercritical carbon dioxide microemulsion." <u>Journal of the American Chemical Society</u> **121**(11): 2631-2632.

Ji, M., X. Y. Chen, et al. (1999). "Synthesizing and dispersing silver nanoparticles in a water-in-supercritical carbon dioxide microemulsion." <u>Journal of the American Chemical Society</u> **121**(11): 2631-2632.

Johnston, K. P., D. Cho, et al. (2001). "Water in Carbon Dioxide Macroemulsions and Miniemulsions with a Hydrocarbon Surfactant." <u>Langmuir</u> **17**(23): 7191-7193.

Johnston, K. P., K. L. Harrison, et al. (1996). "Water-in-Carbon Dioxide Microemulsions: An Environment for Hydrophiles Including Proteins." <u>Science</u> **271**: 624.

Johnston, K. P., D. G. Peck, et al. (1989). "Modeling supercritical mixtures: how predictive is it?" <u>Industrial & Engineering Chemistry Research</u> **28**(8): 1115-25.

Johnston, K. P. and P. S. Shah (2004). "Materials science: Making nanoscale materials with supercritical fluids." <u>Science (Washington, DC, United States)</u> **303**(5657): 482-483.

Jung, J. and M. Perrut (2001). "Particle design using supercritical fluids: Literature and patent survey." <u>Journal of Supercritical Fluids</u> **20**(3): 179-219.

Karthikeyan, J., C. C. Berndt, et al. (1997). "Plasma spray synthesis of nanomaterial powders and deposits." Materials Science & Engineering, A: Structural Materials: Properties, Microstructure and Processing **A238**(2): 275-286.

Khomane, R. B., A. Manna, et al. (2002). "Synthesis and Characterization of Dodecanethiol-Capped Cadmium Sulfide Nanoparticles in a Winsor II Microemulsion of Diethyl Ether/AOT/Water." Langmuir **18**(21): 8237-8240.

Kiely, C. J., J. Fink, et al. (1998). "Spontaneous ordering of bimodal ensembles of nanoscopic gold clusters." Nature (London) **396**(6710): 444-446.

Kitchens, C. L., M. C. McLeod, et al. (2003). "Solvent Effects on the Growth and Steric Stabilization of Copper Metallic Nanoparticles in AOT Reverse Micelle Systems." Journal of Physical Chemistry B **107**(41): 11331-11338.

Kitchens, C. L. and C. B. Roberts "Copper Nanoparticle Synthesis in Compressed Liquid and Supercritical Fluid Reverse Micelle Systems." Industrial & Engineering Chemistry Research: ACS ASAP.

Kitchens, C. L. and C. B. Roberts (2004). "Copper nanoparticle synthesis in compressed liquid and supercritical fluid reverse micelle systems." Industrial & Engineering Chemistry Research **43**(19): 6070-6081.

Kordikowski, A., A. P. Schenk, et al. (1995). "Volume expansions and vapor-liquid equilibria of binary mixtures of a variety of polar solvents and certain near-critical solvents." Journal of Supercritical Fluids **8**(3): 205-16.

Korgel, B. A., S. Fullam, et al. (1998). "Assembly and Self-Organization of Silver Nanocrystal Superlattices: Ordered "Soft Spheres"." Journal of Physical Chemistry B **102**(43): 8379-8388.

Korgel, B. A., S. Fullam, et al. (1998). "Assembly and Self-Organization of Silver Nanocrystal Superlattices: Ordered \"Soft Spheres\"." Journal of Physical Chemistry B **102**(43): 8379-8388.

Kung, H. H. and E. I. Ko (1996). "Preparation of oxide catalysts and catalyst supports- a review of recent advances." Chemical Engineering Journal (Lausanne) **64**(2): 203-214.

Lee, C. T., Jr., K. P. Johnston, et al. (2001). "Droplet Interactions in Water-in-Carbon Dioxide Microemulsions Near the Critical Point: A Small-Angle Neutron Scattering Study." Journal of Physical Chemistry B **105**(17): 3540-3548.

Li, D., Z. Liu, et al. (2000). "Phase equilibria of CO2-PET-phenol system and generation of PET powders by supercritical CO2 anti-solvent." Polymer **41**(15): 5707-5712.

Li, M. and J. C. Li (2006). "Size effects on the band-gap of semiconductor compounds." Materials Letters **60**(20): 2526-2529.

Lide, D. R. (1994). Handbook of Chemistry and Physics, 75th Edition.

Lide, D. R. (1995). Handbook of Organic Solvents, CRC: Boca Raton, FL.

Lin, X. M., H. M. Jaeger, et al. (2001). "Formation of Long-Range-Ordered Nanocrystal Superlattices on Silicon Nitride Substrates." Journal of Physical Chemistry B **105**(17): 3353-3357.

Liu, C. and Z. J. Zhang (2001). "Size-Dependent Superparamagnetic Properties of Mn Spinel Ferrite Nanoparticles Synthesized from Reverse Micelles." Chemistry of Materials **13**(6): 2092-2096.

Liu, D., J. Zhang, et al. (2003). "Recovery of TiO2 nanoparticles synthesized in reverse micelles by antisolvent CO2." Colloids and Surfaces, A: Physicochemical and

Engineering Aspects **227**(1-3): 45-48.

Liu, J., M. Anand, et al. (2006). "Synthesis and Extraction of b-D-Glucose-Stabilized Au Nanoparticles Processed into Low-Defect, Wide-Area Thin Films and Ordered Arrays Using CO2-Expanded Liquids." Langmuir **22**(9): 3964-3971.

Liu, J., B. Han, et al. (2001). "Investigation of nonionic surfactant Dynol-604 based reverse microemulsions formed in supercritical carbon dioxide." Langmuir **17**(26): 8040-8043.

Liu, J., B. Han, et al. (2003). "Effect of antisolvent carbon dioxide on the polymerization of methyl methacrylate in different solvents." Journal of Supercritical Fluids **25**(1): 91-97.

Liu, J., G. Qin, et al. (2006). "Facile \"green\" synthesis, characterization, and catalytic function of b-D-glucose-stabilized Au nanocrystals." Chemistry--A European Journal **12**(8): 2131-2138.

Liu, J., P. Raveendran, et al. (2005). "Self-assembly of b-d glucose-stabilized Pt nanocrystals into nanowire-like structures." Chemical Communications (Cambridge, United Kingdom)(23): 2972-2974.

Liu, J., P. Raveendran, et al. (2005). "Synthesis of Ag and AgI quantum dots in AOT-stabilized water-in-CO2 microemulsions." Chemistry--A European Journal **11**(6): 1854-1860.

Liu, Z., J. Wang, et al. (2002). "Study on the phase behavior of cholesterol-acetone-CO2 system and recrystallization of cholesterol by antisolvent CO2." Journal of Supercritical Fluids **24**(1): 1-6.

Lora, M., F. Rindfleisch, et al. (1999). "Influence of the alkyl tail on the solubility of

poly(alkyl acrylates) in ethylene and CO2 at high pressures: experiments and modeling." Journal of Applied Polymer Science **73**(10): 1979-1991.

Lu, Q., F. Gao, et al. (2004). "Biomolecule-assisted reduction in the synthesis of single-crystalline tellurium nanowires." Advanced Materials (Weinheim, Germany) **16**(18): 1629-1632.

Lu, Q., F. Gao, et al. (2005). "A Green Chemical Approach to the Synthesis of Tellurium Nanowires." Langmuir **21**(13): 6002-6005.

Lu, Y., G. L. Liu, et al. (2005). "High-Density Silver Nanoparticle Film with Temperature-Controllable Interparticle Spacing for a Tunable Surface Enhanced Raman Scattering Substrate." Nano Letters **5**(1): 5-9.

Mahamuni, S. (1999). "Optical properties of semiconductor nanoparticles." Solid State Physics, Proceedings of the DAE Solid State Physics Symposium, 41st, Kurukshetra, India, Dec. 27-31, 1998: 33-36.

Maillard, F., S. Schreier, et al. (2005). "Influence of particle agglomeration on the catalytic activity of carbon-supported Pt nanoparticles in CO monolayer oxidation." Physical Chemistry Chemical Physics **7**(2): 385-393.

Martin, J. E., J. P. Wilcoxon, et al. (2000). "Control of the Interparticle Spacing in Gold Nanoparticle Superlattices." Journal of Physical Chemistry B **104**(40): 9475-9486.

McHugh, M. A. and V. J. Krukonis (1986). Supercritical Fluid Extraction: Principles and Practice.

McLeod, M. C., M. Anand, et al. (2004). "Nanoparticle Size Selection and Deposition Using CO_2-Gas Expanded Liquids as Tunable Solvent Systems." (In preparation).

246

McLeod, M. C., M. Anand, et al. (2005). "Precise and Rapid Size Selection and Targeted Deposition of Nanoparticle Populations Using CO2 Gas Expanded Liquids." Nano Letters **5**(3): 461-465.

McLeod, M. C., W. F. Gale, et al. (2004). "Metallic Nanoparticle Production Utilizing a Supercritical Carbon Dioxide Flow Process." Langmuir **20**(17): 7078-7082.

McLeod, M. C., C. L. Kitchens, et al. (2004). "CO_2-Expanded Liquid Deposition of Ligand Stabilized Nanoparticles as Uniform, Wide Area Nanoparticle Films." (Submitted to Langmuir).

McLeod, M. C., C. L. Kitchens, et al. (2005). "CO2-Expanded Liquid Deposition of Ligand-Stabilized Nanoparticles as Uniform, Wide-Area Nanoparticle Films." Langmuir **21**(6): 2414-2418.

McLeod, M. C., R. S. McHenry, et al. (2003). "Synthesis and Stabilization of Silver Metallic Nanoparticles and Premetallic Intermediates in Perfluoropolyether/CO_2 Reverse Micelle Systems." Journal of Physical Chemistry B **107**(12): 2693-2700.

Messing, G. L., S. C. Zhang, et al. (1993). "Ceramic powder synthesis by spray pyrolysis." Journal of the American Ceramic Society **76**(11): 2707-26.

Mukasa, K., K. Sueoka, et al. (1995). "Spin-polarized STM and its family." Materials Science & Engineering, B: Solid-State Materials for Advanced Technology **B31**(1-2): 69-76.

Murcia, M. J., D. L. Shaw, et al. (2006). "Facile Sonochemical Synthesis of Highly Luminescent ZnS-Shelled CdSe Quantum Dots." Chemistry of Materials **18**(9): 2219-2225.

Murray, C. B., C. R. Kagan, et al. (1995). "Self-organization of CdSe nanocrystallites

into three-dimensional quantum dot superlattices." <u>Science (Washington, D. C.)</u> **270**(5240): 1335-8.

Murray, C. B., C. R. Kagan, et al. (2000). "Synthesis and characterization of monodisperse nanocrystals and close-packed nanocrystal assemblies." <u>Annual Review of Materials Science</u> **30**: 545-610.

Murray, C. B., D. J. Norris, et al. (1993). "Synthesis and characterization of nearly monodisperse CdE (E = sulfur, selenium, tellurium) semiconductor nanocrystallites." <u>Journal of the American Chemical Society</u> **115**(19): 8706-15.

Nakamoto, K. (1997). <u>Infrared and Raman Spectra of Inorganic and Coordination Compounds</u>. New York, John Wiley & Sons.

Nakashima, P. N. H., T. Tsuzuki, et al. (1999). "Particle size dependence of the volume plasmon energy in cadmium sulfide quantum dots by electron energy loss spectroscopy." <u>Journal of Applied Physics</u> **85**(3): 1556-1559.

Napper, D. H. (1983). <u>Polymeric Stabilization of Colloidal Dispersions</u>.

Nave, S., J. Eastoe, et al. (2000). "What Is So Special about Aerosol-OT? 2. Microemulsion Systems." <u>Langmuir</u> **16**(23): 8741-8748.

Nave, S., J. Eastoe, et al. (2000). "What Is So Special about Aerosol-OT? 1. Aqueous Systems." <u>Langmuir</u> **16**(23): 8733-8740.

Nenadovic, M. T., T. Rajh, et al. (1985). "Size quantization in small semiconductor particles." <u>Journal of Physical Chemistry</u> **89**(3): 397-9.

Ohara, P. C. and W. M. Gelbart (1998). "Interplay between Hole Instability and Nanoparticle Array Formation in Ultrathin Liquid Films." <u>Langmuir</u> **14**(12): 3418-3424.

Ohara, P. C., D. V. Leff, et al. (1995). "Crystallization of opals from polydisperse nanoparticles." Physical Review Letters **75**(19): 3466-9.

Ohde, H., F. Hunt, et al. (2001). "Synthesis of silver and copper nanoparticles in a water-in-supercritical-carbon dioxide microemulsion." Chemistry of Materials **13**(11): 4130-4135.

O'Neill, M. L., Q. Cao, et al. (1998). "Solubility of homopolymers and copolymers in carbon dioxide." Industrial & Engineering Chemistry Research **37**(8): 3067-3079.

Pal, B., T. Torimoto, et al. (2004). "Size and Structure-Dependent Photocatalytic Activity of Jingle-Bell-Shaped Silica-Coated Cadmium Sulfide Nanoparticles for Methanol Dehydrogenation." Journal of Physical Chemistry B **108**(48): 18670-18674.

Peck, D. G., A. J. Mehta, et al. (1989). "Pressure tuning of chemical reaction equilibria in supercritical fluids." Journal of Physical Chemistry **93**(10): 4297-304.

Peng, D.-Y. and D. B. Robinson (1976). "A new two-constant equation of state." Industrial & Engineering Chemistry Fundamentals **15**(1): 59-64.

Peng, X., J. Wickham, et al. (1998). "Kinetics of II-VI and III-V Colloidal Semiconductor Nanocrystal Growth: \"Focusing\" of Size Distributions." Journal of the American Chemical Society **120**(21): 5343-5344.

Perrut, M. and J.-Y. Clavier (2003). "Supercritical Fluid Formulation: Process Choice and Scale-up." Industrial & Engineering Chemistry Research **42**(25): 6375-6383.

Petit, C., P. Lixon, et al. (1993). "In Situ Synthesis of Silver Nanocluster in AOT Reverse Micelles." Journal of Physical Chemistry **97**(49): 12974-83.

Petroski, J. and M. A. El-Sayed (2003). "FTIR Study of the Adsorption of the Capping

Material to Different Platinum Nanoparticle Shapes." <u>Journal of Physical Chemistry A</u> **107**(40): 8371-8375.

Pileni, M. P., T. Zemb, et al. (1985). "Solubilization by reverse micelles: solute localization and structure perturbation." <u>Chemical Physics Letters</u> **118**(4): 414-20.

Poole, C. P. J. and F. J. Owens (2003).

<u>Introduction to Nanotechnology</u>. Hoboken, Wiley-Interscience.

Porter, M. D., T. B. Bright, et al. (1987). "Spontaneously organized molecular assemblies. 4. Structural characterization of n-alkyl thiol monolayers on gold by optical ellipsometry, infrared spectroscopy, and electrochemistry." <u>Journal of the American Chemical Society</u> **109**(12): 3559-68.

Potluri, V. K., J. Xu, et al. (2002). "Peracetylated Sugar Derivatives Show High Solubility in Liquid and Supercritical Carbon Dioxide." <u>Org. Lett.</u> **4**(14): 2333.

Prasad, B. L. V., S. I. Stoeva, et al. (2002). "Digestive ripening of thiolated gold nanoparticles: the effect of alkyl chain length." <u>Langmuir</u> **18**(20): 7515-7520.

Randolph, T. W., A. D. Randolph, et al. (1993). "Sub-micrometer-sized biodegradable particles of poly(L-lactic acid) via the gas antisolvent spray precipitation process." <u>Biotechnology Progress</u> **9**(4): 429-35.

Rao, N. P., H. J. Lee, et al. (1997). "Nanostructured materials production by hypersonic plasma particle deposition." <u>Nanostructured Materials</u> **9**(1-8): 129-132.

Raveendran, P., J. Fu, et al. (2003). "Completely green synthesis and stabilization of metal nanoparticles." <u>Journal of the American Chemical Society</u> **125**(46): 13940-13941.

Raveendran, P. and S. L. Wallen (2003). "Dissolving carbohydrates in CO2: Renewable

materials as CO2-philes." <u>ACS Symposium Series</u> **860**(Supercritical Carbon Dioxide): 270-284.

Reverchon, E. (1999). "Supercritical antisolvent precipitation of micro- and nano-particles." <u>Journal of Supercritical Fluids</u> **15**(1): 1-21.

Rindfleisch, F., T. DiNoia, et al. (1996). "Solubility of Polymers and Copolymers in Supercritical CO2." <u>J. Phys. Chem.</u> **100**: 15581.

Rogach, A. L., A. Kornowski, et al. (1999). "Synthesis and Characterization of a Size Series of Extremely Small Thiol-Stabilized CdSe Nanocrystals." <u>Journal of Physical Chemistry B</u> **103**(16): 3065-3069.

Rossetti, R., S. Nakahara, et al. (1983). "Quantum size effects in the redox potentials, resonance Raman spectra, and electronic spectra of cadmium sulfide crystallites in aqueous solution." <u>Journal of Chemical Physics</u> **79**(2): 1086-8.

Ryoo, W., S. E. Webber, et al. (2003). "Water-in-Carbon Dioxide Microemulsions with Methylated Branched Hydrocarbon Surfactants." <u>Industrial & Engineering Chemistry Research</u> **42**(25): 6348-6358.

Sadangi, R. K., O. A. Voronov, et al. (1999). "Synthesis of WC/Co/diamond nanocomposites." <u>Advances in Science and Technology (Faenza, Italy)</u> **15**(Ceramics: Getting into the 2000's, Pt. C): 305-312.

Sarbu, T., T. Styranec, et al. (2000). "Non-fluorous polymers with very high solubility in supercritical CO2 down to low pressures." <u>Nature (London)</u> **405**(6783): 165-168.

Sarbu, T., T. J. Styranec, et al. (2000). "Design and Synthesis of Low Cost, Sustainable CO$_2$-philes." <u>Ind. Eng. Chem. Res.</u> **39**(12): 4678.

Sarbu, T., T. J. Styranec, et al. (2000). "Non-fluorous Polymers with Very High

Solubility in Supercritical CO_2 Down to Low Pressures." <u>Nature</u> **405**: 165.

Saunders, A. E. and B. A. Korgel (2004). "Second Virial Coefficient Measurements of Dilute Gold Nanocrystal Dispersions Using Small-Angle X-ray Scattering." <u>Journal of Physical Chemistry B</u> **108**(43): 16732-16738.

Saunders, A. E., P. S. Shah, et al. (2004). "Solvent Density-Dependent Steric Stabilization of Perfluoropolyether-Coated Nanocrystals in Supercritical Carbon Dioxide." <u>Journal of Physical Chemistry B</u> **108**(41): 15969-15975.

Saunders, A. E., P. S. Shah, et al. (2004). "Inverse Opal Nanocrystal Superlattice Films." <u>Nano Letters</u> **4**(10): 1943-1948.

Saunders, A. E., M. B. Sigman, Jr., et al. (2004). "Growth Kinetics and Metastability of Monodisperse Tetraoctylammonium Bromide Capped Gold Nanocrystals." <u>Journal of Physical Chemistry B</u> **108**(1): 193-199.

Shafi, K. V. P. M., A. Ulman, et al. (2001). "Sonochemical synthesis of functionalized amorphous iron oxide nanoparticles." <u>Langmuir</u> **17**(16): 5093-5097.

Shah, P. S., T. Hanrath, et al. (2004). "Nanocrystal and Nanowire Synthesis and Dispersibility in Supercritical Fluids." <u>Journal of Physical Chemistry B</u> **108**(28): 9574-9587.

Shah, P. S., J. D. Holmes, et al. (2000). "Steric Stabilization of Nanocrystals in Supercritical CO2 Using Fluorinated Ligands." <u>Journal of the American Chemical Society</u> **122**(17): 4245-4246.

Shah, P. S., J. D. Holmes, et al. (2002). "Size-Selective Dispersion of Dodecanethiol-Coated Nanocrystals in Liquid and Supercritical Ethane by Density Tuning." <u>Journal of Physical Chemistry B</u> **106**(10): 2545-2551.

Shah, P. S., S. Husain, et al. (2001). "Nanocrystal Arrested Precipitation in Supercritical Carbon Dioxide." Journal of Physical Chemistry B **105**(39): 9433-9440.

Shah, P. S., S. Husain, et al. (2002). "Role of Steric Stabilization on the Arrested Growth of Silver Nanocrystals in Supercritical Carbon Dioxide." Journal of Physical Chemistry B **106**(47): 12178-12185.

Shah, P. S., K. P. Johnston, et al. (2003). "Effect of steric stabilization on the synthesis of nanocrystals in supercritical carbon dioxide." Proceedings of the National Conference on Environmental Science and Technology, Greensboro, NC, United States, Sept. 8-10, 2002: 323-332.

Shah, P. S., B. J. Novick, et al. (2003). "Kinetics of Nonequilibrium Nanocrystal Monolayer Formation: Deposition from Liquid Carbon Dioxide." Nano Letters **3**(12): 1671-1675.

Shah, P. S., M. B. Sigman, Jr., et al. (2003). "Single-step self-organization of ordered macroporous nanocrystal thin films." Advanced Materials (Weinheim, Germany) **15**(12): 971-974.

Shekunov, B. Y., J. Baldyga, et al. (2001). "Particle Formation by Mixing with Supercritical Antisolvent at High Reynolds Numbers." Chem. Eng. Sci. **56**: 2421.

Shen, Z., M. A. McHugh, et al. (2003). "CO2-solubility of oligomers and polymers that contain the carbonyl group." Polymer **44**(5): 1491-1498.

Shi, L., V. De Paoli, et al. (2006). "Synthesis and Application of Quantum Dots FRET-Based Protease Sensors." Journal of the American Chemical Society **128**(32): 10378-10379.

Shipway, A. N., E. Katz, et al. (2000). "Nanoparticle arrays on surfaces for electronic,

optical, and sensor applications." <u>ChemPhysChem</u> **1**(1): 18-52.

Siebrands, T., M. Giersig, et al. (1993). "Steric exclusion chromatography of nanometer-sized gold particles." <u>Langmuir</u> **9**(9): 2297-300.

Sigman, M. B., Jr., A. E. Saunders, et al. (2004). "Metal Nanocrystal Superlattice Nucleation and Growth." <u>Langmuir</u> **20**(3): 978-983.

Span, R. and W. Wagner (1996). "A new equation of state for carbon dioxide covering the fluid region from the triple-point temperature to 1100 K at pressures up to 800 MPa." <u>Journal of Physical and Chemical Reference Data</u> **25**(6): 1509-1596.

Spuller, M. T. and D. W. Hess (2004). "CO2-expanded liquids as alternatives to conventional solvents for resist and residue removal." <u>Proceedings - Electrochemical Society</u> **2003-26**(Cleaning Technology in Semiconductor Device Manufacturing VIII): 240-245.

Spuller, M. T. and D. W. Hess (2004). Gas-expanded liquids, methods of use thereof, and systems using gas-expanded liquids for cleaning integrated circuits of photoresists. <u>U.S. Pat. Appl. Publ.</u> Us, (USA). 9 pp.

Stallings, W. E. and H. H. Lamb (2003). "Synthesis of nanostructured titania powders via hydrolysis of titanium isopropoxide in supercritical carbon dioxide." <u>Langmuir</u> **19**(7): 2989-2994.

Stone, M. T., S. R. P. Da Rocha, et al. (2003). "Molecular Differences between Hydrocarbon and Fluorocarbon Surfactants at the CO2/Water Interface." <u>Journal of Physical Chemistry B</u> **107**(37): 10185-10192.

Stone, M. T., P. G. Smith, Jr., et al. (2004). "Low interfacial free volume of Stubby surfactants stabilizes water-in-carbon dioxide microemulsions." <u>Journal of</u>

Physical Chemistry B **108**(6): 1962-1966.

Stowell, C. and B. A. Korgel (2001). "Self-Assembled Honeycomb Networks of Gold Nanocrystals." Nano Letters **1**(11): 595-600.

Sun, L. and R. M. Crooks (2002). "Dendrimer-Mediated Immobilization of Catalytic Nanoparticles on Flat, Solid Supports." Langmuir **18**(21): 8231-8236.

Sun, Y., B. Y. Shekunov, et al. (2003). "Refractive index of supercritical CO2-ethanol solvents." Chemical Engineering Communications **190**(1): 1-14.

Talapin, D. V., A. L. Rogach, et al. (2001). "Highly Luminescent Monodisperse CdSe and CdSe/ZnS Nanocrystals Synthesized in a Hexadecylamine-Trioctylphosphine Oxide-Trioctylphosphine Mixture." Nano Letters **1**(4): 207-211.

Tao, Y. T. (1993). "Structural comparison of self-assembled monolayers of n-alkanoic acids on the surfaces of silver, copper, and aluminum." Journal of the American Chemical Society **115**(10): 4350-8.

Templeton, A. C., W. P. Wuelfing, et al. (2000). "Monolayer-Protected Cluster Molecules." Accounts of Chemical Research **33**(1): 27-36.

Thomas, C. A., R. J. Bonilla, et al. (2001). "Hydrogenation of carbon dioxide catalyzed by ruthenium trimethylphosphine complexes - Effect of gas pressure and additives on rate in the liquid phase." Canadian Journal of Chemistry **79**(5/6): 719-724.

Valden, M., X. Lai, et al. (1998). "Onset of catalytic activity of gold clusters on titania with the appearance of nonmetallic properties." Science (Washington, D. C.) **281**(5383): 1647-1650.

Vincent, B., P. F. Luckham, et al. (1980). "The effect of free polymer on the stability of sterically stabilized dispersions." Journal of Colloid and Interface Science **73**(2):

508-21.

Viswanatha, R., S. Sapra, et al. (2005). "Electronic structure of and quantum size effect in III-V and II-VI semiconducting nanocrystals using a realistic tight binding approach." Physical Review B: Condensed Matter and Materials Physics **72**(4): 045333/1-045333/10.

Vossmeyer, T., L. Katsikas, et al. (1994). "CdS Nanoclusters: Synthesis, Characterization, Size Dependent Oscillator Strength, Temperature Shift of the Excitonic Transition Energy, and Reversible Absorbance Shift." Journal of Physical Chemistry **98**(31): 7665-73.

Watkins, J. J., J. M. Blackburn, et al. (1999). "Chemical Fluid Deposition: Reactive Deposition of Platinum Metal from Carbon Dioxide Solution." Chemistry of Materials **11**(2): 213-215.

Wei, M., T. Musie Ghezai, et al. (2002). "CO_2-expanded solvents: unique and versatile media for performing homogeneous catalytic oxidations." Journal of the American Chemical Society **124**(11): 2513-7.

Wei, M., G. T. Musie, et al. (2002). "CO2-Expanded Solvents: Unique and Versatile Media for Performing Homogeneous Catalytic Oxidations." Journal of the American Chemical Society **124**(11): 2513-2517.

Weller, H., H. M. Schmidt, et al. (1986). "Photochemistry of colloidal semiconductors. Onset of light absorption as a function of size of extremely small cadmium sulfide particles." Chemical Physics Letters **124**(6): 557-60.

Whetten, R. L., J. T. Khoury, et al. (1996). "Nanocrystal gold molecules." Advanced Materials (Weinheim, Germany) **8**(5): 428-33.

Wilson, O. M., R. W. J. Scott, et al. (2004). "Separation of Dendrimer-Encapsulated Au and Ag Nanoparticles by Selective Extraction." Chem. Mater. **16**(22): 4202-4204.

Wilson, W. L., P. F. Szajowski, et al. (1993). "Quantum confinement in size-selected, surface-oxidized silicon nanocrystals." Science **262**(5137): 1242-4.

Wohltjen, H. and A. W. Snow (1998). "Colloidal metal-insulator-metal ensemble chemiresistor sensor." Analytical Chemistry **70**(14): 2856-2859.

Wu, M. K., R. S. Windeler, et al. (1993). "Controlled synthesis of nanosized particles by aerosol processes." Aerosol Science and Technology **19**(4): 527-48.

Wu, N., L. Fu, et al. (2004). "Interaction of Fatty Acid Monolayers with Cobalt Nanoparticles." Nano Letters **4**(2): 383-386.

Xie, X., J. S. Brown, et al. (2002). "Phase-transfer catalyst separation by CO2 enhanced aqueous extraction." Chemical Communications (Cambridge, United Kingdom)(10): 1156-1157.

Xie, X., C. L. Liotta, et al. (2004). "CO2-Protected Amine Formation from Nitrile and Imine Hydrogenation in Gas-Expanded Liquids." Industrial & Engineering Chemistry Research **43**(24): 7907-7911.

Yeo, S., P. G. Debenedetti, et al. (1993). "Supercritical Antisolvent Process for Substituted Para-Linked Aromatic Polyamides: Phase Equilibrium and Morphology Study." Macromolecules **26**: 6207.

Yosef, M., A. K. Schaper, et al. (2005). "Stabilization of the Thermodynamically Favored Polymorph of Cadmium Chalcogenide Nanoparticles CdX (X = S, Se, Te) in the Polar Mesopores of SBA-15 Silica." Inorganic Chemistry **44**(16): 5890-5896.

Yu, K. M. K., A. M. Steele, et al. (2003). "Synthesis of well-dispersed nanoparticles

within porous solid structures using surface-tethered surfactants in supercritical CO2." Journal of Materials Chemistry **13**(1): 130-134.

Zeng, J., W. Lu, et al. (2006). "Fine tuning photoluminescence properties of CdSe nanoparticles by surface states modulation." Journal of Colloid and Interface Science **298**(2): 685-688.

Zhang, J., B. Han, et al. "Recovery of silver nanoparticles synthesized on AOT/C(12)E(4) mixed reverse micelles by antisolvent CO(2)." Chemistry (Weinheim an der Bergstrasse, Germany) FIELD Publication Date:2002 Sep 2 **8**(17): 3879-83. FIELD Reference Number: FIELD Journal Code:9513783 FIELD Call Number:.

Zhang, J., B. Han, et al. (2002). "Recovery of silver nanoparticles synthesized in AOT/C12E4 mixed reverse micelles by antisolvent CO2." Chemistry--A European Journal **8**(17): 3879-3883.

Zhang, J., B. Han, et al. (2001). "A new method to recover the nanoparticles from reverse micelles: recovery of ZnS nanoparticles synthesized in reverse micelles by compressed CO$_2$." Chemical Communications(24): 2724-2725.

Zhang, J., B. Han, et al. (2004). "Size tailoring of ZnS nanoparticles synthesized in reverse micelles and recovered by compressed CO2." Journal of Supercritical Fluids **30**(1): 89-95.

Zhang, J., M. Xiao, et al. "Preparation of ZnS/CdS composite nanoparticles by coprecipitation from reverse micelles using CO2 as antisolvent." Journal of colloid and interface science FIELD Publication Date:2004 May 1 **273**(1): 160-4. FIELD Reference Number: FIELD Journal Code:0043125 FIELD Call Number:.

Zhang, J., M. Xiao, et al. (2004). "Preparation of ZnS/CdS composite nanoparticles by

coprecipitation from reverse micelles using CO2 as antisolvent." Journal of Colloid and Interface Science **273**(1): 160-164.

Zhang, R., J. Liu, et al. (2003). "Organic reactions and nanoparticle preparation in CO2-induced water/P104/p-Xylene microemulsions." Chemistry--A European Journal **9**(10): 2167-2172.

Zhang, R., J. Liu, et al. (2002). "Compressed CO2-Assisted Formation of Reverse Micelles of PEO-PPO-PEO Copolymer." Macromolecules **35**(21): 7869-7871.

Zhang, Y., D. Kang, et al. (2005). "Supported Platinum Nanoparticles by Supercritical Deposition." Industrial & Engineering Chemistry Research **44**(11): 4161-4164.

Zhang, Z., R. C. Patel, et al. (2000). "Stable silver clusters and nanoparticles prepared in polyacrylate and inverse micellar solutions." Journal of Physical Chemistry B **104**(6): 1176-1182.

Zhu, J., Y. Koltypin, et al. (2000). "General Sonochemical Method for the Preparation of Nanophasic Selenides: Synthesis of ZnSe Nanoparticles." Chemistry of Materials **12**(1): 73-78.

Zinola, C. F., C. Gomis-Bas, et al. (1998). "A Semiempirical Quantum Approach to the Formation of Carbon Dioxide Adsorbates on Pt(100) and Pt(111) Cluster Surfaces." Langmuir **14**(14): 3901-3908.